CORA Cork Open Research Archive
Cartlann Taighde Oscailte Chorcaí

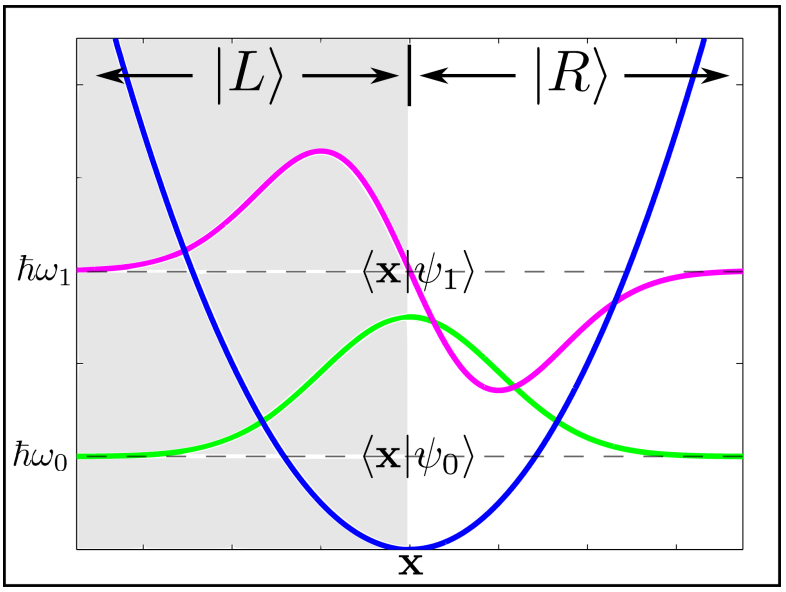
Title	Spatial and energetic mode dynamics of cold atomic systems
Authors	O'Sullivan, Brian
Publication date	2012-12
Original Citation	O'Sullivan, Brian, 2012. Spatial and energetic mode dynamics of cold atomic systems. PhD Thesis, University College Cork.
Type of publication	Doctoral thesis
Link to publisher's version	http://pra.aps.org/pdf/PRA/v79/i3/e033602, http://arxiv.org/abs/1001.1331v1, http://pra.aps.org/pdf/PRA/v83/i5/e053620
Rights	© 2012, Brian O'Sullivan - http://creativecommons.org/licenses/by-nc-nd/3.0/
Download date	2026-11-03 14:04:00
Item downloaded from	https://hdl.handle.net/10468/963



UCC
University College Cork, Ireland
Coláiste na hOllscoile Corcaigh

UNIVERSITY COLLEGE CORK

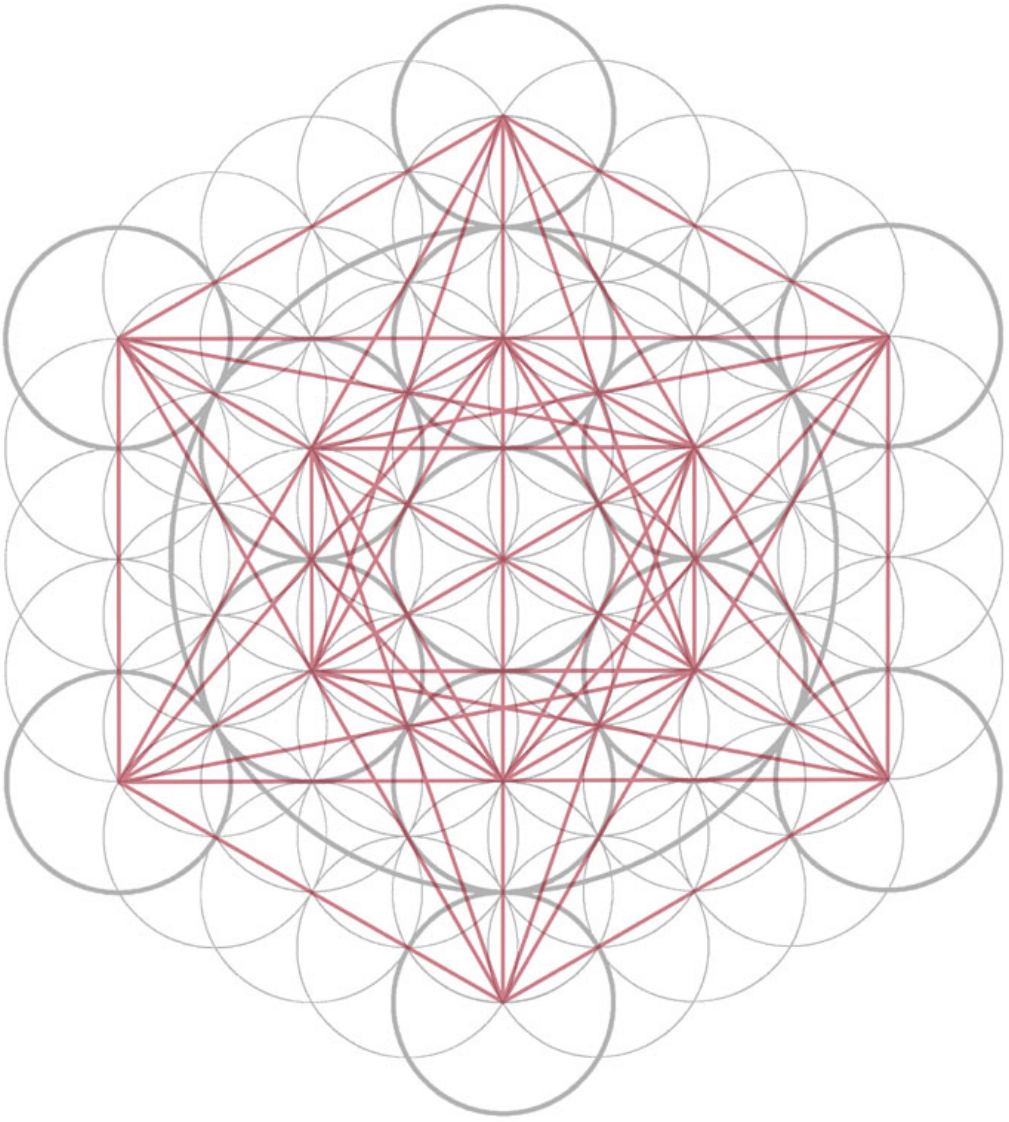
Spatial and Energetic Mode Dynamics of Cold Atomic Systems



Brian O'Sullivan

A thesis submitted in partial fulfillment for the
degree of Doctor of Philosophy, in the
College of Science, Engineering and Food Science
Department of Physics

December 2012



Metatron's Cube (MC). The red lines form an orthographic projection of the five Platonic solids. The Tetrahedron (4 faces), Hexahedron (Cube, 6 faces), Octahedron (8 faces), Dodecahedron (12 faces) and the Icosahedron (20 faces). The first three platonic solids are perfectly blueprinted in MC. The last two platonic solids are imperfectly blueprinted in MC, but are perfectly blueprinted in the transcendental form of MC, i.e. to first order, a single MC bordered by 6 MCs. *Image: Charles Gilchrist.*

"I regard consciousness as fundamental. I regard matter as derivative from consciousness. We cannot get behind consciousness. Everything that we talk about, everything that we regard as existing, postulates consciousness. ... All matter originates and exists only by virtue of a force which brings the particle of an atom to vibration and holds this most minute solar system of the atom together. We must assume behind this force the existence of a conscious and intelligent mind. This mind is the matrix of all matter."[1]

[1]Max Planck; The Observer (1931) and a speech in Florence, Italy (1944) respectively.

The Heist

"and they comin' over here
takin' all our jobs and all our women"
- Contemporary Irish folk saying

They arrived in the middle of the night
in a Hi Ace van, untaxed, uninsured,
and broke in without a sound.
They took Mary from the warmth of her bed
and bungled her into the van's hold
right in between the minimum wage gig
at Freddie's Fresh Fish and Chips
and the local meat processor's
twelve-hour a day cleaning job.

Imelda was perched
on top of the under-the-table,
part-time, no love, all abuse, glass washer
cum sick mopper stint at Barry's Bar.
They exchanged worried looks, Mary
and Imelda. More worrying
however, was the aura of content
around the younger lad, John.

He was sat beneath
the Barista's job at Coco's Café
where you'd be lucky to get paid
the correct wage, let alone on time.
He had enjoyed being at the mercy
of the Pole's and Nigerian's grip,
because ever since he was shoveled
into the middle of a hurling pitch
by the spade of his father's hand
he has always felt like
a stranger in a strange land.

Cal Doyle

UNIVERSITY COLLEGE CORK

Abstract

College of Science, Engineering and Food Science
Department of Physics

Doctor of Philosophy

by Brian O'Sullivan

In this thesis we relate the formal description of various cold atomic systems in the energy eigenbasis, to the observable spatial mode dynamics. Herein the 'spatial mode dynamics' refers to the direction of photon emission following the spontaneous emission of an excited fermion in the presence of a same species and spin ideal anisotropic Fermi sea in its internal ground state. Due to the Pauli principle, the presence of the ground state Fermi sea renders the phase space, anisotropic and only partially accessible, thereby affecting the direction of photon emission following spontaneous emission.

The spatial and energetic mode dynamics also refers to the quantum 'tunneling' interaction between localised spatial modes, synonymous with double well type potentials. Here we relate the dynamics of the wavefunction in both the energetic and spatial representations. Using this approach we approximate the relationship between the spatial and energetic representations of a wavefunction spanning three spatial and energetic modes. This is extended to a process known as Spatial Adiabatic Passage, which is a technique to transport matter waves between localised spatial modes. This approach allows us to interpret the transport of matter waves as a signature of a geometric phase acquired by the one of the internal energy eigenstates of the system during the cyclical evolution. We further show that this geometric phase may be used to create spatial mode qubit and qutrit states.

Acknowledgements

Getting to the point where I am now writing the acknowledgements for this thesis has been a long struggle. There were many instances when I could not see when, or if, this work would come to a point where I could consider it finished. Whilst the thesis itself has found it own inevitable conclusion after these 6 years, and I am left to accept it as it is, there are many questions that I have been unable to answer for myself, so the work itself continues. To be in a position where one has the time to spend struggling to resolve, and finding meaning in, the dissatisfaction that comes with confusion is to be truly privileged. It is a testament to the countless lives that have touched my own which have made this a reality for me. To acknowledge them all is a task that I do not expect to be able to achieve, but if I can be so pardoned, here I will briefly mention those with whom I recognise the most direct correlation. Whilst some know who they are, most don't realise.

First of all, I would like to thank my parents and brothers; Louise, Michael, Barry, Colum and Ciaràn, whose unfledging support and encouragement has made the writing of this thesis possible. I cannot thank you enough, but only acknowledge that this work was only possible with the support and opportunity you have afforded me. This incorporates my extended family and relations. I'd like to thank the friends that have been a part of my life and have helped to forge me to become the person I am today. These span back to school and otherwise in Laois, Cork and beyond, and have came into and parted from my life throughout the years. The class of 2002 in Pres., and class of 2006 in U.C.C., and the many people I have been so lucky to know as an extension from these relationships. To all the guys and girls involved with football and skating, from C.A.S. crew to Rain-Sleet-Snow, and pre- to post- times, you've kept me sane and hungry for exploration. To the women that have graced my life during the creation of this thesis, Nicola, Sandra and Karen, for your invaluable support and encouragement which made this possible. For helping to put the final touches on, and proof reading my drafts (I don't know how you did it!) and for just being a generally amazing woman, thank you K!

From a physics point of view, I would like to thank Thomas Busch for his commitment to, and natural ability for, creating an environment in which physics can flourish, with always an open door and time to discuss whatever (physics or otherwise) may be on your mind. Of the many inspirational teachers that provided the necessary glimpses of physics that have sparked and fueled my curiosity, I'd like to mention and acknowledge Michel Vandyck and Paddy McCarthy. Of special note, I'd like to acknowledge Nicolino LoGullo, whose wealth of knowledge and clarity of reasoning, coupled with a hunger and dedication to wisdom, made possible the resolution of this ridiculous tunneling problem

that I found so difficult. I don't think I would have ever finished otherwise!! I'd also like to thank the members, past and present, of the Ultracold Quantum Gases group, and my peers in U.C.C. for the coffees, discussions, lunches, chats and their general enthusiasm which is inspirational. Finally, I would like to acknowledge those intangible forces that have guided me through.

Brian O'Sullivan

Declaration of Authorship

I, Brian o'Sullivan, declare that this thesis titled, 'Spatial and Energetic Mode Dynamics of Cold Atomic Systems', and the work presented in it are my own. I confirm that:

- This work was done wholly or mainly while in candidature for a research degree of Doctor of Philosophy at University College Cork.
- Where any part of this thesis has previously been submitted for a degree or any other qualification at this University or any other institution, this has been clearly stated.
- Where I have consulted the published work of others, this is always clearly cited.
- Where I have quoted from the work of others, the source is always given. With the exception of such quotations, this thesis is entirely my own work.
- I have acknowledged all main sources of help.
- This thesis is based on work done by myself under the supervision of Thomas Busch. Work that has been done in collaboration with others is clearly stated.

Signed: (12/12/12)

The viva voce for this PhD thesis was performed on the 12^{th} of December, 2012, in the presence of Prof. Jordi Mompart, Dr. Andreas Ruschhaupt and Prof. Thomas Busch.

External Examiner:
Prof. Jordi Mompart - Universitat Autónoma de Barcelona, Spain.

Internal Examiner:
Dr. Andreas Ruschhaupt - University College Cork, Ireland.

Principle Supervisor:
Prof. Thomas Busch - Okinawa Institute of Science and Technology, Japan.

Secondary Supervisor:
Dr. Paddy McCarthy - University College Cork, Ireland.

To Mam and Dad . . .

Contents

Acknowledgements **vii**

Declaration of Authorship **ix**

1 Introduction **1**

2 Spontaneous Emission in Anisotropic Fermi Seas **12**
2.1 Fermi's Golden Rule . . . 13
2.1.1 Time Dependent Perturbations . . . 13
2.1.2 The Interaction Picture . . . 14
2.1.3 Time Evolution Operator in the Interaction Picture . . . 15
2.1.4 Perturbative Expansion . . . 16
2.1.5 Formal Solution . . . 18
2.2 The Anisotropic Harmonic Oscillator . . . 19
2.2.1 Eigenenergies of the Pancake and Cigar Trap Shapes . . . 20
2.2.2 Energy Level Degeneracy . . . 22
2.2.2.1 Energy Level Degeneracy for the Pancake Trap . . . 23
2.2.2.2 Energy Level Degeneracy for the Cigar Trap . . . 23
2.2.3 Three Further Identities . . . 24
2.2.3.1 First Identity . . . 24
2.2.3.2 Second Identity . . . 25
2.2.3.3 Third Identity . . . 26
2.2.4 Sum of States up to the Fermi Level for the Pancake and Cigar Traps . . . 27
2.3 Model . . . 28
2.4 The Transition Matrix . . . 30
2.4.1 Free Transition Matrix Element . . . 31
2.4.1.1 Evaluation of the Matrix Element . . . 31
2.4.1.2 Formal Solution . . . 32
2.4.1.3 Zero Temperature Transition . . . 33
2.4.2 Angular Emission . . . 33
2.4.2.1 Application of the Translation Matrix Element . . . 34
2.4.2.2 Preliminary Reduction - Pancake Case . . . 35
2.4.2.3 General Solution . . . 37
2.5 Emission Patterns in Anisotropic Traps . . . 39
2.5.1 Emission Probabilities . . . 39
2.5.2 Tight and Soft Axes Emission . . . 44

2.5.3 Fine Structure 45
2.6 Conclusions and Outlook 49

3 Spatial Adiabatic Passage 51
3.1 The Dressed Atom 53
3.2 Stimulated Raman by Adiabatic Passage 56
3.2.1 Three Level Atom 57
3.2.2 System Hamiltonian 59
3.2.3 Eigensystem of the Hamiltonian 60
3.2.4 Adiabaticity Constraints 61
3.2.5 Population Transfer 62
3.2.6 Rabi Oscillations in Optical and Matter Wave Settings 64
3.2.7 From STIRAP to SAP 65
3.2.8 Further Remarks 67
3.2.9 Numerical Methods 68
3.3 SAP in Waveguide Settings 69
3.3.1 Summary of Experimental Cooling and Trapping Processes 70
3.3.2 Magnetic Guiding and Trapping 71
3.3.3 Linear Quadrupole Waveguide 75
3.3.4 Majorana Losses 76
3.3.5 Bias Field 77
3.3.6 Waveguide SAP: Model 78
3.3.7 Waveguide SAP: Experimental Parameters 82
3.3.8 Concluding Remarks 84
3.4 SAP in Radio Frequency Dressed Potentials 85
3.4.1 Atom Trapping Via Radio Frequency Radiation 86
3.4.2 Landau-Zener Hamiltonian 89
3.4.3 Multimode Radio Frequency Arrays 90
3.4.4 Multimode Radio Frequency SAP: Experimental Parameters . . . 92
3.4.5 Non-linear Systems 94
3.4.6 Concluding Remarks 99

4 Spatial Mode Dynamics 101
4.1 Quantum Tunneling 103
4.1.1 Statement of the Tunneling Phenomenon 104
4.1.2 Density Evolution in the Energetic Mode Basis 105
4.1.3 Density Evolution in the Spatial Mode Basis 107
4.2 Mapping the Spatial and Energetic Hamiltonians 108
4.2.1 Analysis 109
4.2.2 Remarks 112
4.3 The Spatial Mode Kets 113
4.4 Discussion 118

5 Three Level Atom Optics via the Tunneling Interaction - Revisited 119
5.1 Spatial Adiabatic Passage: Model 121
5.1.1 The Hamiltonian And The Time Dependent Potential 121
5.1.2 The Trap Motions 123

5.1.3 The Energy Eigensystem . . . 123
5.2 SAP in the Spatial Mode Basis . . . 129
5.2.1 The Trap Basis Approximation . . . 130
5.2.2 Temporal Evolution of the Spatial Modes . . . 131
5.2.3 Numerical Calculations . . . 132
5.3 SAP in the Energetic Basis . . . 134
5.3.1 SAP: Adiabaticity And The Geometric Phase . . . 136
5.3.2 SAP: Counter-Intuitive Trap Paths . . . 138
5.3.3 SAP: Intuitive Trap Paths . . . 140
5.4 Fractional SAP . . . 141
5.5 Discussion . . . 146

6 SAP In Four Mode Systems - Qubit and Qutrit States 148
6.1 The Hamiltonian And The Time Dependent Potential . . . 149
6.1.1 The Trap Motions . . . 151
6.1.2 The Finite Difference Method . . . 152
6.1.3 The Energy Eigensystem and Initialisation of the State Vector . . . 154
6.2 Spatial Adiabatic Passage . . . 155
6.2.1 The Spatial Hamiltonian Matrix . . . 156
6.2.2 Phase Evolution of the Wavefunction . . . 158
6.3 Spatial Mode Phase Imprinting . . . 161
6.4 Dynamic Phases in Four Mode SAP . . . 163
6.5 Discussion . . . 164

7 Conclusion and Outlook 166

A Supplementary Calculations 169
A.1 Chapter 2: Transition Matrix . . . 169
A.2 Chapter 2: Cigar Trap . . . 170
A.3 Chapter 3: Laser Mode . . . 170
A.4 Chapter 3: Magnetic Field of a Linear Conductor . . . 172
A.5 Chapter 3: Commutator Evaluation . . . 174
A.6 Chapter 4: N Spatial-Energetic Mode Relationship . . . 175
A.7 Chapter 4: Non Diagonal Hamiltonian Matrix . . . 177

B Numerical Techniques 181
B.1 The Split Operator Method . . . 181
B.2 The Finite Difference Method . . . 183

Bibliography 185

Chapter 1

Introduction

With the dawn of the 20th century rose two new physical theories, relativity and quantum mechanics (QM), which have irreversibly changed our perception of the natural world. The former professes that space and time are not the absolute concepts they were previously believed to be, but are in fact relative concepts. The latter, which is the focus of this thesis, infers that specific physical processes cannot be known deterministically, but only probabilistically. The strength of both theories has been the unequivocal agreement of their predictions with experiment. These schools of thought have left such an indelible mark on modern physics that theories, deviating from the principles of relativity and quantum mechanics, are now specified by the titles 'non-relativistic' and 'classical' physics respectively.

Whilst both theories call into question 'old truths' that have been axioms of physics for centuries, none is more paradigm shattering than the quantum formalism. Max Plank's discovery that monochromatic light is a stable stream of discrete packets of energy, called photons, stimulated a progressive departure from the 'continuous process' viewpoint of classical physics. Similarly, it emerged that observables such as angular momentum, electric charge, and spin can only assume certain allowed values. The transition between two values being a discrete quantum jump. For instance, the electron (classically thought of as a particle) orbiting the nucleus of an atom, is described by QM as a standing wave; i.e. it has a frequency and wave nature associated with it. The transition energy between two standing wave orbitals is carried by an absorbed or emitted photon (a light particle). From here quantum mechanics begins to establish a world view to contrast classical notions. We have not only learned that states are discrete, but also that light and matter exhibit the characteristics of both waves and particles.

The predictions of quantum theory are so contrary to common experience that it is often perceived as a secondary description of reality, out of which the classical world

emerges. Built upon the mathematics of linear algebra, QM makes use of wavefunctions to describe physical processes. The favoured interpretation of the wavefunction is the probabilistic interpretation; *"Quantum mechanics gives only the probability of an experimental result."*[1] *"The wave function does not in any way describe a state which could be that of a single system; it relates rather to many systems, to an 'ensemble of systems' in the sense of statistical mechanics."*[2] In this manner QM departs dramatically from the classical view as we are forced to relinquish any hope of knowing a quantum object's state with certainty. The wavefunction is assumed to be composed of a weighted distribution of possible states until measurement is taken, at which point the wavefunction 'collapses' into the classical 'reality'. This is the so-called 'Copenhagen Interpretation.'

Not only is QM confined to predicting the results of experimental measurements, but there lies a deeper and more fundamental bound to the knowledge that can be extracted from a given system. Accurate knowledge of one measured component of a pair of complimentary observables (such as position and momentum), implies a broad uncertainty of the other. The act of measuring is commonly referred to as observation, which is performed by an observer. However, the observer itself is loosely defined; There is no clear relationship between the measuring apparatus, and the operator. In the absence of knowing, how does one determine whether a measurement occurred? *"Are you and I observers? Is a cow an observer? What about a stone?"*[3] In any case, observation of an observable requires an exchange of energy which results in the observed 'data', but also perturbs the state of the quantum object. Thus the system is affected by the observation. For the complimentary observables of position and momentum, both cannot be known with certainty, and are bounded by Heisenberg's uncertainty relation. *"We must give up the idea of complete localization of the particle in a theoretical model. This seems to me the permanent upshot of Heisenberg's principle of uncertainty."*[4]

The dual particle-wave nature of both matter and light is elegantly captured in Young's double slit experiment. Therein, a continuous stream of electrons bombard a double slit, whose separation is of the order of the de Broglie wavelength of the particles, to produce an interference pattern indicative of the wave nature of the electron. Measuring the slits to determine which one the electron passes through, destroys its wave nature. The pattern on the screen then exhibits the characteristics of a particle. In a literal sense we can say that the observer creates the particle, but rather than prematurely lend ourselves to flights of fancy, it is appropriate to first recall, *"what we observe is not*

[1] David Bohm; With the exception of 3, the quotes in this text were selected from a resource of quotes found at www.spaceandmotion.com.

[2] Albert Einstein.

[3] Michael A. Vandyck. Co-author of 'Geometry Spinors and Applications', and 'Topics in Differential Geometry'.

[4] Albert Einstein.

nature itself, but nature exposed to our method of questioning ... Light and matter are both single entities, and the apparent duality arises in the limitations of our language."[5] Furthermore, movement in QM *"is discontinuous, not causally determinate and not well defined ... Heisenberg's uncertainty principle made a detailed ordering of space and time impossible."*[6] The results of the double slit experiment are both intriguing and shocking, and in effect point to either a void in our interpretation or to a conceptual limitation of the quantum theory. *"The more success the quantum physics has, the sillier it looks. ... I think that a 'particle' must have a separate reality independent of the measurements. That is an electron has spin, location and so forth even when it is not being measured. I like to think that the moon is there even if I am not looking at it."*[7]

QM continues to challenge the classical world view, as the theory states that under certain conditions there is an apparent immediate connection of distant particles; coined 'Entanglement'. When particles interact and are separated, the states of the particles are interdependent. The quantum object is assumed to occupy a superposition until a measurement is performed, at which point, the state of the measured particle exactly determines the partner particle's state. This 'non local' connection between the particles is a purely quantum mechanical effect. It has been thought that *"the statistical theories hide a completely determined and ascertainable reality behind variables which elude our experimental techniques,"*[8] but this point is contested by QM. The signature of the entangled quantum object's 'non-classicality', for lack of a better word, is found in the violation of the Bell inequalities, which uphold that no local hidden variable theory can reproduce the predictions of QM. The quantum theory infers that quantum objects are not independent or separable in the classical sense, but rather they maintain a spatially unbounded, and non local connection of varying degrees. *"That the guiding wave, in the general case, propagates not in ordinary three-space but in a multi-dimensional configuration space is the origin of the notorious 'non-locality' of quantum mechanics."*[9]

If we accept that the quantum mechanical model of reality is adequate, it follows that the classical world view is itself inadequate. Such a profound statement does not come without friction, and, throughout the development of QM many conflicting views have arisen. Whilst QM professes that nature is both an indeterminate, and non-locally interconnected whole, a general feeling of discontent and uneasiness with the theory remains. *"Quantum mechanics is very impressive. But an inner voice tells me that it is not yet the real thing. The theory produces a good deal but hardly brings us closer to*

[5] Werner Heisenberg.
[6] David Bohm.
[7] Albert Einstein.
[8] Louis DeBroglie
[9] John Steward Bell. *"... It is a merit of the de Broglie-Bohm version to bring this out so explicitly that it cannot be ignored."*

the secret of the Old One. I am at all events convinced that [God] does not play dice."[10] With QM certainly comes frustration, as we are left with a philosophy from which one cannot ascertain where QM leaves off, and our classical 'reality' begins. For some, this is a satisfactory state of affairs; *"It is wrong to think that the task of physics is to find out how Nature is. Physics concerns what we say about Nature."*[11] But for others, the partial view of reality offered by QM is unacceptable; *"Let me say at the outset, that in this discourse, I am opposing not a few special statements of quantum physics held today (1950s), I am opposing as it were the whole of it, I am opposing its basic views that have been shaped 25 years ago, when Max Born put forward his probability interpretation, which was accepted by almost everybody ... I don't like it, and I'm sorry I ever had anything to do with it."*[12]

There persists a hope that QM points to a more tangible physical theory, remaining to be uncovered. It has been argued that QM cannot be embedded in a locally causal physical theory, but this is based on the assumption that the chosen experimental parameters are free variables. However, *"it might be that this apparent freedom is illusory. Perhaps experimental parameters and experimental results are both consequences, or partially so, of some common hidden mechanism. Then the apparent non-locality could be simulated."*[13] On the other hand it may arise that QM, as it stands, will prove inadequate as a natural philosophy. QM may resist precise formulation, in the sense that when precise formulation *"is attempted, we find an unmovable finger obstinately pointing outside the subject, to the mind of the observer, to the Hindu scriptures, to God, or even only Gravitation."*[14] In any event, what cannot be contested, is that QM has endured the trials of the 20^{th} century, and today it remains one of the best available natural theories. With the above in mind, we continue making our way through the dark cave of QM, until a means of shedding further light on the quantum realm becomes obvious. *"It is my task to convince you not to turn away because you don't understand it. You see my physics students don't understand it. ... That is because I don't understand it. Nobody does."*[15]

"This statistical interpretation is now universally accepted as the best possible interpretation for quantum mechanics, even though many people are unhappy with it. People had got used to the determinism of the last century, where the present determines the future completely, and they now have to get used to a different situation in which the present only gives one information of a statistical nature about the future. A good many

[10] Albert Einstein.
[11] Neils Bohr.
[12] Erwin Schrödinger.
[13] John Steward Bell.
[14] John Steward Bell.
[15] Richard Feynman.

people find this unpleasant; Einstein has always objected to it. The way he expressed it was: 'The good God does not play with dice.' Schrödinger also did not like the statistical interpretation and tried for many years to find an interpretation involving determinism for his waves. But it was not successful as a general method. I must say that I also do not like indeterminism. I have to accept it because it is certainly the best that we can do with our present knowledge. One can always hope that there will be future developments which will lead to a drastically different theory from the present quantum mechanics and for which there may be a partial return of determinism. However, so long as one keeps to the present formalism, one has to have this indeterminism."[16]

The success of QM cannot be ignored, and as the field progressively advances, QM demands attention to its underlying world view. QM has reversed the usual classical notion that the independent elementary parts of the world are the fundamental reality, and that various systems are merely particular contingent forms and arrangements of these parts. Rather, we say that inseparable quantum interconnectedness of the whole universe is the fundamental reality, and that relatively independent behaving parts are merely particular and contingent forms within this whole. Each of the aspects of quantum theory combine to suggest that the universe is an indivisible whole, rather than being composed of individual elements which interact as if separately existent. In quantum mechanics the whole is objective and the parts are the result of analysis. Areas of quantum mechanics whereby the whole behaves (to some extent) like independent parts are limiting cases which allow to recover a classical analysis.[17]

The difficulty that arises in coming to grips with QM is that there remains a conflict between the quantum mechanical description of reality, and our feeling of *"what reality ought to be."*[18] In discussing the inherent non-locality of nature, revealed by the quantum theory, John Bell offers the following words; *"The discomfort that I feel is associated with the fact that the observed perfect quantum correlations seem to demand something like the 'genetic' hypothesis. For me, it is so reasonable to assume that the photons in those experiments carry with them programs, which have been correlated in advance, telling them how to behave. This is so rational that I think that when Einstein saw that, and the others refused to see it, he was the rational man. The other people, although history has justified them, were burying their heads in the sand ... So for me, it is a pity that Einstein's idea doesn't work. The reasonable thing just doesn't work."*[19]

[16] Paul Dirac.
[17] Adapted from various statements made by David Bohm in his interviews and books.
[18] Richard Feynman.
[19] John Stewart Bell.

Crescendo

The sophistication of modern experimental apparatus and techniques has facilitated unprecedented access to the quantum realm. Quantum mechanical systems are fundamentally very hard to observe; they are highly sensitive to perturbations and decoherence from the external environment, which destroy the system's quantum nature. In relative terms, the lifetime of quantum systems is very short, but the high degree of precision and control offered by state of the art technologies maintains their lifetime well beyond that necessary for experimental purposes.

The complimentary theoretical and experimental development of quantum mechanics has seen the emergence of quantum technologies, which exploit properties unique to quantum mechanical systems. At the core of many quantum technologies is the concept that information is the fundamental building block of reality. Quantum information is then the physical information encoded in quantum objects, the smallest unit of which is the qubit. As the Hilbert space dimension of a many particle quantum system grows exponentially large with particle number, the number of possible quantum states, and information encoded within the system, grows exponentially. A quantum computer takes advantage of quantum mechanical properties to perform operations on a registrar of qubits; offering the possibility to simulate complex quantum systems, which is presently well beyond the capability of classical computers.

Quantum computing and quantum information processing has grown to become a central topic in QM, but many other subdisciplines and related fields have emerged. The experimental and theoretical study of the transfer of quantum information between two parties has given rise to disciplines such as quantum information theory, quantum communication, quantum cryptography, quantum error correction and quantum teleportation. Whilst the sensitivity of such quantum systems to noise from the external environment remains a formidable challenge, these quantum systems offer potentialities that are unachievable in classical systems. The exception being quantum teleportation, which refers to the transfer of a quantum state between two quantum objects, rather than the classical 'star trek' teleportation, which is waaaaay cooler. In a general sense, the potential for quantum technologies to far surpass the precision offered by classical approaches is a key motivation for the study and experimental realisation of quantum technologies in fields such as quantum imaging (high resolution imaging), quantum metrology (high precision measurements) and quantum clocks (unparalleled accuracy of time measurements). The correlation between experimental and theoretical development of quantum mechanical phenomena, such as quantum tunneling, has produced (to name a few) extremely sensitive magnetometers, quantum tunnel diodes, and the scanning tunneling microscope which has facilitated the imaging of individual atoms on the surface of a metal.

Reminiscent of the rapid development of classical computing technology; the progressive maturity of experimental technology has reached the point where single and composite quantum objects, can be confined to stable environments. Ultracold quantum gases are one class of quantum objects that are central to both the experimental and theoretical study of QM. The many formidable experimental challenges of reaching the quantum degenerate regime have, to a large extent, been overcome. Today the production of ultracold quantum gases is commonplace. A dilute gas of identical integer-spin particles (bosons), cooled close to absolute zero, occupy the lowest available energetic mode (ground state) forming a state of matter known as a Bose-Einstein condensate. Conversely a gas of identical half integer-spin particles (fermions), cooled close to absolute zero, 'stack up' to occupy all available energetic modes, from the ground state to the so-called Fermi level, forming what is known as a Fermi sea. Cutting edge technologies such as Feshbach resonances, allow for precise control over, and study of, the inter-atomic interactions in ultracold quantum gases. Furthermore, the geometry of the trapping environments can be dynamically fashioned using available technologies such as the atom chip, optical dipole traps, and optical lattices to name a few. Advances in lasing technologies has made single spatial site addressing possible. The technical detailing of these and other techniques has been so refined that they are applicable to not only ultracold quantum gases, but also to single and small number quantum particle systems.

Although the challenge of developing technological applications is appealing from both a practical and theoretical point of view, in this thesis we explore a select number of quantum mechanical systems from a fundamental point of view, that have only recently come within reach of experimental realisation. This thesis is dedicated to establishing an understanding as to the relationship between the observable spatial mode dynamics of ultracold atomic systems, and their formal descriptions in the energy eigenbasis. The context of the spatial mode dynamics studied herein specifically refers to the spatial direction of photon emission, following the decay of an excited atom, and the tunneling interaction between spatial modes, exhibited by single and composite bosonic systems. The stimulation and inhibition of spontaneous emission in optical cavities is currently well understood. Here we study an alternative means of not only inhibiting, but also directing the spontaneous emission of an excited atom, without the use of an optical cavity. It has been shown that processes involving the transport of matterwaves between localised spatial modes, and the transfer of electrons between atomic orbitals, display a complimentary relationship. Whilst quantum state transport in optical settings is well established, from both theoretical and experimental perspectives, the same cannot be said for matterwave transport. Here we propose two novel schemes that show promise of demonstrating the transport of matterwaves between localised spatial modes. A fundamental aspect of matterwave transport processes, is the so-called quantum tunneling

interaction. As this phenomenon is of interest to a wide range of communities in quantum mechanics, we detail the relationship between the evolution of a quantum state in the energy eigenbasis and the spatial mode basis, thereby providing a mapping between the Hamiltonian operators in each basis, and subsequently a closed form solution for the tunneling interaction matrix elements. We then apply this knowledge to the transport of matterwaves, to relate the formal description of the quantum state transport in the spatial and energetic mode settings. This approach provides an intuitive understanding as to the mechanisms of matterwave transport and the creation of spatial qubit and qutrit states.

Outline Of Thesis

The thesis consists of three different sections, which are connected through presenting new ideas for quantum engineering, and detailing the relationship between the observable spatial mode dynamics of quantum systems, and their formal description in the energy eigenbasis. To begin we draw a parallel between, the probable direction of photon emission and the geometry of the underlying phase space, which may be modified using ultracold Fermi gases. Thereafter we propose two experimentally accessible schemes that show promise of demonstrating matterwave transport between localised spatial regions. The remainder of the thesis is then dedicated to studying the time evolution of matterwaves in the spatial and energetic representations. We first pronounce the spatial-energetic relationship for a wavefunction occupying two spatial and energetic modes. We show that the Hamiltonians in both bases are related by a rotation, which allows the recovery of the correct phase and amplitude dynamics of the wavefunction in the assigned spatial regions. We compliment this study, by applying the knowledge gained, to a pioneering work on the transport of matterwaves. We find that this approach derives a robust picture of the underlying mechanisms of matterwave transport. Thereafter, we examine a four spatial mode system in a two dimensional setting, and demonstrate the possibility for the creation of spatial qubit and qutrit states. The content of each chapter is as follows;

Chapter 2: Inhibition of Spontaneous Emission In Anisotropic Fermi Seas. *We examine the process of spontaneous emission in cold fermionic samples and show how a directional photon source can be constructed without an optical cavity.* The inhibition and stimulation of spontaneous emission is an intriguing area of study from technological (lasers etc.) and conceptual (fundamental principles) points of view. In this chapter we study the following model; an idealised spin polarised Fermi Sea (FS) at

zero temperature, in its internal ground state, confined to a harmonic trapping potential. A same species and spin fermion occupies the ground state energetic mode of the harmonic potential and is in an internally excited state. We investigate in detail how the presence of the FS effects the spontaneous emission rate (also called decay rate) of the excited fermion. We find that there are three essential contributing factors that effect the decay rate; these are the Fermi energy of the FS, the Lamb-Dicke parameter (the ratio of the recoil and trap energy), and finally the geometry of the trapping potential, whether this be isotropic, cigar or pancake shaped.

To begin, we first review Fermi's golden rule, which tells us the transition rate between two energy eigenmodes. As the degeneracies of the energy levels for anisotropic trapping geometries are fundamental to this work, we derive the closed form relations for the energy level degeneracy (and the sum of states) for the cigar and pancake shaped traps, as a function of the aspect ratio. Thereafter we present the theoretical and mathematical model of our system, and establish the expression for the angular decay rate of our excited fermion, as a function of the Fermi energy, the Lamb-Dicke parameter, and the aspect ratio. This relation predicts spatially anisotropic decay rates for anisotropic settings. We progressively explain the source of the emission pattern's fine structure, and show that in the one dimensional limit (cigar trap), spontaneous emission is tightly confined along the soft axis; which is of potential interest and use as a directional photon source. The journal reference for this work is; Physical Review A **79**, 033602 (2009).

Chapter 3: Spatial Adiabatic Passage. *We propose two novel schemes for the experimental realisation of matterwave transport between localised spatial regions.* Quantum state transfer in quantum optical systems is a topic that has experienced an explosion of growth over the past number of years. The matterwave counterpart, dubbed spatial adiabatic passage (SAP), is the transfer of matterwaves between localised spatial modes. Whilst many theoretical studies have been developed, this subject remains experimentally challenging. To help bridge the gap, we outline in this chapter two experimental proposals that offer the potential to observe the transport of matterwaves, via the SAP technique.

The chapter is organised as follows; as SAP is a subject that has its origins in optics, we first provide the theoretical description of the light matter interaction for a two level system. We extend this analysis to a three level time dependent optical scheme, under the rotating wave approximation, to arrive at the usual 3×3 interaction Hamiltonian. We discuss the procedure for adiabatic quantum state transfer, and then outline the relationship between state transfer in optics and the matterwave setting. Thereafter we make our two experimental proposals; the first of which is the transfer of a neutral atom between the outer waveguides of a three waveguide system. The waveguide geometry

is created using a technological marvel known as the 'atom chip'. We sketch the background of the cooling process and detail the interaction between the atom and magnetic field which makes the trapping possible. Subsequently we provide numerical results of our approach which demonstrate the feasibility of our proposal. The journal reference for this work is; Physica Scripta **T140**, 014029 (2010).

Our second experimental proposal applies multi-mode radio frequency dressed potentials to an inhomogeneous magnetic field, thereby creating a three site time dependent trapping geometry, suitable for the SAP protocol. We derive the related Landau-Zener Hamiltonian and extend this model to the multi-mode radio frequency case. For the remainder of the chapter, we focus on the numerical analysis of the adiabatic trap motions that facilitate the transport of the quantum state. We demonstrate that in the case of a single atom/non-interacting BEC, the state is transferred with high fidelity. For a weakly interacting BEC, the fidelity of the transport is inhibited. We show that suitably adjusting the trapping frequencies of the outer traps increases the transport fidelity. The journal reference for this work is; Physical Review A **83**, 053620 (2011).

Chapter 4: Spatial Mode Dynamics. *We deduce the relationship of the wavefunction in the energy eigenbasis and the left-right or spatial mode basis, synonymous with the double well potential.* Quantum tunneling was originally used to statistically describe nuclear decay, as an alpha particle's probability to emerge from the nucleus by penetrating an energetic barrier. Today quantum tunneling is a fundamental component of quantum physics, with a broad range of applications. An open question that arises with respect to SAP processes, is on the relationship between the numerical integration of Schrödinger's equation, and the 'spatial mode' Hamiltonian matrix. This operator describes the local energy of, and the tunneling interaction between, the spatial modes. Here we derive a mapping between both pictures for the two spatial-energetic mode case.

We consider a potential divided into two spatial regions or 'spatial modes' which can have an arbitrary size but collectively span the whole Hilbert space. We compare the density dynamics of a wavefunction occupying two energetic modes, according to the Schrödinger picture, and the spatial mode (or Rabi) picture. Equating both representations results in two sets of closed form solutions, for each matrix element of the spatial mode Hamiltonian. We apply the mapping to a quantum state in a one dimensional harmonic oscillator, and provide an interpretation of the results.

To conclude, we propose three reasonable criteria one may expect from a definition of the spatial mode kets, and consequently show that a proper definition of these kets is not obvious. We present a trial solution, and discuss why it fails.

Chapter 5: Three Level Atom Optics Via The Tunneling Interaction - Revisited. *We apply our knowledge, gained from chapter 4, to an original work on matterwave transport, with an aim to establish the relationship between the time evolution of the proposed system in both the energy eigenbasis, and the spatial mode basis.* We apply our spatial mode mapping (suitably adapted) to a well known SAP scheme. We outline a technique to approximate the three level spatial mode Hamiltonian matrix. To achieve this, we first derive the energy eigenfunctions of the piecewise triple-well harmonic oscillator potential. A basis for the spatial modes can be defined via the energy eigenfunctions, which we use to rotate between the Schrödinger and spatial mode representations. In this approach, the local energy and tunneling interaction terms exhibit the expected behaviour, and a significant coupling between the outer traps appears toward the midpoint of the process. The transport of a quantum state between spatial modes is (as expected) observed.

To conclude, we analyse the system in the energy eigenmode basis, which offers an easy and accessible explanation for the *counter-intuitive* trap motions. This approach is developed to provide an alternative interpretation as to why the *intuitive* trap motions does not facilitate state transport. Adhering to the SAP protocol, we compare the initial and final states in the energy eigenbasis showing that the cyclical process has imprinted a π phase on the so-called 'dark state' energy eigenfunction. As the acquired phase is independent of the total time taken for the process, matterwave transport in SAP protocols may be interpreted as the signature of a geometric phase, acquired by the system from the cyclical evolution.

Chapter 6: SAP In Four Mode Systems - Qubit and Qutrit States. *We extend our tools developed in chapter 5 to a four mode system, and show the potentiality of creating qubit and qutrit states between localised spatial modes.* Geometric phases in four (and multi) level optical systems allow for a much richer phenomenology, in the fact that they afford the creation of qubit and qutrit spatial mode states. Here we make use of four harmonic traps in a Y-shaped arrangement on a two-dimensional plane. We provide an outline of the numerical methods used to recover the energy eigenfunctions of this potential. The usual 'counter-intuitive' trap motions creates an even superposition state between the target traps. Thereafter this state can be transported back to the initial trap by reversing the protocol. Here we show that applying a phase difference between the spatial modes of the even superposition state, inhibits the transfer to the initial trap. This effect permits the creation of a qutrit state between the outer spatial modes, and we account for this effect. Thereafter we show that by breaking the symmetry of the trap motions, qutrit states may also be created but are subject to dynamical contributions that detract from the predictability of the final state. We demonstrate this effect, discuss and conclude.

Chapter 2

Spontaneous Emission in Anisotropic Fermi Seas

An observable facet of atomic matter is the finite lifetime of "excited" atomic states. Whilst an atom may absorb a quanta of energy, and thus assume an "excited" state, its ability to retain this energy is limited. In free space, vacuum fluctuations drive every excited atom to its ground state, resulting in the emission of a photon with an energy equal to the energy difference of these two states. This form of interaction between the atom and the vacuum is known as spontaneous emission.

The vacuum plays a key role in spontaneous emission and without it this phenomenon would not occur. As the available vacuum modes can be altered with an optical cavity, the lifetime of an excited atom confined to such a cavity, is also altered. Like a guitar string, the frequency of the modes of a cavity are integer multiples of its fundamental frequency f_c. It was observed by Purcell [1] that the lifetime of an atom's 'excited state' is reduced when the atom is embedded in a cavity tuned to its transition frequency f_t. This is the *stimulation* of spontaneous emission. Conversely the lifetime of the atom is increased when the cavity is mistuned. It was later shown by Kleppner [2] that for an ideal (or high quality factor) cavity, spontaneous emission is *inhibited* when the fundamental frequency of the cavity is greater than the excited atom's transition frequency $f_c > f_t$. In the ideal case, the atom and vacuum are decoupled, and this is known as the inhibition of spontaneous emission.

Inhibited spontaneous emission is not limited to cavity settings. Of particular interest is the effect of ultracold fermionic gases [3] on the decay rate of a same-species (and spin) excited fermion. The inhibition of spontaneous emission in the presence of a ground state Fermi sea is another fundamental prediction which results directly from the Pauli principle [4, 5]. A degenerate spin polarised Fermi sea occupies the available

Hilbert space for a single, excited atom of the same species and spin. Due to the Pauli principle, the Fermi sea effectively blocks out a large amount of the phase space that would otherwise be available to the excited atom after a de-excitation transition. This leads to a modification of the emission properties of the excited atom, characterised by the size of the Fermi sea, the temperature of the system, and the anisotropy of the trapping potential [5]. The influence on the lifetime of the excited atom has been recently investigated [5, 6] and the effect was shown to be an atom-optical analogue of well known effects in cavity quantum electrodynamics [1].

In this work we investigate the influence of this Pauli-blocking effect on the spatial decay rate of a single excited fermion, in the presence of an anisotropic (ground state) FS. The fact that the emission spectrum becomes anisotropic was first shown in [5, 6] and a simple explanation for this effect was given. Here we investigate and account for the pattern formation in detail. In particular we consider highly anisotropic traps, which can be experimentally produced today using atom chips, or optical lattices [7–9].

2.1 Fermi's Golden Rule

The fingerprint of each atomic element is found in its own unique emission spectrum. As the energy of the electron is quantised, each spectral line of the emission line spectrum is an allowed transition between atomic orbitals. However these spectral lines differ in intensity, which is physically related to the transition probability (per unit time) from an occupied energy eigenstate, into a continuum of final states. Fermi's Golden Rule is an equation that allows for the calculation of transition rates, by considering the decay of the excited atom as a time dependent perturbation.

2.1.1 Time Dependent Perturbations

In this section we review the general formalism of Fermi's Golden rule. The following derivation largely follows the procedure outlined in J.J. Sakurai's 'Modern Quantum Mechanics' [10]. We consider a system, whereby a time dependent perturbation $\mathbf{V}(t)$ is imparted to the system at $t = 0$. This perturbation is constant in time, and acts to provide the required energy to facilitate a transition between the basis states of the Hilbert space:

$$\mathbf{V}(t) = \mathbf{k} \cdot \mathbf{r}\, \Theta(t - t_0), \tag{2.1}$$

where $\mathbf{k}$ is the wavevector of the photon released due to the perturbation and $\mathbf{r} = (\hat{x}, \hat{y}, \hat{z})$. $\Theta(x)$ is the Heaviside step function, with $\Theta(t - t_0) = 0$ for $t < t_0$ and $\Theta(t) = 1$ for $t \geq t_0$.

The perturbation $\mathbf{V}(t)$ is assumed to not deform the basis states $|\psi_\nu\rangle$ of the Hilbert space and as such they remain time independent. It follows that the Hamiltonian of the system $\mathbf{H}(t)$ may be decomposed into a sum of the Hamiltonian of the unperturbed system $\mathbf{H}_0$ and the time dependent perturbation $\mathbf{V}(t)$.

$$\mathbf{H}(t) \;=\; \mathbf{H}_0 \;+\; \mathbf{V}(t). \tag{2.2}$$

The Hilbert space of $\mathbf{H}_0$ is spanned by an infinite set of orthogonal eigenfunctions $|\psi_\nu\rangle$, for $\nu = 0, 1, 2, \ldots, \infty$. The "unperturbed" Hamiltonian operates on the basis states as, $\mathbf{H}_0|\psi_\nu\rangle = E_\nu|\psi_\nu\rangle$, where E_ν is the eigenenergy of $|\psi_\nu\rangle$. These basis states constitute the accessible energetic modes of the Hilbert space.

2.1.2 The Interaction Picture

At $t = 0$, the state of the system is given by,

$$|\Psi(0)\rangle_S \;=\; \sum_\nu \; c_\nu(0)\; |\psi_\nu\rangle. \tag{2.3}$$

We wish to find $c_\nu(t)$ for $t > 0$ such that,

$$|\Psi(t)\rangle_S \;=\; \sum_\nu \; c_\nu(t)\; e^{-\imath E_\nu t/\hbar}\; |\psi_\nu\rangle. \tag{2.4}$$

The effect of the time dependent perturbation $\mathbf{V}(t)$ is to incur a transition between the basis states, therefore the coefficients $c_\nu(t)$ are time dependent. This interaction makes the phase evolution of the basis states coefficients difficult to evaluate. In order to resolve for the time dependence of the coefficients $c_\nu(t)$, we 'wash out' the usual dynamical evolution to consider only the interaction induced by the perturbation term. This is commonly referred to as the interaction picture, and is given by,

$$|\Psi(t)\rangle_I \;=\; e^{\imath \mathbf{H}_0 t/\hbar}\; |\Psi(t)\rangle_S, \tag{2.5a}$$

$$|\Psi(t)\rangle_I \;=\; \sum_\nu \; c_\nu(t)\; |\psi_\nu\rangle, \tag{2.5b}$$

At $t = 0$ the state ket in the interaction picture $|\Psi(t)\rangle_I$ coincides with the state ket in the Schrödinger picture $|\Psi(t)\rangle_S$, which can be seen easily by comparing (2.4) and (2.5b).

2.1.3 Time Evolution Operator in the Interaction Picture

In the interaction picture, the state $|\Psi(t)\rangle_I$ can be related to the initial state $|\Psi(t_0)\rangle_I$, through the time evolution operator $\mathbf{U}_I(t,t_0)$,

$$|\Psi(t)\rangle_I \;=\; \mathbf{U}_I(t,t_0)|\Psi(t_0)\rangle_I. \tag{2.6}$$

The Schrödinger picture is related to the interaction picture through the unitary operator $\mathbf{U}_0(t)$ as,

$$|\Psi(t)\rangle_S \;=\; \mathbf{U}_0(t)\,|\Psi(t)\rangle_I, \tag{2.7}$$

$$\mathbf{U}_0(t) \;=\; e^{-\imath\mathbf{H}_0 t/\hbar}. \tag{2.8}$$

We consider the evolution of the wavefunction according to Schrödinger's equation,

$$\imath\hbar\frac{d}{dt}|\Psi(t)\rangle_S \;=\; (\mathbf{H}_0+\mathbf{V}(t))\,|\Psi(t)\rangle_S. \tag{2.9}$$

From (2.7) we have,

$$\imath\hbar\,\frac{d\mathbf{U}_0(t)}{dt}|\Psi(t)\rangle_I+\imath\hbar\,\mathbf{U}_0(t)\,\frac{d}{dt}|\Psi(t)\rangle_I \;=\; (\mathbf{H}_0+\mathbf{V}(t))\,\mathbf{U}_0(t)\,|\Psi(t)\rangle_I. \tag{2.10}$$

We note that $d\mathbf{U}_0(t)/dt=(1/\imath\hbar)\,\mathbf{H}_0\mathbf{U}_0(t)$, and introduce the definition,

$$\mathbf{V}_I(t) \;\equiv\; \mathbf{U}_0^\dagger(t)\,\mathbf{V}(t)\,\mathbf{U}_0(t). \tag{2.11}$$

Projecting on the left hand side of (2.10) with $\mathbf{U}_0^\dagger(t)$ and making use of (2.11) we find,

$$\frac{d}{dt}|\Psi(t)\rangle_I \;=\; \frac{1}{\imath\hbar}\,\mathbf{V}_I(t)\,|\Psi(t)\rangle_I. \tag{2.12}$$

As (2.6) is true for any initial state the above reduces to,

$$\frac{d}{dt}\mathbf{U}_I(t,t_0) \;=\; \frac{1}{\imath\hbar}\,\mathbf{V}_I(t)\,\mathbf{U}_I(t,t_0), \tag{2.13}$$

with the boundary condition $\mathbf{U}_I(t_0,t_0)=\mathbb{1}$. The formal solution to the time evolution operator is thus given by,

$$\mathbf{U}_I(t,t_0) \;=\; \mathbb{1}\;+\;\frac{1}{\imath\hbar}\int_{t_0}^{t}dt_1\;\mathbf{V}_I(t_1)\,\mathbf{U}_I(t_1,t_0). \tag{2.14}$$

Similarly we may find a solution for $\mathbf{U}_I(t_1,t_0)$ using (2.14),

$$\mathbf{U}_I(t,t_0) \;=\; \mathbb{1}\;+\;\frac{1}{\imath\hbar}\int_{t_0}^{t}dt_1\;\mathbf{V}_I(t_1)\;\left[\;\mathbb{1}\;+\;\frac{1}{\imath\hbar}\int_{t_0}^{t_1}dt_2\;\mathbf{V}_I(t_2)\,\mathbf{U}_I(t_2,t_0)\;\right], \tag{2.15}$$

and so on. This results in an iterative solution for $\mathbf{U}_I(t,t_0)$ known as the Dyson series,

$$\mathbf{U}_I(t,t_0) \;=\; \sum_{n=0}^{\infty} \left(\frac{1}{\imath\hbar}\right)^n \int_{t_0}^{t} dt_1 \int_{t_0}^{t_1} dt_2 \ldots \int_{t_0}^{t_{n-1}} dt_n \; \mathbf{V}_I(t_1)\, \mathbf{V}_I(t_2) \ldots \mathbf{V}_I(t_n). \quad (2.16)$$

Time ordering of the above operators is implicitly imposed.

2.1.4 Perturbative Expansion

What remains to be done, is to reconcile the time evolution operator of the interaction picture $\mathbf{U}_I(t,t_0)$ with the coefficients, $c_\nu(t)$, of (2.5b). The system is prepared in an initial state $|\Psi(t_0)\rangle_I \;=\; |\psi_\nu\rangle$, i.e. $c_\nu(t_0) = 1$. The time evolution of this state (in the interaction picture) is given by,

$$|\Psi(t)\rangle_I \;=\; \mathbf{U}_I(t,t_0)|\psi_\nu\rangle, \quad (2.17)$$

$$|\Psi(t)\rangle_I \;=\; \sum_\mu |\psi_\mu\rangle\langle\psi_\mu|\mathbf{U}_I(t,t_0)|\psi_\nu\rangle, \quad (2.18)$$

The phase evolution of the coefficients of the basis states $c_\mu(t)$ are given in the interaction picture by,

$$c_\mu(t) \;=\; \langle\psi_\mu|\mathbf{U}_I(t,t_0)|\psi_\nu\rangle. \quad (2.19)$$

The time evolved wavefunction in the interaction picture may be written,

$$|\Psi(t)\rangle_I = \sum_\mu \; c_\mu(t)\; |\psi_\mu\rangle. \quad (2.20)$$

To formulate a solution for the time dependent complex coefficients $c_\mu(t)$ we consider the perturbative expansion,

$$c_\mu(t) \;=\; c_\mu^{(0)}(t) \;+\; c_\mu^{(1)}(t) \;+\; c_\mu^{(2)}(t) \;+\; \cdots\; . \quad (2.21)$$

We perform an analogous expansion for the time evolution operator in the interaction picture,

$$\mathbf{U}(t,t_0) \;=\; \mathbf{U}^{(0)}(t,t_0) \;+\; \mathbf{U}^{(1)}(t,t_0) \;+\; \mathbf{U}^{(2)}(t,t_0) \;+\; \cdots\; . \quad (2.22)$$

According to the Dyson series (2.16) each of these terms is given by,

$$\mathbf{U}^{(0)}(t,t_0) \;=\; \mathbb{1}, \quad (2.23a)$$

$$\mathbf{U}^{(1)}(t,t_0) \;=\; \left(\frac{1}{\imath\hbar}\right) \int_{t_0}^{t} dt_1 \; \mathbf{V}_I(t_1), \quad (2.23b)$$

$$\mathbf{U}^{(2)}(t,t_0) \;=\; \left(\frac{1}{\imath\hbar}\right)^2 \int_{t_0}^{t} dt_1 \; \mathbf{V}_I(t_1) \int_{t_0}^{t_1} dt_2 \; \mathbf{V}_I(t_2). \quad (2.23c)$$

Plugging the perturbative expansions of (2.21) for $c_\mu(t)$ and (2.22) for $\mathbf{U}(t,t_0)$ into (2.19) and equating the perturbative terms with each other, we find the following formal solutions for the perturbed components of the complex coefficients,

$$c_\mu^{(0)}(t) \;=\; \langle\psi_\mu|\mathbb{1}|\psi_\nu\rangle \;=\; \delta_{\mu\nu}, \tag{2.24a}$$

$$c_\mu^{(1)}(t) \;=\; \left(\frac{1}{\imath\hbar}\right)\int_{t_0}^{t} dt_1\; \langle\psi_\mu|\mathbf{V}_I(t_1)|\psi_\nu\rangle, \tag{2.24b}$$

$$c_\mu^{(2)}(t) \;=\; \left(\frac{1}{\imath\hbar}\right)^2\sum_m \int_{t_0}^{t} dt_1\; \langle\psi_\mu|\mathbf{V}_I(t_1)|\psi_m\rangle\times \tag{2.24c}$$

$$\times\int_{t_0}^{t_1} dt_2\; \langle\psi_m|\mathbf{V}_I(t_2)|\psi_\nu\rangle. \tag{2.24d}$$

The above matrix elements are expanded using (2.8) and (2.11) as,

$$\begin{aligned}
\langle\psi_\mu|\mathbf{V}_I(t)|\psi_\nu\rangle \;&=\; \langle\psi_\mu|\;\mathbf{U}_0^\dagger(t)\;\mathbf{V}(t)\;\mathbf{U}_0(t)\;|\psi_\nu\rangle,\\
&=\; \langle\psi_\mu|\;\mathbf{U}_0^\dagger(t)\;\mathbf{V}(t)\;\mathbf{U}_0(t)\;|\psi_\nu\rangle,\\
&=\; \langle\psi_\mu|\;\exp\left[\;\frac{\imath}{\hbar}\mathbf{H}_0 t\;\right]\mathbf{V}(t)\;\exp\left[-\frac{\imath}{\hbar}\mathbf{H}_0 t\;\right]|\psi_\nu\rangle,\\
&=\; \langle\psi_\mu|\;\exp\left[\;\frac{\imath}{\hbar}\mathbf{H}_0 t\;\right]\mathbf{V}(t)\;\exp\left[-\frac{\imath}{\hbar}\mathbf{H}_0 t\;\right]|\psi_\nu\rangle,\\
&=\; \langle\psi_\mu|\mathbf{V}(t)|\psi_\nu\rangle\;\exp\left[\imath\frac{E_\mu-E_\nu}{\hbar}t\;\right].
\end{aligned} \tag{2.25}$$

Using the following abbreviations,

$$\omega_{\mu\nu} \;\equiv\; \frac{E_\mu - E_\nu}{\hbar}, \tag{2.26a}$$

$$V_{\mu\nu}(t) \;\equiv\; \langle\psi_\mu|\mathbf{V}(t)|\psi_\nu\rangle, \tag{2.26b}$$

allows to express (2.25) in the compact form,

$$\langle\psi_\mu|\mathbf{V}_I(t)|\psi_\nu\rangle \;=\; V_{\mu\nu}(t)\;e^{\imath\omega_{\mu\nu}t}. \tag{2.27}$$

Thereby, (2.24) is condensed to,

$$c_\mu^{(0)}(t) \;=\; \langle\psi_\mu|\mathbb{1}|\psi_\nu\rangle \;=\; \delta_{\mu\nu}, \tag{2.28a}$$

$$c_\mu^{(1)}(t) \;=\; \left(\frac{1}{\imath\hbar}\right)\int_{t_0}^{t} dt_1\; V_{\mu\nu}(t_1)\;e^{\imath\omega_{\mu\nu}t_1}, \tag{2.28b}$$

$$c_\mu^{(2)}(t) \;=\; \left(\frac{1}{\imath\hbar}\right)^2\sum_m \int_{t_0}^{t} dt_1\; V_{\mu m}(t_1)\;e^{\imath\omega_{\mu m}t_1}\;\int_{t_0}^{t_1} dt_2\; V_{m\nu}(t_2)\;e^{\imath\omega_{m\nu}t_2}. \tag{2.28c}$$

The transition matrix element $V_{\mu\nu}(t)$ will be discussed in detail in section 2.4.1.

2.1.5 Formal Solution

According to the perturbation theory of sections 2.1.3 and 2.1.4, the probability of effecting a transition from the state $|\psi_\nu\rangle$ to $|\psi_\mu\rangle$ for $\mu \neq \nu$ is given by,

$$\mathcal{P}_{\nu\to\mu}(t) \;=\; |c_\mu(t)|^2 \;=\; |c_\mu^{(0)}(t) \;+\; c_\mu^{(1)}(t) \;+\; c_\mu^{(2)}(t) \;+\; \cdots|^2. \tag{2.29}$$

Taken to first order,

$$\mathcal{P}_{\nu\to\mu}(t) \;\approx\; |c_\mu^{(1)}(t)|^2, \tag{2.30}$$

since $\mu \neq \nu$.

The initial time is taken to be $t_0 = 0$, thus $V_{\mu\nu}(t)$ assumes the form,

$$V_{\mu\nu}(t) \;=\; \langle\psi_\mu|e^{\imath\mathbf{k}\cdot\mathbf{r}\;\Theta(t)}|\psi_\nu\rangle, \tag{2.31}$$

where $\Theta(t)$ is the Heaviside step function and $\mathbf{k}$ is the wavevector of the photon released due to the perturbation. When $t < 0$, $\Theta(t) = 0$ and (2.31) is given by the Kronecker delta function $\delta_{\mu\nu}$. For $t \geq 0$ we have $\Theta(t) = 1$ and the operator is $e^{\imath\mathbf{k}\cdot\mathbf{r}}$. Even though (2.31) is written as a function of time, it is treated as a constant in the evaluation of the integral (2.28b). As we are only interested in the regime $t \geq 0$, we abbreviate $V_{\mu\nu}(t) \equiv V_{\mu\nu}$, to find,

$$\begin{aligned} c_\mu^{(1)}(t) \;&=\; \left(\frac{1}{\imath\hbar}\right)\int_0^t dt_1\; V_{\mu\nu}\; e^{\imath\omega_{\mu\nu}t_1}, \\ &=\; \frac{V_{\mu\nu}}{\imath\hbar}\;\left(\frac{e^{\imath\omega_{\mu\nu}t}-1}{\imath\omega_{\mu\nu}}\right), \end{aligned} \tag{2.32}$$

Consequently,

$$|c_\mu^{(1)}(t)|^2 \;=\; \frac{|V_{\mu\nu}|^2}{\hbar^2}\;\frac{\sin^2(\omega_{\mu\nu}/2)t}{(\omega_{\mu\nu}/2)^2}. \tag{2.33}$$

Setting $\alpha = \omega_{\mu\nu}/2$, the probability takes the form $\sin^2\alpha t/\alpha^2$, with a maximum at $\alpha = 0$. The maximum value is t^2 and its width is of order $1/t$. Therefore, as $t \to \infty$ the functional form of the above equation tends toward a δ-function centered at $t = 0$. The probability of transition is proportional to the time elapsed.

Of principle interest is the rate of transition, which is given by the probability of transition divided by the time. To evaluate the transition rate we make use of the identity,

$$\lim_{t\to\infty}\frac{1}{t}\frac{\sin^2\alpha t}{\alpha^2} \;=\; \pi\;\delta(\alpha) \;=\; 2\pi\;\delta(2\alpha). \tag{2.34}$$

The transition rate is subsequently given by,

$$\mathcal{R}_{\nu\to\mu} \;=\; \lim_{t\to\infty}\frac{\mathcal{P}_{\nu\to\mu}}{t} \;=\; \frac{2\pi}{\hbar^2}\;|V_{\mu\nu}|^2\;\delta(\omega_{\mu\nu}). \tag{2.35}$$

This expression is known as Fermi's Golden Rule.

2.2 The Anisotropic Harmonic Oscillator

The harmonic oscillator potential holds a unique importance in quantum mechanics. As it is one of the few problems that can be solved in closed form, it is in general a useful solution. It provides an invaluable tool through which arbitrary potentials can be approximated in the vicinity of a stable equilibrium point. A very good description of the system dynamics may then often be recovered using the harmonic oscillator model.

The quantum states of the simple harmonic oscillator have been studied since the earliest days of quantum mechanics. The harmonic oscillator being among the first applications of the matrix mechanics of Heisenberg and the wave mechanics of Schrödinger, which were both developed as mathematical tools used to explain electron orbits. These two competing approaches were later shown to be equivalent by Schrödinger [11].

The harmonic oscillator is the foundation for the understanding of complex modes of vibration in diatomic and larger molecules, the motion of atoms in a solid lattice, the theory of heat capacity, and many others. In addition, physical systems, such as vibrating molecules, mechanical resonators, or modes of electromagnetic fields, can be modeled as harmonic oscillators [12–15], so that the theoretical results can be compared to experiments.

Here we use the quantum harmonic oscillator model to describe the confining potential of an ultra cold Fermi gas. We present situations where we vary the strength of the Fermi gas's trapping potential, in the different spatial directions, to study spontaneous emission in the resulting anisotropic Fermi seas. The most prominent results of these modulations are the change of the energy spectrum and degeneracy of the different energy levels. Developing a deterministic formalism to characterise these regimes is the focus of this section.

In contrast to Bose-Einstein Condensation (BEC) [16, 17] whereby an ultracold gas of bosons collectively occupy the lowest available energy eigenstate thus forming a matterwave, an ultracold Fermi gas becomes 'stacked' due to the Pauli exclusion principle, whereby all available energy eigenstates are occupied up to the Fermi energy, forming what is known as a Fermi Sea. This is, of course, in the ideal and zero temperature case. Whilst BECs are becoming a standard in laboratories around the world, the production of highly degenerate ultracold Fermi seas remains a challenge, yet they have nonetheless been achieved [9, 18, 19].

A signature of the ultracold Fermi sea confined in a harmonic oscillator potential is its shell structure [20, 21]. This shell structure is a result of higher energy levels of the Fermi sea having a greater degeneracy, thereby a greater number of fermionic atoms can occupy them. In 1999, the first realization of quantum degeneracy using two spin components of ^{40}K was achieved [22]. Degeneracy is an important property of Fermi gases which modifies the scattering properties of atoms, leading to a reduced efficiency of evaporative cooling [23, 24]. Quantum degeneracy also plays a role in the narrowing of the linewidth of light propagating through the gas [25, 26], and the suppression of off-resonant light scattering [27–29].

In this chapter we show that quantum degeneracy plays a dominant role in modifying the lifetime of an excited fermion confined in a ground state Fermi sea. The degeneracy of any level can be changed when the shape of the trapping potential is changed. As the degeneracy of energy levels change, the lifetime (or decay rate) of the excited fermion in the different spatial directions also changes. In the limit of highly anisotropic cigar shaped trapping potentials, the degeneracies can be eliminated and only one non-degenerate quantum state is available, which produces a tightly focused direction of emission. To quantify the directional dependence of spontaneous emission as a function of the trap shape, it is necessary to describe the energy level degeneracy as a function of the anisotropy parameter λ. In this section we derive a set of equations that give the degeneracy of any energy level of the anisotropic harmonic oscillator as a function of λ for both the cigar and pancake shaped traps.

The harmonic traps we consider are of three forms: isotropic, cigar and pancake shaped. To maintain a clear relationship between the three, we choose the value of the anisotropy parameter (whose exact definition we discuss momentarily) so that it forms either the cigar or pancake shape, relative to the isotropic case. To date, it has been noted that the relationship between Fermi energy and particle number in the anisotropic potential is not as straightforward as in the well-known isotropic case [21]. This is the point from which we now move forward. We shall omit to derive the well known results for the isotropic case, which can be recovered by simply setting the anisotropy parameter, or as we shall refer to it from now on, the aspect ratio $\lambda = 1$.

2.2.1 Eigenenergies of the Pancake and Cigar Trap Shapes

The trapping frequencies of the anisotropic harmonic oscillator in the different spatial directions are not necessarily equal, i.e. $\omega_x \neq \omega_y \neq \omega_z$. To coherently move from the isotropic to the anisotropic regimes, it is useful to define the different trapping frequencies

in the different spatial directions in terms of a gereralised trapping frequency ω. In this manner $\omega_i = \lambda_i \omega$, for $i = x, y, z$.

The anisotropic harmonic-oscillator oscillator is defined in the following standard form,

$$\mathbf{V}(\mathbf{x}) = \frac{m\omega^2}{2} (\boldsymbol{\lambda} \cdot \mathbf{x})^2 = \frac{m\omega^2}{2} \left(\lambda_x^2 x^2 + \lambda_y^2 y^2 + \lambda_z^2 z^2 \right), \tag{2.36}$$

where m is the mass of the particle and the values of $\lambda_{x,y,z}$ determine the degree of anisotropy in the different directions. Using the above definition, we are at liberty to set the coefficient of the smallest trapping frequency equal to 1, eg. $\omega_x = \omega$ and $\lambda_x = 1$. The remaining coefficients, $\lambda_{y,z}$, are therefore greater than or equal to 1.

The potentials used in experiments are often either partially or completely asymmetric. Therefore, it is of interest to derive a completely general solution for energy level degeneracies of an arbitrary potential. For integer values of the aspect ratios λ_i, the confining potential of the Fermi gas maintains the shell structure [21] and Fermi degeneracy [9]. If we were to consider the use of non-integer aspect ratios, λ_i, this in turn would mean that the energy levels can no longer be represented as integer numbers. Furthermore, the evaluation of the degeneracies of non-integer energy levels is quite difficult and, for the purposes of this work, unnecessary. We will show in the following that it is possible to derive general relations to describe the degeneracies and the density of states for the cigar and pancake harmonic potentials when the aspect ratios are chosen to be integer numbers. To the best of our knowledge, this is the first time these relations have been derived. An extension of the analysis presented here to include all possible trap shapes, whilst certainly possible, is quite involved.

From this point on we choose the axis of symmetry to be the z-axis, (this is more important in the following sections when we make use of spherical polar co-ordinates, but to keep the theme consistent, we will do the same here) and we define the aspect ratios of the cigar and pancake traps as ($\lambda \geq 1$),

$$\lambda_x = \lambda_y = 1, \text{ and } \lambda_z = \lambda, \qquad \text{pancake shape,} \tag{2.37a}$$

$$\lambda_x = \lambda_y = \lambda, \text{ and } \lambda_z = 1, \qquad \text{cigar shape.} \tag{2.37b}$$

It follows that the eigenenergies of the harmonic potential in (2.36) are given by,

$$E_{n_\mathrm{p}} = \left(n_\mathrm{p} + \left(\frac{\lambda}{2} + 1 \right) \right) \hbar\omega, \qquad \text{pancake shape,} \tag{2.38a}$$

$$E_{n_\mathrm{c}} = \left(n_\mathrm{c} + \left(\lambda + \frac{1}{2} \right) \right) \hbar\omega, \qquad \text{cigar shape.} \tag{2.38b}$$

To allow for easy identifications between the trap shapes we use the subscript 'p' to denote the energy level n of the pancake trap, n_{p}. Similarly we use the subscript 'c' to denote the energy level n of the cigar trap, n_{c}.

The "shell quantum numbers" of the pancake and cigar shaped harmonic traps are defined as,

$$n_{\mathrm{p}} = n_x + n_y + \lambda n_z, \tag{2.39a}$$

$$n_{\mathrm{c}} = \lambda n_x + \lambda n_y + n_z. \tag{2.39b}$$

As usual, n_x, n_y and n_z refer to the integer quantum numbers of the harmonic oscillator potentials in the respective directions.

As the anisotropy of a trapping potential is increased, the resulting energy levels typically have a reduced degeneracy relative to the isotropic case [30]. For the purposes of this work, and without loss of generality, from this point on we will consider only integer values of λ, allowing us in turn to restrict ourselves to integer values for $n_{\mathrm{p,c}}$.

The degeneracies of the energy levels for the pancake and cigar potentials are found in section 2.2.2. Thereafter, in section 2.2.4 we derive a closed form expression for the sum of states up to and including the Fermi level. The Fermi level refers to the highest occupied shell by a Fermi gas at zero temperature.

2.2.2 Energy Level Degeneracy

The degree of degeneracy $g_{\mathrm{p,c}}(\lambda, n_{\mathrm{p,c}})$ of any energy level $E_{n_{\mathrm{c,p}}}$ is given by the number of different sets $\{n_x, n_y, n_z\}$ which satisfy the conditions of (2.39). Whilst these are well known for the isotropic case [30], the same cannot be said for the pancake and cigar traps. In the following we will derive $g_{\mathrm{p,c}}(\lambda, n_{\mathrm{p,c}})$, firstly for pancake traps (sec. 2.2.2.1), and afterwards for cigar shaped traps (sec. 2.2.2.2).

The following well known identities will be used throughout the remainder of this section. We present them all together at this point for the convenience of the reader,

$$\sum_{k=0}^{n} 1 = n + 1, \tag{2.40a}$$

$$\sum_{k=0}^{n} k = \frac{1}{2} n(n+1), \tag{2.40b}$$

$$\sum_{k=0}^{n} k^2 = \frac{n(n+1)(2n+1)}{6}. \tag{2.40c}$$

2.2.2.1 Energy Level Degeneracy for the Pancake Trap

A close examination of (2.39a) allows us to see that for a given energy level $n_{\rm p}$, n_z may only take a value in the range, $n_z = \lfloor 0/\lambda \rfloor, \lfloor 1/\lambda \rfloor, \lfloor 2/\lambda \rfloor, \ldots, \lfloor n_{\rm p}/\lambda \rfloor$. where $\lfloor x \rfloor$ is the floor function which takes the largest integer less than or equal to x. Since we will make frequent use of the floor functions throughout this chapter it is convenient to define the following abbreviation,

$$\tilde{x} \;=\; \left\lfloor \frac{x}{\lambda} \right\rfloor, \tag{2.41}$$

for any variable x, and λ being an integer.

For a fixed value of n_z, we can see from (2.40a) that there are $n_{\rm p} - \lambda n_z + 1$ combinations of $n_x + n_y$. The degeneracy of a particular level $n_{\rm p}$ is subsequently given by the summation over the possible values of n_z as,

$$g_{\rm p}(\lambda, n_{\rm p}) = \sum_{n_z=0}^{\tilde{n}_{\rm p}} \left(n_{\rm p} + 1 - \lambda n_z\right). \tag{2.42}$$

From (2.40) this relation simplifies to,

$$g_{\rm p}(\lambda, n_{\rm p}) \;=\; \frac{1}{2}\left(\tilde{n}_{\rm p} + 1\right)\left(2n_{\rm p} - \lambda\tilde{n}_{\rm p} + 2\right). \tag{2.43}$$

2.2.2.2 Energy Level Degeneracy for the Cigar Trap

To recover the degeneracies of the energy levels $n_{\rm c}$ for the cigar trap we rewrite (2.39b) as,

$$n_{\rm c} = \lambda N + n_z, \tag{2.44}$$

where $N = n_x + n_y$. We can see that for a particular value of n_z, N may take any value in the range $N = \lfloor 0/\lambda \rfloor, \lfloor 1/\lambda \rfloor, \ldots, \lfloor (n_{\rm c} - n_z)/\lambda \rfloor$. However, we must be very careful here; we cannot simply sum over n_z, as is possible for the pancake case. Since n_z must satisfy (2.44), if we choose to sum over n_z we would end up counting states that violate this equation.

There are in fact only $\tilde{n}_{\rm c} + 1$ choices of n_z. This is most easily seen by looking at an example. For instance, if we take $\lambda = 5$ and $n_{\rm c} = 22$, the possibilities of N and n_z are $(N, n_z) = (0, 22), (1, 17), (2, 12), (3, 7), (4, 2)$. For $n_z = 2$, there are $\tilde{n}_c + 1$ choices of N, i.e. $(n_x, n_y) = (4, 0), (3, 1), (2, 2), (1, 3), (0, 4)$. Similarly, for $n_z = 7$, there are $\tilde{n}_c$ choices of N, and so on. Therefore, if we continue along these lines we can count the degeneracies of N for the different "excitations" of n_z. For this particular example, $n_z = 2$ is the zeroth "excitation", $n_z = 7$ is the first, etc.

The above example clarifies that we may find the degeneracy of an energy level $n_{\rm c}$ by summing over the degeneracy of N relative to the n_z "excitation" as,

$$g_{\rm c}(\lambda, n_{\rm c}) = \sum_{n_z=0}^{\tilde{n}_{\rm c}} (\tilde{n}_{\rm c} + 1 - n_z)\,. \tag{2.45}$$

From (2.40) this relation simplifies to,

$$g_{\rm c}(\lambda, n_{\rm c}) = \frac{1}{2}\,(\tilde{n}_{\rm c} + 1)\,(\tilde{n}_{\rm c} + 2)\,. \tag{2.46}$$

2.2.3 Three Further Identities

As we will be dealing with an ideal Fermi sea, we are interested in the total number of quantum states with an energy equal to and smaller than $E_{n_{\rm F}}$ given by (2.38), where $n_{\rm F}$ is the highest occupied energy level of the Fermi sea. This is called the Fermi level or Fermi shell. Consequently, the number of states up to and including the Fermi level is given by,

$$S_i(\lambda, n_{\rm F}) = \sum_{n_i=0}^{n_{\rm F}} g_i(\lambda, n_i). \tag{2.47}$$

where $i = {\rm p}, {\rm c}$ refers to the pancake and cigar traps respectively.

From (2.43) and (2.46) we can see that in evaluating (2.47) above we encounter the following terms,

$$\sum_{n_i=0}^{n_{\rm F}} \tilde{n}_{\rm i}, \qquad \sum_{n_i=0}^{n_{\rm F}} \tilde{n}_{\rm i}^2, \qquad \sum_{n_i=0}^{n_{\rm F}} \tilde{n}_i\, n_i. \tag{2.48}$$

In this subsection we evaluate a closed form expression for each of the above terms. We refer to these identities as the first, second and third identity respectively.

2.2.3.1 First Identity

For the first summation,

$$\sum_{n_i=0}^{n_{\rm F}} \tilde{n}_i, \tag{2.49}$$

we note that $\tilde{n}_i$ has a constant value for groups of size λ, i.e. for $\lambda = 2$, $\tilde{n}_i = 0, 0, 1, 1, 2, 2, \ldots$. However the maximum value of the series, $\tilde{n}_{\rm F}$, belongs to a group of numbers which may not be of length λ. Therefore, we can assert that the first of these expressions may be written,

$$\sum_{n_i=0}^{n_{\rm F}} \tilde{n}_i = \lambda \sum_{n_i=0}^{\tilde{n}_{\rm F}} n_i - \Delta, \tag{2.50}$$

where Δ is the term which we now proceed to define. On the left hand side of (2.50) the maximum value of $\tilde{n}_i$ is $\tilde{n}_\mathrm{F}$. The sum of the terms in the series with this value is given by $\tilde{n}_\mathrm{F}(1+mod(n_\mathrm{F},\lambda))$, where $mod(n_\mathrm{F},\lambda) = n_\mathrm{F} - \lambda\tilde{n}_\mathrm{F}$, is the modulus of n_F/λ. However, the first term on the right hand side of (2.50) sums the maximum value term as $\lambda\tilde{n}_\mathrm{F}$, therefore we find that Δ is the difference between the two, $\lambda\tilde{n}_\mathrm{F} - \tilde{n}_\mathrm{F}(1 + mod(n_\mathrm{F},\lambda))$. Simplifying we have,

$$\Delta = \lambda\tilde{n}_\mathrm{F}(\tilde{n}_\mathrm{F}+1) - \tilde{n}_\mathrm{F}(n_\mathrm{F}+1). \tag{2.51}$$

Plugging this relation into (2.50) and using (2.40b), we obtain the closed form of the first identity,

$$\sum_{n_i=0}^{n_\mathrm{F}} \tilde{n}_i = \tilde{n}_\mathrm{F}(n_\mathrm{F}+1) - \frac{\lambda}{2}\tilde{n}_\mathrm{F}(\tilde{n}_\mathrm{F}+1). \tag{2.52}$$

2.2.3.2 Second Identity

We may find a closed form of

$$\sum_{n_i=0}^{n_\mathrm{F}} \tilde{n}_i^2, \tag{2.53}$$

by applying the same logic used in section 2.2.3.1. The summation is rewritten in the form,

$$\sum_{n_i=0}^{n_\mathrm{F}} \tilde{n}_i^2 = \lambda \sum_{n_i=0}^{\tilde{n}_\mathrm{F}} n_i^2 - \Delta'. \tag{2.54}$$

where Δ' is the term which we now proceed to define. On the left hand side of (2.54) the maximum value of $\tilde{n}_i^2$ is $\tilde{n}_\mathrm{F}^2$. The sum of the terms in the series with this value is given by $\tilde{n}_\mathrm{F}^2(1 + mod(n_\mathrm{F},\lambda))^2$. However, the first term on the right hand side of (2.54) sums the maximum value term as $\lambda\tilde{n}_\mathrm{F}^2$. As before, we find that Δ' is the difference between the two, $\lambda\tilde{n}_\mathrm{F}^2 - \tilde{n}_\mathrm{F}^2(1 + mod(n_\mathrm{F},\lambda))^2$.

$$\Delta' = \lambda\tilde{n}_\mathrm{F}^2(\tilde{n}_\mathrm{F}+1) - \tilde{n}_\mathrm{F}^2(n_\mathrm{F}+1). \tag{2.55}$$

Plugging this relation into (2.54) and using (2.40b), we obtain the closed form of the second identity,

$$\sum_{n_i=0}^{n_\mathrm{F}} \tilde{n}_i^2 = \tilde{n}_\mathrm{F}^2(\tilde{n}_\mathrm{F}+1) - \frac{\lambda}{6}\tilde{n}_\mathrm{F}(\tilde{n}_\mathrm{F}+1)(4\tilde{n}_\mathrm{F}-1). \tag{2.56}$$

2.2.3.3 Third Identity

Finally, we move our attention to finding the value of,

$$\sum_{n_i=0}^{n_\mathrm{F}} \tilde{n}_i \, n_i. \tag{2.57}$$

Again, we would like to change the sum from $n_i = 0 \to n_\mathrm{F}$, to $m = 0 \to \tilde{n}_\mathrm{F}$. It becomes necessary to change variable here ($n_i \to m$) because we need to use a nested sum. We have,

$$\sum_{n_i=0}^{n_\mathrm{F}} \tilde{n}_i n_i = \sum_{m=0}^{\tilde{n}_\mathrm{F}} m \left[\sum_{n=\lambda m}^{\lambda(m+1)-1} n \right] - \Delta'', \tag{2.58}$$

where Δ'' is to be determined. The nested sum over the range, $n = \lambda m \to \lambda(m+1)-1$, allows us to count all the product terms $\tilde{n}_i n_\mathrm{i}$ over the range of length λ. However in doing so, we end up counting extra terms which are removed by Δ''. These arise when $m = \tilde{n}_\mathrm{F}$. The nested sum of (2.58) counts extra product terms for $n \geq \lambda\tilde{n}_\mathrm{F} + 1$. Subsequently we find,

$$\Delta'' = \tilde{n}_\mathrm{F} \sum_{n=n_\mathrm{F}+1}^{\lambda(n_\mathrm{F}+1)-1} n. \tag{2.59}$$

Plugging this relation into (2.58) and using (2.40b) we find the closed form for the third summation as,

$$\sum_{n_i=0}^{n_\mathrm{F}} \tilde{n}_i \, n_i = \tilde{n}_\mathrm{F} \frac{n_\mathrm{F}}{2}(n_\mathrm{F}+1) - \lambda \frac{\tilde{n}_\mathrm{F}}{12}(\tilde{n}_\mathrm{F}+1)(2\lambda\tilde{n}_\mathrm{F} + \lambda - 3). \tag{2.60}$$

In summary, the three identities are given by,

$$\sum_{n_i=0}^{n_\mathrm{F}} \tilde{n}_i = \tilde{n}_\mathrm{F}(n_\mathrm{F}+1) - \frac{\lambda}{2}\tilde{n}_\mathrm{F}(\tilde{n}_\mathrm{F}+1), \tag{2.61a}$$

$$\sum_{n_i=0}^{n_\mathrm{F}} \tilde{n}_i^2 = \tilde{n}_\mathrm{F}^2(\tilde{n}_\mathrm{F}+1) - \frac{\lambda}{6}\tilde{n}_\mathrm{F}(\tilde{n}_\mathrm{F}+1)(4\tilde{n}_\mathrm{F}-1), \tag{2.61b}$$

$$\sum_{n_i=0}^{n_\mathrm{F}} \tilde{n}_i \, n_i = \tilde{n}_\mathrm{F} \frac{n_\mathrm{F}}{2}(n_\mathrm{F}+1) - \lambda \frac{\tilde{n}_\mathrm{F}}{12}(\tilde{n}_\mathrm{F}+1)(2\lambda\tilde{n}_\mathrm{F} + \lambda - 3). \tag{2.61c}$$

These relations are equivalent to (2.40) when $\lambda = 1$.

2.2.4 Sum of States up to the Fermi Level for the Pancake and Cigar Traps

The sum of states up to and including the Fermi level n_{F} for the pancake and cigar trapping geometries are given respectively as,

$$S_{\mathrm{p}}(\lambda, n_{\mathrm{F}}) = \frac{1}{2}\sum_{n_p=0}^{n_{\mathrm{F}}} (\tilde{n}_{\mathrm{p}}+1)\,(2n_{\mathrm{p}} - \lambda\tilde{n}_{\mathrm{p}} + 2)\,, \tag{2.62a}$$

$$S_{\mathrm{c}}(\lambda, n_{\mathrm{F}}) = \frac{1}{2}\sum_{n_c=0}^{n_{\mathrm{F}}} (\tilde{n}_{\mathrm{c}}+1)\,(\tilde{n}_{\mathrm{c}} + 2)\,. \tag{2.62b}$$

Using the identities given by (2.40) and those of the last section (2.61), we may evaluate the above summation to arrive at a compact expression for the number of states up to and including the Fermi shell for both anisotropic settings. After some simplification, we find that the sum of states for each trapping geometry may be reduced to the following compact forms;

$$\begin{aligned} S_{\mathrm{p}}(\lambda, n_{\mathrm{F}}) &= \frac{1}{6}(\tilde{n}_{\mathrm{F}}+1)(2n_{\mathrm{F}} - \lambda\tilde{n}_{\mathrm{F}} + 2) \\ &\quad \left(\frac{3}{2}n_{\mathrm{F}} - \frac{3}{4}\lambda\tilde{n_{\mathrm{F}}} + \frac{\lambda^2\tilde{n}_{\mathrm{F}}(2+\tilde{n}_{\mathrm{F}})}{8+8n_{\mathrm{F}} - 4\lambda\tilde{n}_{\mathrm{F}}} + 3\right), \end{aligned} \tag{2.63a}$$

$$S_{\mathrm{c}}(\lambda, n_{\mathrm{F}}) = \frac{1}{6}(\tilde{n}_{\mathrm{F}}+1)(\tilde{n}_{\mathrm{F}}+2)(3n_{\mathrm{F}} - 2\tilde{n}_{\mathrm{F}}\lambda + 3). \tag{2.63b}$$

It can easily be confirmed that these relations, along with (2.43) and (2.46), reduce to the isotropic case for $\lambda = 1$.

An interesting consequence of these equations ((2.43), (2.46) and (2.63)) is that for any given value of λ they form an integer sequence. These integer sequences have been included in Sloane's 'Online Encyclopedia of Integer Sequences' under the references: A002620, A001840, A001972, A008732, A002623, A014125, A122046, A122047, A006918, A144677, A144678, and A144679. The last three of which are new integer series.

In our model we assume a spin polarised gas in which each oscillator state is filled with one fermion only. Equations (2.63) therefore determine the number of particles confined for a given Fermi energy $E_F = n_{\mathrm{F}}\hbar\omega + E_G$, where E_G is the ground state energy of the potential. We assume that all states up to and including the Fermi level n_{F} are occupied with probability 1 (T=0).

2.3 Model

We consider an ideal gas of spin polarised fermions trapped in a harmonic potential. All atoms are assumed to be in their internal ground state, $|g\rangle$, so that the gas becomes quantum degenerate at low enough temperatures and forms a perfect Fermi sea at absolute zero. In the following, we restrict our calculations to the zero temperature limit. In this regime the effects we describe are most pronounced, and the extension to finite temperatures, while computationally challenging, is conceptually straightforward.

In addition to the Fermi sea, we assume the presence of a single extra fermion, which is distinguished from the others by being in an internally excited state, $|e\rangle$. As above, and with the same implications for higher temperatures, we assume this particle to be in the motional ground state, and furthermore that it feels, to a good approximation, the same potential as the ground state Fermi sea. After some time, this atom will spontaneously emit a photon, make a transition into the ground state and become part of the Fermi sea. As all atoms are assumed to be spin polarised, the Pauli principle demands that the new ground state atom has to join the Fermi sea with an energy larger than the Fermi energy. Energetically this is a very unfavourable process, and the presence of the Fermi sea leads to an inhibition of the spontaneous emission rate, with respect to the case of a lone particle [4, 5].

When the confining potential is isotropic, the decay rate of the excited fermion is equal in all spatial directions. One interesting aspect to this study is to show how the decay rate deviates from the isotropic case when the harmonic trap, and subsequently the ground state Fermi sea, becomes anisotropic. When we move into the cigar and pancake regimes, we find the radial magnitude of the decay rate is no longer isotropic. The goal of this work is to investigate how the observed emission patterns arise. In doing so, we will neglect the effects of reabsorption of the emitted photon. In fact, reabsorption can be seen as the same situation where a single atom in the ground state is excited by a weak laser pulse, treated in [5], for which it was shown that emission happens overwhelmingly in the forward direction, thereby not fundamentally affecting the results of this work.

In the following, we denote the spontaneous emission rate of photons along the direction Ω and into the solid angle $d\Omega$ in the presence of N ground-state fermions by $\Gamma(\Omega)\, d\Omega$, and compare it to the free case ($N = 0$), denoted by $\Gamma_0(\Omega) d\Omega$. We use Fermi's golden rule (2.35) to determine the spontaneous emission rate. The initial state of the excited fermion is denoted $|\psi_i\rangle = |\boldsymbol{m}\rangle$ and the final state $|\psi_f\rangle = |\boldsymbol{n}\rangle$, where $|\boldsymbol{m}\rangle, |\boldsymbol{n}\rangle$ are the energy eigenstates of the harmonic oscillator. The bold font is used here to indicate that the energy levels are themselves degenerate. The emission of a photon in the direction

Ω as it makes a transition from $|\boldsymbol{m}\rangle \to |\boldsymbol{n}\rangle$ is described by the perturbation operator, $\mathbf{V}(t) = e^{-i\mathbf{k}(\Omega)\cdot\mathbf{r}}\,\Theta(t)$.

As the single excited fermion is in an orthogonal internally excited state with respect to the ground state Fermi sea, it is free to occupy any energy eigenstate of the harmonic trap. At any temperature, the probability distribution of the occupation of a state $|\boldsymbol{m}\rangle$ of the harmonic trap is described by the Boltzmann distribution function, $P_{\boldsymbol{m}} = P_0 e^{-(\hbar\omega/k_B T)\boldsymbol{\lambda}\cdot\boldsymbol{m}}$, where $(\omega_x, \omega_y, \omega_z) = \omega(\lambda_x, \lambda_y, \lambda_z) \equiv \omega\boldsymbol{\lambda}$.

Once decay occurs and a photon is emitted, the excited fermion returns to its internal ground state. By the Pauli exclusion principle, the particle may only make a transition to an unoccupied center of mass mode $|\boldsymbol{n}\rangle$. The probability distribution of the occupied modes of the Fermi sea is described by the Fermi-Dirac distribution function $F_{\boldsymbol{n}} = (e^{(\hbar\omega/k_B T)(\boldsymbol{\lambda}\cdot\boldsymbol{n})} + 1)^{-1}$. Available and unoccupied energy levels $|\boldsymbol{n}\rangle$ are therefore given by the distribution $1 - F_{\boldsymbol{n}}$.

Considering all the above, we may consolidate the ratio of the decay rates in the presence of a ground state Fermi sea with respect to the free case using Fermi's golden rule (2.35) as,

$$\frac{\Gamma(\Omega)}{\Gamma_0(\Omega)} = \sum_{\boldsymbol{n},\boldsymbol{m}=0}^{\infty} P_{\boldsymbol{m}}(1 - F_{\boldsymbol{n}}) \left|\langle \boldsymbol{n}|\; e^{-i\mathbf{k}(\Omega)\cdot\mathbf{r}}\; |\boldsymbol{m}\rangle\right|^2 , \tag{2.64}$$

Since we restrict ourselves to the zero temperature regime, the Fermi-Dirac distribution function becomes a step function. Hence only the states with an energy greater than the Fermi energy have a finite value, for $1 - F_{\boldsymbol{n}}$. Similarly, the excited fermion will occupy the ground state of the harmonic trap, $|\boldsymbol{m}\rangle = |0\rangle$, and (2.64) simplifies immediately to

$$M_f(\Omega) = \frac{\Gamma(\Omega)}{\Gamma_0(\Omega)} = \sum_{\boldsymbol{n}=\boldsymbol{n}_{\mathrm{F}}+\mathbf{1}}^{\infty} \left|\langle \boldsymbol{n}|\; e^{-i\mathbf{k}(\Omega)\cdot\mathbf{r}}\; |0\rangle\right|^2 , \tag{2.65}$$

where n_{F} represents the (degenerate) Fermi shell. The most well known result originating from (2.64) is the inhibition of spontaneous emission from the excited atom [5]. However, the spatial emission probability is also known to become anisotropic [5, 6] and in the following, we present a thorough and detailed investigation into this effect. This is of interest with regards to the new parameter ranges that have become experimentally available in recent years. These include lower and lower temperature Fermi gases and, in particular, highly anisotropic traps.

2.4 The Transition Matrix

The goal of this section is to arrive at a closed form expression for the transition matrix element,

$$|\langle \boldsymbol{n}|e^{-i\mathbf{k}(\Omega)\cdot\mathbf{r}}|0\rangle|^2. \tag{2.66}$$

To begin, we consider the generalised (or free) transition matrix element,

$$|\langle \boldsymbol{n}|e^{-i\mathbf{k}(\Omega)\cdot\mathbf{r}}|\boldsymbol{m}\rangle|^2, \tag{2.67}$$

and thereafter, we recover the closed form of (2.66).

Coherent states are an appropriate basis for many optical fields. The coherent state of the harmonic oscillator, $|\alpha\rangle$, is an eigenstate of the annihilation operator, $\hat{a}|\alpha\rangle = \alpha|\alpha\rangle$. The notation $|\alpha\rangle$ refers to a poissonian distribution over the available states with a mean photon number of unity, and α represents its location in phase space. These states are most easily generated using the unitary translation operator,

$$\mathscr{T}(\alpha) \;=\; e^{-\alpha^*\hat{a}+\alpha\hat{a}^\dagger}. \tag{2.68}$$

The translation operator permits us to define the coherent state as the operation of the translation operator on the vacuum mode $|0\rangle$ as,

$$|\alpha\rangle = \mathscr{T}(\alpha)|0\rangle. \tag{2.69}$$

Given that the harmonic oscillator modes $|\boldsymbol{m}\rangle$ are linear sums of the excitations in the different spatial directions as $|\boldsymbol{m}\rangle \;=\; |m_x\rangle|m_y\rangle|m_z\rangle$, we may separate the transitions between the modes $|\boldsymbol{m}\rangle$ and $|\boldsymbol{n}\rangle$ of the harmonic oscillator in the different spatial directions.

In the following we map the translation operator to the transition operator as, $\mathscr{T}(\alpha) = e^{-i\mathbf{k}(\Omega)\cdot\mathbf{r}}$ and resolve for α. To do so we wish to first evaluate,

$$|\langle n|\mathscr{T}(\alpha)|m\rangle|^2, \tag{2.70}$$

where m and n are the excitations of the harmonic oscillator in a particular spatial direction ($x, y,$ or z). We have dropped the bold font notation as these states are no longer degenerate.

By appropriate mapping of the translation operator $\mathscr{T}(\alpha)$ to the operator $e^{-i\mathbf{k}(\Omega)\cdot\mathbf{r}}$, we may subsequently find a closed form expression for (2.66).

2.4.1 Free Transition Matrix Element

The exponent of (2.68) contains a linear sum of two operators $\hat{a}$ and $\hat{a}^\dagger$. Using the operator theorem, we may separate an exponential sum of two operators, $\mathbf{A}$ and $\mathbf{B}$ as,

$$\exp(\mathbf{A}+\mathbf{B}) = \exp(\mathbf{A})\exp(\mathbf{B})\exp\left(-\frac{[\mathbf{A},\mathbf{B}]}{2}\right), \tag{2.71}$$

when,

$$[\mathbf{A},[\mathbf{A},\mathbf{B}]] = [\mathbf{B},[\mathbf{A},\mathbf{B}]] \;=\; 0. \tag{2.72}$$

Applying relation (2.71) to the translation operator we find $\mathbf{A} = -\alpha^*\,\hat{a}$ and $\mathbf{B} = \alpha\,\hat{a}^\dagger$, which we use to evaluate the commutator $[\mathbf{A},\mathbf{B}]$. We find that this may be expressed as $[\mathbf{A},\mathbf{B}] = -|\alpha|^2[\hat{a}^\dagger,\hat{a}] = |\alpha|^2$, and (2.72) is satisfied. The translation operator is thus given by,

$$\mathscr{T}(\alpha) = e^{|\alpha|^2/2} e^{\,-\alpha^*\,\hat{a}} e^{\alpha\,\hat{a}^\dagger}, \tag{2.73}$$

and using the identity $(\mathbf{XY})^\dagger = \mathbf{Y}^\dagger\mathbf{X}^\dagger$,

$$\mathscr{T}^\dagger(\alpha) = e^{|\alpha|^2/2} e^{\alpha^*\,\hat{a}} e^{\,-\alpha\,\hat{a}^\dagger}. \tag{2.74}$$

The goal of this section is to find the general form of,

$$|\langle n|\mathscr{T}(\alpha)|m\rangle|^2 = \langle n|\mathscr{T}(\alpha)|m\rangle\langle m|\mathscr{T}^\dagger(\alpha)|n\rangle. \tag{2.75}$$

For the purposes of clarity, we evaluate both $\langle n|\mathscr{T}(\alpha)|m\rangle$ and $\langle m|\mathscr{T}^\dagger(\alpha)|n\rangle$ separately, and refer to them as the first and second matrix element respectively.

2.4.1.1 Evaluation of the Matrix Element

From (2.73) we have,

$$\langle n|\mathscr{T}(\alpha)|m\rangle = e^{|\alpha|^2/2}\langle n|e^{\,-\alpha^*\,\hat{a}} e^{\alpha\,\hat{a}^\dagger}|m\rangle. \tag{2.76}$$

The ladder operators respectively obey,

$$\hat{a}|n\rangle \;=\; \sqrt{n}|n-1\rangle, \qquad (\hat{a})^m|n\rangle \;=\; \sqrt{\frac{n!}{(n-m)!}}|n-m\rangle, \tag{2.77a}$$

$$\hat{a}^\dagger|n\rangle \;=\; \sqrt{n+1}|n+1\rangle, \qquad \left(\hat{a}^\dagger\right)^m|n\rangle \;=\; \sqrt{\frac{(n+m)!}{n!}}|n+m\rangle. \tag{2.77b}$$

Expanding the exponential on the right hand side of (2.76) and using the identities (2.77) we find,

$$\begin{aligned} e^{\alpha\,\hat{a}^\dagger}|m\rangle &= \sum_{p=0}^{\infty}\frac{\alpha^p}{p!}(\hat{a}^\dagger)^p|m\rangle, \\ &= \sum_{p=0}^{\infty}\frac{\alpha^p}{p!}\sqrt{\frac{(m+p)!}{m!}}|m+p\rangle. \end{aligned} \tag{2.78}$$

Similarly we consider the operation of $e^{-\alpha^*\,\hat{a}}$ on the state ket $|m+p\rangle$ by expanding the exponential and using the identities (2.77),

$$\begin{aligned} e^{-\alpha^*\,\hat{a}}|m+p\rangle &= \sum_{q=0}^{\infty}\frac{(-\alpha^*)^q}{q!}\hat{a}^q|m+p\rangle, \\ &= \sum_{q=0}^{m+p}\frac{(-\alpha^*)^q}{q!}\sqrt{\frac{(m+p)!}{(m+p-q)!}}|m+p-q\rangle. \end{aligned} \tag{2.79}$$

Plugging both these relations into (2.76), we find the right hand side reduces to,

$$e^{|\alpha|^2/2}\sum_{p=0}^{\infty}\frac{\alpha^p}{p!}\sqrt{\frac{(m+p)!}{m!}}\sum_{q=0}^{m+p}\frac{(-\alpha^*)^q}{q!}\sqrt{\frac{(m+p)!}{(m+p-q)!}}\langle n|m+p-q\rangle. \tag{2.80}$$

Since $\langle n|m+p-q\rangle = \delta_{n,m+p-q}$, we obtain the condition $q = m+p-n$, and that the outer sum must begin at $p = n$. Therefore (2.76) is given by,

$$\langle n|\mathscr{T}(\alpha)|m\rangle = e^{|\alpha|^2/2}\frac{(-\alpha^*)^{m-n}}{\sqrt{m!n!}}\sum_{p=n}^{\infty}\frac{\left(-|\alpha|^2\right)^p}{p!}\frac{(m+p)!}{(m+p-n)!}. \tag{2.81}$$

Similarly (see Appendix A.1) we find,

$$\langle m|\mathscr{T}^\dagger(\alpha)|n\rangle = e^{|\alpha|^2/2}\frac{(\alpha^*)^{m-n}}{\sqrt{m!n!}}\sum_{p=m}^{\infty}\frac{\left(-|\alpha|^2\right)^p}{p!}\frac{(n+p)!}{(n+p-m)!}. \tag{2.82}$$

2.4.1.2 Formal Solution

The generalised transition matrix element,

$$|\langle n|\mathscr{T}(\alpha)|m\rangle|^2 = \langle m|\mathscr{T}^\dagger(\alpha)|n\rangle\langle n|\mathscr{T}(\alpha)|m\rangle, \tag{2.83}$$

is given from (2.81) and (2.82) to be,

$$e^{|\alpha|^2}(-1)^{m-n}\left[\sum_{\mu=m}^{\infty}\frac{(-|\alpha|^2)^\mu}{\mu!}\frac{(n+\nu)!}{m!(n+\mu-m)!}\right]\left[\sum_{\nu=n}^{\infty}\frac{(-|\alpha|^2)^\nu}{\nu!}\frac{(m+\nu)!}{n!(m+\nu-n)!}\right]. \tag{2.84}$$

The binomial coefficient,

$$\binom{r}{s} = \frac{r!}{s!(r-s)!}, \tag{2.85}$$

allows for a compact representation of (2.83),

$$|\langle n|\mathscr{T}(\alpha)|m\rangle|^2 = e^{|\alpha|^2}(-1)^{m-n}\left[\sum_{\mu=m}^{\infty}\frac{(-|\alpha|^2)^\mu}{\mu!}\binom{n+\mu}{m}\right]\left[\sum_{\nu=n}^{\infty}\frac{(-|\alpha|^2)^\nu}{\nu!}\binom{m+\nu}{n}\right]. \tag{2.86}$$

2.4.1.3 Zero Temperature Transition

When the initial state is given by, $|m\rangle = |0\rangle$, (2.86) may be expressed as,

$$\begin{aligned}|\langle n|\mathscr{T}(\alpha)|0\rangle|^2 &= e^{|\alpha|^2}\frac{(-1)^{-n}}{n!}\left[\sum_{\mu=0}^{\infty}\frac{(-|\alpha|^2)^\mu}{\mu!}\right]\left[\sum_{\nu=n}^{\infty}\frac{(-|\alpha|^2)^\nu}{(\nu-n)!}\right], \\ &= \frac{(-1)^{-n}}{n!}\left[\sum_{\nu=n}^{\infty}\frac{(-|\alpha|^2)^\nu}{(\nu-n)!}\right],\end{aligned} \tag{2.87}$$

To continue to simplify this relation, we use a change of variable, $l = \nu - n$.

$$\begin{aligned}|\langle n|\mathscr{T}(\alpha)|0\rangle|^2 &= \frac{(-1)^{-n}}{n!}\left[\sum_{l=0}^{\infty}\frac{(-|\alpha|^2)^{l+n}}{l!}\right], \\ &= \frac{(-1)^{-n}}{n!}\left(-|\alpha|^2\right)^n\left[\sum_{l=0}^{\infty}\frac{(-|\alpha|^2)^l}{l!}\right],\end{aligned} \tag{2.88}$$

which gives,

$$|\langle n|\mathscr{T}(\alpha)|0\rangle|^2 = e^{-|\alpha|^2}\frac{|\alpha|^{2n}}{n!}. \tag{2.89}$$

2.4.2 Angular Emission

In equation (2.39), we defined the 'shell quantum numbers' of the pancake and cigar traps n_p and n_c to be symmetric about the $\hat{z}$-axis. As a result, both trap shapes are symmetric through a 2π rotation around the $\hat{z}$-axis. Similarly, the spontaneous emission rate is symmetric through a 2π rotation around the $\hat{z}$-axis.

In this section, we take advantage of the $\hat{z}$-axis symmetry by making use of spherical polar co-ordinates; Thereby, we find that the angular emission may be expressed on a two dimensional plane. Furthermore, the transition matrix may be expressed in terms of incomplete gamma functions which are advantageous for numerical work as they are computationally inexpensive.

To begin, we rewrite $\mathbf{k}\cdot\mathbf{r}$ in spherical polar co-ordinates,

$$\mathbf{k}(\Omega)\cdot\mathbf{r} = \sin\theta\cos\vartheta\,\mathbf{k}\cdot\hat{x} + \sin\theta\sin\vartheta\,\mathbf{k}\cdot\hat{y} + \cos\theta\,\mathbf{k}\cdot\hat{z}, \tag{2.90}$$

The position and momentum operators $\mathbf{r}$ and $\mathbf{p}$ are defined in terms of the ladder operators as,

$$\mathbf{r} \;=\; \sqrt{\frac{\hbar}{2m\omega_j}}\left(\hat{a} \;+\; \hat{a}^\dagger\right)\hat{j}, \tag{2.91a}$$

$$\mathbf{p} \;=\; \imath\sqrt{\frac{m\hbar\omega_j}{2}}\left(-\hat{a} \;+\; \hat{a}^\dagger\right)\hat{j}, \tag{2.91b}$$

where ω_j is the trapping frequency in the $\hat{j}$ spatial direction. Thereby we find that $\mathbf{k}\cdot\hat{x}$, $\mathbf{k}\cdot\hat{y}$ and $\mathbf{k}\cdot\hat{z}$ are respectively given by,

$$\mathbf{k}\cdot\hat{j} \;=\; k_0\sqrt{\frac{\hbar}{2m\omega_j}}\left(\hat{a} \;+\; \hat{a}^\dagger\right)\hat{j} \;\equiv\; \eta_j\left(\hat{a} \;+\; \hat{a}^\dagger\right), \tag{2.92}$$

for $\hat{j} = \hat{x}, \hat{y}$ and $\hat{z}$. The Lamb-Dicke parameter η_j is a key term that allows us to interpret the rate of spontaneous emission as being proportional to the square root of the ratio between the recoil energy of the atom and the trapping frequency (in a given spatial direction), $\eta_j = k_0\sqrt{\hbar/2m\omega_j} = \sqrt{(\hbar^2k_0^2/2m)(1/\hbar\omega_j)}$. Explicitly this may be expressed,

$$\eta_j^2 \;=\; \frac{E_R}{\hbar\omega_j}, \tag{2.93}$$

where $E_R = \hbar^2k_0^2/2m$ is the recoil energy of the atom.

Plugging (2.92) into (2.90), we find,

$$\mathbf{k}(\Omega)\cdot\mathbf{r} = \left(\eta_x\sin\theta\cos\vartheta + \eta_y\sin\theta\sin\vartheta + \eta_z\cos\theta\right)\left(\hat{a} + \hat{a}^\dagger\right), \tag{2.94}$$

By inserting (2.94) into (2.65) the transition matrix becomes separable in the three orthogonal spatial directions. Therefore we may evaluate each direction individually.

2.4.2.1 Application of the Translation Matrix Element

For the purposes of abbreviation, we let η_j' represent η_j times its coefficient, i.e. $\eta_x' = \eta_x\sin\theta\cos\vartheta$, etc. This allows us to separate the transition matrix into the three orthogonal spatial directions as,

$$|\langle\boldsymbol{n}|e^{\imath\mathbf{k}(\Omega)\cdot\mathbf{r}}|0\rangle|^2 = |\langle n_x|e^{\imath\eta_x'(\hat{a}+\hat{a}^\dagger)}|0\rangle|^2|\langle n_y|e^{\imath\eta_y'(\hat{a}+\hat{a}^\dagger)}|0\rangle|^2|\langle n_z|e^{\imath\eta_z'(\hat{a}+\hat{a}^\dagger)}|0\rangle|^2. \tag{2.95}$$

In section 2.4.1.3 we showed that,

$$|\langle n|e^{-\alpha^*\hat{a}+\alpha\hat{a}^\dagger}|0\rangle|^2 = e^{-|\alpha|^2}\frac{|\alpha|^{2n}}{n!}. \tag{2.96}$$

We let $\alpha = \imath\eta_j'$, to find

$$|\langle n_j|e^{\imath\eta_j'\left(\hat{a}+\hat{a}^\dagger\right)}|0\rangle|^2 = e^{-(\eta_j')^2}\frac{\left(\eta_j'\right)^{2n_j}}{n_j!}. \tag{2.97}$$

Plugging the above into (2.95) and removing the abbreviated notation we recover,

$$\begin{aligned}|\langle \boldsymbol{n}|e^{\imath\mathbf{k}(\Omega)\cdot\mathbf{r}}|0\rangle|^2 = e^{-\eta_x^2\sin^2\theta\cos^2\vartheta-\eta_y^2\sin^2\theta\sin^2\vartheta-\eta_z^2\cos^2\theta}\ &\frac{\left(\eta_x^{2n_x}\right)\left(\eta_y^{2n_y}\right)\left(\eta_z^{2n_z}\right)}{n_x!\,n_y!\,n_z!}\\ &\times\left(\sin\theta\cos\vartheta\right)^{2n_x}\left(\sin\theta\sin\vartheta\right)^{2n_y}\left(\cos\theta\right)^{2n_z}\end{aligned} \tag{2.98}$$

As in section 2.2, we will consider both the cigar and pancake regimes simultaneously, and from these, the isotropic case may be recovered by setting $\lambda = 1$.

The Lamb-Dicke parameter η_j is the dominant term that separates spontaneous emission of an excited atom in the pancake and cigar trapping geometries. The two cases are,

$$\eta_x^2 = \eta_y^2 = \eta^2, \ \text{ and } \ \eta_z^2 = \frac{\eta^2}{\lambda}, \qquad \text{pancake shape,} \tag{2.99a}$$

$$\eta_x^2 = \eta_y^2 = \frac{\eta^2}{\lambda}, \ \text{ and } \ \eta_z^2 = \eta^2, \qquad \text{cigar shape.} \tag{2.99b}$$

The axis of symmetry for both cases is the $\hat{z}$-axis. For the pancake trap, there is one tight axis, the $\hat{z}$-axis, and two soft axes, the $\hat{x}$ and $\hat{y}$ axes. For the cigar trap the inverse is true. The tight axes are the $\hat{x}$ and $\hat{y}$ axes, whereas, the soft axis is the $\hat{z}$-axis. Using these conventions, we can resolve the transition matrix for both anisotropies quite easily.

2.4.2.2 Preliminary Reduction - Pancake Case

A consequence of being in the zero temperature regime $|\Psi(t=0)\rangle = |\psi_0\rangle = |0\rangle$, and of the Pauli exclusion principle, is that we may only sum over the unoccupied modes as these are the only ones available to the recoiling atom. In the derivation that follows, we first sum over all modes, and thereafter in section 2.4.2.3, we subtract the modes occupied by the Fermi Sea.

We apply the Lamb-Dicke Parameter for the pancake trap as given by (2.99) to simplify (2.98) as,

$$\sum_{\boldsymbol{n}=0}^{\infty}|\langle\boldsymbol{n}|e^{\imath\mathbf{k}(\Omega)\cdot\mathbf{r}}|0\rangle|^2=\sum_{(n_x,n_y,n_z)=0}^{\infty}e^{-\eta^2\left(\sin^2\theta\cos^2\vartheta+\sin^2\theta\sin^2\vartheta\right)-\frac{\eta^2}{\lambda}\cos^2\theta}\,\frac{\left(\eta^2\right)^{n_x+n_y}\left(\frac{\eta^2}{\lambda}\right)^{n_z}}{n_x!\,n_y!\,n_z!}\\ \times\left(\sin^2\theta\right)^{n_x+n_y}\left(\cos^2\vartheta\right)^{n_x}\left(\sin^2\vartheta\right)^{n_y}\left(\cos^2\theta\right)^{n_z} \tag{2.100}$$

To further reduce this expression, we make a change of variables, $N=n_x+n_y$, which allows us to rearrange the sums $\sum_{n_x=0}^{\infty}\sum_{n_y=0}^{\infty}\to\sum_{N=0}^{\infty}\sum_{n_x=0}^{N}$,

$$\sum_{\boldsymbol{n}=0}^{\infty}|\langle\boldsymbol{n}|e^{\imath\mathbf{k}(\Omega)\cdot\mathbf{r}}|0\rangle|^2=\sum_{N=0}^{\infty}\sum_{n_x=0}^{N}\sum_{n_z=0}^{\infty}e^{-\eta^2\sin^2\theta-\frac{\eta^2}{\lambda}\cos^2\theta}\frac{\eta^{2(N+n_z)}}{N!n_z!\lambda^{n_z}}(\sin^2\theta)^N(\cos^2\theta)^{n_z}\\ \times\left(\sum_{n_x=0}^{N}\frac{N!}{n_x!(N-n_x!)}\left(\sin^2\vartheta\right)^{N-n_x}\left(\cos^2\vartheta\right)^{n_x}\right). \tag{2.101}$$

Using the identity,

$$\sum_{n_x=0}^{N}\frac{N!}{n_x!(N-n_x)!}\left(\sin^2\vartheta\right)^{N-n_x}\left(\cos^2\vartheta\right)^{n_x}=\left(1+\cot^2\vartheta\right)^N\left(\sin^2\vartheta\right)^N=1. \tag{2.102}$$

we reduce (2.100) to the following compact form,

$$\sum_{\boldsymbol{n}=0}^{\infty}|\langle\boldsymbol{n}|e^{\imath\mathbf{k}(\Omega)\cdot\mathbf{r}}|0\rangle|^2=e^{-\eta^2\sin^2\theta-\frac{\eta^2}{\lambda}\cos^2\theta}\sum_{N=0}^{\infty}\sum_{n_z=0}^{\infty}\frac{\left(\eta^2\sin^2\theta\right)^N}{N!}\frac{\left(\frac{\eta^2}{\lambda}\cos^2\theta\right)^{n_z}}{n_z!}. \tag{2.103}$$

Similarly, for the cigar case (see Appendix A.2), we find

$$\sum_{\boldsymbol{n}=0}^{\infty}|\langle\boldsymbol{n}|e^{\imath\mathbf{k}(\Omega)\cdot\mathbf{r}}|0\rangle|^2=e^{-\frac{\eta^2}{\lambda}\sin^2\theta-\eta^2\cos^2\theta}\sum_{N=0}^{\infty}\sum_{n_z=0}^{\infty}\frac{\left(\frac{\eta^2}{\lambda}\sin^2\theta\right)^N}{N!}\frac{\left(\eta^2\cos^2\theta\right)^{n_z}}{n_z!}. \tag{2.104}$$

Defining the following relations allows us to move quite easily between both trapping geometries,

$$\alpha(\theta)=\eta^2\cos^2\theta,\quad \beta(\theta)=\eta^2\sin^2\theta \qquad \text{pancake shape,} \tag{2.105a}$$

$$\alpha(\theta)=\eta^2\sin^2\theta,\quad \beta(\theta)=\eta^2\cos^2\theta \qquad \text{cigar shape,} \tag{2.105b}$$

Therefore (2.103) and (2.104), for the pancake and cigar trap shapes, may be respectively written as,

$$\sum_{\boldsymbol{n}=0}^{\infty} |\langle \boldsymbol{n}|e^{\imath \mathbf{k}(\Omega)\cdot\mathbf{r}}|0\rangle|^2 = e^{-\beta(\theta)-\frac{\alpha(\theta)}{\lambda}} \sum_{N=0}^{\infty}\sum_{n_z=0}^{\infty} \frac{(\beta(\theta))^N}{N!}\frac{\left(\frac{\alpha(\theta)}{\lambda}\right)^{n_z}}{n_z!}, \tag{2.106a}$$

$$\sum_{\boldsymbol{n}=0}^{\infty} |\langle \boldsymbol{n}|e^{\imath \mathbf{k}(\Omega)\cdot\mathbf{r}}|0\rangle|^2 = e^{-\beta(\theta)-\frac{\alpha(\theta)}{\lambda}} \sum_{N=0}^{\infty}\sum_{n_z=0}^{\infty} \frac{(\beta(\theta))^{n_z}}{n_z!}\frac{\left(\frac{\alpha(\theta)}{\lambda}\right)^{N}}{N!}. \tag{2.106b}$$

The only major remaining difference between the two is the summations over N and n_z are interchanged. In the next section, we find the general solution for the angular probability of spontaneous emission in the presence of a perfect Fermi sea, with Fermi shell $|\boldsymbol{n}_{\mathrm{F}}\rangle$.

2.4.2.3 General Solution

Close examination shows that equations (2.106) are equal to 1. This is to be expected as the probability for an excited fermion to recoil into *any* of the available states $|\boldsymbol{n}\rangle$ is 1. In this work, we assume the presence of a perfect ground state spin polarised Fermi sea, wherein all modes of the anisotropic harmonic oscillator are occupied up to and including the degenerate Fermi shell $|\boldsymbol{n}_{\mathrm{F}}\rangle$. Due to the Pauli principle, the available modes $|\boldsymbol{n}\rangle$ for the excited Fermion to recoil into are those unoccupied by the ground state Fermi sea, where $|\boldsymbol{n}\rangle \geq |\boldsymbol{n}_{\mathrm{F}}+1\rangle$. We may sum over the available states as,

$$\begin{aligned}\sum_{\boldsymbol{n}=\boldsymbol{n}_{\mathrm{F}}+\mathbf{1}}^{\infty} |\langle \boldsymbol{n}|e^{\imath \mathbf{k}(\Omega)\cdot\mathbf{r}}|\mathbf{0}\rangle|^2 &= \sum_{\boldsymbol{n}=0}^{\infty} |\langle \boldsymbol{n}|e^{\imath \mathbf{k}(\Omega)\cdot\mathbf{r}}|0\rangle|^2 - \sum_{\boldsymbol{n}=0}^{\mathbf{n}_{\mathrm{F}}} |\langle \boldsymbol{n}|e^{\imath \mathbf{k}(\Omega)\cdot\mathbf{r}}|0\rangle|^2, \\ &= 1 - \sum_{\boldsymbol{n}=0}^{\mathbf{n}_{\mathrm{F}}} |\langle \boldsymbol{n}|e^{\imath \mathbf{k}(\Omega)\cdot\mathbf{r}}|0\rangle|^2.\end{aligned} \tag{2.107}$$

Herein, we consider the solution for the pancake trap. We recall from (2.39a) that for any energy level of the pancake trap, $n_{\mathrm{p}} = N + \lambda n_z$. For the range of modes n_{p} which are part of the Fermi sea $0 \leq n_{\mathrm{p}} \leq n_{\mathrm{F}}$, N may take any of the values in the range $N = 0, 1, 2, \ldots, n_{\mathrm{p}}$, whereas, the values that n_z may assume depend on N. These are $n_z = 0, 1, 2, \ldots, \lfloor (n_{\mathrm{F}} - N)/\lambda \rfloor$. The sum over the modes occupied by the Fermi sea is thus given by,

$$\sum_{\boldsymbol{n}=0}^{\boldsymbol{n}_{\mathrm{F}}} |\langle \boldsymbol{n}|e^{\imath \mathbf{k}(\Omega)\cdot\mathbf{r}}|0\rangle|^2 = e^{-\beta(\theta)} \sum_{N=0}^{n_{\mathrm{F}}} \frac{(\beta(\theta))^N}{N!} \left(e^{-\frac{\alpha(\theta)}{\lambda}} \sum_{n_z=0}^{\lfloor \frac{n_{\mathrm{F}}-N}{\lambda} \rfloor} \frac{\left(\frac{\alpha(\theta)}{\lambda}\right)^{n_z}}{n_z!} \right), \tag{2.108}$$

To simplify (2.107), we use the well known incomplete gamma functions [31], which satisfy

$$\Gamma(n+1) = \int_0^t t^n e^{-t} dt \;=\; n!, \tag{2.109a}$$

$$\gamma(n+1,a) = \int_0^a t^n e^{-t} dt, \qquad \Gamma(n+1,a) = \int_a^\infty t^n e^{-t} dt, \tag{2.109b}$$

$$\frac{\Gamma(n+1,a)}{\Gamma\,(n+1)} = e^{-a} \sum_{k=0}^{n} \frac{a^k}{k!}, \tag{2.109c}$$

$$\Gamma(n+1) = \Gamma(n+1,a) + \gamma(n+1,a), \tag{2.109d}$$

where $\Gamma(n+1,a)$ is known as the upper incomplete gamma function and $\gamma(n+1,a)$ is the lower incomplete gamma function.

From (2.109) we may simplify (2.108) as,

$$\sum_{\boldsymbol{n}=\boldsymbol{0}}^{\boldsymbol{n}_\mathrm{F}} |\langle \boldsymbol{n}| e^{\imath \mathbf{k}(\Omega)\cdot\mathbf{r}} |0\rangle|^2 \;=\; e^{-\beta(\theta)} \sum_{N=0}^{n_\mathrm{F}} \frac{(\beta(\theta))^N}{N!} \left(1 - \frac{\gamma(\lfloor \frac{n_\mathrm{F}-N}{\lambda} \rfloor + 1, \frac{\alpha(\theta)}{\lambda})}{\Gamma(\lfloor \frac{n_\mathrm{F}-N}{\lambda} \rfloor + 1)}\right), \tag{2.110}$$

Plugging the above into (2.107),

$$\begin{aligned} \sum_{\boldsymbol{n}=\boldsymbol{n}_\mathrm{F}+\boldsymbol{1}}^{\infty} |\langle \boldsymbol{n}| e^{\imath \mathbf{k}(\Omega)\cdot\mathbf{r}} |0\rangle|^2 \;=\; 1 \;-\; & \left(1 - \frac{\gamma(n_\mathrm{F}+1, \beta(\theta))}{\Gamma(n_\mathrm{F}+1)}\right) \\ & +\; e^{-\beta(\theta)} \sum_{N=0}^{n_\mathrm{F}} \frac{(\beta(\theta))^N}{N!} \frac{\gamma(\lfloor \frac{n_\mathrm{F}-N}{\lambda} \rfloor + 1, \frac{\alpha(\theta)}{\lambda})}{\Gamma(\lfloor \frac{n_\mathrm{F}-N}{\lambda} \rfloor + 1)}, \end{aligned} \tag{2.111}$$

which finally leads us to a closed form solution for (2.65) in terms of the lower incomplete gamma functions for both trap shapes.

$$M_f(\theta) = \frac{\gamma(n_\mathrm{F}+1, \beta(\theta))}{\Gamma(n_\mathrm{F}+1)} + e^{-\beta(\theta)} \sum_{N=0}^{n_\mathrm{F}} \frac{(\beta(\theta))^N}{N!} \frac{\gamma(\lfloor \frac{n_\mathrm{F}-N}{\lambda} \rfloor + 1, \frac{\alpha(\theta)}{\lambda})}{\Gamma(\lfloor \frac{n_\mathrm{F}-N}{\lambda} \rfloor + 1)}\,. \tag{2.112}$$

With this choice of notation, $n_\mathrm{F} = 0$ represents a trap in which solely the ground state is occupied. Therefore, the absence of any Fermi sea can be treated by setting $n_\mathrm{F} = -1$ in (2.112).

2.5 Emission Patterns in Anisotropic Traps

In order to grasp the mechanics behind the spatially anisotropic decay rates, it is necessary to firstly look at the emission probabilities into the different energy levels or energy shells. For the isotropic case, this probability distribution is poissonian in character, and has a maximum value centered on particular energy level, given by the square of the Lamb-Dicke parameter $\eta^2 = E_R/\hbar\omega$. This variable determines the range of accessible states and is given by the ratio between the recoil energy, $E_R = \hbar^2 k_0^2/2m$, and the trapping strength, $\hbar\omega_{x,y,z}$, in the different directions. Here k_0 is the wave vector corresponding to the transition $|e\rangle \to |g\rangle$.

In the presence of an anisotropic Fermi sea the rate of spontaneous emission along a specific direction is determined by three parameters: (1) the number of ground state atoms (in the zero temperature case n_{F}), (2) the degeneracy of the available states, $g_{\mathrm{p,c}}(\lambda, n_{\mathrm{p,c}})$, and (3) the Lamb-Dicke parameter $\eta = \sqrt{E_R/\hbar\omega}$.

As we will show in this section, introducing anisotropy to the trapping potential has a distinct effect on the accessibility of the various energy levels. Moving to this regime incurs discontinuities in the previously smooth distribution of accessible states (isotropic regime). These discontinuities arise as the degeneracy of the individual energy levels change and the energy excitations of the respective quantum states change. These changes cause 'kinks' in the distribution. Since we are dealing with integer aspect ratios λ the discontinuities appear every integer multiple of λ, i.e. between every $n = m(\lambda - 1)$ and $n = m\lambda$ energy level (n is the energy level and $m = 0, 1, 2, \dots$). However, the distribution remains smooth over a range of length λ inbetween these discontinuities. The cause of these anomalies is the focus of this section.

2.5.1 Emission Probabilities

Let us first focus on the influence of the degeneracies by examining the matrix elements for individual transitions from the ground cm-state (center of mass state) of the excited atom to a single final state, $|\boldsymbol{n}_{\mathrm{p,c}}\rangle$. We have,[1]

$$P_e(n_{\mathrm{p,c}}) = |\langle \boldsymbol{n}_{\mathrm{p,c}} | e^{i\mathbf{k}\cdot\mathbf{r}} | 0 \rangle|^2 \,. \tag{2.113}$$

To evaluate this equation we rewrite (2.39a) as $n_{\mathrm{p}} = N + \lambda n_z$, where $N = n_x + n_y$. Since n_z may take any of the values $n_z = \lfloor 0/\lambda \rfloor, \lfloor 1/\lambda \rfloor, \dots, \lfloor n_{\mathrm{p}}/\lambda \rfloor$, we can sum over all the modes of a particular shell knowing that $N = n_{\mathrm{p}} - \lambda n_z$. To determine the decay

[1] Here and in the following (see the top rows of figures 2.1 and 2.2) we are evaluating the coherent states of the anisotropic harmonic oscillator.

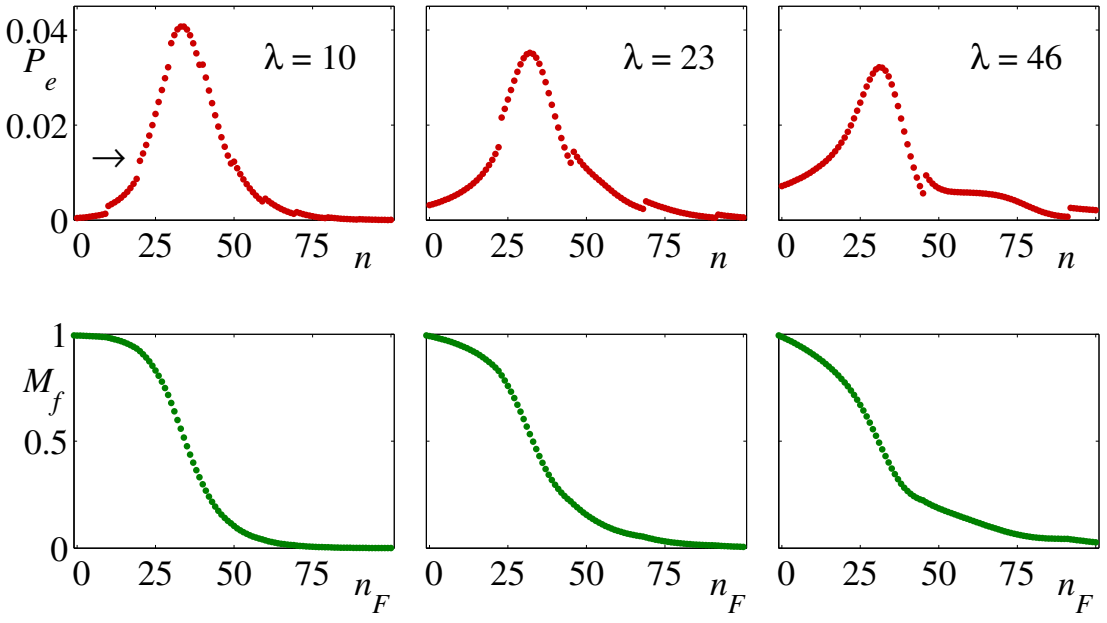


FIGURE 2.1: Top row: emission probability, P_e, into individual shells in a pancake shaped trap for $\eta^2 = 36$ and $\lambda = 10, 23, 46$. The arrow indicates the $n = 20$ energy level of the harmonic trap, which is referred to in the text. Bottom row: decay rate of the excited particle, M_f, for the same parameters as above.

rate into a particular mode, we need to integrate the decay rate over all possible spatial directions. Firstly, we note that the volume integral in spherical polar co-ordinates is written,

$$\int dV = \int_0^\infty dr \int_0^{2\pi} d\vartheta \int_0^\pi \sin\theta \, d\theta. \tag{2.114}$$

Hence, the probability for an atom to emit into any angle in space is given by the integral over all the available angles as,

$$\int d\Omega = \frac{1}{4\pi} \int_0^{2\pi} d\vartheta \int_0^\pi \sin\theta \, d\theta, \tag{2.115}$$

where we normalise using $(4\pi)^{-1}$. Therefore, we can construct the shell emission as the integral over all angles Ω using (2.101) as,

$$P_e(n_\mathrm{p}) = \frac{1}{2} \int_0^\pi d\theta \, \sin\theta \, e^{-\eta^2 \sin^2\theta - \frac{\eta^2}{\lambda}\cos^2\theta} \sum_{n_z=0}^{\lfloor n_\mathrm{p}/\lambda \rfloor} \frac{\left(\eta^2 \sin^2\theta\right)^{n_\mathrm{p}-\lambda n_z}}{(n_\mathrm{p} - \lambda n_z)!} \frac{\left(\frac{\eta^2}{\lambda}\cos^2\theta\right)^{n_z}}{n_z!}. \tag{2.116}$$

For the cigar trap, we rewrite (2.39b) as $n_\mathrm{c} = \lambda N + n_z$. With N only able to take values in the range, $N = \lfloor 0/\lambda \rfloor, \lfloor 1/\lambda \rfloor, \ldots, \lfloor n_\mathrm{c}/\lambda \rfloor$, leading to,

$$P_e(n_\mathrm{c}) = \frac{1}{2} \int_0^\pi d\theta \, \sin\theta \, e^{-\frac{\eta^2}{\lambda}\sin^2\theta - \eta^2\cos^2\theta} \sum_{N=0}^{\lfloor n_\mathrm{c}/\lambda \rfloor} \frac{\left(\frac{\eta^2}{\lambda}\sin^2\theta\right)^N}{N!} \frac{\left(\eta^2\cos^2\theta\right)^{n_\mathrm{c}-\lambda N}}{(n_\mathrm{c} - \lambda N)!}, \tag{2.117}$$

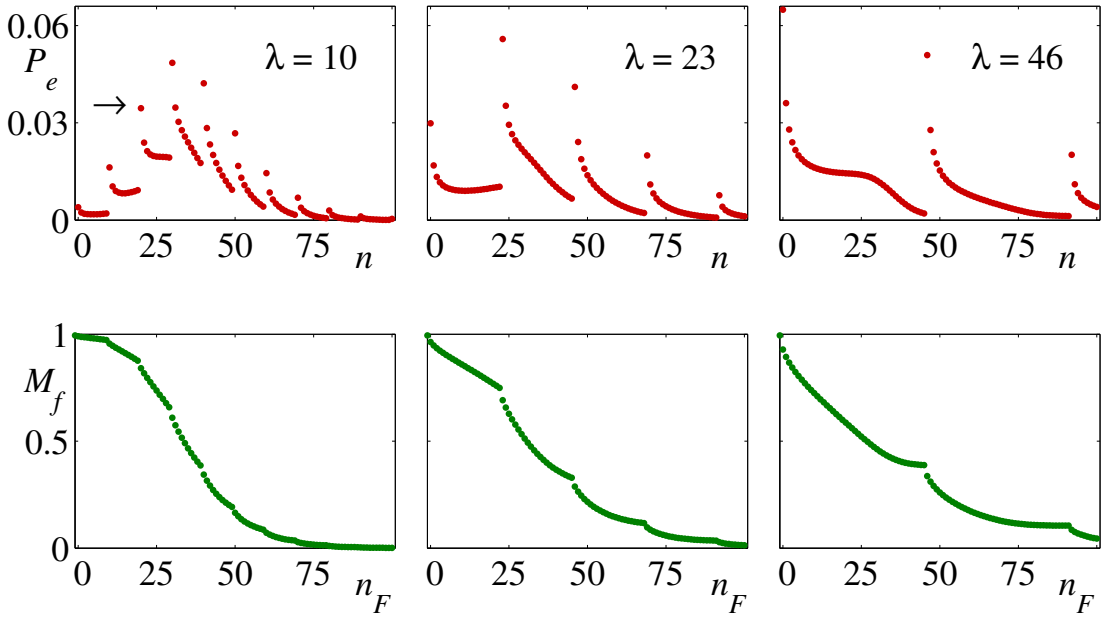


FIGURE 2.2: Top row: emission probability, P_e, into individual shells in a cigar shaped trap for $\eta^2 = 36$ and $\lambda = 10, 23, 46$. The arrow indicates the $n = 20$ energy level of the harmonic trap, which is referred to in the text. Bottom row: decay rate of the excited particle, M_f, for the same parameters as above.

For an isotropic trap, this a continuous distribution of finite width which is centered around the energy level $n = \eta^2$. The effects introduced by an anisotropy are significant and can be clearly seen in the graphs in the upper rows of figures 2.1 and 2.2, where we show $P_e(n_\mathrm{p})$ for the pancake trap and $P_e(n_\mathrm{c})$ for the cigar shaped trap, respectively, for increasing values of the anisotropy, $\lambda = 10$, 23 and 46. The most obvious feature in both situations is the appearance of a λ-dependent discontinuity in the distribution, which is more pronounced in the cigar shaped setting.

To explain this behaviour, let us first intuitively argue its existence. When an internally excited atom which is trapped in the ground state of an empty isotropic harmonic trap decays, the probability of the photon being emitted is the same in all directions. This is rather easy to understand as, in this situation, the density of states is identical in all directions. However, for the anisotropic trap the situation is different. As the aspect ratio is increased, the degeneracy of any energy level will either decrease or remain the same. Therefore up to a specific shell, the number of quantum states, as given by (2.63a) and (2.63b) is reduced, and as a result, the density of states in the different directions changes.

As the recoil of the de-excited fermion to a certain quantum state and the direction of the emitted photon are directly related, it seems rather surprising that for the free case spontaneous emission remains isotropic, irrespective of the diminishing number of quantum states. However, it is exactly the modified distribution shown in the upper

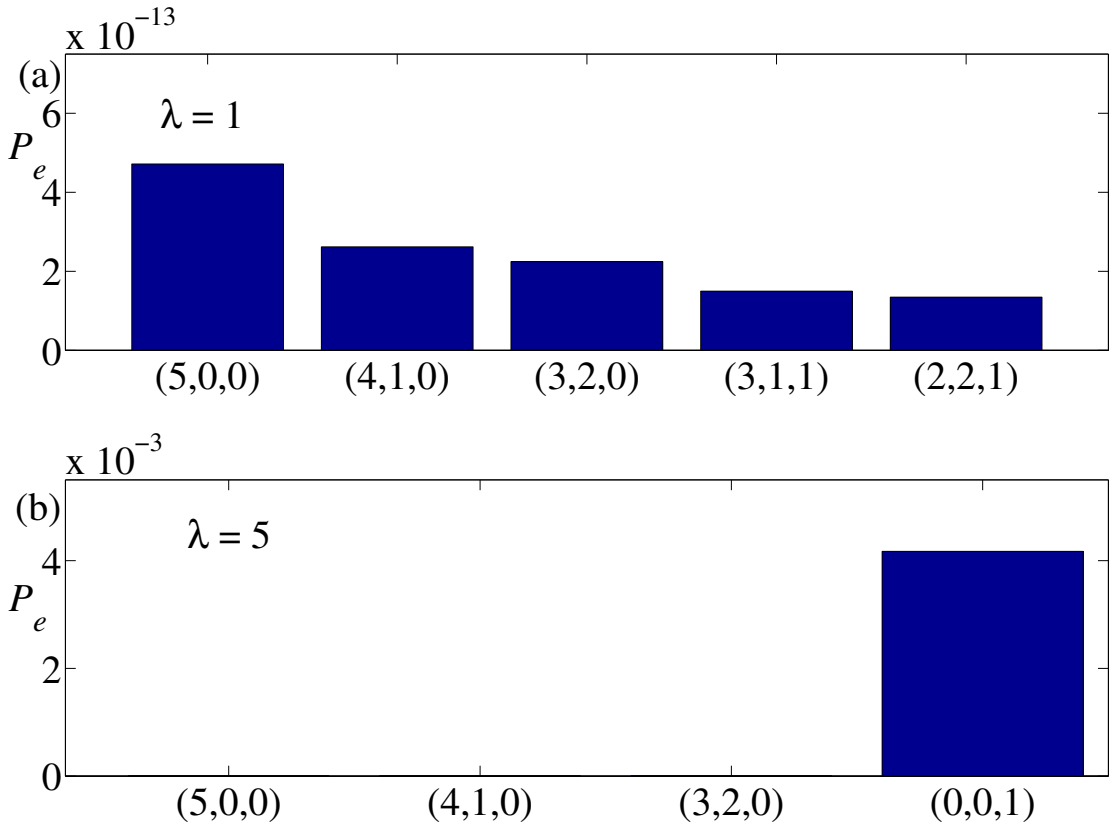


FIGURE 2.3: (a) Emission probability into individual states within the shell $n = 5$ in an isotropic trap. The triplets represent (n_x, n_y, n_z) and all permutations of each triplet have the same probability. The Lamb-Dicke factor is $\eta = 5$, however changing this value only scales all values. (b) Emission probability into individual states within the shell $n = 5$ in a pancake trap with $\lambda = 5$. The values for the three states on the left are not visible on this scale.

rows in figures 2.1 and 2.2 that preserves the isotropic decay rate of a lone atom in an anisotropic Hilbert space.

To gain more insight into the source of the discontinuities, let us consider the emission probability into specific states within a degenerate shell n of an isotropic and a pancake shaped ($\lambda = 5$) trap. Figure 2.3 shows $P_e(n_x, n_y, n_z)$ for a fixed shell, in which all combinations of the triplet (in both (a) and (b)) of quantum numbers adds up to $n_\mathrm{p} = 5$. It can be seen that, in general, states which include ground state excitations have a higher probability for occupation, relative to ones which do not. This is due to the fact that the excited atom is initially in its center-of-mass ground state.

When we move from the isotropic to the anisotropic setting, it is therefore clear that whenever the value of an energy shell, n, reaches an integer multiple of the anisotropy parameter, the shell contains a state with two ground state excitations. For example, with the pancake trap, when $n_\mathrm{p} = m\lambda$, where $m = 0, 1, 2, \ldots$, there exists the state

$(n_x, n_y, n_z) = (0, 0, m)$, in the shell n_p. For the cigar trap we have the doubly degenerate state $(n_x, n_y, n_z) = (m, 0, 0)$ and $(0, m, 0)$, for the energy state $n_\mathrm{c} = m\lambda$.

As these states have a higher probability of occupation (see figure 2.3(b)), the overall emission probability into this energy shell is increased, leading to the observed discontinuous jump. As an example, let us consider a pancake shaped trap with an aspect ratio of $\lambda = 10$. For the shell $n_\mathrm{p} = 19$, the degenerate states are $(n_x + n_y, n_z) = (19, 0)$ and $(9, 1)$, whereas for the $n_\mathrm{p} = 20$ energy level (indicated by the arrow in figure 2.1) the states are $(n_x + n_y, n_z) = (20, 0), (10, 1)$ and $(0, 2)$. The *extra* $(0, 2)$ state is the dominant contributor to the shell occupation probability, and its appearance is responsible for the discontinuous increase in emission probability. For the cigar trap, this effect is even more pronounced as there are two tight directions, and in the example above, the states $(n_x, n_y, n_z) = (2, 0, 0)$ and $(0, 2, 0)$ both become available. Closer examination shows that the state $(1, 1, 0)$ also gives a large (but smaller) contribution to emission into the $n_\mathrm{c} = 20$ shell, followed by the $(1, 0, 10)$ state, whereas the $(0, 0, 20)$ state's occupation probability is negligible.

Transitions into states which have a ground state excitation, possess a larger overlap with the initial state, and are therefore more likely. In this respect, a transition into a state with two ground state excitations combined with a small change in the principle quantum number contributes to the high probability of the state's occupation. The smallest change in principle quantum number is in the tight direction, therefore making transition into states with low tight excitations (numbering > 0) and low soft excitations (≈ 0) more likely. This is in contrast to states with high soft excitations and ground state tight excitations. The probability of transition into these states is smaller, making them unlikely candidates for occupation.

For completeness, we show the total emission probability for increasing particle number (i.e. increasing Fermi energy or Fermi level) and different anisotropies in the bottom rows of figures 2.1 and 2.2. This equality is given by

$$M_f^{\mathrm{c,p}}(n_\mathrm{F}) = \sum_{n_\mathrm{c,p}=n_\mathrm{F}+1}^{\infty} P_e(n_\mathrm{c,p}). \tag{2.118}$$

Fermi inhibition is absent for the empty trap ($M_f = 1$), shown for $n_\mathrm{F} = -1$, and slowly increases for $n_\mathrm{F} \geq 0$ and accelerates for $n_\mathrm{F} \sim \eta^2$. The discontinuity in the variable $P_e(n_\mathrm{c,p})$ translates into non-smooth kinks in this distribution. Furthermore, it is clear that the decay rate of the excited fermion in the presence of an ideal Fermi sea, with Fermi level n_F, is different for the different trap shapes. In other words the trap shape, and consequently the shape of the Fermi Sea, plays a role which affects the total lifetime

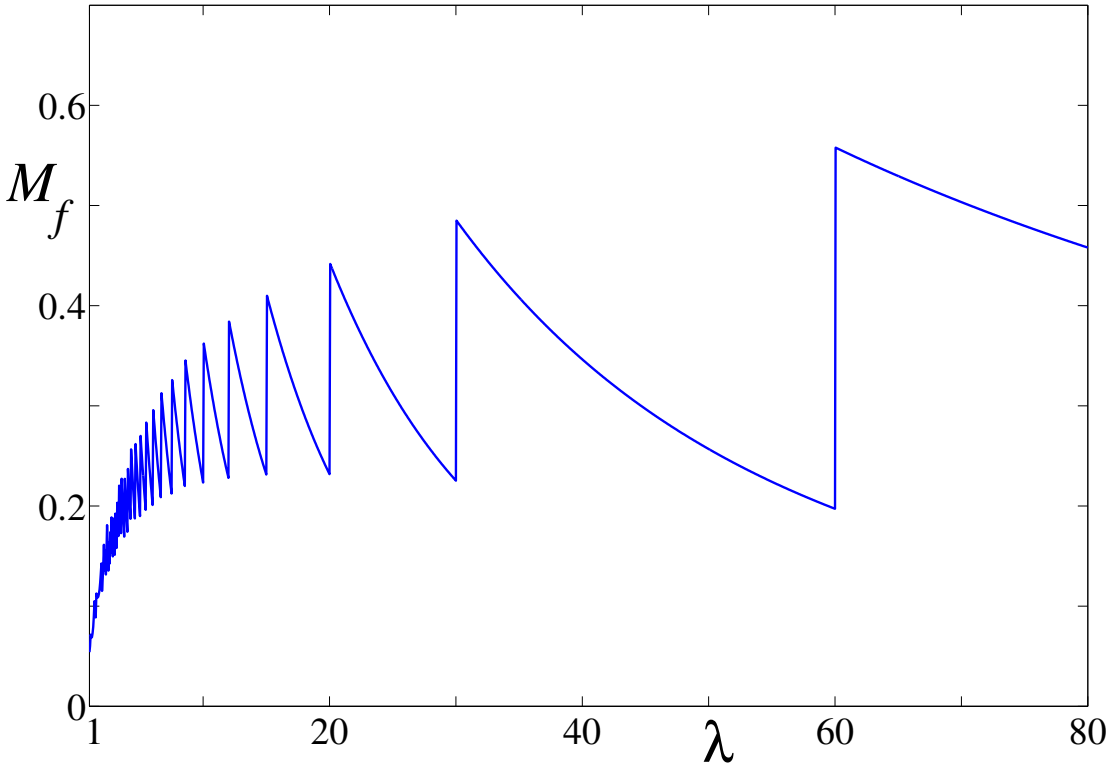


FIGURE 2.4: (Color online) M_f along the tight axis at $T = 0$. $\eta^2 = 49$, $n_\mathrm{F} = 60$. Note that we use a continuous distribution of λ for this graph.

of the excited fermion with respect to the free case. This is in conjunction with the Lamb-Dicke parameter η, the squeezing parameter λ and the Fermi level n_F.

2.5.2 Tight and Soft Axes Emission

The fact that the presence of an anisotropic Fermi sea will lead to anisotropic emission patterns was already noted in [5, 6], and in the following, we develop a detailed understanding of the directional features. Since for the pancake, as well as for the cigar shaped trap, the angular decay rate is rotationally equivalent in the plane through the respective symmetry axis, $(0, \pi)$, we can treat both geometries in a quasi 2D picture. It is then immediately clear that the results for the angular decay rate in this plane for both settings will be related by a simple $\pi/2$ rotation (due to our definition of $\lambda \geq 1$).

Let us first look at the emission along the principal axes of the anisotropic trap only in the tight and the soft direction. Choosing the tight direction in the pancake (cigar) shaped trap along $\theta = 0$ ($\theta = \pi/2$), the modification factor in (2.112) simplifies to

$$M_f = \frac{\gamma(\tilde{n}_\mathrm{F} + 1, \frac{\eta^2}{\lambda})}{\Gamma(\tilde{n}_\mathrm{F} + 1)} \,. \tag{2.119}$$

This equation is easily found from (2.101) (or the equivalent version for the cigar trap) by setting $\theta = 0$ ($\theta = \pi/2$) and following the same procedure outlined in section 2.4.2.

The behaviour of (2.119) with increasing anisotropy is shown in figure 2.4 for a system with $n_{\mathrm{F}} = 60$. The most obvious feature of the plot is a series of sawtooth-like discontinuities. Careful examination shows that n_{F} of these exist and they appear whenever the value of the aspect ratio, λ, increases beyond the values of $\frac{n_{\mathrm{F}}}{m}$, $(m = 1, 2, \ldots, n_{\mathrm{F}})$. The increase in emission probability for values just after these points is due to the availability of an extra free state with a lower tight excitation just outside the Fermi edge. For example, in the pancake trap, when one moves from $\lambda = 30$ to $\lambda > 30$ the state $(n_x + n_y, n_z) = (0, 2)$ emerges from the Fermi sea for $n_{\mathrm{F}} = 60$. As discussed in Section 2.5.1, this state has a high probability to be emitted into as it contains ground state excitations in the soft direction, hence the large increase in the decay rate. By increasing λ further this state moves away from the Fermi edge and the emission probability decreases until the next state with a lower tight excitation emerges from the Fermi sea. For values of $\lambda > n_{\mathrm{F}}$ no more discontinuities appear since the Fermi sea only occupies energy states with ground state excitations in the tight direction. Emission along the soft direction can be calculated from (2.119) by taking $\lambda = 1$. The decay rate along this direction is determined exclusively by the Fermi shell n_{F} and the value of the Lamb-Dicke parameter η.

Considering a fixed value of the aspect ratio λ in either anisotropic trapping potential and changing n_{F} one notices a degeneracy in the emission probability in the tight direction, shown in figure 2.5(a). This behaviour was already mentioned in [5] and we can see from (2.119) that it stems from the fact that $\tilde{n}_{\mathrm{F}}$ only changes its value in steps of λ. An increase in the value of $\tilde{n}_{\mathrm{F}}$ coincides with the Fermi sea occupying a state with a higher tight excitation (and ground state soft excitations), leading to a decrease in the decay rate along the tight direction. For example, when moving from $n_{\mathrm{F}} = 35$ to $n_{\mathrm{F}} = 36$, the state $(n_x + n_y, n_z) = (0, 9)$ becomes occupied by the Fermi sea, producing the discontinuous reduction of the decay rate (see figure 2.5(a)).

2.5.3 Fine Structure

The emission spectrum between the principal axes is characterised by the appearance of a fine structure (see figure 2.5(b)), which exists for a wide range of parameters. The first hint to understanding the origins of the visible extrema comes from noticing that the number of maxima between the soft and tight axes is related to the number of excitations in the tight direction that are occupied by the Fermi sea, $\tilde{n}_{\mathrm{F}}$. To show this relation let

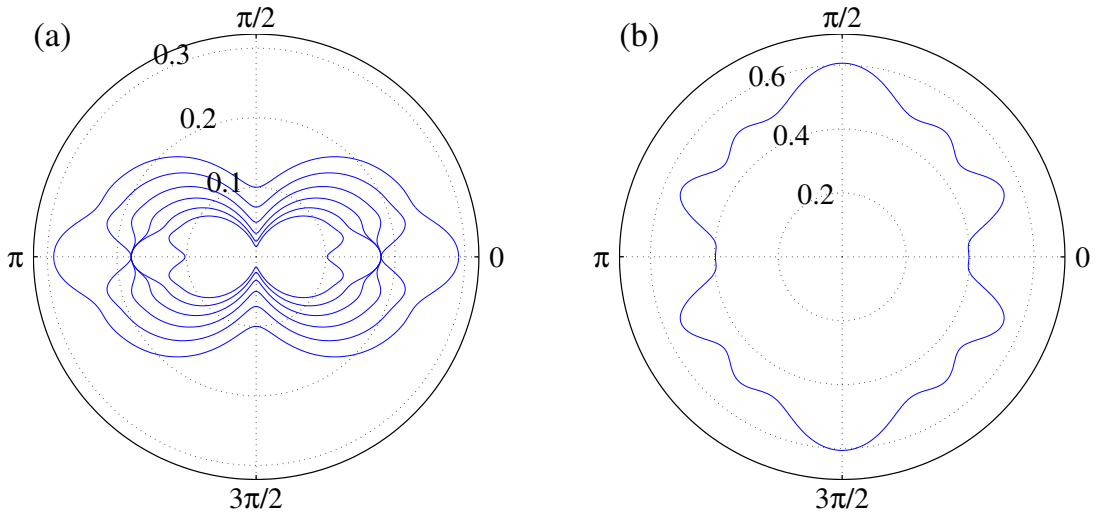


FIGURE 2.5: (Color online) (a) $M_f(\theta)$ in a pancake shaped trap at $T = 0$. $\eta^2 = 25$, $\lambda = 4$ with $n_{\rm F} = 31$ (outermost) to $n_{\rm F} = 36$ (innermost). (b) $M_f(\theta)$ in a pancake shaped trap with $\lambda = 11$, $\eta^2 = 25$ and $n_{\rm F} = 23$.

us consider the emission probability into all shells with a fixed value for n_z in a pancake shaped trap.

Let us reconstruct (2.107) for a fixed n_z. The first term in this equation is written as, $e^{-\alpha(\theta)/\lambda}\left(\alpha(\theta)/\lambda\right)^{n_z}/n_z!$. The second term, which removes the occupied modes of the Fermi sea, has a condition attached to it which we need to incorporate into the expression. The condition is that we may only remove the mode if it is within the Fermi sea. Therefore, for each n_z, the soft excitations may only take values between 0 and $n_{\rm F} - \lambda n_z$. With these considerations the second term of (2.107) is written as,

$$e^{-\beta-\frac{\alpha(\theta)}{\lambda}}\sum_{N=0}^{n_{\rm F}}\sum_{n_z=0}^{\lfloor\frac{n_{\rm F}-N}{\lambda}\rfloor}\frac{\left(\beta(\theta)\right)^N}{N!}\frac{\left(\frac{\alpha(\theta)}{\lambda}\right)^{n_z}}{n_z!}, \tag{2.120}$$

we fix the value of n_z in the Fermi Sea,

$$\frac{\left(\frac{\alpha(\theta)}{\lambda}\right)^{n_z}}{n_z!}e^{-\beta(\theta)-\frac{\alpha(\theta)}{\lambda}}\sum_{N=0}^{n_{\rm F}-\lambda n_z}\frac{\left(\beta(\theta)\right)^N}{N!}. \tag{2.121}$$

This allows us to write,

$$M_f(\theta,n_z) = e^{-\frac{\alpha(\theta)}{\lambda}}\frac{\left(\frac{\alpha(\theta)}{\lambda}\right)^{n_z}}{n_z!}\left(1-\frac{\Gamma(n_{\rm F}-\lambda n_z+1,\beta(\theta))}{\Gamma(n_{\rm F}-\lambda n_z+1)}\right). \tag{2.122}$$

However the argument of $\Gamma\left(n_{\rm F}-\lambda n_z+1,\beta(\theta)\right)$ must be zero for $n_{\rm F}-\lambda n_z+1\leq 0$, and we rewrite it as $\max(0,n_{\rm F}-\lambda n_z+1)$ to find the decay rate as a function of available n_z

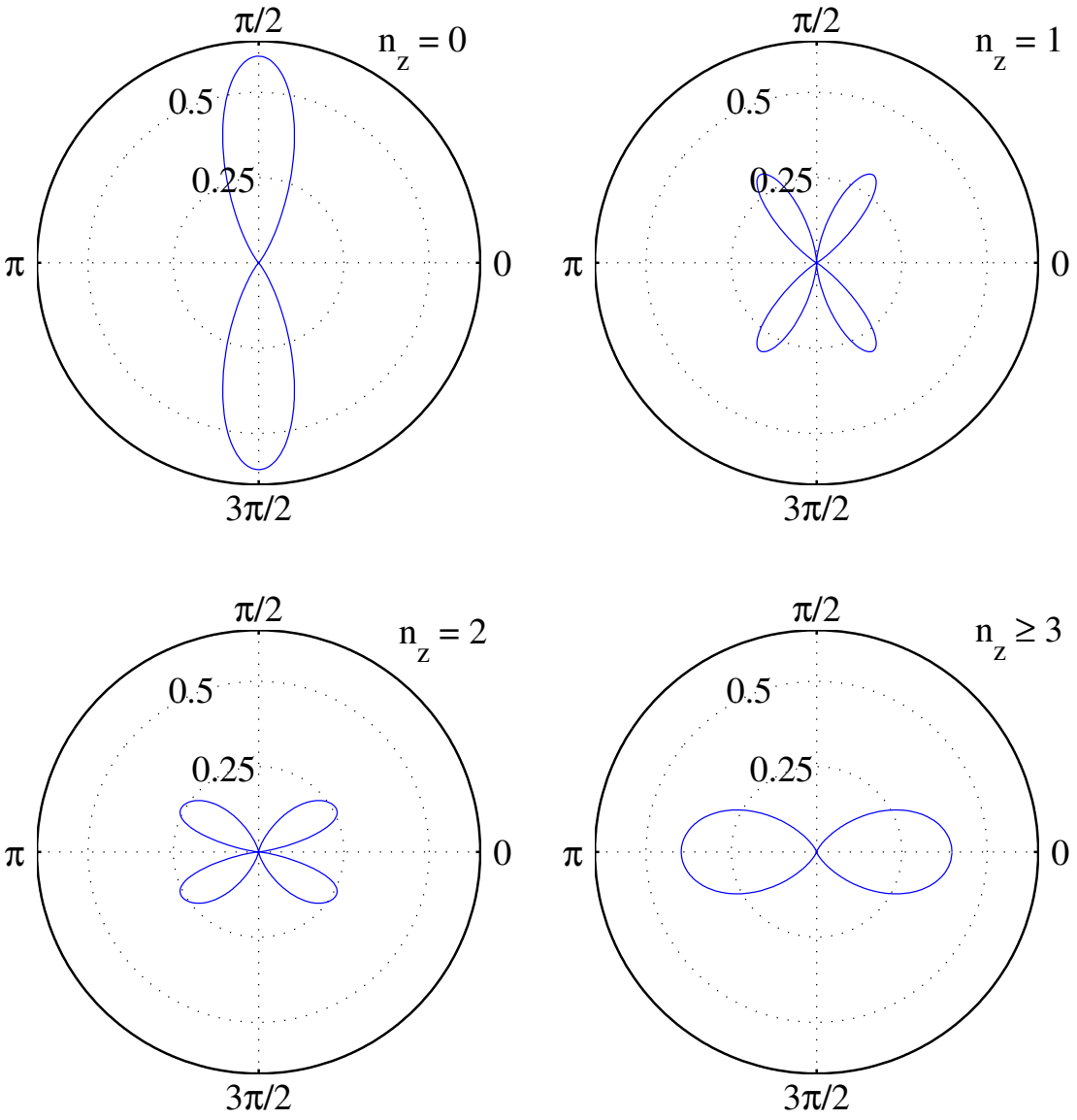


FIGURE 2.6: (Color online) $M_f(\theta, n_z)$ for a pancake shaped trap with, $\lambda = 11$ $\eta^2 = 25$ and $n_F = 23$. In the four graphs the decay is only allowed into quantum states of the harmonic trap with $n_z = 0$, 1, 2, and $n_z \geq 3$, respectively.

modes as,

$$M_f(\theta, n_z) = e^{-\frac{\alpha(\theta)}{\lambda}} \frac{\left(\frac{\alpha(\theta)}{\lambda}\right)^{n_z}}{n_z!} \frac{\gamma(\max(0, n_F - \lambda n_z + 1), \beta(\theta))}{\Gamma(\max(0, n_F - \lambda n_z + 1))} \tag{2.123}$$

with the definition of $\alpha(\theta)$ and $\beta(\theta)$ given in (2.105). As a specific example we show in figure 2.5(b) a gas with $n_F = 23$, $\eta^2 = 25$ and $\lambda = 11$. In this case we find $\tilde{n}_F = 2$ maxima in any $\pi/2$ arc between the tight to the soft axis. Comparing this emission pattern to the results from (2.123), one can see (figure 2.6) that each isolated contribution from a transition into a state with a fixed value of n_z is responsible for one of the maxima. For values of $n_z > \tilde{n}_F$ the emission is predominantly into the tight direction, therefore originating from transitions into states for which both ground state excitations in the

soft direction are available. This is the angular form of the phenomenon analysed in section 2.5.1.

When restricting the recoiling atom to occupying states with a ground state excitation in the tight direction, $n_z = 0$, the emission is mainly focused around small angles about the soft axis. The intermediate excitations, $n_z = 1, 2$, make up the two intermediate ripples between the principle axes and summing up the contributions to the photon emission of all four plots in figure 2.6 gives the emission plot shown in figure 2.5(b). In contrast, if we calculate (2.123) for an isotropic trap for different values of n_z, each individual term would show a similar behaviour of having a single maximum at a finite angle between the principle axes. However, the sum of those will give the isotropic emission pattern which corresponds to the decay rate being the same in all directions.

It is now obvious that for the limit $\lambda > n_{\mathrm{F}}$ the fine structure disappears and the extrema of emission will be located around the directions of the principal axes (see figure 2.7(a)). As $\lambda \to \infty$, emission into the tight direction is reduced, whereas the emission in the soft direction ($(0, \pi)$-axis for the cigar trap) remains constant, figure 2.7(b). In this regime the Fermi sea is completely confined to states with ground state excitations in the tight direction. Therefore, it becomes easier for the recoiling atom to access states in the soft direction due to the diminishing density of states in the tight direction. In the limit of $\lambda \to \infty$ the emission probability can be written as

$$M_f(\theta; \lambda \to \infty) = \frac{\gamma(n_{\mathrm{F}} + 1, \beta(\theta))}{\Gamma(n_{\mathrm{F}} + 1)} \, . \tag{2.124}$$

For both trapping geometries, the emission probability in the tight direction has completely vanished. This is shown for the cigar trap in the inner plot of figure 2.7(a). As we have discussed, the spontaneous emission rate plots are rotationally symmetric around the $(0, \pi)$ axis.

Shown in (b) is a 3-D illustration of an excited atom's angular lifetime in a cigar trap ($\lambda \to \infty$) relative to the free case. For the cigar trap, the emission is symmetric through a 2π rotation about the $(0, \pi)$ axis. Note that for a pancake shaped trap this effect would correspond to emission into a well defined plane perpendicular to the tight principal axis. i.e. a 2π rotation about the $(\pi/2, 3\pi/2)$ axis.

It is possible to make use of this behaviour and create a system where photon emission becomes highly directional. While directional photon emission is usually achieved by using optical cavities, and therefore engineering the Hilbert space of the photon, this example is complementary in that it uses a confining geometry of an anisotropic harmonic trap to modify the energetic modes available to the Fermi Sea. This means of engineering

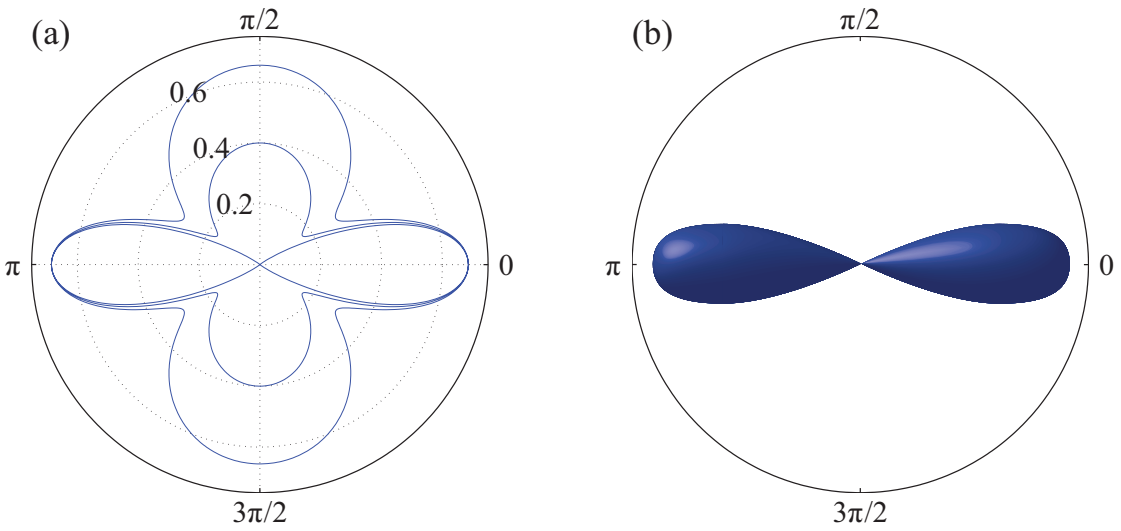


FIGURE 2.7: (Color online) (a) $M_f(\theta)$ in a cigar shaped trap at T = 0 with $n_{\mathrm{F}} = 45$ and $\eta^2 = 49$. $\lambda = 46$ (outermost), $\lambda = 96$ (center plot) and $\lambda = \infty$ (innermost). The plot is symmetric through a 2π rotation about the $(0, \pi)$ axis. (b) A three-dimensional illustration of the excited particles decay rate in a cigar trap in the large anisotropy limit.

the available Hilbert space of the particles, in conjunction with an ultracold Fermi Sea, is analogous to the modification achieved by the use of an optical cavity.

Let us stress that it is not primarily the size of the Fermi sea that is responsible for the inhibition of spontaneous emission, merely the presence of the Fermi sea. The strength of the effect is therefore independent of the strength of the inhibition effect uncovered earlier and the emission probability of the photon in the presence of a Fermi sea can still be close to the emission probability in free space whilst $\eta^2 \gtrsim n_{\mathrm{F}}$. (see figure 2.7(a)).

2.6 Conclusions and Outlook

In this chapter we have given a detailed investigation into the directional properties of spontaneous emission of a single atom in the presence of an anisotropic, ideal and spin polarised ultracold Fermi gas. The demand to obey the Pauli principle leads to the formation of a non-trivial, anisotropic emission pattern for the photon, which can be explained by carefully examining the allowed transitions the recoiling atom can make.

We first calculated the relation between the Fermi energy and particle number and then investigated the single particle transition matrix element, for both geometries of anisotropic traps. The change in the density of states into the different spatial directions was found to be accompanied by the appearance of discontinuities in the distribution of the emission probability spectrum for different shells. While in an isotropic trap these

two effects cancel and produce an isotropic emission spectrum, in an anisotropic trap they lead to an intricate fine-structure in the presence of a Fermi sea.

In a next step we have managed to explain this fine-structure by attributing the extrema to the emissions which come from the transitions of the recoiling atom into well defined states in the tight direction. If the aspect ratio exceeds the Fermi energy, the fine-structure vanishes and the emission spectrum becomes smooth, though not isotropic, again.

Finally, we have pointed out that this system can be used to create a highly directional photon source. The effect uncovered is complementary to the common use of optical cavities to influence a photons direction after emission and makes use of the ability to influence the atom's phase space. The experimental observation of directional photon emission in anisotropic, cold, fermionic gases would therefore be a sign of a fundamental consequence of the asymmetric nature of the wavefunction for of fermionic particles.

Chapter 3

Spatial Adiabatic Passage

Coherence is a phenomenon central to the study of cold atomic physics. The term 'coherence' may be found in many disciplines, for instance in literature, a piece is said to be coherent if there is a quality of harmony to the written text. Coherence is a unifying element in good writing whereby all parts of the text are clearly connected.

In physics, coherence refers to the relationship between constituent elements of a physical system. Electromagnetic waves are said to be coherent when there is a fixed relationship between the phase of the waves at different locations or different times. If this relationship is random the light is incoherent, such as light from the sun or a light bulb. A laser (which is an acronym for light amplification by stimulated emission of radiation) is a source of coherent light. Ideal laser light exhibits both spatial coherence, which is a fixed phase relationship between the electric fields at different locations across the beam profile and temporal coherence, a fixed phase relationship between the electric fields at one location but different times.

Atoms have a wave nature, typically modeled as de Broglie waves, and therefore share many characteristics of light. The onset of experimentally realisable ultra-low temperature physics has provided a platform to probe analogous experiments for matter and light [32]. A state of matter that has received notable attention, especially over the past two decades, is the Bose-Einstein Condensate (BEC) [16, 33]. Predicted by Albert Einstein using a description of the quantum statistics for photons introduced by Nathan Bose, a bosonic gas of atoms cooled below a critical temperature, condenses to occupy the lowest available quantum state. In the non-interacting limit, this many particle state exhibits the properties of a single atom. Moreover the BEC exhibits long-range spatial phase coherence. Since its first observation in low density gases in 1995 [34, 35], the study of BEC has become a field in its own right. Whilst the theory of coherence in

matter waves is rapidly developing, it is not yet as well understood as its optical counterpart. A traveling BEC, displaying both spatial and temporal coherence, is propagated by what is known as an atom laser [36, 37]. An output beam of atoms with (ideally) a well defined direction, phase and intensity, is produced by extraction from a previously realised BEC. The relationship between light and matter is not restricted to the fact that they are both different forms of energy, but extends far beyond. Coherence is a property that is demonstrable in both light and matter.

Whilst coherence in light and atoms may be regarded as separate (but related) entities in their own right, one can also talk about coherence *between* atoms and light. Atom-light coherence can be achieved by coupling of internal electronic states of (usually an ensemble of) atoms to an applied coherent electromagnetic field. If a coherent narrow bandwidth laser interacts with a two level atom, whose ground state is $|g\rangle$ and excited state $|e\rangle$, it will continuously absorb and re-emit photons via stimulated emission. When the laser is tuned in resonance with the energy difference (or transition frequency) between the two states the probability to find an atom in either state exhibits complete oscillations between $|g\rangle$ and $|e\rangle$. If the laser is detuned with respect to the transition frequency, incomplete oscillations are observed. This cycle is known as the Rabi cycle. By virtue of the interaction between the two level atom and coherent light field, the atom is said to be in a state of atomic coherence between $|g\rangle$ and $|e\rangle$. This is atom-light coherence.

Due to spontaneous emission, the atom will, at some statistically random time, emit a photon and return to its ground state thus interrupting the Rabi cycle. For an ensemble of atoms exhibiting coherent oscillations between $|g\rangle$ and $|e\rangle$, spontaneous emission in any one atom has the effect of changing the phase of that atom with respect to the ensemble. Over time spontaneous emission occurs in many atoms (at statistically random times) and as a result fewer atoms will be in phase with each other leading to the decoherence of the ensemble. Photons are lost from the cavity in the spontaneous emission process and decoherence sets in as the light field the atoms interact with decays. If the laser light continuously irradiates the sample, coherence is maintained. However some optical processes require a dynamic pulsing of laser light and decoherence is of paramount importance.

From the perspective of quantum engineering, quantum control, and most notably quantum information processing/computing, cold atomic systems that permit high fidelity state transfer are particularly desirable from both experimental and theoretical points of view. The high fidelity transfer of occupation density, for an ensemble of atoms initially prepared in their internal ground state $|g\rangle$, to a target state $|e\rangle$, is a challenging prospect

as a consequence of Rabi oscillations [38], i.e. the exchange of probability density between $|g\rangle$ and $|e\rangle$ (also referred to as Rabi flopping). However, controlled population transfer between internal states of atoms may be achieved using a technique known as Stimulated Raman Adiabatic Passage (STIRAP). This technique not only circumvents the decoherence problems associated with spontaneous emission, but also the fidelity of the transfer process is robust against the temporal dynamics of Rabi oscillations.

STIRAP relies on coupling three states, an initial $|0\rangle$, intermediate $|1\rangle$ and target state $|2\rangle$ using two laser fields. The initial and target states being long lived metastable states, whereas as the intermediate state may be short lived and subject to spontaneous decay into either of the available states. One laser field couples the initial and intermediate states whereas the other couples the intermediate and target state. An appropriate sequence of laser pulses facilitates high fidelity population transfer from the initial to the target state $|0\rangle \rightarrow |2\rangle$.

To begin we outline in this chapter the basics of the atom photon interaction and detail its mathematical formalism in section 3.1. We extend this analysis to a three level atom in section 3.2. Therein we arrive at the Hamiltonian in the interaction picture for STIRAP processes and outline the constraints for coherent population transfer. Finally we conclude the first section by discussing the matter wave counterpart of STIRAP, known as spatial adiabatic passage (SAP) [39–44] in section 3.2.6. The theoretical development and experimental realisation of STIRAP in matter wave settings is the focus of the remainder of this chapter. We propose two novel experimentally realistic scenarios for the implementation of SAP. The first is SAP on an atom chip waveguide, section 3.3, and thereafter SAP using multimode radio frequency dressed potentials in section 3.4.

3.1 The Dressed Atom

In this section we outline the basic theory of the atom-photon interaction. The theory found in this section largely follows the direction contained in Atom-Photon Interactions by Cohen-Tannoudji [13].

The model used herein is as follows; We consider a two level atom, whose lower and upper levels are denoted by $|g\rangle$ and $|e\rangle$. These eigenstates of the atom have energies $\hbar\omega_g$ and $\hbar\omega_e$ respectively, where $\hbar\omega_g < \hbar\omega_e$. The atom is confined in a lossless cavity of volume V, which is sufficiently large that such there is no inhibition of spontaneous emission [1, 2], and detuned sufficiently such that there is no stimulated emission [45]. This allows us to avoid to deal with the effects of cavity quantum electrodynamics.

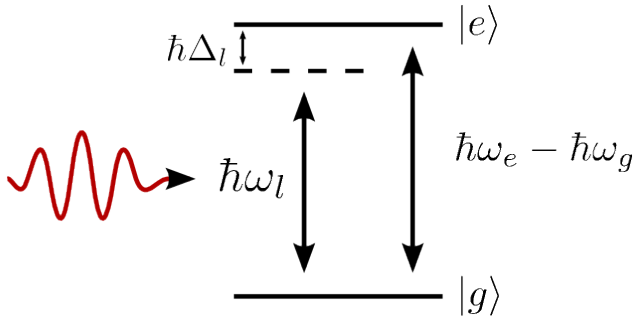


FIGURE 3.1: A laser pulse of energy $\hbar\omega_l$ couples the ground $|g\rangle$ and excited $|e\rangle$ states of a two level atom with energies $\hbar\omega_g$ and $\hbar\omega_e$ respectively. The laser is detuned with respect to the atomic transition by $\hbar\Delta_l = \hbar\omega_e - \hbar\omega_g - \hbar\omega_l$.

A single mode laser field of frequency ω_l, containing N photons, exists in the cavity. The average number of photons $\langle N\rangle$ is assumed to be large. The energy density in the cavity is given by the ratio of the average number of photons to the volume of the cavity, $\langle N\rangle/V$.

During the fluorescence cycle, an absorption followed by stimulated emission, the average number of photons in the cavity $\langle N\rangle$ is reduced. We assume that the width ΔN of the distribution of the number of photons is very large, but also very small compared to the average number of photons $\langle N\rangle$, i.e. $\langle N\rangle \gg \Delta N \gg 1$. Therefore over a large time scales the atom is subjected to the same laser intensity, and the process is assumed coherent.

The Hamiltonians of the individual subsystems are; the atomic Hamiltonian $\mathbf{H}_\mathrm{A}$ and the laser mode Hamiltonian $\mathbf{H}_l$, where

$$\mathbf{H}_\mathrm{A} = \hbar\omega_g|g\rangle\langle g| + \hbar\omega_e|e\rangle\langle e|, \tag{3.1a}$$

$$\mathbf{H}_l = \hbar\omega_l\left(\hat{a}_l^\dagger\hat{a}_l + \frac{1}{2}\right). \tag{3.1b}$$

$\hat{a}_l^\dagger$, $\hat{a}_l$ are the creation and annihilation operators which create a photon in the cavity energetic mode $|l\rangle$.

The global Hamiltonian is a sum of the subsystem Hamiltonians and the interaction Hamiltonian between the atom and the applied electric field.

$$\mathbf{H}(t) = \mathbf{H}_\mathrm{A} + \mathbf{H}_l + \mathbf{V}(t). \tag{3.2}$$

In the electric dipole approximation, the interaction Hamiltonian between the atom and the laser mode is written

$$\mathbf{V}(t) = -\mathbf{d}\cdot\mathbf{E}(\mathbf{x},t),$$

where $\mathbf{d}$ is the atomic dipole and $\mathbf{E}(\mathbf{x})$ is the field operator, evaluated at the position $\mathbf{x}$ of the atom, and is given by

$$\mathbf{E}(\mathbf{x}) \;=\; \boldsymbol{\epsilon}_l \sqrt{\frac{\hbar\omega_l}{2\epsilon_0 V}} \left(\hat{a}_l + \hat{a}_l^\dagger\right), \tag{3.3}$$

where $\boldsymbol{\epsilon}_l$ is the polarization of the laser mode at $\mathbf{x}$. We assume that the laser mode is in the coherent state $|\alpha_l e^{-\imath\omega_l t}\rangle$. Here we expand the coherent state via the unitary displacement operator as, $|\alpha_l e^{-\imath\omega_l t}\rangle = \mathscr{D}(\alpha e^{-\imath\omega_l t})|0_l\rangle$, with

$$\mathscr{D}(\alpha e^{-\imath\omega_l t}) \;=\; e^{\alpha_l e^{-\imath\omega_l t}\hat{a}_l^\dagger - \alpha_l^* e^{\imath\omega_l t}\hat{a}_l} \;=\; e^{-|\alpha_l|^2/2} e^{\alpha_l e^{-\imath\omega_l t}\hat{a}_l^\dagger} e^{-\alpha_l^* e^{\imath\omega_l t}\hat{a}_l}. \tag{3.4}$$

Similarly $\mathscr{D}^\dagger(\alpha e^{-\imath\omega_l t}) = e^{-|\alpha_l|^2/2} e^{-\alpha_l e^{-\imath\omega_l t}\hat{a}_l^\dagger} e^{\alpha_l^* e^{\imath\omega_l t}\hat{a}_l}$. Therefore the coherent states are defined by,

$$\begin{aligned} |\alpha_l e^{-\imath\omega_l t}\rangle \;&=\; e^{-|\alpha_l|^2/2} e^{\alpha_l e^{-\imath\omega_l t}\hat{a}_l^\dagger} e^{-\alpha_l^* e^{\imath\omega_l t}\hat{a}_l}|0_l\rangle \;=\; e^{-|\alpha_l|^2/2} e^{\alpha_l e^{-\imath\omega_l t}\hat{a}_l^\dagger}|0_l\rangle, \\ \langle\alpha_l e^{-\imath\omega_l t}| \;&=\; e^{-|\alpha_l|^2/2}\langle 0_l|\, e^{\alpha_l e^{-\imath\omega_l t}\hat{a}_l^\dagger} e^{-\alpha_l^* e^{\imath\omega_l t}\hat{a}_l} \;=\; e^{-|\alpha_l|^2/2}\langle 0_l|\, e^{-\alpha_l^* e^{\imath\omega_l t}\hat{a}_l}, \end{aligned} \tag{3.5}$$

The notation $|\alpha_l\rangle$ refers to $|\alpha|^2$ photons in the energetic mode l. The projection of the laser field on its coherent state, from (3.3) and (3.5), is

$$\langle\alpha_l e^{-\imath\omega_l t}|\mathbf{E}(\mathbf{x})|\alpha_l e^{-\imath\omega_l t}\rangle \;=\; \boldsymbol{\epsilon}_l \sqrt{\frac{\hbar\omega_l}{2\epsilon_0 V}} \langle\alpha_l e^{-\imath\omega_l t}| \left(\hat{a}_l + \hat{a}_l^\dagger\right) |\alpha_l e^{-\imath\omega_l t}\rangle, \tag{3.6}$$

This projection is explicitly evaluated in appendix A.3. Therein we recognise the photon number α, in the energetic mode l, is real valued (i.e. $\alpha_l = \alpha_l^*$), so that the average photon number is given by $\langle N\rangle = \alpha_l^2$. The above is shown to be given by,

$$\langle\alpha_l e^{-\imath\omega_l t}|\mathbf{E}(\mathbf{x})|\alpha_l e^{-\imath\omega_l t}\rangle \;=\; \boldsymbol{\xi}_l \cos(\omega_l t), \tag{3.7}$$

where,

$$\boldsymbol{\xi}_l \;\equiv\; 2\sqrt{\frac{\hbar\omega_l}{2\epsilon_0}} \sqrt{\frac{\langle N\rangle}{V}}\, \boldsymbol{\epsilon}_l. \tag{3.8}$$

The electric dipole moment of the atom is $\mathbf{d}_{ge} = \langle g|\mathbf{d}|e\rangle = \mathbf{d}_{eg}^*$. Typically the dipole matrix elements are $\langle g|\mathbf{d}|g\rangle = \langle e|\mathbf{d}|e\rangle = 0$, and the operator assumes the form,

$$\mathbf{d} \;=\; \mathbf{d}_{ge}^*\, |e\rangle\langle g| + \mathbf{d}_{ge}\, |g\rangle\langle e|. \tag{3.9}$$

Combining (3.7) and (3.9) the interaction term is

$$\mathbf{V}(t) \;=\; -\left(\mathbf{d}_{ge}^*\, |e\rangle\langle g| + \mathbf{d}_{ge}\, |g\rangle\langle e|\right) \cdot \left(\boldsymbol{\xi}_l\, e^{\imath\omega_l t} + \boldsymbol{\xi}_l\, e^{-\imath\omega_l t}\right). \tag{3.10}$$

For the purposes of brevity we define,

$$\hbar\Omega \equiv -\mathbf{d}_{ge} \cdot \boldsymbol{\xi}_l, \tag{3.11}$$

and the light-matter interaction is expressed,

$$\mathbf{V}(t) \;=\; \left(\hbar\Omega^* e^{\imath\omega_l t} + \hbar\Omega^* e^{-\imath\omega_l t}\right)|e\rangle\langle g| + \left(\hbar\Omega e^{\imath\omega_l t} + \hbar\Omega e^{-\imath\omega_l t}\right)|g\rangle\langle e|. \tag{3.12}$$

The coupling amplitude $\hbar\Omega$ is a measure of the coherence strength between $|g\rangle \leftrightarrow |e\rangle$. In the absence of any coupling ($\hbar\Omega = 0$) the atom laser system exhibits no Rabi oscillations. As $\hbar\Omega$ is increased the rate of Rabi oscillations increases. From (3.7), the coupling term is explicitly written

$$\hbar\Omega \;=\; -2\sqrt{\frac{\hbar\omega_l}{2\epsilon_0}}\sqrt{\frac{\langle N\rangle}{V}}\;\mathbf{d}_{eg} \cdot \boldsymbol{\epsilon}_l. \tag{3.13}$$

This term is dependent on both the energy of the applied laser field and the value of the average photon number $\langle N\rangle$ with respect to the size of the cavity volume V. For experimental purposes, the frequency of the applied field is typically a constant and the coupling frequency Ω (the Rabi frequency) is changed by adjusting the intensity $\langle N\rangle/V$, thereby changing the rate of the Rabi oscillations.

3.2 Stimulated Raman by Adiabatic Passage

The two level atom light system of section 3.1 can be easily extended to multi-level systems. Of primary interest for this thesis is quantum state transfer between two chosen levels in a three level system. Stimulated Raman adiabatic passage (STIRAP) [46] is a method that facilitates population transfer between two suitable states of an atom or molecule. A sample of atoms (or molecules) is prepared in its internal ground state $|0\rangle$. Known as a two photon Raman process, a pump pulse $\hbar\Omega_p(t)e^{-\imath\omega_p t}$ couples the $|0\rangle$ and $|1\rangle$ states, and a Stokes pulse $\hbar\Omega_s(t)e^{-\imath\omega_s t}$ couples the $|1\rangle$ and $|2\rangle$ states, as found in figure 3.2. The initial $|0\rangle$ and target $|2\rangle$ states are typically long lived metastable states whereas the $|1\rangle$ state may undergo spontaneous emission into $|0\rangle$ or $|2\rangle$, or more importantly, into a different state not considered in our level scheme. Alternatively $|0\rangle$ may be a rotational level in the vibrational ground state of a molecule and $|2\rangle$ may be some highly excited vibrational state. The objective of this process is to successfully transfer population from $|0\rangle \rightarrow |2\rangle$ without losing any population from $|1\rangle$ by spontaneous emission.

Complete population transfer is achieved in STIRAP processes by what is known as a 'counter-intuitive' application of the time dependent pump and Stokes pulses. By

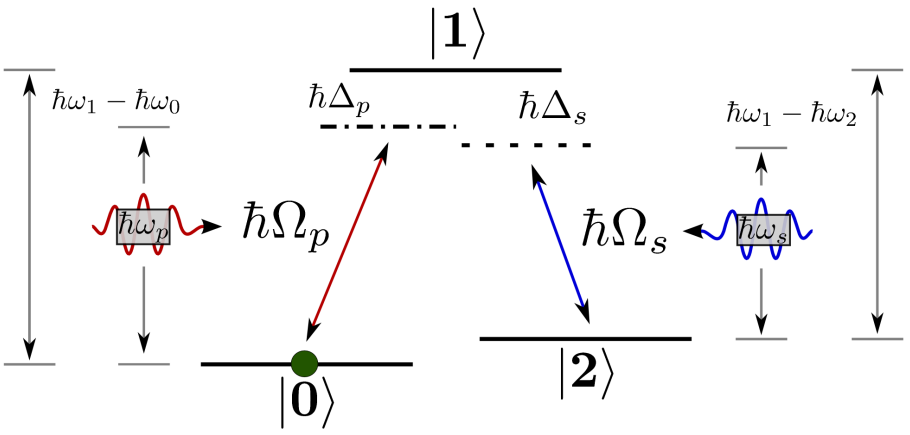


FIGURE 3.2: Three level Λ structure. The pump pulse Ω_p couples levels $|0\rangle$ and $|1\rangle$ with a detuning Δ_p. The Stokes pulse Ω_s coupling levels $|1\rangle$ and $|2\rangle$ with detuning Δ_s.

applying these pulses in this manner no population is transferred to the $|1\rangle$ throughout the process. Therefore this technique is robust against spontaneous decay from $|1\rangle$. As spontaneous emission plays no significant role, we omit to include a description of it in the system's Hamiltonian.

In this section we extend the analysis of the two level atom from section 3.1 to a three level atom, and arrive at the Hamiltonian in section 3.2.1. This is extended to the time dependent case in section 3.2.2. The Hamiltonian eigensystem and the transfer process are found in sections 3.2.3 and 3.2.5.

3.2.1 Three Level Atom

The electronic structure in three level atoms are typically Λ, V and ladder-type arrangements. The Λ-type structure is illustrated in figure 3.2. The V structure is an inverted Λ configuration, whilst the ladder structure has three energy levels $|0\rangle, |1\rangle$ and $|2\rangle$, with energies $\hbar\omega_0 < \hbar\omega_1 < \hbar\omega_2$. The intermediate state $|1\rangle$ is coupled to state $|0\rangle$ by means of a Pump laser pulse of energy $\hbar\omega_p$ and a coupling strength $\hbar\Omega_p$. Similarly $|1\rangle$ is coupled to state $|2\rangle$ by means of a Stokes laser pulse of energy $\hbar\omega_s$ and a coupling strength $\hbar\Omega_s$, as found in figure 3.2.

For STIRAP processes we are interested in the dynamics in the atom due to the interaction with the laser. As the backaction onto the laser field is here unimportant, we neglect to include the Hamiltonian of the laser field $\mathbf{H}_l$. The Hamiltonian of the system is given by,

$$\mathbf{H}(t) = \mathbf{H}_\mathrm{A} + \mathbf{V}(t), \tag{3.14}$$

where,

$$\mathbf{H}_{\mathrm{A}} \;=\; \hbar\omega_0|0\rangle\langle 0| \;+\; \hbar\omega_1|1\rangle\langle 1| \;+\; \hbar\omega_2|2\rangle\langle 2|, \tag{3.15a}$$

$$\begin{aligned}\mathbf{V}(t) \;=\; &\big(\hbar\Omega_p^* e^{\imath\omega_p t} + \hbar\Omega_p^* e^{-\imath\omega_p t}\big)|1\rangle\langle 0| + \big(\hbar\Omega_p e^{\imath\omega_p t} + \hbar\Omega_p e^{-\imath\omega_p t}\big)|0\rangle\langle 1| + \\ &+ \big(\hbar\Omega_s e^{\imath\omega_s t} + \hbar\Omega_s e^{-\imath\omega_s t}\big)|1\rangle\langle 2| + \big(\hbar\Omega_s^* e^{\imath\omega_s t} + \hbar\Omega_s^* e^{-\imath\omega_s t}\big)|2\rangle\langle 1|.\end{aligned} \tag{3.15b}$$

In the Schrödinger picture we have,

$$\imath\hbar\frac{d}{dt}|\Psi(t)\rangle_{\mathrm{S}} \;=\; \mathbf{H}(t)\;|\Psi(t)\rangle_{\mathrm{S}}. \tag{3.16}$$

Parameterizing the correct evolution of the wavefunction is difficult due to the time dependence of the operator $\mathbf{H}(t)$. It helps to move to a rotated basis, i.e. the interaction picture, via the unitary transformation $\mathbf{U}(t)$, where $|\Psi(t)\rangle_{\mathrm{S}} = \mathbf{U}(t)|\Psi(t)\rangle_{\mathrm{I}}$. From (3.16) the time evolution of the state vector in the interaction picture is,

$$\imath\hbar\frac{d}{dt}|\Psi(t)\rangle_{\mathrm{I}} \;=\; \Big(-\imath\hbar\mathbf{U}^\dagger(t)\dot{\mathbf{U}}(t) + \mathbf{U}^\dagger(t)\left(\mathbf{H}_{\mathrm{A}} + \mathbf{V}(t)\right)\mathbf{U}(t)\Big)\;|\Psi(t)\rangle_{\mathrm{I}}. \tag{3.17}$$

We are free to choose any form of the unitary transformation. For our purposes, a particular form of $\mathbf{U}(t)$ that is very useful is,

$$\mathbf{U}(t) \;\equiv\; \exp\big[-\imath\big(\omega_0|0\rangle\langle 0| + (\omega_0+\omega_p)|1\rangle\langle 1| + (\omega_0+\omega_p-\omega_s)|2\rangle\langle 2|\big)t\big]. \tag{3.18}$$

We proceed to simplify the right hand side of (3.17) using the above unitary transformation. The first term becomes,

$$-\imath\hbar\mathbf{U}^\dagger(t)\dot{\mathbf{U}}(t) \;=\; -\hbar\omega_0|0\rangle\langle 0| - (\hbar\omega_0+\hbar\omega_p)|1\rangle\langle 1| - (\hbar\omega_0+\hbar\omega_p-\hbar\omega_s)|2\rangle\langle 2|. \tag{3.19}$$

Since $\mathbf{U}(t)$ commutes with $\mathbf{H}(t)$, the second term is given by,

$$\mathbf{U}^\dagger(t)\mathbf{H}_{\mathrm{A}}\mathbf{U}(t) \;=\; \hbar\omega_0|0\rangle\langle 0| \;+\; \hbar\omega_1|1\rangle\langle 1| \;+\; \hbar\omega_2|2\rangle\langle 2|. \tag{3.20}$$

We define $\hbar\Delta_p \equiv \hbar\omega_1 - \hbar\omega_0 - \hbar\omega_p$ and $\hbar\Delta_s \equiv \hbar\omega_1 - \hbar\omega_2 - \hbar\omega_s$ and combine (3.19) and (3.20) as,

$$-\imath\hbar\mathbf{U}^\dagger(t)\dot{\mathbf{U}}(t) + \mathbf{U}^\dagger(t)\mathbf{H}_{\mathrm{A}}\mathbf{U}(t) = \hbar\Delta_p|1\rangle\langle 1| + \hbar(\Delta_p-\Delta_s)|2\rangle\langle 2|. \tag{3.21}$$

When we evaluate the last term, $\mathbf{U}^\dagger(t)\mathbf{V}(t)\mathbf{U}(t)$ of (3.17), we encounter four components, $\mathbf{U}^\dagger(t)|1\rangle\langle 0|\mathbf{U}(t)$, $\mathbf{U}^\dagger(t)|0\rangle\langle 1|\mathbf{U}(t)$, $\mathbf{U}^\dagger(t)|1\rangle\langle 2|\mathbf{U}(t)$ and $\mathbf{U}^\dagger(t)|2\rangle\langle 1|\mathbf{U}(t)$. By expanding the exponential in the usual way these terms simplify to $|1\rangle\langle 0|\hbar\Omega^* e^{\imath\omega_p t}$, $|0\rangle\langle 1|\hbar\Omega e^{-\imath\omega_p t}$,

$|1\rangle\langle 2|\hbar\Omega e^{\imath\omega_s t}$ and $|2\rangle\langle 1|\hbar\Omega^* e^{-\imath\omega_s t}$ respectively. Thereby we find,

$$\begin{aligned}\mathbf{U}^\dagger(t)\mathbf{V}(t)\mathbf{U}(t) \;=\; &\left(\hbar\Omega_p^* e^{2\imath\omega_p t} + \hbar\Omega_p^*\right)|1\rangle\langle 0| \;+\; \left(\hbar\Omega_p + \hbar\Omega_p e^{-2\imath\omega_p t}\right)|0\rangle\langle 1| \\ &+\; \left(\hbar\Omega_s e^{2\imath\omega_s t} + \hbar\Omega_s\right)|1\rangle\langle 2| \;+\; \left(\hbar\Omega_s^* + \hbar\Omega_s^* e^{-2\imath\omega_s t}\right)|2\rangle\langle 1|.\end{aligned} \tag{3.22}$$

When the electric field is near resonance ($\Delta_p \ll \omega_p + \omega_1 - \omega_0$ and $\Delta_s \ll \omega_s + \omega_1 - \omega_2$) the dipole approximation is valid. In this regime, the $e^{\pm 2\imath\omega_p t}$ and $e^{\pm 2\imath\omega_s t}$ terms are rapidly oscillating and over significantly long time scales they average to zero. We make the rotating wave approximation by assuming theses terms are negligible,

$$\mathbf{U}^\dagger(t)\mathbf{V}(t)\mathbf{U}(t) \;=\; \hbar\Omega_p^*|1\rangle\langle 0| \;+\; \hbar\Omega_p|0\rangle\langle 1| \;+\; \hbar\Omega_s|1\rangle\langle 2| \;+\; \hbar\Omega_s^*|2\rangle\langle 1|. \tag{3.23}$$

Combining (3.21) and (3.23), the Hamiltonian in the interaction picture, under the rotating wave approximation is defined,

$$\begin{aligned}\mathbf{H}_\mathrm{I} \;&=\; -\imath\hbar\mathbf{U}^\dagger(t)\dot{\mathbf{U}}(t) + \mathbf{U}^\dagger(t)\mathbf{H}_\mathrm{A}\mathbf{U}(t) + \mathbf{U}^\dagger(t)\mathbf{V}\mathbf{U}(t), \\ \mathbf{H}_\mathrm{I} \;&=\; \hbar\begin{pmatrix} 0 & \Omega_p & 0 \\ \Omega_p^* & \Delta_p & \Omega_s \\ 0 & \Omega_s^* & \Delta_p - \Delta_s \end{pmatrix}.\end{aligned} \tag{3.24}$$

3.2.2 System Hamiltonian

The time dependence of the pump and Stoke pulses is imposed when the intensity of the applied laser pulses is changed. The 'counter-intuitive' application of the laser pulses is achieved by smoothly increasing (and then decreasing) the intensity of the Stokes pulse first and then the pump pulse after an appropriate delay. As we have seen in section 3.1, the coupling terms assume the form,

$$\hbar\Omega_p(t)|0\rangle\langle 1| = -\mathbf{d}_{01}\cdot\boldsymbol{\xi}_p(t)|0\rangle\langle 1| = -2\sqrt{\frac{\hbar\omega_p}{2\epsilon_0}}\sqrt{\frac{\langle N(t)\rangle}{V}}|0\rangle\langle 0|\mathbf{d}_{01}\cdot\boldsymbol{\epsilon}_p|1\rangle\langle 1|, \tag{3.25a}$$

$$\hbar\Omega_s(t)|2\rangle\langle 1| = -\mathbf{d}_{12}\cdot\boldsymbol{\xi}_s(t)|2\rangle\langle 1| = -2\sqrt{\frac{\hbar\omega_s}{2\epsilon_0}}\sqrt{\frac{\langle N(t)\rangle}{V}}|2\rangle\langle 2|\mathbf{d}_{12}\cdot\boldsymbol{\epsilon}_s|1\rangle\langle 1|. \tag{3.25b}$$

Here $\xi_p(t)$ ($\xi_s(t)$) is the envelope of the pump (Stokes) laser electric field amplitude at the location of the atom or molecule, and $\mathbf{d}_{01}$ ($\mathbf{d}_{12}$) is the component of the transition dipole along the electric field. The pump $\hbar\Omega_p(t)$ and Stokes $\hbar\Omega_s(t)$ pulses assume a time dependence as the average photon number $\langle N\rangle$ is changed with respect to the (constant) spatial volume V. It is important to note here that the frequency of the applied laser pulses does not change in time, only the intensity. Careful examination of (3.25) shows that there may exist a phase difference between the Rabi frequencies of the pump and Stokes pulses, should there be a phase difference between $\mathbf{d}_{01}\cdot\boldsymbol{\epsilon}_p$ and

$\mathbf{d}_{12} \cdot \boldsymbol{\epsilon}_s$. The STIRAP process works for any phase difference between the fields. As this phase difference is incorporated by adiabatically following the dark state, and does not contribute to the dynamics of the system, it is convenient to neglect any phase difference between the pump and Stokes pulses. Therefore we may assume the pulses to be real valued, $\hbar\Omega_p(t) = \hbar\Omega_p^*(t)$, $\hbar\Omega_s(t) = \hbar\Omega_s^*(t)$. The Hamiltonian (3.24) under the RWA in the interaction picture takes the form,

$$\mathbf{H}_{\mathrm{I}}(t) = \hbar \begin{pmatrix} 0 & \Omega_p(t) & 0 \\ \Omega_p(t) & \Delta_p & \Omega_s(t) \\ 0 & \Omega_s(t) & \Delta_p - \Delta_s \end{pmatrix}. \tag{3.26}$$

The magnitude of the off diagonal coupling terms $\Omega_p(t)$ and $\Omega_s(t)$ controls the rate of population transfer between the respective energy levels, whilst their frequency remains constant, and therefore the detunings Δ_p and Δ_s remain time independent. The time dependence of the pump and Stokes pulses controls the rate of the Rabi oscillations between $|0\rangle \leftrightarrow |1\rangle$ and $|1\rangle \leftrightarrow |2\rangle$ respectively.

Coupling between energy levels is strongest when the laser pulses are in resonance with their respective transition frequencies, $\Delta_p = \Delta_s = 0$, which is single photon resonance. However, for the purposes of population transfer, we may use the single photon detunings $\Delta_p, \Delta_s \neq 0$ as long as the combination of the pump and Stokes frequencies be resonant with the two photon Raman transition, $\Delta_p - \Delta_s = 0$. Two photon resonance $\Delta_p = \Delta_s$ is a necessary condition for population transfer.

3.2.3 Eigensystem of the Hamiltonian

The generalised eigenvalues and eigenstates of (3.26) are found in [47]. As we have no practical use in this thesis for the case when $\Delta_s - \Delta_p \neq 0$ we concern ourselves only with the two photon resonance regime $\Delta_s - \Delta_p = 0$,

$$\mathbf{H}_{\mathrm{I}}(t) = \hbar \begin{pmatrix} 0 & \Omega_p(t) & 0 \\ \Omega_p(t) & \Delta_p & \Omega_s(t) \\ 0 & \Omega_s(t) & 0 \end{pmatrix}. \tag{3.27}$$

The eigenvalues of this operator are,

$$\hbar\lambda_0(t) = \frac{\hbar}{2}\left(\Delta_p - \sqrt{\Delta_p^2 + 4\Omega_p^2(t) + 4\Omega_s^2(t)}\right), \tag{3.28a}$$

$$\hbar\lambda_1(t) = 0, \tag{3.28b}$$

$$\hbar\lambda_2(t) = \frac{\hbar}{2}\left(\Delta_p + \sqrt{\Delta_p^2 + 4\Omega_p^2(t) + 4\Omega_s^2(t)}\right). \tag{3.28c}$$

We define the following mixing angles,

$$\tan\vartheta(t) \;=\; \frac{\Omega_p(t)}{\Omega_s(t)}; \qquad \tan\varphi_{\pm}(t) \;=\; \frac{2\sqrt{\Omega_p^2(t)+\Omega_s^2(t)}}{\Delta_p \pm \sqrt{\Delta_p^2+4\Omega_p^2(t)+4\Omega_s^2(t)}}, \tag{3.29}$$

to write the eigenvectors of (3.27) as,

$$|\phi_0(t)\rangle = \sin\vartheta(t)\,\sin\varphi_-(t)|0\rangle + \cos\varphi_-(t)|1\rangle + \cos\vartheta(t)\,\sin\varphi_-(t)|2\rangle, \tag{3.30a}$$

$$|\phi_1(t)\rangle = \cos\vartheta(t)|0\rangle - \sin\vartheta(t)|2\rangle, \tag{3.30b}$$

$$|\phi_2(t)\rangle = \sin\vartheta(t)\,\sin\varphi_+(t)|0\rangle + \cos\varphi_+(t)|1\rangle + \cos\vartheta(t)\,\sin\varphi_+(t)|2\rangle. \tag{3.30c}$$

When considered with respect to the mean photon numbers of the applied laser fields (as in (3.7)) these eigenstates are considered the 'dressed states' of the matter-field system. For a quantum state prepared in the $|\phi_1(t)\rangle$ dressed state it never sends out florescence due to spontaneous emission from the intermediate excited state $|1\rangle$, subsequently it is known as the 'dark state'. The remaining $|\phi_0(t)\rangle$ and $|\phi_2(t)\rangle$ eigenvectors have contributions from the intermediate excited state $|1\rangle$ and may be exhibit spontaneous emission, and are therefore referred to as 'bright states'.

The kets are written in vector form as,

$$|0\rangle \;=\; \begin{pmatrix}1\\0\\0\end{pmatrix}, \qquad |1\rangle \;=\; \begin{pmatrix}0\\1\\0\end{pmatrix}, \qquad |2\rangle \;=\; \begin{pmatrix}0\\0\\1\end{pmatrix}. \tag{3.31}$$

At any time t equations (3.27), (3.28) and (3.30) satisfy $\mathbf{H}_{\mathrm{I}}(t)|\phi_\nu(t)\rangle = \lambda_\nu(t)|\phi_\nu(t)\rangle$.

3.2.4 Adiabaticity Constraints

Adiabaticity and adiabatic process are fundamental concepts of the quantum theory. At the core of adiabaticity is the quantum adiabatic theorem (QAT) which is widely known and used in both theory and experiment. The general statement of the QAT is as follows; given a time dependent non-degenerate Hamiltonian $\mathbf{H}(t)$, a quantum state may be prepared in an eigenstate $|\psi_\mu(0)\rangle$ (with energy $\hbar\omega_\mu(0)$) of the initial Hamiltonian $\mathbf{H}(0)$. If $\mathbf{H}(t)$ evolves slowly enough, the system will be remain in $|\psi_\mu(t)\rangle$ at all times t up to a multiplicative phase factor. What determines slow enough is captured by the quantitative condition (QC),

$$\frac{|\langle\psi_\nu(t)|\dot{\mathbf{H}}(t)|\psi_\mu(t)\rangle|}{|\hbar\omega_\nu(t)-\hbar\omega_\mu(t)|^2} \ll 1, \qquad \text{or} \qquad \left|\frac{\langle\psi_\nu(t)|\dot{\psi}_\mu(t)\rangle}{\hbar\omega_\nu(t)-\hbar\omega_\mu(t)}\right| \ll 1, \qquad \nu\neq\mu. \tag{3.32}$$

Adiabatic processes remains a lively area of study and research and to some extent, it is quite a controversial topic. Initially sparked by a paper from by Marzlin and Sanders [48], the authors showed using counterexamples that the QC is insufficient to guarantee the validity of the QAT. It was later shown that the QC is applicable for only a special class of systems in quantum mechanics [49]. Thereafter it was pointed out that the violations of the QAT arise from resonant transitions between energy levels [50]. However, some authors remain unconvinced and show the QC to be necessary but insufficient to guarantee the validity of the adiabatic approximation [51]. Violating the QC invalidates the QAT, whereas satisfying it may not guarantee the QAT, but does in most cases.

Since the initial concerns raised by Marzlin and Sanders, the area has been a source of rigorous debate. Rather than attempt to tackle the finer points of the adiabatic constraints, we simply present the widely acknowledged conditions of adiabatic following for STIRAP systems. The derivation of which is largely deduced from that provided in Messiah (1999) [52].

Non-adiabatic coupling between the bright and dark states remains small when the matrix element $\langle\phi_{0,2}(t)|\dot{\phi}_1(t)\rangle$ is small with respect to the differences in the eigenvalues $\lambda_{0,2}(t) - \lambda_1(t)$. From (3.30) we see that $\langle\phi_{0,2}(t)|\dot{\phi}_1(t)\rangle = \dot{\vartheta}(t)\sin\ \varphi_{\mp}(t)$. Since the maximum value of $\sin\ \varphi_{\mp}(t) = 1$, the criterion for adiabatic following is given by,

$$\left|\frac{\dot{\Omega}_p(t)\Omega_s(t) - \Omega_p(t)\dot{\Omega}_s(t)}{\Omega_p^2(t) + \Omega_s^2(t)}\right| \ll |\lambda_{0,2}(t) - \lambda_1(t)|. \tag{3.33}$$

If the system is evolved slowly enough $\dot{\Omega}_p(t) \approx \dot{\Omega}_s(t) \approx 0$ and the above condition is satisfied. As long as this constraint is satisfied throughout the STIRAP processes, non-adiabatic coupling between the bright and dark states remains small.

3.2.5 Population Transfer

Intuitively one may consider that in order to transfer population from $|0\rangle \rightarrow |2\rangle$ the pump laser $\Omega_p(t)$ should be applied first, thereby coupling the $|0\rangle \leftrightarrow |1\rangle$ states. Thereafter it follows that the application of the Stokes laser $\Omega_s(t)$ to couple $|1\rangle \leftrightarrow |2\rangle$ should transfer population to $|2\rangle$. To combat Rabi oscillations and achieve 100% transport fidelity, only an absolutely accurate timing of 'intuitively' ordered pump and Stokes pulses would transfer population first from $|0\rangle \rightarrow |1\rangle$ and then $|1\rangle \rightarrow |2\rangle$. Such high precision timing and control of laser pulse sequencing is experimentally challenging and not robust. Additionally, spontaneous emission from $|1\rangle$ is an extra complication preventing attainment of high fidelity population transfer using this method.

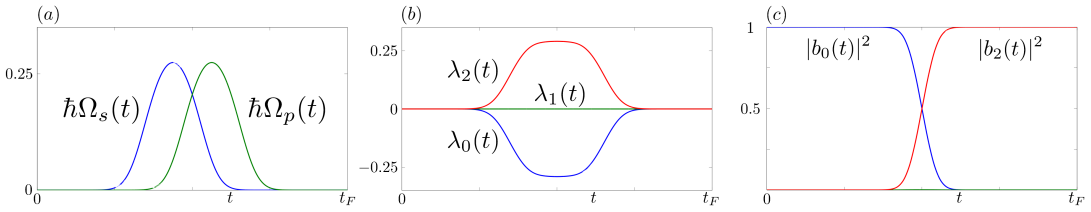


FIGURE 3.3: (a) The coupling amplitudes of the Stokes $\hbar\Omega_s(t)$ and pump $\hbar\Omega_p(t)$ laser pulses during the transfer process. (b) The eigenvalues $\lambda_\nu(t)$ of (3.28) (divided by $\hbar$). (c) The probability densities of the $|0\rangle$ state $|b_0(t)|^2$ and the $|2\rangle$ state $|b_2(t)|^2$, showing complete population transfer. Resonant tunings assumed $\Delta_p = 0$.

The 'counter-intuitive' pulse ordering employed in STIRAP processes facilitates complete population transfer whilst avoiding any contribution from the radiatively decaying $|1\rangle$ state. The system first interacts with the Stokes laser and then the pump laser. The Stokes laser first couples the unoccupied $|1\rangle$ and $|2\rangle$ states. When the pump pulse is employed, one of the three eigenstates of the system Hamiltonian is the dark state (3.30b) which has no contribution from $|1\rangle$. An adiabatic progression of the system parameters ensures that for the duration of the STIRAP process only the dark state is occupied, and there is not enough energy supplied to excite the system to occupy the bright states. Consequently there is no possibility of decoherence due to spontaneous emission.

The time evolution of the STIRAP process is encapsulated in the following rate equation,

$$\begin{pmatrix} b_0(t) \\ b_1(t) \\ b_2(t) \end{pmatrix} = \exp\left[-\imath\int_0^t dt' \begin{pmatrix} 0 & \Omega_p(t') & 0 \\ \Omega_p(t') & \Delta_p & \Omega_s(t') \\ 0 & \Omega_s(t') & 0 \end{pmatrix}\right] \begin{pmatrix} b_0(0) \\ b_1(0) \\ b_2(0) \end{pmatrix}. \tag{3.34}$$

Initially all population is $|0\rangle$ and the state vector $(b_0(0), b_1(0), b_2(0))^{\mathrm{T}} = (1, 0, 0)^{\mathrm{T}}$.

In figure 3.3 we have plotted the time dependent Rabi frequencies $\Omega_s(t)$ and $\Omega_p(t)$ in (a), the eigenvalues $\lambda_\nu(t)$ in (b) and the probability densities $|b_\nu(t)|^2$ of the $|0\rangle, |1\rangle$ and $|2\rangle$ states in (c); we note $|b_1(t)|^2 = 0$. The eigenvalues at the beginning of the process are degenerate $\lambda_\nu(t) = 0$, $(\nu = 0, 1, 2)$ found in figure 3.3(b). The time dependent pulsing of the pump and Stokes laser pulses induces a splitting of the eigenvalues of the bright states $\lambda_0(t)$ and $\lambda_2(t)$ throughout the process, whilst the eigenvalue of the system dark state $\lambda_1(t)$ remains 0.

The STIRAP process proceeds as follows; initially all population is found in the $|0\rangle$ state, and the Rabi frequencies of the pump and Stokes pulses $\Omega_s(t) = \Omega_p(t) = 0$. Initially the system is in some linear superposition of the dressed states (3.30). If the process as a whole is adiabatic the system remains in the designated dressed states. Increasing $\Omega_s(t)$, while $\Omega_p(t) \approx 0$ changes the mixing angle $\vartheta(t)$ from $\pi/4 \to 0$, therefore $\cos\vartheta(t) = 1$.

Experimentally tuning the mixing angle in this way adiabatically moves the system into the 'dark state' $|\phi_1(t)\rangle$, where it remains until the end of the process.

The pump pulse succeeds the Stokes pulse as in figure 3.3(a) thereby tuning the mixing angle $\vartheta(t)$ from $0 \to \pi/2$. In this way the coefficient of the $|2\rangle$ state, $\sin\vartheta(t)$, changes from $0 \to 1$, whilst the opposite happens for the $|0\rangle$ coefficient. Accordingly population has been transferred from $|0\rangle \to |2\rangle$ as found in figure 3.3(c). Finally the Rabi frequencies of both lasers reach 0 and the system again relaxes into some superposition of the dressed states (3.30). This method of counter-intuitive laser pulsing facilitates a high fidelity population transfer from $|0\rangle \to |2\rangle$.

The delay between the Stokes and pump pulses is an essential component of STIRAP processes, and must be short enough so that the splitting between the eigenvalues in (b) remains large at the midpoint of the evolution. If this is satisfied non-adiabatic coupling between the bright and dark states remains negligible (see section 3.2.4). However, should the delay between the Stokes and pump pulses be too large, the bright state eigenvalues approach that of the dark state at the midpoint of the process, and leakage into $|1\rangle$ is observed.

3.2.6 Rabi Oscillations in Optical and Matter Wave Settings

Since the first observation of magnetically trapped neutral atoms [53] in 1985, the ability to study the quantum nature of matter has become possible through the many advances in laser cooling and trapping techniques [38]. Techniques to isolate and manipulate individual atoms [54] offer exciting possibilities to explore matter-wave systems with locally addressable potentials. An interesting area of study that is shared by coherent optical and matter wave systems is the property known as Rabi oscillations. Any coherent two state system can display Rabi oscillations; in optical systems Rabi oscillations can be observed between coupled internal electronic states (as outlined above), and in matter wave settings they can appear as the density oscillations between coupled spatial modes. An atom, molecule or weakly interacting BEC trapped in one spatial region may exhibit Rabi oscillations between its region and a neighbouring one in a manner quite similar to that found in optical systems (of section 3.1). Systems of study that display these properties are usually referred to as atom-optical systems.

Given that Rabi oscillations exists for two level systems it may naturally be extended to multilevel atom-optical systems to provide a platform for the experimental and theoretical exploration of the matter wave analogue of many well studied phenomena in quantum optics, such as Stimulated Raman Adiabatic Passage [46] and Electromagnetically Induced Transparency [55]. The study of these optical systems from the matter-wave (also

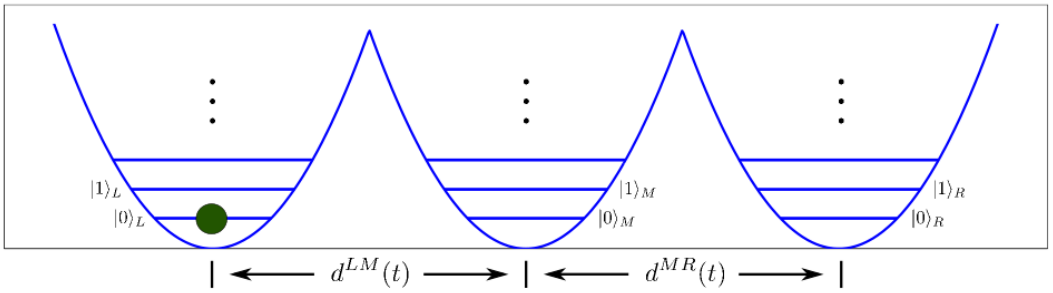


FIGURE 3.4: Three trap potential. d^{LM} (d^{MR}) is the separation between the left and middle (middle and right) traps. In the limit of large separation $|n\rangle_L$, $|n\rangle_M$ and $|n\rangle_R$ are the n-th vibrational energy eigenstates corresponding to the single trap potentials.

referred to as the 'atom-optical') viewpoint offers a fresh approach to these areas with the possibility of uncovering a new and deeper understanding of these phenomena and moreover the quantum nature of matter itself.

3.2.7 From STIRAP to SAP

In 2004, the relationship between STIRAP and the transport of a matter wave via the tunneling interaction was clarified [56, 57]. Eckert *et al.* showed that neutral atoms can be transferred between an alignment of optical dipole traps [56] and Greentree *et al.* demonstrated the feasibility of electron transfer in quantum dots [57] using an analogous technique.

In this section we briefly review a paper by Eckert *et al.* [56] which illustrates the (almost) one-to-one relationship between atom optical system and optical systems. They pointed out that whilst the STIRAP technique allows for population transfer by means of the electric dipole interaction between a three level atom and two laser fields, a similar technique exists for atoms trapped in dipole traps made by focusing light through an array of microlenses [58]. The distances between different sites may be adiabatically varied in a manner that increases the rate of Rabi oscillations between neighbouring sites. In the matter wave setting, the frequency of the Rabi oscillations is more commonly referred to as the Rabi 'tunneling' frequency. The term 'tunneling' refers to a matter wave transversing a potential barrier separating neighbouring spatial regions. By varying the tunneling frequency in a manner that parallels that in the optical case, an atom may be transported from an initial (spatial) site to a target site with a high fidelity.

Three inline dipole traps may be modeled by a linear one dimensional arrangement of three piecewise harmonic traps as found in figure 3.4. An atom is assumed to be cooled to a temperature low enough such that it occupies the vibrational ground state of the left most trap $|0\rangle_L$. Each trap is assumed to have the same trapping frequency ω and as

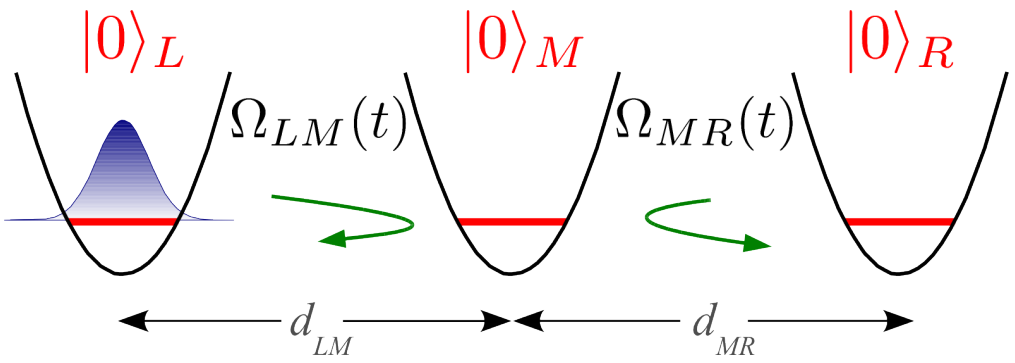


FIGURE 3.5: Schematic of the SAP process for an atom in the left trap. Reducing the distances between the traps leads to an increase in the tunneling strengths.

such all vibrational states, of each trap $|n\rangle_{L,M,R}$, are in resonance. The Rabi tunneling interaction between any two neighbouring traps may be increased by reducing the distance d between the trap centers. In [56] a good approximation for the Rabi tunneling frequency between the lowest vibrational ground state of neighbouring resonant traps is provided. As a function of d and in harmonic oscillator units ($\sqrt{\hbar/m\omega} = 1$),

$$\frac{\Omega(d)}{\omega} = \frac{-1 + e^{d^2}\left[1 + d(1 - \mathrm{erf}(d))\right]}{\sqrt{\pi}(e^{2d^2} - 1)/2d}, \tag{3.35}$$

where erf() is the error function [31].

For an adiabatic change of the distances between the trap centers, the atom remains at all times in the lowest vibrational state of the system's traps and the Hamiltonian describing the evolution of this time dependent system is,

$$\mathbf{H}(t) = \hbar \begin{pmatrix} 0 & \Omega_{LM}(t) & 0 \\ \Omega_{LM}(t) & 0 & \Omega_{MR}(t) \\ 0 & \Omega_{MR}(t) & 0 \end{pmatrix}, \tag{3.36}$$

where $\Omega_{LM}(t)$ and $\Omega_{MR}(t)$ are the tunneling frequencies between $|0\rangle_L \leftrightarrow |0\rangle_M$ and $|0\rangle_M \leftrightarrow |0\rangle_R$ respectively. Since the outer traps are separated a large distance, the tunneling interaction between them is negligible at all times during the process. Given that the three inline harmonic potentials all have the same trapping frequency, we can renormalise the diagonal elements of $\mathbf{H}(t)$ to 0.

For the purposes of population transfer the eigenvector of $\mathbf{H}(t)$ that plays the crucial role is (again) the so-called 'dark state',

$$\begin{aligned} |\phi_1(t)\rangle &= \cos\vartheta(t)|0\rangle_L - \sin\vartheta(t)|0\rangle_R, \\ \tan\vartheta(t) &= \frac{\Omega_{LM}(t)}{\Omega_{MR}(t)}. \end{aligned} \tag{3.37}$$

This state has a non-degenerate eigenvalue $\lambda_1(t) = 0$.

The (optical) STIRAP process is mimicked here as the tunneling rate between the middle and right traps $\Omega_{MR}(t)$ is first increased followed in sequence by increasing $\Omega_{LM}(t)$, see figure 3.5. Adhering to the appropriate 'counter-intuitive' motion of the trap centers throughout the evolution, the system will remain in the dark state and adiabatically transport its population from $|0\rangle_L \to |0\rangle_R$ as $\vartheta(t)$ is tuned from $0 \to \pi/2$.

3.2.8 Further Remarks

Techniques to allow for coherent population transfer between internal states of an atom or molecule were originally developed for nuclear magnetic resonance and applications in optics. A thorough review of which is found in [59]. STIRAP has been experimentally demonstrated in the metastable states of neon (Ne^*) [46]. The extension of such schemes to matter wave settings is paving the way for the convergence of quantum optics [60] and condensed matter [61], which has already been explored in [62]. Further studies along this avenue include electron transport in solid state devices [39, 57, 63–66], of which many consider electron transport in quantum dots [40, 67–69].

Since the pioneering works of [56, 57], SAP has become a field of study in its own right, and numerous studies and proposals to actualise SAP, have arisen. Such schemes come under the headings of Coherent Tunneling by Adiabatic Passage (CTAP) [56, 70], Spatial Adiabatic Passage (SAP) [39, 63–66], transport without transit (TWT) [62], and have also been referred to as Atomtronics techniques since they hold promise of mimicking the properties of electronic devices [71–73]. Proposals for implementing SAP in quantum dot systems [57], optical traps and waveguides [70] were amongst the original concepts along this avenue. Extensions of SAP processes also hold promise for applications in quantum computing and quantum information schemes [57, 74], and provide a platform to allow for properties of quantum systems such as entanglement [75] and interferometry [40] to be engineered, and to study the mean field dynamics in the transport of a BEC [62, 76]. SAP has been explored as a means of studying other aspects of quantum mechanics such as entanglement generation [75, 77], interaction-free measurement [41], atomtronic devices [71–73], quantum information technologies [43, 74, 78], interferometry [40, 79], matter wave filtering [42] and Bose-Hubbard dynamics [80]. To date the only experimental demonstration has remained the transfer of a classical light source in a triple waveguide structure [81, 82]. Motivated by the apparent difficulties that thus far exist in experimentally actualising SAP we propose, in the following two sections, two schemes to experimentally demonstrate SAP with single atoms or weakly interacting BECs using currently available technologies.

3.2.9 Numerical Methods

Although the model Hamiltonian (3.36) serves well to explain the underlying physics of the system, for numerical work, typically the time dependent Schrödinger's equation is numerically integrated using the split operator method. The details of this approach are found in appendix B.

In the following two sections (3.3 and 3.4) we present two proposals for the experimental realisation of SAP. The temporal dynamics of each system is time evolved numerically using the split operator method, which serves well for our purposes. In order to probe the relationship between the full numerical integration of Schrödinger's equation and the model Hamiltonian (3.36) it is necessary to examine the time evolution of the wavefunction in the energetic mode basis. The energetic eigenfunctions are recovered easily using the finite difference method (also detailed in Appendix B). The relationship between the evolution of the quantum state in the energetic mode basis and the spatial basis (for two spatial and energetic modes) is deduced in chapter 4. This approach is extended in chapter 5 for SAP, where the phase evolution of the three mode system in described in both the energetic and spatial bases.

3.3 SAP in Waveguide Settings

Over the past three decades the trapping and controlling of atomic matter waves has become a dominant theme in ultracold physics [83–86]. The landmark achievement of the production and confinement of ultracold quantum gases (UCQG), has paved the way for deeper experimental and theoretical development of ultracold atomic physics. Three Nobel prizes have been awarded to acknowledge the rapid progression of this discipline. The first in 1997 (to Steven Chu, Claude Cohen-Tannoudji and William D. Phillips) "for development of methods to cool and trap atoms with laser light" and the second in 2001 (to Eric A. Cornell, Wolfgang Ketterle and Carl E. Wieman) "for the achievement of Bose-Einstein condensation ...". In particular, the realisation of the Bose Einstein condensation (BEC) has opened a branch of physics devoted to the study of coherent matter waves. The third Nobel Prize was awarded this year (2012) to Serge Haroche and David J. Wineland, "for ground-breaking experimental methods that enable measuring and manipulation of individual quantum systems."

Potential future development in experimental cold atomic physics, looks as promising as the rapid development of the computer, i.e. the equipment becoming progressively smaller and the output (production of UCQGs) becoming more efficient. These are components of a general trend, which Nobel laureate Theodor Hänsch refers to as, the movement 'towards a quantum laboratory on a chip.' The miniaturization and fabrication of quantum potentials, whose size are of the order of the de Broglie wavelength of atoms, have become known as 'Atom Chips'. The Atom Chip utilizes the mature technology of the semi-conductor industry to provide a versatile environment for the coherent manipulation of atomic matter waves in the magnetic fields above microfabricated current carrying wires. Since the introduction of the Atom Chip [87–90] in 1999 the scientific community has seen the realisation of the first BEC on a chip [91, 92] in 2001 and sympathetic cooling to Fermi degeneracy demonstrated on an atom chip [9] in 2006.

Subsequent technological developments have aided the creation of experiments that answer fundamental questions in quantum mechanics [93, 94] and hold great promise for the realisation of quantum information processing [95–97]. Advances in the technology of optical lattices and micro-traps have allowed for substantial progress in this area [58, 98–101]. Whilst techniques for controlling and preparing the internal states of atoms using appropriate electromagnetic fields are well developed, only a few concepts exist for achieving the same control over the spatial part of the wavefunction [56, 70, 96, 102, 103]. Such control would complement currently existing techniques and allow for the complete engineering of a particle's quantum state. SAP is a technique that allows for coherent control over the spatial part of the wavefunction, in particular the controlled transport of

atoms between different regions in space. In optical lattices this corresponds to moving between discrete regions in space, and in waveguide settings this allows for the transfer from one guide to another, originally explored in [70].

Here we focus on atom-chip systems and investigate their suitability as a platform for the experimental realisation of SAP. These micro-fabricated chips contain surface mounted current carrying wires which provide guiding potentials for matter waves. The wire geometry and therefore the waveguide geometry, which is created at the micrometer and nanometer scale, can be chosen almost at will [90], and may be loaded with ultracold atomic gases at low densities [104, 105].

To begin we briefly present the basic protocol (section 3.3.1) and theoretical framework involved in experimentally cooling and trapping neutral atoms (section 3.3.2). Therein we sketch the theory concerned with magnetic trapping of neutral atoms with current carrying wires. The model waveguide potential we use is outlined in section 3.3.6 where we provide a theoretical analysis of SAP on an atom chip waveguide structure. Whilst the initial state can be prepared with a large degree of localisation, one of the problems following the subsequent evolution inside the waveguide is that the wavefunction disperses along the guide. This makes it hard to exactly measure the final state of the system and put a quantitative number on the efficiency of the adiabatic process. In section 3.3.6 we introduce a simple harmonic potential along the longitudinal direction of the trap, allowing for the recombination of the wavefunction at the end of the process. This permits a perfect measure of SAP fidelity on waveguide structures. In section 3.3.7 we describe a realistic situation by examining three waveguides mounted on an atom chip. We show that whilst the resonance condition is not satisfied at all times, a counter-intuitive approach and departure sequence will lead to high fidelity transport and can be clearly distinguished from a direct tunneling approach.

3.3.1 Summary of Experimental Cooling and Trapping Processes

Achieving quantum degeneracy of ultracold neutral atoms is a multistep process. Modern experiments may use a combination of a number of cooling techniques developed over the past several decades [106] to reach quantum degeneracy. Here we give an overview of the process involved in creating a BEC mounted on an atom chip waveguide. The details of the cooling are not important for this work, but are presented here briefly for completeness sake. Whilst the theoretical analysis contained in the remainder of the section is concerned with the transport via SAP of a single atom in a triple waveguide structure, the physics of the single atom is analogus to that of a BEC in the non-interacting limit.

A magneto-optical trap (MOT) cools and traps atoms from a (room temperature) vapor gas [38, 107]. The MOT consists of a vacuum chamber wherein the vapor gas is injected and makes use of magnetic and optical components to create the desired trapping geometry to confine and produce an ultracold gas of neutral atoms. The magnetic field is generated by a Helmholtz pair, which is two circular magnetic coils that can generate a near uniform magnetic field through the vacuum chamber. When they are arranged in what is called an anti Helmholtz configuration, they produce a quadrupole magnetic field and the magnitude of the magnetic field $|\mathbf{B}|$ increases linearly in all directions from a central point in the vacuum chamber, where $|\mathbf{B}| = 0$. Three pairs of counter-propagating red-detuned laser beams, which have the same polarizations relative to the photon momentum, are focused on the point of the zero magnetic field inside the vacuum chamber. The lasers work to confine atoms to this point through the mechanism of stimulated absorption and emission which redirects the atom's momentum toward the central point. Laser cooling makes use of the Doppler effect, as the probability of an atom to scatter a photon becomes velocity dependent. For an atom moving away from the zero point of the magnetic field, the laser light is closer in resonance with the atom due to the Doppler effect. This increases the rate of stimulated absorption and as a result the laser imparts momentum to the atom (by the absorption of a photon), slowing it down. The emitted fluorescent light by spontaneous and/or stimulated emission also changes the momentum of an atom, but due to spatial symmetry the net momentum change is zero. The combination of the magnetic and optical fields creates a restoring force that directs the atoms toward the $|\mathbf{B}| = 0$ center.

For the purposes of Atom chip experiments a more useful configuration than the above is what is known as a mirror MOT [108]. Here the two anti-Helmholtz coils are replaced with a U-shaped wire in combination with an external bias field to create the same quadrupole field. Instead of using three pairs of counter-propagating laser beams only two pairs need to be used. The Atom chip surface acts as a mirror with each laser beam angled at $\pm 45^o$ to the Atom Chip surface. Configurations such as this are most desirable in experiments involving Atom Chips as the loading procedure is most straight forward. More developed modern techniques also allow for the transport of a BEC by making use of what are known as optical tweezers [104].

3.3.2 Magnetic Guiding and Trapping

Experimental control of neutral atoms is governed by their interaction with magnetic, electric and optical fields [38, 107]. Magnetic trapping relies on the interaction of the magnetic moment of an atom $\boldsymbol{\mu}$ with an external magnetic field $\mathbf{B}$. The field exerts

a torque on the magnetic moment which in general aligns $\boldsymbol{\mu}$ with $\mathbf{B}$. Thus when $\boldsymbol{\mu}$ is parallel to the field the energy is a minimum [38, 107].

The coupling between $\boldsymbol{\mu}$ of the atom and the external field $\mathbf{B}$ is known as the Zeeman effect. This effect is responsible for the splitting of a spectral line in the presence of an applied magnetic field. It is the magnetic counterpart of the Stark effect, whereby a spectral line splits into several components in the presence of an applied electric field. The interaction between a static magnetic field, $\mathbf{B}$, and the magnetic moment of the atom, $\boldsymbol{\mu}$, lifts the energetic degeneracy of the state, resulting in the splitting of a single emission spectral line into several lines. The interaction assumes the form,

$$\mathbf{V}_I \;=\; -\boldsymbol{\mu}\cdot\mathbf{B}. \tag{3.38}$$

The alkali metals are the elements in the first column of the periodic table. Their electronic configuration consists of closed shells and a single outer valence electron. As a result the total orbital angular momentum L and spin angular momentum S of the atom are determined by this valence electron [13]. It follows that the magnetic moment of an atom $\boldsymbol{\mu}$ is a sum of the contributions from the orbital $\mathbf{L}$ and spin $\mathbf{S}$ magnetic moments of the electron and the magnetic moment of the nucleus $\mathbf{I}$, each multiplied by their appropriate gyromagnetic ratio.

$$\boldsymbol{\mu} \;=\; -\frac{\mu_B}{\hbar}\left(g_l\mathbf{L}+g_s\mathbf{S}\right)-\frac{\mu_N}{\hbar}g_i\mathbf{I}, \tag{3.39}$$

where,

$$\mu_B \;=\; \frac{e\hbar}{2m_e}, \qquad \mu_N \;=\; \frac{e\hbar}{2m_p}, \tag{3.40}$$

are Bohr magneton and nuclear magneton respectively, e is the electric charge, m_e and m_p are the electron and proton mass. The electron orbital g-factor $g_l = 1$. Paul Dirac's relativistically invariant Schrödinger equation predicted the electron spin, g-factor $g_s = 2$. A correction to this value of less than 0.1% arises when quantum electrodynamical effects are taken into account [109, 110].

The magnetic moment of the nucleus $\mathbf{I}$ is also a sum of the orbital $\mathbf{L}$ and spin $\mathbf{S}$ magnetic moments of the protons and neutrons in the nucleus [13]. As the treatment of the orbital and spin magnetic moments of the nucleus is analogus to the treatment of those same components for the electron, for the purposes of brevity and to avoid repetition we omit to detail their contributions here.

In the presence of a weak magnetic field the orbital $\mathbf{L}$ and spin $\mathbf{S}$ magnetic moments are considered coupled. For strong magnetic fields the spin-orbit coupling is broken and we have what is referred to as the Paschen-Bach effect, i.e. the splitting of spectral

lines with a strong magnetic field [111]. Here we confine ourselves to the regime of weak magnetic fields, where the total electric magnetic moment $\mathbf{J} = \mathbf{L}+\mathbf{S}$, is considered to be a good quantum number. In this manner the spin and orbital angular momentum vectors precess about the total orbital angular momentum vector $\mathbf{J}$, and the corresponding quantum number is in the range $|L - S| \leq J \leq |L + S|$. Of interest are the time averaged spin and angular momentum vectors, which are given by their projection onto the direction of $\mathbf{J}$,

$$\langle \mathbf{S} \rangle = \frac{\mathbf{S} \cdot \mathbf{J}}{J^2} \mathbf{J}, \tag{3.41a}$$

$$\langle \mathbf{L} \rangle = \frac{\mathbf{L} \cdot \mathbf{J}}{J^2} \mathbf{J}. \tag{3.41b}$$

The time averaged magnetic moment for the electron is then written,

$$\langle \boldsymbol{\mu} \rangle_e = -\frac{\mu_B}{\hbar} \left(g_l \frac{\mathbf{L} \cdot \mathbf{J}}{J^2} + g_s \frac{\mathbf{S} \cdot \mathbf{J}}{J^2} \right) \mathbf{J}. \tag{3.42}$$

Given that, $\mathbf{S} \cdot \mathbf{J} = S^2 + \mathbf{S} \cdot \mathbf{L}$; $\mathbf{L} \cdot \mathbf{J} = L^2 + \mathbf{S} \cdot \mathbf{L}$; $\mathbf{J} \cdot \mathbf{J} = J^2 = S^2 + L^2 + 2\mathbf{S} \cdot \mathbf{L}$; and $S^2|s, m_s\rangle = \hbar^2 s(s+1)|s, m_s\rangle$; $L^2|l, m_l\rangle = \hbar^2 l(l+1)|l, m_l\rangle$; $J^2|j, m_j\rangle = \hbar^2 j(j+1)|j, m_j\rangle$; we have,

$$\begin{aligned} \mathbf{S} \cdot \mathbf{J} &= \frac{1}{2}\left(J^2 + S^2 - L^2\right) = \frac{\hbar^2}{2}\left[j(j+1) + s(s+1) - l(l+1)\right], \\ \mathbf{L} \cdot \mathbf{J} &= \frac{1}{2}\left(J^2 - S^2 + L^2\right) = \frac{\hbar^2}{2}\left[j(j+1) - s(s+1) + l(l+1)\right]. \end{aligned} \tag{3.43}$$

Plugging these relations into (3.42) results in a simple expression for the time averaged magnetic moment for the electron.

$$\begin{aligned} \langle \boldsymbol{\mu} \rangle_e &= -\frac{\mu_B}{\hbar} g_j \, \mathbf{J}, \\ g_j &\equiv g_l \frac{j(j+1) - s(s+1) + l(l+1)}{2j(j+1)} + g_s \frac{j(j+1) + s(s+1) - l(l+1)}{2j(j+1)}. \end{aligned} \tag{3.44}$$

The total magnetic moment of the atom is made up from the contributions of the spin and orbital angular momentum of the protons, neutrons and electrons. The total angular momentum is the vector sum of the total nuclear and orbital angular momentum,

$$\mathbf{F} = \mathbf{I} + \mathbf{J}. \tag{3.45}$$

The total time averaged magnetic moment is derived using the same approach as that for the time averaged magnetic moment for the electron (3.44). The total time averaged magnetic moment for atom is the projection of the components of the nuclear and orbital

angular momentum onto the direction of $\mathbf{F}$.

$$\langle \boldsymbol{\mu} \rangle \;=\; -\frac{\mu_B}{\hbar}\left(g_j \,\frac{\mathbf{J}\cdot\mathbf{F}}{F^2} + \frac{\mu_N}{\mu_B} g_i \,\frac{\mathbf{I}\cdot\mathbf{F}}{F^2}\right)\mathbf{F}. \tag{3.46}$$

As before we note that, $\mathbf{J}\cdot\mathbf{F} = J^2 + \mathbf{J}\cdot\mathbf{I}$; $\mathbf{I}\cdot\mathbf{F} = I^2 + \mathbf{J}\cdot\mathbf{I}$; $\mathbf{F}\cdot\mathbf{F} = F^2 = J^2 + I^2 + 2\mathbf{J}\cdot\mathbf{I}$. and $J^2|j,m_j\rangle = \hbar^2 j(j+1)|j,m_j\rangle$; $I^2|i,m_i\rangle = \hbar^2 i(i+1)|i,m_i\rangle$ and $F^2|f,m_f\rangle = \hbar^2 f(f+1)|f,m_f\rangle$, we have

$$\begin{aligned} \mathbf{J}\cdot\mathbf{F} \;&=\; \frac{1}{2}\left(F^2 + J^2 - I^2\right) \;=\; \frac{\hbar^2}{2}\left[f(f+1) + j(j+1) - i(i+1)\right], \\ \mathbf{I}\cdot\mathbf{F} \;&=\; \frac{1}{2}\left(F^2 - J^2 + I^2\right) \;=\; \frac{\hbar^2}{2}\left[f(f+1) - j(j+1) + i(i+1)\right]. \end{aligned} \tag{3.47}$$

Plugging the above into (3.46) we find the total time averaged angular momentum for the atom is,

$$\begin{aligned} \langle \boldsymbol{\mu} \rangle \;&=\; -\frac{\mu_B}{\hbar} g_f \,\mathbf{F}, \\ g_f \;&\equiv\; g_j \frac{f(f+1) + j(j+1) - i(i+1)}{2f(f+1)} + \frac{\mu_N}{\mu_B} g_i \frac{f(f+1) - j(j+1) + i(i+1)}{2f(f+1)}. \end{aligned} \tag{3.48}$$

The magnetic field $\mathbf{B}$ is aligned along the $\hat{z}$ direction therefore $\mathbf{F}\cdot\mathbf{B} = \mathbf{F}\cdot\hat{z}B = F_z B$. We note that $F_z|f,m_f\rangle \;=\; \hbar m_f |f,m_f\rangle$, where $m_f = -f,\ldots,f$. Finally we may write the time averaged interaction of the atom with the magnetic field as,

$$\begin{aligned} \langle \mathbf{V}_I \rangle \;&=\; -\langle \boldsymbol{\mu} \rangle \cdot \mathbf{B}, \\ \langle \mathbf{V}_I \rangle \;&=\; -\mu_B g_f m_f B. \end{aligned} \tag{3.49}$$

Depending on the sign of $g_f m_f$, atoms are trapped in either a local minimum or local maximum. For $g_f m_f < 0$ the atoms are in a strong field seeking state and for $g_f m_f > 0$ they are weak field seekers. A local maximum in free space is forbidden by the Earnshaw theorem [92]. Since a three dimensional magnetic maximum cannot be produced - only weak field seeking states can be magnetically trapped.

The simplest form of a magnetic field that is suitable for the trapping of neutral atoms is the magnetic field generated by a current carrying wire [112, 113]. The wire's magnetic field decays as $1/r$ with the distance r from the wire. When a homogeneous external magnetic bias field is applied in a direction perpendicular to the wire, the two fields cancel at some distance r_0 from the wire. This creates a two dimensional quadrupole field that confines the atoms along a line parallel to the wire at a distance r_0. At the zero point of the magnetic field 'spin-flip' transitions may occur between trapped and untrapped states [114]. The loss of trapped atoms in this manner is known as Majorana 'spin-flip' losses, and may be circumvented by using a further magnetic field along a

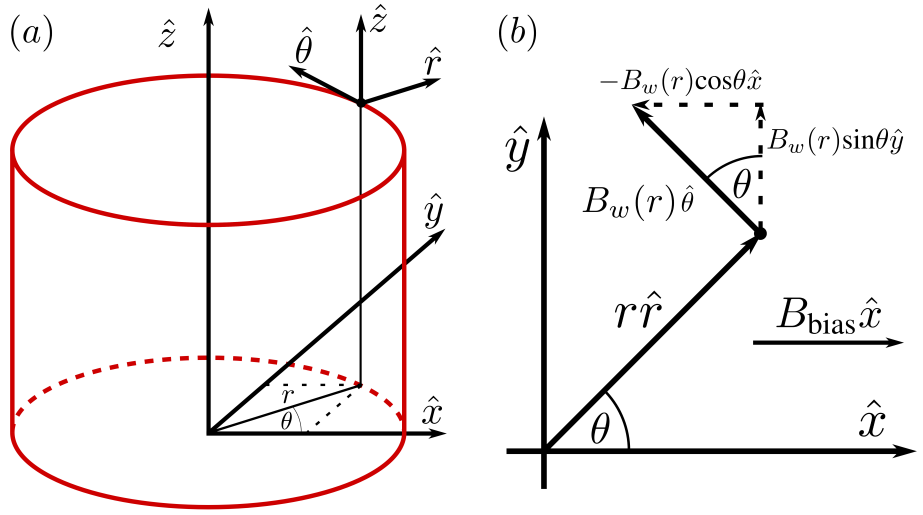


FIGURE 3.6: (a) Polar and Cartesian co-ordinates. (b) Magnetic field due to a current carrying wire in the presence of a bias field aligned orthogonally to the direction of current (out of page). See text for details.

direction parallel to the wire, thus creating a non-vanishing magnetic field minimum at r_0. Developing the background theory to the above is the focus of the following sections.

3.3.3 Linear Quadrupole Waveguide

From Ampére's circuital law (outlined in appendix A.4), the magnetic field ($B_w(r)$) at a distance r from an infinitely long current carrying conductor, of negligible cross section with a current I_w flowing along the $+\hat{z}$ direction, in cylindrical co-ordinates $(\hat{r}, \hat{\theta}, \hat{z})$ is,

$$\mathbf{B}(r) \;=\; B_w(r)\,\hat{\theta} \;=\; \frac{\mu_0 I_w}{2\pi r}\,\hat{\theta}. \tag{3.50}$$

The wire's magnetic field according to eq. (3.50) can be expressed in Cartesian co-ordinates, illustrated in figure 3.6(a), by

$$\mathbf{B}_w(x,y,z) = -\frac{\mu_0 I_w}{2\pi(x^2+y^2)} y\,\hat{x} + \frac{\mu_0 I_w}{2\pi(x^2+y^2)} x\,\hat{y}. \tag{3.51}$$

The current I_w in the wire is in the $+\hat{z}$ direction. An external homogeneous magnetic bias field, $\mathbf{B}_{\text{bias}} = B_{\text{bias}}\hat{x}$, is applied along the $\hat{x}$ direction, as in figure. 3.6(b),

$$\mathbf{B}(x,y,z) = \left(B_{\text{bias}} - \frac{\mu_0 I_w}{2\pi(x^2+y^2)} y\right)\hat{x} + \frac{\mu_0 I_w}{2\pi(x^2+y^2)} x\,\hat{y}. \tag{3.52}$$

This applied magnetic field cancels the magnetic field due to the wire along a line parallel to the wire (with $x = 0$) at a distance $y = r_0$. Since $r = \sqrt{x^2 + y^2}$, from (3.52) above,

$$r_0 \;=\; \left(\frac{\mu_0}{2\pi}\right) \frac{I_w}{B_{\text{bias}}}. \tag{3.53}$$

The magnetic field increases in all directions from this point which is the local minimum, see figure 3.7. The potential energy of an atom in a weak field seeking state ($g_f m_f > 0$) increases with increasing field strength in all directions along $(\hat{x}, \hat{y})$ from r_0. Therefore this quadrupole field confines and guides weak field seeking atoms in the vicinity of the magnetic field minimum, along a line parallel to the current carrying wire.

$$\mathbf{B}(r, \theta) \;=\; \frac{\mu_0 I_w}{2\pi} \left(\frac{1}{r_0} - \frac{\cos\theta}{r}\right) \hat{x} + \frac{\sin\theta}{r}\, \hat{y}. \tag{3.54}$$

As long as the bias field is orthogonal to the wire the two fields cancel exactly. At the zero point of the magnetic field atoms can be lost due to Majorana transitions between trapped and untrapped spin states. This problem is resolved by adding a small B-field component $\mathbf{B}_{\text{ip}} = B_{\text{ip}}\hat{z}$ along the wire direction removing the energetic degeneracy between the trapped and untrapped spin states.

3.3.4 Majorana Losses

An atom of magnetic moment $\boldsymbol{\mu}$ confined in a magnetic field $\mathbf{B}$ experiences a torque given by $\boldsymbol{\mu} \times \mathbf{B}$. This torque causes the magnetic moment of the atom to precess about the direction of the magnetic field rather than remain aligned with it. This is known as Larmor precession and the associated frequency of the precession [114],

$$\omega_{\text{L}} \;=\; \frac{\mu_B}{\hbar} |\mathbf{B}|, \tag{3.55}$$

is the Larmor frequency.

The major draw back of the linear quadrupole trap is that due to the orbital motion of the atoms, losses may occur in the vicinity of the zero field. At r_0 the magnetic field, and therefore the Lamor frequency, both increase with distance from r_0. When the Larmor frequency (3.55) is small with respect to the rate of change of the magnetic field, $\omega_{\text{L}} \ll d\mathbf{B}/d\mathbf{x}$, there is a large probability of a diabatic spin flip transition occurring, from a trapped to an untrapped state. These are Majorana losses and in the vicinity of the zero field this transition probability and the Majorana loss rate is high, limiting the lifetime of the trap [38].

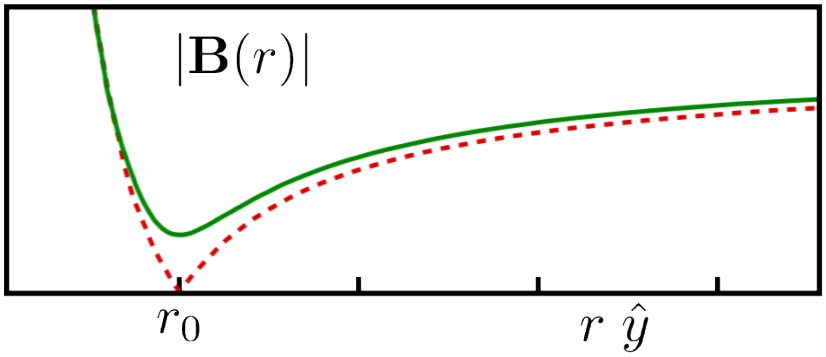


FIGURE 3.7: A cross section of the magnetic field's magnitude vs. the distance from the conductor. In dashed red is the magnetic field in the absence of the bias field $B_{\rm ip}\hat{z}$. In solid green, the magnetic field exhibits a parabolic shape, as the additional $B_{\rm ip}\hat{z}$ component lifts the energetic degeneracy at the distance r_0 from the surface of the wire. Also see figure 3.12.

3.3.5 Bias Field

Adding a small magnetic field component along the direction of the wire, removes the energetic degeneracy between trapped and untrapped spin states [112]. In the vicinity of r_0 the trapping potential becomes approximately harmonic (figure 3.7), and the rate of change of the magnetic field is significantly reduced near r_0 so that $\omega_{\rm L} \approx d\mathbf{B}/d\mathbf{x}$. Thus increasing the trap lifetime. The magnetic field is,

$$\mathbf{B}(r) \;=\; \frac{\mu_0 I_w}{2\pi}\left(\frac{1}{r_0} - \frac{\cos\theta}{r}\right)\hat{x} + \frac{\sin\theta}{r}\;\hat{y} + B_{\rm ip}\;\hat{z}. \tag{3.56}$$

The magnitude of the magnetic field is found to be,

$$|\mathbf{B}(r)| \;=\; \left(\left(\frac{\mu_0 I_w}{2\pi}\right)^2 \frac{r^2 + r_0^2 - 2rr_0\cos\theta}{r^2 r_0^2} \;+\; B_{\rm ip}^2\right)^{1/2}. \tag{3.57}$$

Near the trap minimum $r \to r_0$ we find $\cos\theta \approx 1$ and $r^2 r_0^2 \approx r_0^4$, so that,

$$\begin{aligned} |\mathbf{B}(r)| \;&=\; \left(B_{\rm ip}^2 \;+\; \left(\frac{\mu_0 I_w}{2\pi}\right)^2 \frac{(r-r_0)^2}{r_0^4}\right)^{1/2} \;=\; B_{\rm ip}\left(1 \;+\; \frac{B_{\rm bias}^2 (r-r_0)^2}{r_0^2 B_{\rm ip}^2}\right)^{1/2}, \\ &\approx\; B_{\rm ip}\hat{z} \;+\; \frac{B_{\rm bias}^2}{B_{\rm ip}}\frac{(r-r_0)^2}{2r_0^2}\hat{z}, \end{aligned} \tag{3.58}$$

which is aligned along the $\hat{z}$ direction. From this we get,

$$\langle \mathbf{V}_I \rangle \;=\; m_f g_f \mu_B B_{\rm ip} \;+\; \frac{m\omega_r^2}{2}(r-r_0)^2. \tag{3.59}$$

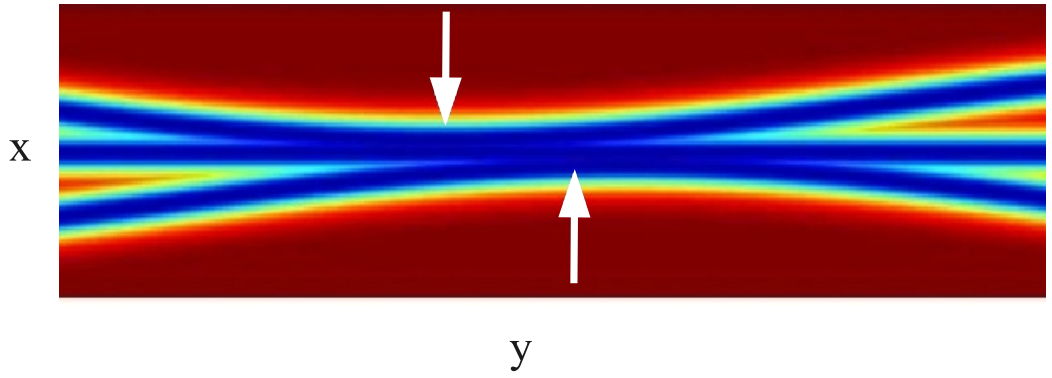


FIGURE 3.8: Waveguide structure near the point of closest approach. The points where the upper and lower waveguides have a minimum distance from the central waveguide are indicated by the arrows. The wave-packet will originally travel in the lowest waveguide from left to right.

where m is the atomic mass and the radial harmonic trap frequency is,

$$\omega_r = \frac{B_{\text{bias}}}{r_0}\sqrt{\frac{m_f g_f \mu_B}{m B_{\text{ip}}}}. \tag{3.60}$$

The 'ip' notation refers to Ioffe-Pritchard, as this is the name given to this type of potential [87]. Shown in figure 3.7 is the change incurred by adding this $B_{\text{ip}}\hat{z}$ component to the magnetic field lifting the minimum of the magnetic field making it harmonic in shape near r_0. As a result $d\mathbf{B}/d\mathbf{x} \approx \omega_{\text{L}}$ and atom losses due to Majorana spin flips are significantly reduced.

3.3.6 Waveguide SAP: Model

A schematic of our waveguide model is found in figure 3.8. Our initial state is localised on the left hand side of the bottom waveguide, which is the $|0\rangle$ spatial mode. The middle waveguide is the $|1\rangle$ spatial mode and the top waveguide is the $|2\rangle$ spatial mode. By adiabatically varying the distances between the waveguides we can adjust the Rabi 'tunneling' frequency between the spatial modes in a manner that tunes the mixing angle (3.37) from $0 \to \pi/2$. An atom moving in this waveguide structure will experience the change of the Rabi 'tunneling' frequency as a function of traveled distance, and its population density will subsequently be transferred from $|0\rangle \to |2\rangle$.

The Schrödinger equation for the evolution of a wave-packet in a two-dimensional waveguide structure is given by

$$\imath\hbar\frac{d}{dt}\langle\mathbf{x}|\Psi(t)\rangle = \left(-\frac{\hbar^2}{2m}\frac{d^2}{d\mathbf{x}^2} + \mathbf{V}(\mathbf{x})\right)\langle\mathbf{x}|\Psi(t)\rangle\ , \tag{3.61}$$

where m is the mass of the atom and $\mathbf{x} = (x, y)$.

As we assume a tight confinement in the $\hat{z}$ direction, the dynamics in this direction can be considered decoupled. The wavefunction can then be split into a product as $\Psi(x,y)\Psi(z)$, and we only consider the x, y components. In this section we will first examine the SAP process using an idealised potential in which the condition of resonance between the individual waveguides is fulfilled at any point. This will help us to illustrate the basic process and in particular highlight the influence of the longitudinal dimension [70]. In Section 3.3.7 we will compare these results to realistic atom chip scenarios in which we will have to relax the resonance condition.

The assumption we make to guarantee that the ground state energy in all three waveguides is the same everywhere is that we can construct our potential $\mathbf{V}(\mathbf{x})$ by stitching three independent waveguides together. In a realistic situation the potentials creating each guide would influence each other and lead to non-symmetric situations between pairs. We assume each guide to have the potential

$$\mathbf{V}_s(\mathbf{x}) = A\tanh[B(x - f(y))]^2, \tag{3.62}$$

where A determines the height, B the width and $f(y)$ the position of the minimum along the x-axis. The overall potential is then assumed to be given by the minimum value of each of the three potentials at any point in space. A schematic view of the area in which the guides approach most closely is shown in figure 3.8.

The eigenstates of matter waves propagating in two-dimensional waveguides at different distances have recently been explored by Jääskeläinen and Stenholm [115]. They determined the conditions under which the movement of a matter wave can be considered adiabatic in a curved waveguide and developed a formalism based on localised and de-localised basis states. Here we will take a more straightforward approach and present a numerical solution to the process, which will show that despite the existence of velocity-dependent potentials due to the curvature of the waveguides [115] the SAP process can be observed with high fidelity.

Our simulations start with a well-localised wave-packet far away from the coupling area. In time, however, this packet will disperse along the waveguide, making it hard to quantify the success of the transfer process. To overcome this problem we introduce an additional harmonic potential of frequency ω_l along the y-axis, which will lead to a refocusing of the wave-packet in the longitudinal direction after a time of $\omega_l/2$. The initial state of our wave-packet is given by the ground state of an isotropic trap of the transverse frequency of the waveguide and its movement along the guide is induced by the harmonic potential as well.

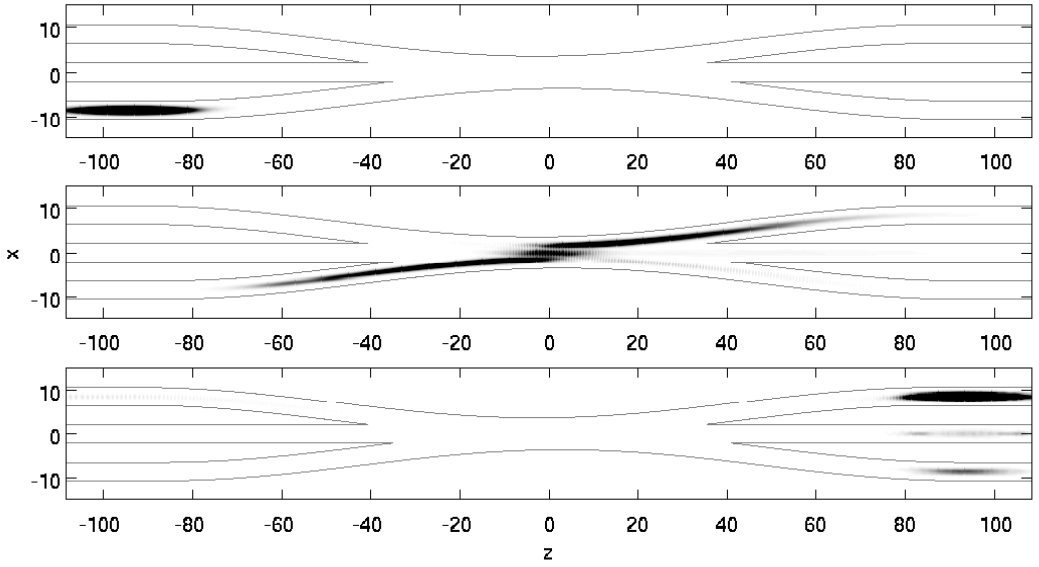


FIGURE 3.9: Time evolution of the wave-packet in a counter-intuitive arrangement of the waveguides at three different times for values of A=20 and B=0.5. The shapes of the waveguides are indicated by the black lines and they are fully separated at the energy of the wave-packet in the coupling zone (not visible).

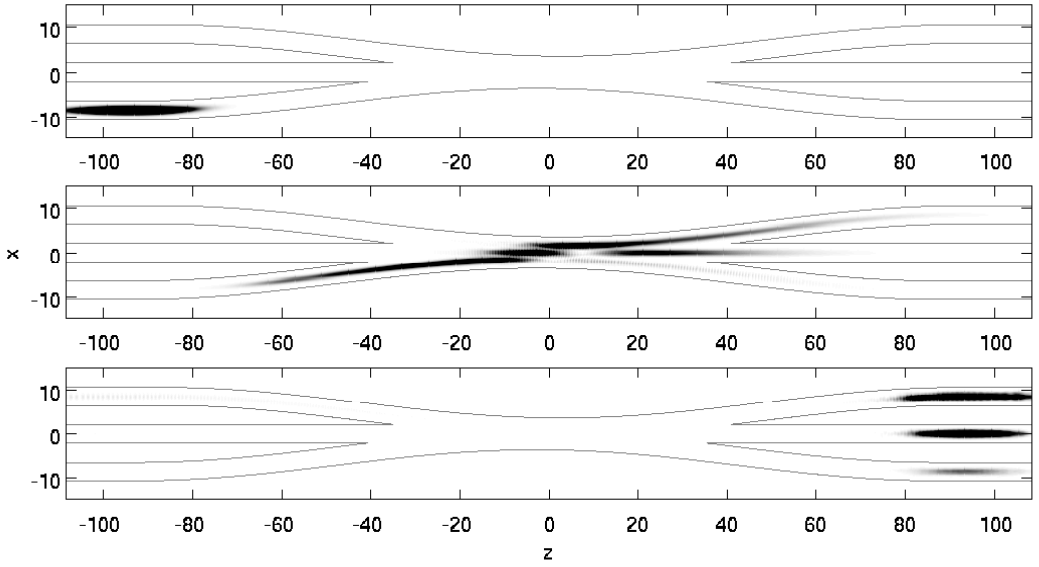


FIGURE 3.10: Time evolution of the wave-packet in an intuitive arrangements of the waveguides (parameters in figure 3.9). Note the Rabi oscillations visible in the middle plot.

In figure 3.9 we show the evolution of the wavefunction at different times throughout the process for a counter-intuitive arrangement of the waveguides. Starting with the wave-packet located in the lower guide, one can clearly see that a majority of the probability is transferred into the upper guide. The evolution of the same initial state in an intuitive arrangement of waveguides (see figure 3.10) shows significantly less transfer.

The amount of transfer varies as a function of several parameters. The first one is the

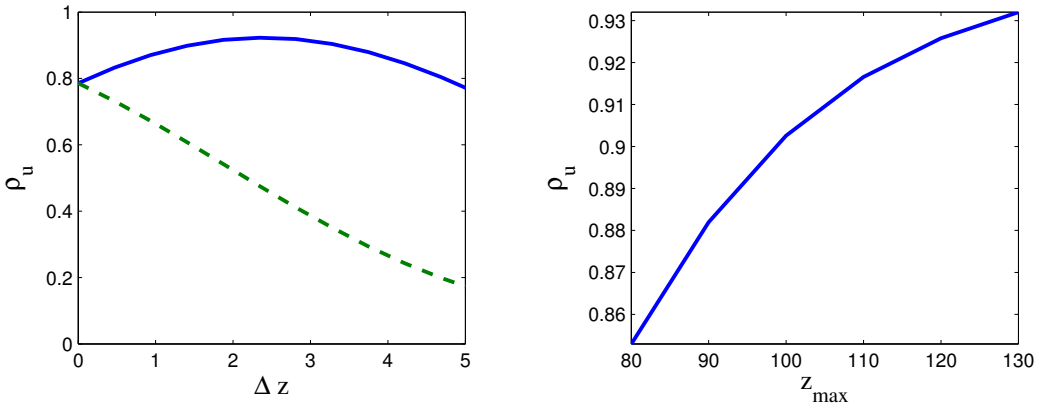


FIGURE 3.11: (Left) Probability transferred into the upper waveguide as a function of offset between the two outer guides (in scaled units $\sqrt{\hbar/m\omega}$). The full line shows the results from the counter-intuitive case and the broken line for the intuitive one. (Right) Maximum probability transferred as a function of the length of the interaction region.

distance between the two points of closest approach of the outer waveguides to the middle one, Δz. We show the amount transferred as a function of this quantity in figure 3.11 on the left hand side. The full line (blue) represents the counter-intuitive case and a maximum at a finite value of Δz is visible. The broken line shows the same quantity for the intuitive setting, clearly indicating that direct tunneling does not lead to high fidelities.

The second parameter that plays an important role is the degree of adiabaticity of the process. For a waveguide system this translates into the velocity with which the atom moves or alternatively the length of the coupling area, i.e. the lower the velocity the more adiabatic the process. Here we keep the velocity small and effectively constant. On the right hand side of figure 3.11 we show the transferred population density versus the overall length of the coupling area. Making the overall structure longer also corresponds to decreasing the curvature of the waveguides and thereby reducing the velocity-dependent couplings introduced by it [115], and increasing the adiabaticity. As expected we find that a more adiabatic process leads to a larger transfer probability.

Our simulations are carried out only for the linear case of a single atom. If one would like to carry out the same process using, say, a Bose-Einstein condensate, one has to take care of the non-linearity that arises from the atomic interactions. Therefore our simulations give a very good approximation for low density condensates or even thermal clouds of atoms.

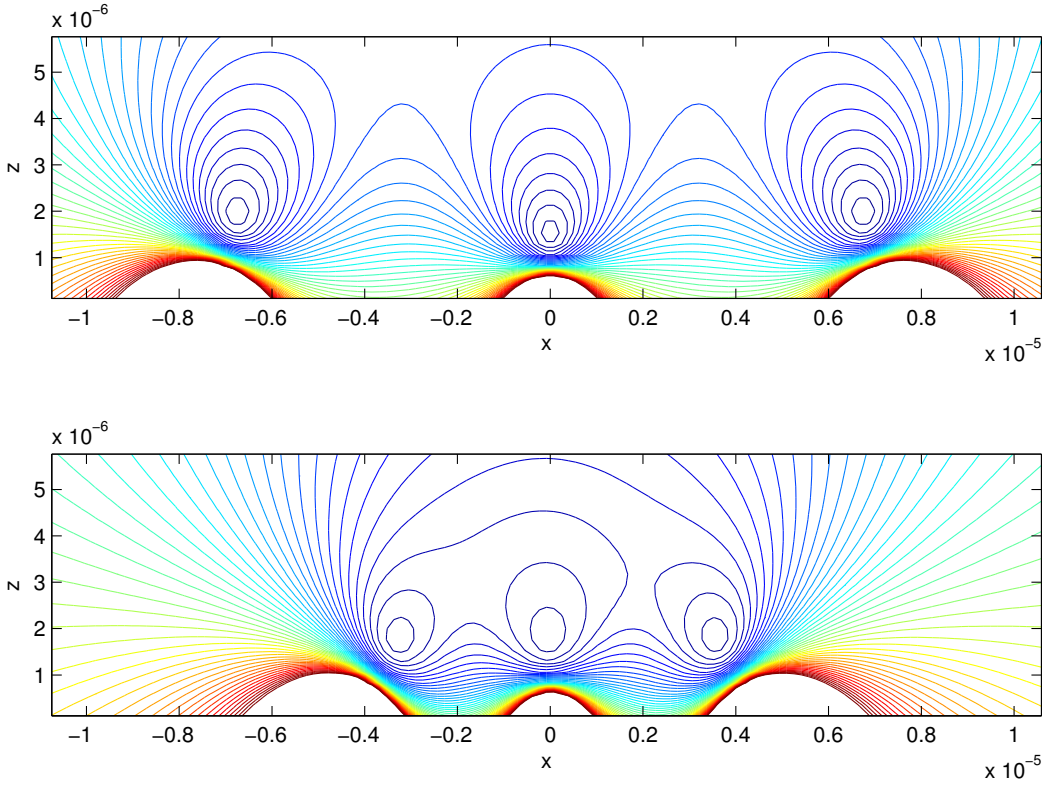


FIGURE 3.12: Potentials above the three wires on an atom chip when all wires are separated at equal distance (upper) and at the point where the wire on the left is closest to the center wire (lower)

3.3.7 Waveguide SAP: Experimental Parameters

While the above results clearly demonstrate the viability of SAP in waveguide structures, it is currently not clear in which experimental system it will be possible to observe it. One of the problems is that the asymptotic eigenstates of the system have to be in resonance at any point in time. This is hard to achieve in many realistic systems as neighbouring trapping potentials usually strongly influence each other when they are close enough to allow for significant tunneling rates.

Atom chips are well developed experimental tools these days and consist of an arrangement of current carrying wires mounted on a surface [112]. We simulate the SAP process by considering three such wires separated by a distance of $9\mu m$ initially. The overall length of the coupling zone is chosen such that in the intuitive case several Rabi oscillations can be expected and the distance between two wire centers at the point of closest approach is chosen as $4.5\mu m$. The applied bias field has a magnitude of $B_b = 100G$ and because of the small curvature of the wires can be regarded as orthogonal at any point. Since a large ground state is advantageous for tunneling the atomic species we consider is ^{6}Li. These parameters are chosen as they are close to experimental settings.

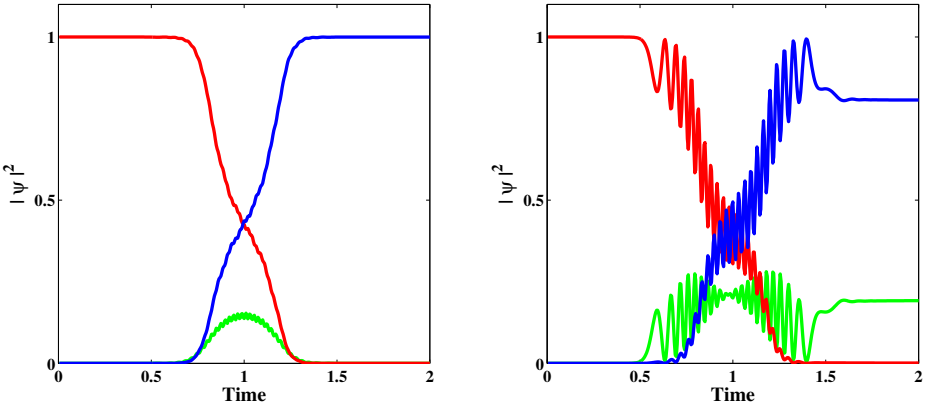


FIGURE 3.13: Population in the individual waveguides as a function of time for the counter-intuitive (left) and intuitive (right) waveguide arrangements. The population in the trap on the left is shown by the blue line, the middle on by the green line and the one on the right by the red line.

In general the central minimum will be influenced by the fields from the two outer wires and increasingly so as the wires come closer. This will effect the resonance condition and ultimately prevent the SAP process from working effectively. In order to minimize this behaviour we make use of a trick and adjust the current going through the middle wire to be slightly lower than the ones going through the outer wires. We have found that $I_m = 700\text{mA}$ for the middle wire and $I_{l,r} = 1000\text{mA}$ for the two outer wires, is a good choice.

Figure 3.12 shows the potential above the wires for the two different situations of symmetric distance between all wires (upper graph) and when the left wire is closer to the center one than the right wire (lower graph). While an asymmetry in the second case is clearly visible, its effect on the potentials is moderate.

A full 3D simulation of the SAP process in these potentials is a numerically taxing task and beyond our current capabilities. We have therefore simulated the process by using the two-dimensional potentials of the kind displayed in figure 3.12 and changing the distance between the wires as a function of time. In doing so we neglect the dispersion of the wavefunction along the longitudinal direction. However, since we have shown in Section 3.3.6 that the dispersion does not have any significant effect on the transfer fidelity, our simulations can be seen as a good approximation to the full situation.

In figure 3.13 we show the results of these simulations by displaying the populations in the individual traps as a function of time for the intuitive (right) and the counter-intuitive case (left). Initially all population is on the left hand side and it can be clearly seen that in the counter-intuitive situation there is a smooth transition over to the right hand side. While in the perfect SAP setup no population should ever appear in the central trap,

the various imperfections of this realistic example lead to a finite occupation during the process. However, at the very end no population is left in the middle trap. Contrary to this, the graph for the intuitive case shows Rabi oscillations between neighbouring waveguides and a less than full transfer of the wavefunction. The final densities of the wavefunction in the spatial modes, depends on the overall duration of the process, for the intuitive case. These are two signs that would allow to distinguish adiabatic transfer from simple tunneling.

The fact that we achieve higher transfer fidelities in this non-perfect situation compared to the results presented in Section 3.3.6 is purely due to being able to evolve more adiabatically in time than in space due to the limitations of our computer hardware.

3.3.8 Concluding Remarks

We have investigated the use of the SAP technique to transfer atomic wave-packets between neighbouring waveguides. Using an idealised system, we have first shown that the dispersion along the guide does not significantly affect the transfer probability. This was done by introducing a harmonic potential along the longitudinal axis, which allowed to refocus the wave-packet after half an oscillation period. We have then simulated the SAP process using realistic potentials created above current-carrying wires on atom chips and shown that by choosing a lower current for the central wire there is a deviation from the energetic resonance condition throughout the SAP process. We demonstrated that whilst this deviation is present the SAP process remains robust and high fidelity state transfer is still achievable. The results of this work clearly show that adiabatic transfer in the counter-intuitive setup is a viable process using experimentally realistic parameters. The counter-intuitive waveguide tunneling scheme can be clearly distinguished from the direct tunneling approach in the intuitive waveguide setup by the absence of Rabi oscillations.

3.4 SAP in Radio Frequency Dressed Potentials

Section 3.3 explored the implementation of Spatial Adiabatic Passage (SAP) of a matter wave on a three wire Atom Chip. A drawback to using microfabricated wires to create multi-site trapping geometries is that the number of potential minima created is equal to or less than the number of wires used. Nonetheless multi-wire Atom Chips have been shown to be potential platforms for the realisation of SAP [116] and quantum gates [117] for quantum information processing. Designing and producing multi-site trapping geometries using carefully aligned nano-to-micrometer sized wires on Atom Chips adds complications and difficulties from an engineering and fabrication perspective. Moreover should an alternative trapping geometry be needed (if for instance a different atomic species is used) a new Atom Chip needs to be made. Whilst atom chips are perfectly feasible for cold atomic experiments, they lack versatility. This desired flexibility is found by combining oscillating radio-frequency (rf-fields) or microwave near fields with a static magnetic potential [30, 118, 119].[1]

The magnetic trapping of neutral atoms is made possible via the Zeeman effect (section 3.3.2). The static magnetic field lifts the energetic degeneracy of the magnetic substates of a hyperfine sublevel and confines weak field seeking atoms in a local potential minimum. When the energy separation between the magnetic sublevels is sufficiently large (made possible via the inclusion of an additional magnetic field) the confined state is metastable with respect to the timescale of the experiment and spin flip losses (Majorana losses) are negligible. Alternatively energetically separated spin states are coupled with an oscillating resonant rf-field which modifies the local properties of the trapping potential of the neutral atoms, thereby creating local (and temporal) control over the trapping potential.

Rf-fields have recently become one of the most versatile tools for trapping cold atoms [120, 121]. They not only allow to create standard trapping potentials [120], but can also be used to coherently manipulate matter waves [121, 122] or create complicated, non-standard trapping geometries [123–125]. Extensions of rf-field schemes to create numerous potential minima [123] via the use of a multi-mode array of rf-fields in the presence of a static inhomogeneous magnetic field creates a versatile microscopic grating potential. Using the technique outlined in [123] a high degree of control over the spatial shape of the potential grating is achievable, allowing for irregular patterns and grating spacings with a very small lattice constant to be created. Moreover by adjusting the frequencies of the multi-mode rf-fields, temporal control over the potential grating is possible. These aspects of multi-mode rf-dressed potentials collectively indicate that

[1] The work in this section was done in collaboration with Tadhg Morgan.

they are an ideal candidate for the coherent transport of single atoms and Bose-Einstein Condensates (BECs) using the SAP protocol. Additionally, they also have very localised resonances, therefore changing each local potential has only a very small effect on the neighbouring one, making it easier to fulfill the resonance condition.

In this section we investigate the feasibility of multi-mode rf-dressed potentials for the experimental implementation of SAP for single atoms and BECs in the low interaction regime. We propose a simple experimental setup that fulfills all necessary conditions to observe SAP for cold atoms. We will also show that our setup offers the possibility for extending adiabatic techniques to clouds of interacting atoms. The presence of interactions between atoms introduces non-linearities into the system [126] which have been shown to inhibit the effectiveness of SAP in transporting atoms [62]. Several strategies to adjust the process and to allow transport in the presence of these non-linear interactions have been suggested, for example a fixed detuning between the potential wells [76]. Here we will show that dynamically controlling the detuning between the potentials provides a marked improvement in the state transfer efficiency over both regular and fixed detuning SAP.

In section 3.4.1 we outline the theoretical description of rf-trapping and describe the system needed for SAP. In section 3.4.4 we demonstrate atomic transport in this system and show that the process allows high fidelity atomic transport in contrast to the intuitive method, which fails. In section 3.4.5 we examine the transport of an interacting atomic cloud and how the presence of non-linear interaction can be compensated for by dynamic detuning. Finally we conclude.

3.4.1 Atom Trapping Via Radio Frequency Radiation

A static inhomogeneous magnetic field splits the energetic degeneracy of the magnetic sublevels of the atom (known as the Zeeman effect, section 3.3.2), which allows the possibility to confine the atom at the magnetic field minimum. Radio frequency radiation couples the magnetic sublevels of the atom in the presence of an inhomogeneous magnetic field [120–123, 127], which modifies the local properties of the potential felt by the atom. The presence of the inhomogeneous magnetic field means that the potential may be addressed spatially selectively, which is the distinct advantage offered by rf-dressed potentials.

In the semi-classical approach, the oscillating rf-field is treated as a classical light field whereas the magnetic sublevels of the atom are quantised. As we will show, only the magnetic component of the rf-field perpendicular to the static magnetic field contributes to the resulting atom's confining potential. The procedure is as follows; the magnetic

field is split into its static and rf components respectively as,

$$\mathbf{B}(t) \;=\; \mathbf{B}_{\rm s} + \mathbf{B}_{\rm rf}(t). \tag{3.63}$$

where $\mathbf{B}_{\rm s}$ is aligned along the $\hat{z}$ direction, $\mathbf{B}_{\rm s}\cdot\hat{z} = B_z^{\rm s}\hat{z}$. The magnetic field due to the oscillating rf-field is split into its contributions in each of the three spatial directions as,

$$\mathbf{B}_{\rm rf}(t) \;=\; \mathbf{B}_{\rm rf}\cos\,\omega_{\rm rf}t \;=\; B_x^{\rm rf}\cos\omega_{\rm rf}t\;\hat{x} \;+\; B_y^{\rm rf}\cos\omega_{\rm rf}t\;\hat{y} \;+\; B_z^{\rm rf}\cos\omega_{\rm rf}t\;\hat{z}, \tag{3.64}$$

where $\omega_{\rm rf}$ is the frequency of the rf-field, and $B_{x,y,z}^{\rm rf}$ is the magnitude of the magnetic component of the rf-field in the different spatial directions.

From equation (3.48), the total time averaged magnetic moment of the atom is $\langle\boldsymbol{\mu}\rangle = \mu_B g_f \mathbf{F}/\hbar$, where μ_B is the Bohr magneton, and g_f is the Landé g-factor. The interaction Hamiltonian, between the atom and the magnetic field, is then given by

$$\mathbf{V}_I(t) \;=\; \frac{\mu_B g_f}{\hbar}\mathbf{F}\cdot\left[\;\mathbf{B}_{\rm s} + \mathbf{B}_{\rm rf}(t)\;\right]. \tag{3.65}$$

Here $\mathbf{F}$ is the total angular momentum of the atom (3.45). This operator may be decomposed into its components in the different spatial directions as,

$$F_x \;=\; \hbar\begin{pmatrix}0&1&0\\1&0&1\\0&1&0\end{pmatrix};\;\; F_y \;=\; \frac{\hbar}{\imath\sqrt{2}}\begin{pmatrix}0&1&0\\-1&0&1\\0&-1&0\end{pmatrix};\;\; F_z \;=\; \hbar\begin{pmatrix}1&0&0\\0&0&0\\0&0&-1\end{pmatrix}. \tag{3.66}$$

The time evolution of a quantum state, according to the Hamiltonian (3.65), is described in the interaction picture as,

$$\imath\hbar\frac{d}{dt}|\Psi(t)\rangle_I \;=\; \mathbf{V}_I(t)|\Psi(t)\rangle_I. \tag{3.67}$$

The temporal evolution of the quantum state is evaluated by moving to the rotating frame via the unitary rotation operator,

$$\begin{aligned}|\Psi(t)\rangle_R \;&=\; \mathbf{U}_z(t)|\Psi(t)\rangle_I,\\ \mathbf{U}_z(t) \;&=\; \exp\left(\imath\omega_{\rm rf}tF_z/\hbar\right).\end{aligned} \tag{3.68}$$

Making use of the rotated basis (3.68), equation (3.67) becomes,

$$\imath\hbar\frac{d}{dt}|\Psi(t)\rangle_R \;=\; \left[\mathbf{U}_z(t)\mathbf{V}_I(t)\mathbf{U}_z^\dagger(t) - \imath\hbar\mathbf{U}_z(t)\frac{d}{dt}\mathbf{U}_z^\dagger(t)\right]|\Psi(t)\rangle_R. \tag{3.69}$$

The second term on the right hand side readily simplifies to, $-\imath\hbar\mathbf{U}_z(t)\frac{d}{dt}\mathbf{U}_z^\dagger(t) = -\omega_{\rm rf}F_z$. The first term, however, requires some development. We expand this term according to

(3.65) and (3.66).

$$\mathbf{U}_z(t)\mathbf{V}_I(t)\mathbf{U}_z^\dagger(t) = \frac{\mu_B g_f}{\hbar}\mathbf{U}_z(t)\big[F_z B_z^{\mathrm{s}} + F_x B_x^{\mathrm{rf}}(t) + F_y B_y^{\mathrm{rf}}(t) + F_z B_z^{\mathrm{rf}}(t)\big]\mathbf{U}_z^\dagger(t). \quad (3.70)$$

The first component of the above is the energy associated with the splitting of the magnetic sublevels according to the Zeeman effect (section 3.3.2). The following three terms describe the coupling between the magnetic sublevels which drives the transitions between the different states, the last of which may be neglected since, $|\mu_B m_f g_f B_z^{\mathrm{rf}}/\hbar| \ll \omega_{\mathrm{rf}}$. This approximation is justified under the assumption that the Larmour frequency, associated with the rf-field, is much smaller than the frequency of the field itself. It follows that (3.70) simplifies as,

$$\mathbf{U}_z(t)\mathbf{V}_I(t)\mathbf{U}_z^\dagger(t) \;\simeq\; \frac{\mu_B g_f}{\hbar}\big[F_z B_z^{\mathrm{s}} + \mathbf{U}_z(t)F_x\mathbf{U}_z^\dagger(t)B_x^{\mathrm{rf}}(t) + \mathbf{U}_z(t)F_y\mathbf{U}_z^\dagger(t)B_y^{\mathrm{rf}}(t)\big]. \quad (3.71)$$

At this point it is prudent to make use of the Baker-Campbell-Hausdorff (BCH) formula. For operators A and B, the statement of the BCH formula is as follows,

$$e^{\imath\lambda B}\, A\, e^{-\imath\lambda B} \;=\; A + \imath\lambda[B,A] + \frac{\imath^2\lambda^2}{2!}[B,[B,A]] + \frac{\imath^3\lambda^3}{3!}[B,[B,[B,A]]] + \ldots, \quad (3.72)$$

We recognise that the commutators of (3.66) satisfy,

$$[F_i, F_j] \;=\; \imath\hbar\epsilon_{ijk}F_k, \quad (3.73)$$

where $\epsilon_{ijk} = 1$ for an even permutation, and $\epsilon_{ijk} = -1$ for an odd permutation. From the above it can easily be shown that (see Appendix A.5),

$$\mathbf{U}_z(t)F_x\mathbf{U}_z^\dagger(t) \;=\; F_x\cos\omega_{\mathrm{rf}}t - F_y\sin\omega_{\mathrm{rf}}t, \quad (3.74a)$$

$$\mathbf{U}_z(t)F_y\mathbf{U}_z^\dagger(t) \;=\; F_y\cos\omega_{\mathrm{rf}}t + F_x\sin\omega_{\mathrm{rf}}t. \quad (3.74b)$$

The ladder (raising and lowering) operators are defined in terms of the x and y components of the total angular momentum operator as,

$$F_\pm \;=\; F_x \pm \imath F_y. \quad (3.75)$$

We make use of the ladder operators to express (3.74) as,

$$\mathbf{U}_z(t)F_x\mathbf{U}_z^\dagger(t) \;=\; \frac{1}{2}\left(F_+ e^{\imath\omega_{\mathrm{rf}}t} + F_- e^{-\imath\omega_{\mathrm{rf}}t}\right), \quad (3.76a)$$

$$\mathbf{U}_z(t)F_y\mathbf{U}_z^\dagger(t) \;=\; \frac{\imath}{2}\left(F_- e^{\imath\omega_{\mathrm{rf}}t} - F_+ e^{-\imath\omega_{\mathrm{rf}}t}\right). \quad (3.76b)$$

It is useful to write these terms using the ladder operators since their eigenvalues are easily determined. We detail this calculation in section 3.4.2. We may now write (3.71)

in the following form;

$$\begin{aligned}\mathbf{U}_z(t)\mathbf{V}_I(t)\mathbf{U}_z^\dagger(t) &= \frac{\mu_B g_f}{\hbar}\Bigg[F_z B_z^{\rm s} + \frac{B_x^{\rm rf}}{4}\left(F_+ e^{\imath\omega_{\rm rf}t} + F_- e^{-\imath\omega_{\rm rf}t}\right)\left(e^{\imath\omega_{\rm rf}t} + e^{-\imath\omega_{\rm rf}t}\right) \\ &\qquad + \frac{\imath B_y^{\rm rf}}{4}\left(F_- e^{\imath\omega_{\rm rf}t} - F_+ e^{-\imath\omega_{\rm rf}t}\right)\left(e^{\imath\omega_{\rm rf}t} + e^{-\imath\omega_{\rm rf}t}\right)\Bigg], \\ &= \frac{\mu_B g_f}{\hbar}\Bigg[F_z B_z^{\rm s} + \frac{B_x^{\rm rf}F_+}{4}\left(1 + e^{2\imath\omega_{\rm rf}t}\right) + \frac{B_x^{\rm rf}F_-}{4}\left(1 + e^{-2\imath\omega_{\rm rf}t}\right) \\ &\qquad + \frac{\imath B_y^{\rm rf}F_+}{4}\left(1 + e^{2\imath\omega_{\rm rf}t}\right) + \frac{\imath B_y^{\rm rf}F_-}{4}\left(1 + e^{-2\imath\omega_{\rm rf}t}\right)\Bigg].\end{aligned} \tag{3.77}$$

It is usual at this point to employ the rotating wave approximation by neglecting the contributions from the $e^{\pm 2\imath\omega_{\rm rf}t}$ terms. This approximation is justified as over long time scales the contributions from these terms effectively average out to zero. We define $\mathbf{H}_R \equiv \mathbf{U}_z(t)\mathbf{V}_I(t)\mathbf{U}_z^\dagger(t) - \imath\hbar\mathbf{U}_z(t)\frac{d}{dt}\mathbf{U}_z^\dagger(t)$ to write the Hamiltonian in the rotated basis as,

$$\mathbf{H}_R = \frac{\mu_B g_f}{\hbar}\left[F_z\left(B_z^{\rm s} - \frac{\hbar\omega_{\rm rf}}{\mu_B g_f}\right) + \frac{F_+}{4}\left(B_x^{\rm rf} - \imath B_y^{\rm rf}\right) + \frac{F_-}{4}\left(B_x^{\rm rf} + \imath B_y^{\rm rf}\right)\right]. \tag{3.78}$$

3.4.2 Landau-Zener Hamiltonian

The ladder operators (3.75) operate on the quantum state in the uncoupled $|f, m_f\rangle$ basis, and satisfy the eigenvalue equation $F_\pm|f, m_f\rangle = c^\pm_{f,m_f}|f, m_f \pm 1\rangle$. The eigenvalues $c^\pm_{f,m_f}$ are known as the Clebsch-Gordan coefficients. Here we evaluate these coefficients to arrive at the Landau-Zener Hamiltonian. To begin we recognise that $F_\pm^\dagger F_\pm = F_x^2 + F_y^2 + \imath[F_x, F_y]$, and since $\mathbf{F}\cdot\mathbf{F} = \mathbf{F}^2 = F_x^2 + F_y^2 + F_z^2$, then

$$F_\pm^\dagger F_\pm = \mathbf{F}^2 - F_z^2 \mp \hbar F_z. \tag{3.79}$$

The total angular momentum operator $\mathbf{F}$, and its component in the $\hat{z}$ direction F_z, satisfy the eigenvalue equations, $\mathbf{F}^2|f, m_f\rangle = f(f+1)|f, m_f\rangle$ and $F_z|f, m_f\rangle = \hbar m_f|f, m_f\rangle$, respectively. The Clebsch-Gordan coefficients are given by the projection of $|f, m_f\rangle$ on both sides of (3.79) as $\left|c^\pm_{f,m_f}\right|^2 = \langle f, m_f|F_\pm^\dagger F_\pm|f, m_f\rangle$, with

$$c^\pm_{f,m_f} = \hbar\sqrt{f(f+1) - m_f(m_f \pm 1)}. \tag{3.80}$$

Consider a hyperfine atomic ground state, with total spin $f = \frac{1}{2}$. In the presence of the magnetic field the two hyperfine sublevels $m_f = \frac{1}{2}$ and $m_f' = -\frac{1}{2}$ are split by an amount $\mu_B g_f m_f B_{\rm s}$, where g_f is the atomic g-factor of the hyperfine level and μ_B is the Bohr magneton. Irradiating such a system with a linearly polarized radio frequency, $\mathbf{B}_{\rm rf}\cos(\omega_{\rm rf}t)$, couples the sublevels $|\frac{1}{2}, \frac{1}{2}\rangle \leftrightarrow |\frac{1}{2}, -\frac{1}{2}\rangle$ with spatial resolution due to the

spatial dependence of the magnetic field. Here we will concentrate on a one dimensional description of such a process, which is valid when the radio frequency and magnetic field are orthogonal to each other. Assuming the inhomogeneous magnetic field to be oriented in the $\hat{z}$-direction, $B_z^{\rm s} \equiv B_{\rm s}(z)$, the Hamiltonian (known as the Landau-Zener Hamiltonian) of the coupled system can be written as,

$$\mathbf{H}_R(z) \;=\; \frac{1}{2}\begin{pmatrix} \mu_B g_f B_{\rm s}(z) - \hbar\omega_{\rm rf} & \hbar\Lambda \\ \hbar\Lambda & -\mu_B g_f B_{\rm s}(z) + \hbar\omega_{\rm rf} \end{pmatrix}. \tag{3.81}$$

Given that the absolute value of the interaction term alone contributes to the dynamics of the quantum state, we define (alternatively see [123, 128]),

$$\hbar\Lambda \;=\; \frac{\mu_B g_f}{2}\left| c^{+}_{f,m_f}\left(B_x^{\rm rf} - \imath B_y^{\rm rf}\right) + c^{-}_{f,m_f}\left(B_x^{\rm rf} + \imath B_y^{\rm rf}\right)\right|. \tag{3.82}$$

The eigenvalues of this Hamiltonian are,

$$E_{\pm}(z) = \pm\frac{1}{2}\sqrt{\hbar^2\Lambda^2 + [\mu_B g_f B_{\rm s}(z) - \hbar\omega_{\rm rf}]^2}\,, \tag{3.83}$$

$$\approx \pm\frac{1}{2}[\mu_B g_f B_{\rm s}(z) - \hbar\omega_{\rm rf}] \pm \frac{\hbar^2\Lambda^2}{4[\mu_B g_f B_{\rm s}(z) - \hbar\omega_{\rm rf}]}\,, \tag{3.84}$$

where the second expression is valid far from the resonance, $\hbar\Lambda \ll [\mu_B g_f B_{\rm s}(z) - \hbar\omega_{\rm rf}]$. The second term in the expression can be viewed as a Stark shift on the energy levels.

3.4.3 Multimode Radio Frequency Arrays

To create a multi-well potential it is necessary to use several frequencies and the above analysis will become significantly more complicated. However, if we assume that the individual frequencies are spaced sufficiently far apart and have low Rabi frequencies with respect to the detuning, we can approximate the dynamics locally by considering only the nearest resonance frequency, $\omega_{\rm rf}(z) = \omega^{\rm rf}_{n(z)}$ [123]. Formally this means that n is chosen such that $|\mu_B g_f B_{\rm s}(z) - \hbar\omega^{\rm rf}_{n(z)}|$ is minimized at any position z. The effects of the combined Stark shifts, produced by the off resonant frequencies can then be summed up as [123],

$$L_n(z) = \sum_{j\neq n}\frac{\hbar^2\Lambda^2}{4[\mu_B g_f B_{\rm s}(z) - \hbar\omega^{\rm rf}_{j(z)}]}, \tag{3.85}$$

so that the eigenvalues are given by

$$E_{\pm}(z) = \pm\frac{1}{2}\sqrt{\hbar^2\Lambda^2 + [\mu_B g_f B_{\rm s}(z) - \hbar\omega_{\rm rf} + 2L_n(z)]^2}. \tag{3.86}$$

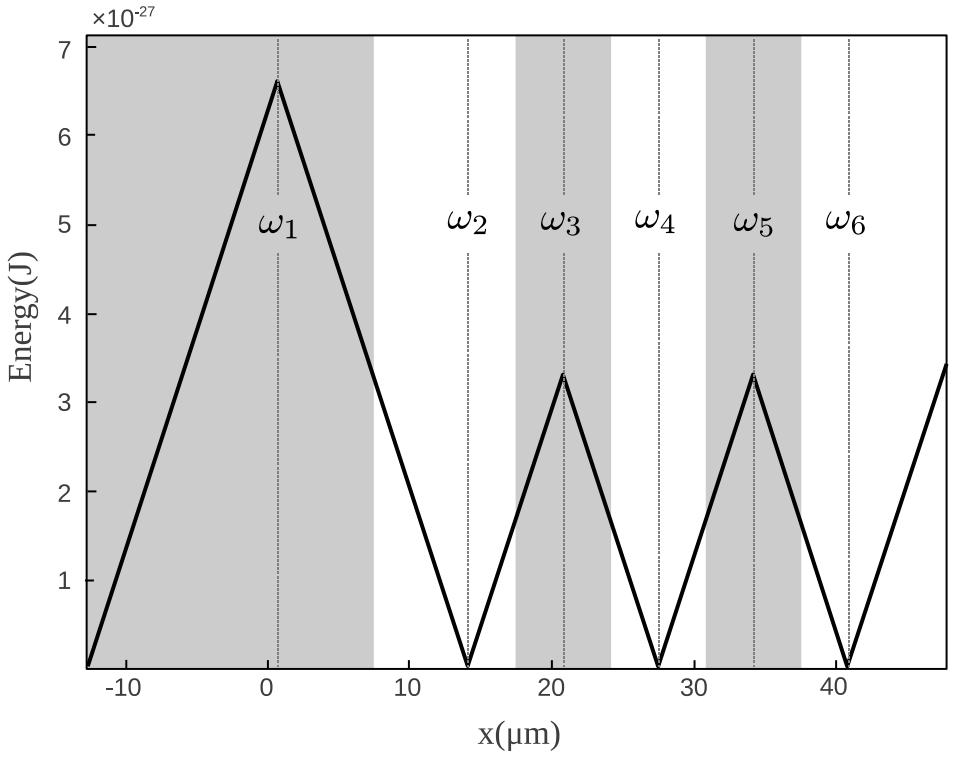


FIGURE 3.14: Trapping potential created by six radio-frequencies $\omega_1^{\mathrm{rf}} = 1000$ kHz and $\omega_n^{\mathrm{rf}} = 2\pi n \times 10000$ kHz, $n = 2:6$. Their resonance-positions are marked by the broken vertical lines and the range over which they are applied is indicated by the grey and white zones. The magnetic field gradient has the strength $b = 213$ Gcm^{-1} and $g_f = -\frac{1}{2}$ for the ^{87}Rb ground state $2S_{\frac{1}{2}}$. The Rabi frequency is chosen to be $2\pi \times 50$ kHz. The traps resemble harmonic oscillator potentials close to each minima.

From this, and considering that the couplings are strong enough to yield Landau-Zener transition probability close to unity, the resulting adiabatic potential is given by

$$V_{ad,\pm}(z) = (-1)^{n(z)} \left[E_{\pm}(z) \mp \frac{\hbar\omega_{n(z)}^{\mathrm{rf}}}{2} \right] \mp \sum_{k=1}^{n(z)-1} (-1)^k \hbar\omega_k^{\mathrm{rf}}. \tag{3.87}$$

To produce a radio frequency potential with three minima along the z-direction we will need six different radio frequencies. In the following we will assume that the 1D linear magnetic field is given by $B_{\mathrm{s}}(z) = bz$ where b is the magnetic field gradient. For convenience we choose five of the six radio frequencies to be equally spaced initially, $\omega_n^{\mathrm{rf}} = 2n\pi \times 10000$ kHz ($n = 2:6$), which produces three equidistant minima. The value of the first radio frequency ω_1^{rf} can be chosen with some liberty, as its value only controls the height of the first maximum (see figure 3.14), it can therefore be adjusted without changing the trap geometry in the area where tunneling takes place. For our potential we set $\omega_1^{\mathrm{rf}} = 1000$ kHz and in Figure 3.14 we indicate the *local* frequencies and show the resulting adiabatic potential in the positive $\hat{z}$-direction.

3.4.4 Multimode Radio Frequency SAP: Experimental Parameters

In this section we will apply the SAP procedure to a single atom trapped in a three well rf-potential. We will show that the strong decay of the influence of the radio frequencies away from their respective resonance points allows us to fulfill the resonance condition between the asymptotic eigenstates at all times during the process. While the Stark shift from neighbouring resonances cannot be neglected, it is small enough to not destroy the process.

Movement of the traps is achieved by changing the individual radio frequencies that are associated with each trap. Traditionally for SAP the middle trap is chosen to be at rest and the two outer ones are moving in and out (see also figure 3.5). Here we will choose a slightly different, but of course a completely analogous route, in that we keep the position of the left trap fixed. This allows us to keep the values of the minima equal which is essential to satisfy the condition of resonance between all traps.

In order to achieve SAP when moving the traps in this non traditional manner the approach of the right trap towards the middle must start earlier than that of the approach of the middle trap to the left. One therefore initially only changes the frequencies ω_5^{rf} and ω_6^{rf}, which determine the shape and position of the right hand side trap. After a delay τ, the two frequencies ω_3^{rf} and ω_4^{rf} are changed as well, allowing to move the middle trap towards the left. Due to the adiabatic nature of the process the exact shape of this time-dependent frequency adjustment, $f(t)$, does not matter and we can formalise this process as

$$\omega_1^{\mathrm{rf}}(t) = \omega_1^{\mathrm{rf}}(t_0), \tag{3.88a}$$

$$\omega_2^{\mathrm{rf}}(t) = \omega_2^{\mathrm{rf}}(t_0), \tag{3.88b}$$

$$\omega_3^{\mathrm{rf}}(t) = \omega_3^{\mathrm{rf}}(t_0) - \frac{1}{2} f(t-\tau)\Theta(t-\tau), \tag{3.88c}$$

$$\omega_4^{\mathrm{rf}}(t) = \omega_4^{\mathrm{rf}}(t_0) - f(t-\tau)\Theta(t-\tau), \tag{3.88d}$$

$$\omega_5^{\mathrm{rf}}(t) = \omega_5^{\mathrm{rf}}(t_0) - \frac{1}{2} f(t) - f(t-\tau)\Theta(t-\tau), \tag{3.88e}$$

$$\omega_6^{\mathrm{rf}}(t) = \omega_6^{\mathrm{rf}}(t_0) - f(t) - f(t-\tau)\Theta(t-\tau), \tag{3.88f}$$

where $\Theta(t)$ is the Heaviside step function. In figure 3.15(a) these changes are shown for the typical system considered here and the resulting movements of the trap minima are displayed in figure 3.15(b). As can been seen, the minimum of the left trap remains stationary while the other traps are moving towards and away from it. The resulting movement between neighbouring traps exactly fulfills the requirement of the

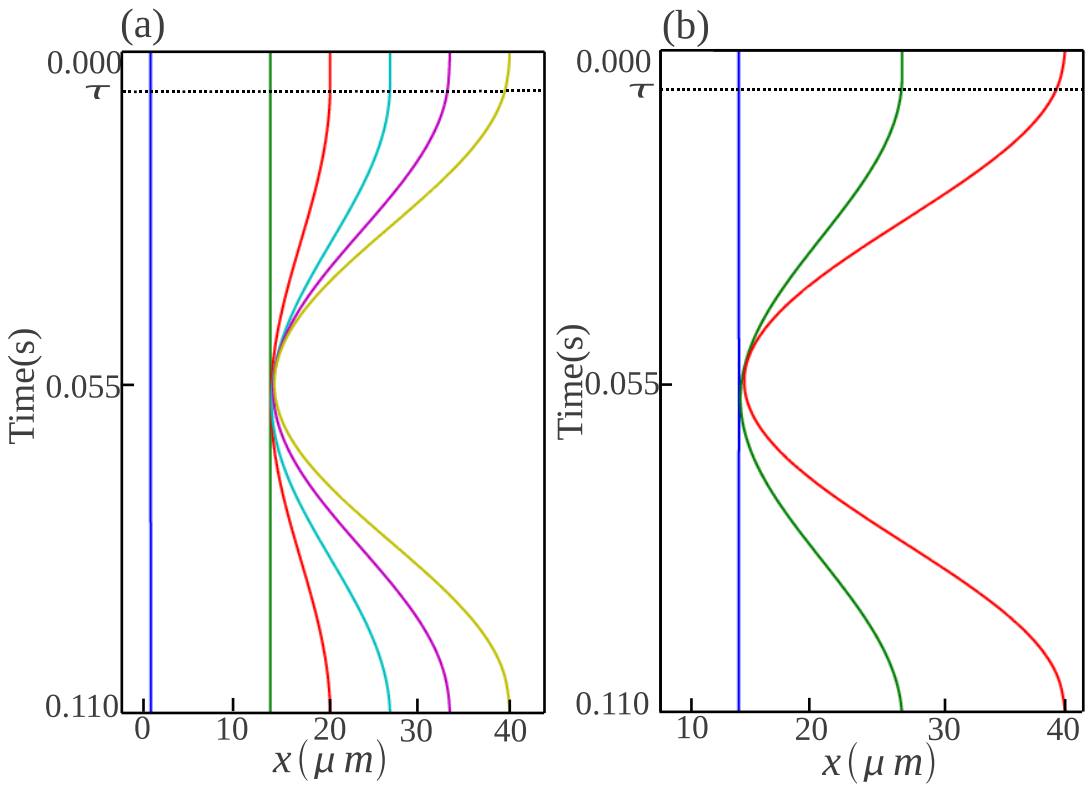


FIGURE 3.15: (a) Radiofrequencies, ω_n^{rf}, as a function of time to achieve the counter-intuitive positioning sequence. (b) Positions of the trap minima as a function of time. The left trap remains stationary while the other two traps move towards it. The delay in the movement of middle trap in comparison to the right trap ($\tau = 0.0055$ s) is indicated by the broken line.

SAP process, leading to the desired increase and decrease in the tunneling strength between initially the middle and right traps before the increase and decrease in tunneling strength between the left and middle traps.

To demonstrate adiabatic passage for single atoms and for typical experimentally realistic parameters, we will in the following show the results of numerical simulations of the full Schrödinger equation. We choose a single ^{87}Rb atom to be initially located in the center-of-mass ground state of the left trap and start the process described in eq. (3.88) with an initial separation between the radio frequencies of 10000 kHz. The minimum distance to which the frequencies approach each other is 200 kHz, which ensures that we are always in the regime of tunneling interaction, as the minimum barrier height between the individual traps is 5.3×10^{-29} J at the point of closest approach, compared to the ground state energy of 1.4×10^{-29} J. The form of the adjustment function $f(t)$ is taken to be a cosine and for numerical simplicity we restrict ourselves to one spatial dimension.

In figure 3.16 we show the probability density function with respect to time for the SAP process. The overall time for this process is chosen to be $T = 0.11s$ which is large compared to the approximate harmonic oscillator frequency of the individual traps of $\omega_{\mathrm{HO}}^{-1} \approx 4 \times 10^{-6}$ s, and we are therefore assured to be at all times in the dark eigenstate of the system. This can also be seen from the fact that the probability for being in the middle trap at any time is zero. The process leads to high fidelity population transfer and an absence of Rabi oscillations.

To compare the above situation to a process in which direct tunneling between two neighbouring traps plays an important role, we show in figure 3.17 the results of the same process, this time however using an intuitive trap-movement. The direct tunneling is clearly manifest in the appearance of Rabi oscillations between the traps and the process therefore does not deliver the required robust population transfer. In fact, the final state becomes highly susceptible to variations of the system parameters [129].

We have confirmed that these results are representative for a large range of parameters, making rf-traps ideal systems to investigate adiabatic processes in all generality.

3.4.5 Non-linear Systems

The extension of adiabatic methods to non-linear systems is of large importance not only to describe experimental situations, but also for the understanding of the underlying physical principles [76, 126, 130, 131]. In this section we show how SAP can be used with time-dependent potentials to coherently transport a cloud of interacting, Bose-condensed atoms. For this, we treat the adiabatic process as a series of stationary states which can be described by the time-independent Gross-Pitaevskii equation

$$\mu\Psi(x) = \left(-\frac{\hbar^2}{2m}\nabla^2 + V(x) + g_{1D}|\Psi|^2 \right) \Psi(x) \,, \tag{3.89}$$

where $V(x)$ is the external and μ the chemical potential at each respective point in time. The one-dimensional interaction strength between bosons with a three-dimensional s-wave scattering length a_s is given by and $g_{1D} = \frac{4N\hbar^2 a_s}{m a_\perp}(a_\perp - C a_s)^{-1}$ [132]. The trap width in the radial direction is given by $a_\perp$ and $C \approx 1.4603$. In the three level approximation the Hamiltonian can therefore be written as

$$H(t) = \hbar \begin{pmatrix} \hbar\xi_L + \mu_L & -\Omega_{LM}(t) & 0 \\ -\Omega_{LM}(t) & \hbar\xi_M & -\Omega_{MR}(t) \\ 0 & -\Omega_{MR}(t) & \hbar\xi_R + \mu_R \end{pmatrix} \,, \tag{3.90}$$

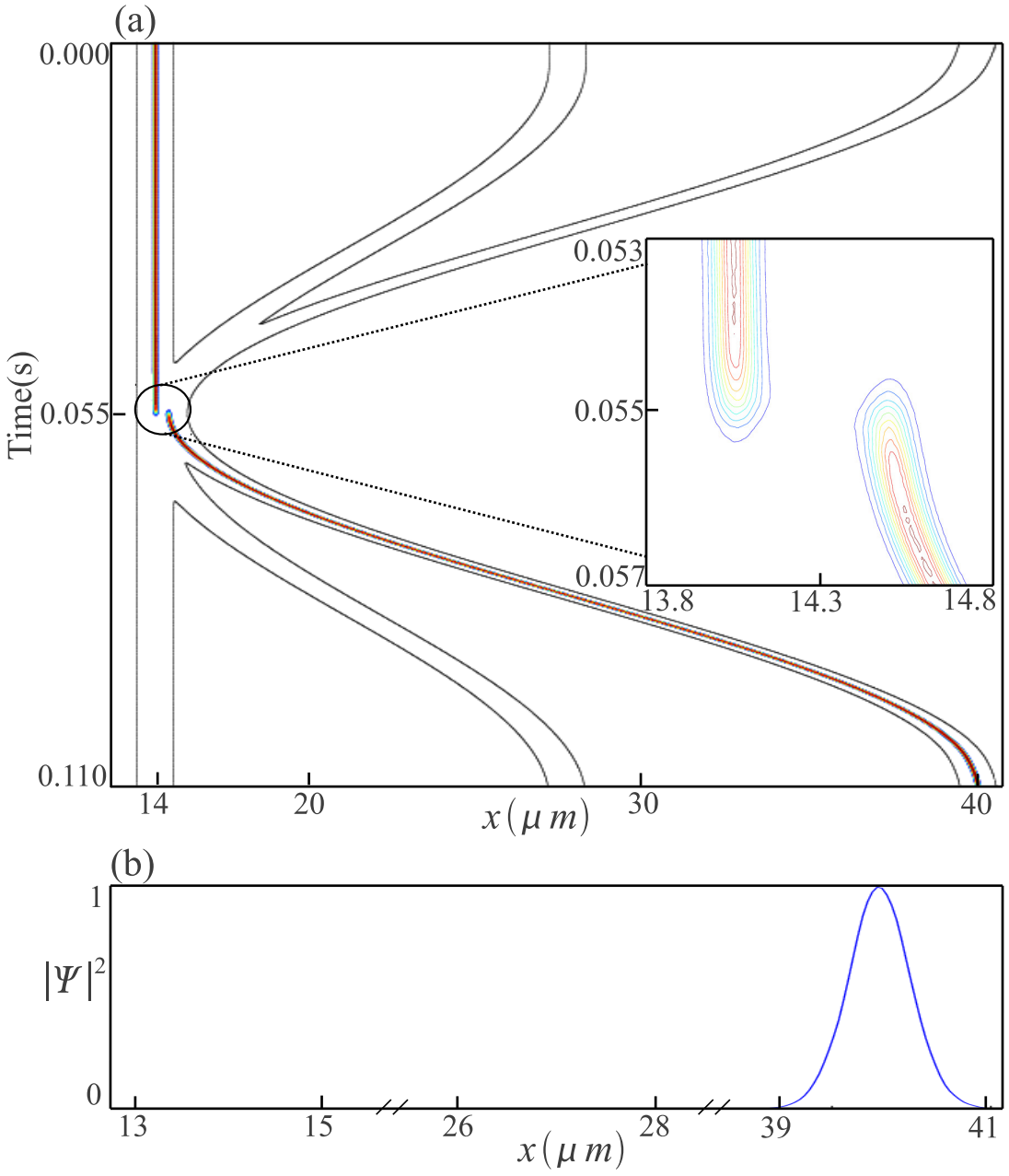


FIGURE 3.16: (a) Probability density for a single atom initially located in the trap on the left hand side with respect to time for *counter-intuitive* trap movement. The inset shows the tunneling area in greater detail. (b) Density of the final state in each of the three traps.

where $\mu_{L,R}$ are the chemical potentials associated with the atomic clouds in left or right trap and $\xi_{L,M,R}$ are the harmonic oscillator frequencies associated with the individual traps. Note that this Hamiltonian has been extensively investigated for constant couplings between the traps [126, 133]. As the particle number in each individual trap is a function of time, the chemical potentials, μ_i will change and destroy the resonances between the traps. To compensate for this we will in the following allow for the trapping

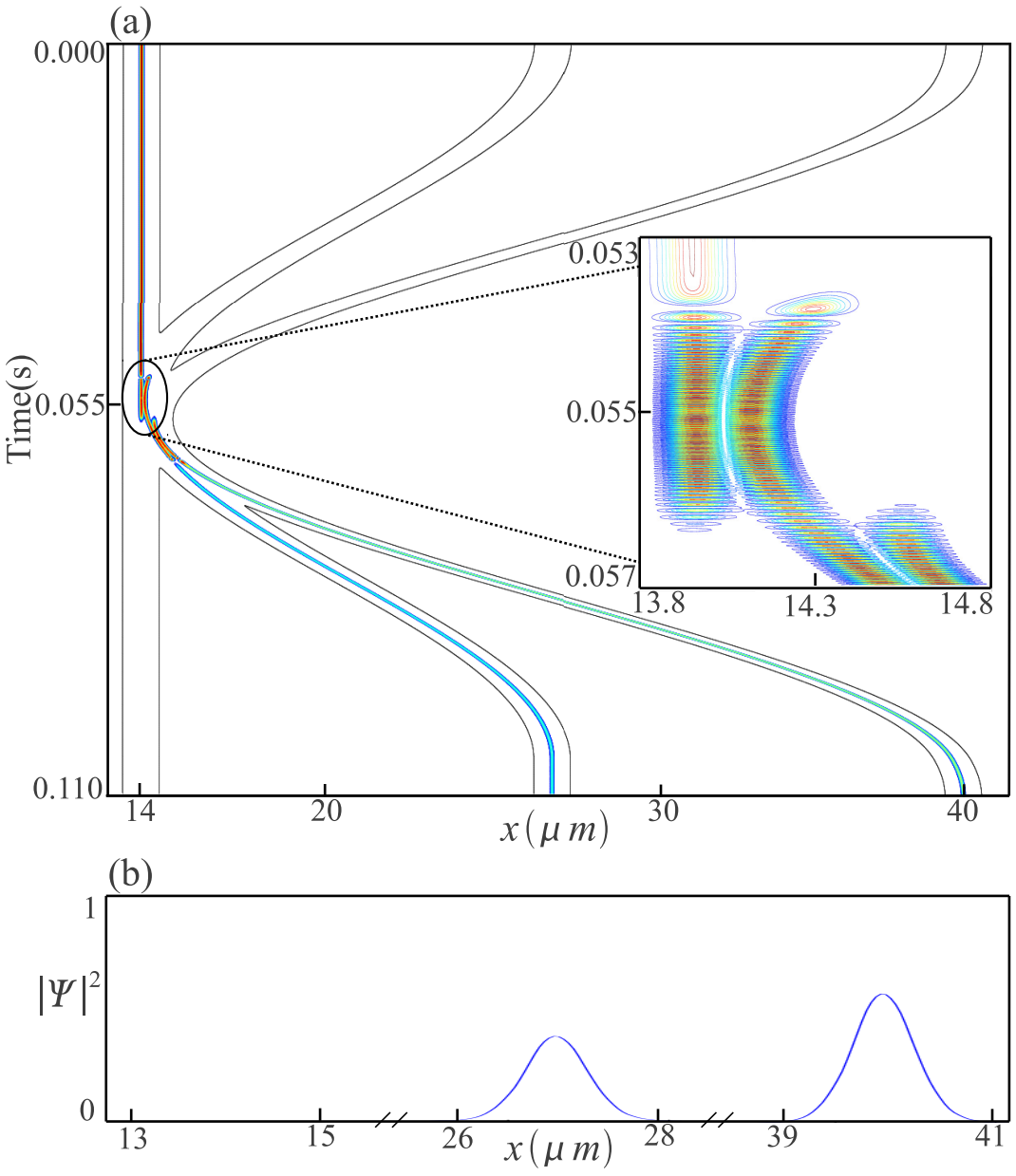


FIGURE 3.17: (a) Probability density for a single atom initially located in the trap on the left hand side with respect to time for *intuitive* trap movement. The inset shows the tunneling area in greater detail, where Rabi oscillations between neighbouring traps are clearly visible. (b) Density of the final state in each of the three traps.

frequencies to be functions of time as well. Starting with a cloud of atoms in the left trap, it is clear that the chemical potential μ_L will decrease during the process, while μ_R will increase. Adjusting the trapping frequencies $\xi_{L,R}$ can restore the resonance between the uncoupled traps by ensuring that $\hbar\xi_i + \mu_i \approx$ constant at all times. However, in order to be able to make the three state approximation, we need to make sure that $\mu_i < \hbar\xi_i$ for all values of μ_i and ξ_i. This means in practice that the process is limited to cold atomic clouds with small non-linearities.

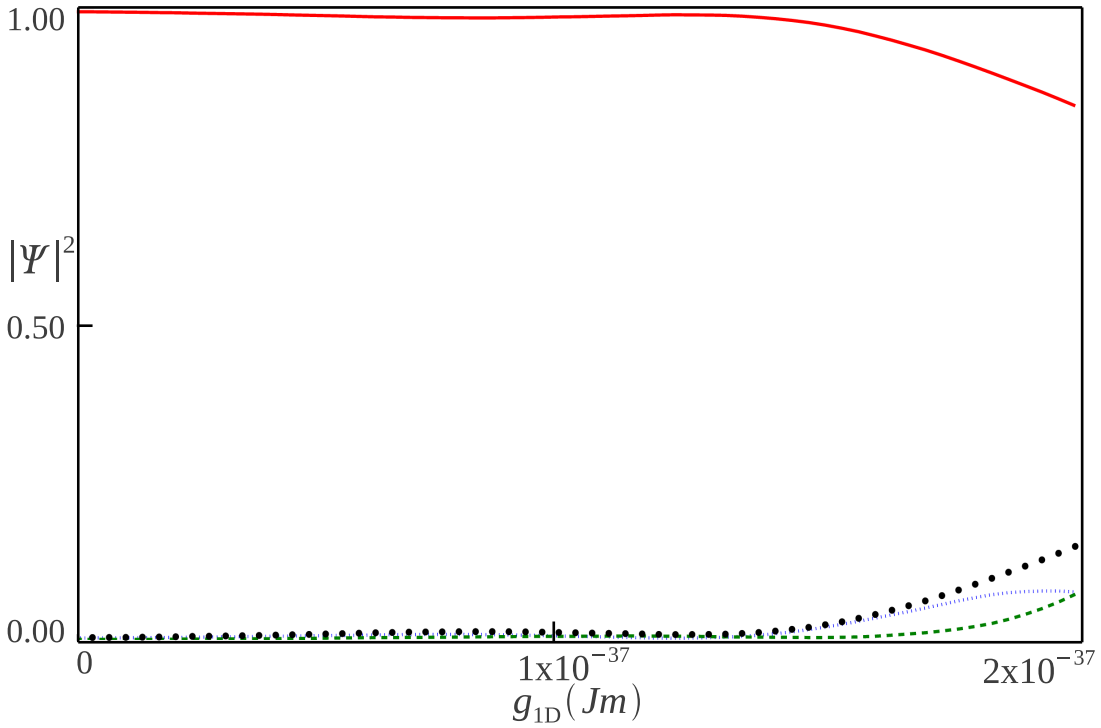


FIGURE 3.18: Final population in left (verticle dashed line, blue), middle (horizontal dashed line, green) and right (solid line, red) traps with increasing interaction strength. The dotted black line shows the total population not occupying the target (right) trap. The maximum value of g_{1D} corresponds to $\mu = 1.4318 \times 10^{-29}$ J which is smaller than $\hbar\xi_{L,M,R}$ at all times.

Using the same radio frequency potential as in the linear case, we place a cloud of interacting ^{87}Rb atoms in the ground state of the left trap by determining the solution to the Gross-Pitaevskii equation for an isolated trapping potential. To show the influence of the non-linear behaviour, we first carry out the same counter-intuitive trap movements as in the linear section *without* the time-dependent change in the trapping frequencies. In figure 3.18 we show the final populations in the individual traps as a function of increasing values for g_{1D}. It is immediately obvious that even for weak interactions the non-linear term is disruptive to the process of SAP. In fact, for $g_{1D} = 2 \times 10^{-37}$ Jm the state transfer efficiency is reduced to 84%. Choosing a typical radial trap width of 130 nm, this value of g_{1D} corresponds to $N = 2$ for ^{87}Rb.

As outlined above, to restore resonance in the presence of a changing chemical potential we must adjust the trapping frequency so that at any point in time $\hbar\xi_L(t) + \mu_L(t) = \hbar\xi_M = \hbar\xi_R(t) + \mu_R(t)$. However, determining the required adjustments is not a simple exercise for at least two reasons. First, the density dependence of the chemical potential will prevent this change from simply being linear in time and, secondly, a conceptual difficulty in determining the individual chemical potentials arises when the traps are

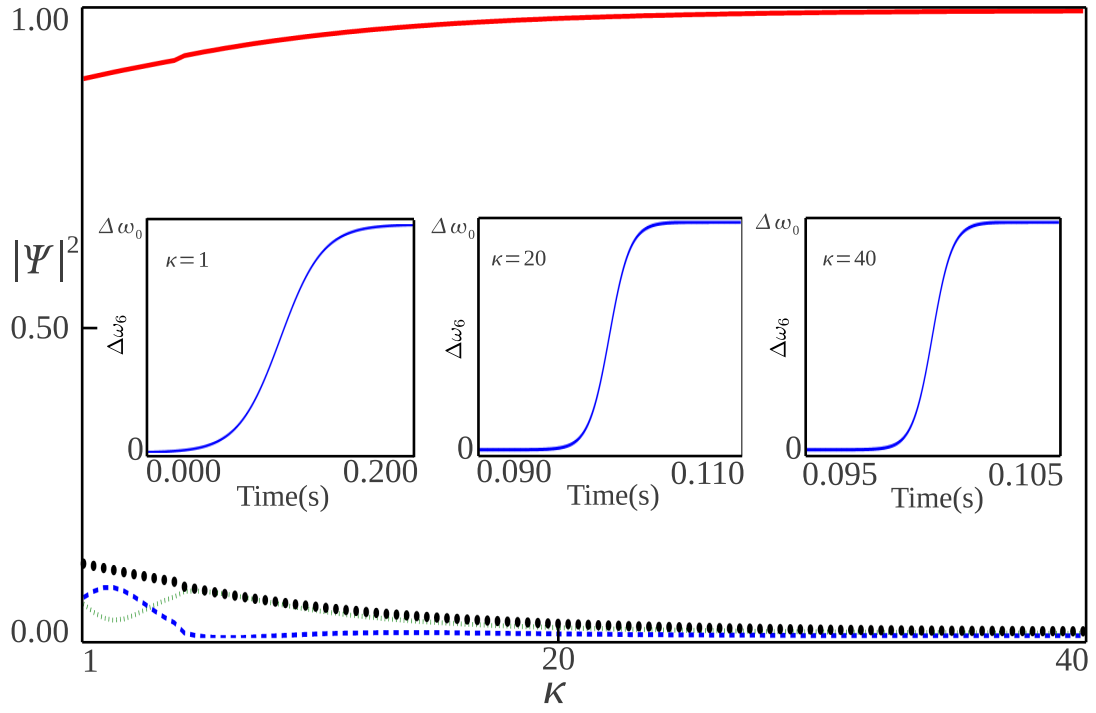


FIGURE 3.19: Final population in left (horizontal dashed blue line), middle (verticle dashed green line) and right (solid red line) traps for non-linear SAP with increasing κ and $\Delta\omega_0^{\mathrm{rf}} = 1.5$ kHz, and $g_{1D} = 2 \times 10^{-37}$ Jm. The dotted black line shows the total population not occupying the target (right) trap. The insets show the shape of $\Delta\omega_6^{\mathrm{rf}}(\kappa;\tilde{t})$ for different values of κ. An increased value of κ increases the time when the adjustment begins and decreases the adjustment time.

close together. While one could try to calculate the chemical potential, and therefore the on-site energies, in all traps at all times to a good approximation, this is certainly not experimentally possible. In the following, we therefore suggest a simple functional form for dynamically detuning the outer traps and we show that it allows us to achieve significantly higher transfer than possible without adjustments. A similar idea, however without time-dependence, was recently proposed by Graefe *et al.* [76], who showed that by detuning the left and the right trap by the same fixed amount throughout the process an improved transfer of population can be achieved.

The outline of our scheme for dynamic detuning is as follows. Initially the cloud is trapped in the left trap which we detune such that resonance with the eigenstates of the other two traps is ensured (since the traps are far apart, it is possible to determine the chemical potential μ_L). As we time evolve the system tunneling sets in and we begin to reduce the detuning on the left trap to zero while increasing the detuning of the right trap, as atoms enter it. This can be achieved by adjusting the radio frequencies ω_2^{rf} and ω_6^{rf}, associated with the left and right hand side trap, respectively. Here we suggest that

a good form of function for the adjustment related to the left hand side trap is

$$\Delta\omega_2^{\mathrm{rf}}(\kappa;\tilde{t}) = \frac{1}{2}[1-\tanh(\kappa\tilde{t})]\Delta\omega_0^{\mathrm{rf}}\,, \tag{3.91}$$

where the initial value for the change in ω_2^{rf} is given by ω_0^{rf}. The function runs between $\Delta\omega_0^{\mathrm{rf}}$ and 0 and the steepness in the crossover region is determined by κ. This gives us an effective handle on both, the time when the adjustment starts, and the duration of the adjustment (see inset of figure 3.19). Here $\tilde{t} = t - T/2$, with T being the overall duration of the process. At the same time the frequency of the right hand side trap needs to be adjusted as well and it is easy to see that a mirror symmetric change in ω_6^{rf} is the best choice.

$$\Delta\omega_6^{\mathrm{rf}}(\kappa;\tilde{t}) = \frac{1}{2}[1+\tanh(\kappa\tilde{t})]\Delta\omega_0^{\mathrm{rf}}\,, \tag{3.92}$$

The dynamic adjustments of the radio frequency equations (3.88) then become

$$\omega_1^{\mathrm{rf}}(t) = \omega_1^{\mathrm{rf}}(t_0), \tag{3.93a}$$
$$\omega_2^{\mathrm{rf}}(t) = \omega_2^{\mathrm{rf}}(t_0) - \Delta\omega_2(\kappa,\tilde{t}), \tag{3.93b}$$
$$\omega_3^{\mathrm{rf}}(t) = \omega_3^{\mathrm{rf}}(t_0) - \frac{1}{2}f(t-\tau)\Theta(t-\tau), \tag{3.93c}$$
$$\omega_4^{\mathrm{rf}}(t) = \omega_4^{\mathrm{rf}}(t_0) - f(t-\tau)\Theta(t-\tau), \tag{3.93d}$$
$$\omega_5^{\mathrm{rf}}(t) = \omega_5^{\mathrm{rf}}(t_0) - \frac{1}{2}f(t) - f(t-\tau)\Theta(t-\tau), \tag{3.93e}$$
$$\omega_6^{\mathrm{rf}}(t) = \omega_6^{\mathrm{rf}}(t_0) - f(t) - f(t-\tau)\Theta(t-\tau) + \Delta\omega_6^{\mathrm{rf}}(\kappa,\tilde{t})\,. \tag{3.93f}$$

In figure 3.19 we show the final population transferred to the right trap for increasing values of κ and for $\Delta\omega_0^{\mathrm{rf}} = 1.5$ kHz. We can see that the dynamic adjustment of the detunings of the outer traps allows us to achieve population transfer of $> 99\%$, up from 84%. This is an improvement over both standard SAP and fixed detuning in the weak interaction regime and, in fact, returns to the transfer efficiency of single particle SAP.

3.4.6 Concluding Remarks

We have shown that radio frequency traps can be used as microtraps for processes in which an adjustable tunneling strength is required. Neighbouring trapping potentials can be overlapped without significantly changing the underlying energy level structure. This property has allowed us to create a triple well radio frequency potential in which coherent transport using adiabatic passage can be demonstrated. For a single atom, it was shown that complete transfer between the left and right traps by utilizing the

dark state of the system is possible, maintaining the advantages of the absence of Rabi oscillations and robustness against variation in system parameters.

For a cloud of weakly interacting atoms we have demonstrated a technique that significantly improves the efficiency of SAP by dynamically detuning the outer traps. Our suggested setup is close to experimental realities, avoids the large overhead of other suggestions and can easily be extended to other adiabatic techniques.

Chapter 4

Spatial Mode Dynamics

In chapter 3 we provided the theoretical outline of Stimulated Raman Adiabatic Passage and its matter wave counterpart Spatial Adiabatic Passage (SAP). Therein we proposed two novel schemes to experimentally realise SAP. In both, the relationship between the 3×3 spatial mode Hamiltonian and the numerical integration of Schrödinger equation (via the split operator method, appendix B.1) was not explored in detail. Whilst the tunneling interaction is built into the numerical integration of Schrödinger's equation, when we move to the spatial representation, the tunneling interaction is effectively inserted by hand to the 3×3 spatial mode Hamiltonian. Although the spatial mode Hamiltonian is a useful model for the conceptual understanding of the underlying physics, a deeper insight can be gained by establishing the relationship between the operators in both representations.[1]

In this chapter we investigate in detail the relationship between the evolution of a quantum state in both the spatial mode, and energetic mode representations. To do so, we first consider a quantum state occupying two energetic modes of the Hilbert space, whose evolution is described by the energetic mode Hamiltonian matrix. Thereafter we move to the spatial representation, wherein the chosen quantum state occupies two spatial modes, and its evolution is described by the spatial mode Hamiltonian matrix. By equating the temporal density of the quantum state in the two spatial modes according to both representations, we show how to derive a mapping between the 2×2 energetic mode Hamiltonian and the 2×2 spatial mode Hamiltonian. The work outlined in this chapter sheds further light on the nature of quantum tunneling.

Quantum tunneling is a quantum mechanical phenomenon wherein a particle may penetrate a potential barrier whose potential energy is larger than the energy of the incident

[1] The work in this chapter was done in collaboration with Nicolino Lo Gullo.

particle. When one approaches this phenomenon from the classical perspective it appears impossible. Initially we tend to think of the barrier and the incident particle as solid objects that we are familiar with on a day to day basis. This leads to a paradox of sorts whereby the whole event seems quite spooky and an apparent violation of common sense, yet it is very much a reality. Noble Laureate Ivar Giaever expressed his bemusement when first introduced to this idea, *"I didn't believe a word of it."* It was relayed to him that classically, if someone throws a tennis ball at a wall it will always bounce back, however, quantum mechanically there exists a finite probability that the ball will appear on the other side of the wall, with no hole in the wall and the ball being exactly as it had been prior to penetrating the wall.

Quantum tunneling is most commonly studied from a semi-classical perspective [14]. The semi-classical formalism of quantum tunneling has proven very successful for practical applications such as for the calculation of tunneling frequencies and the transmission and reflection coefficients for a particle incident on a potential barrier, and alpha decay. The major drawback of the semi-classical approach to the quantum tunneling phenomenon is that it leads to conceptually incorrect interpretations of the underlying physics. For the quantum double well we have two classically allowed regions separated by a classically forbidden region (the potential barrier). Over time a particle or wavepacket, localised in one potential well, 'penetrates' the potential barrier to appear in the neighbouring potential well. Habitually we tend to think of the particle and the potential barrier as localised physical objects and momentarily forget that in quantum mechanics, matter is described in terms of wavefunctions that span the entire coordinate space. The gap between the classical 'localised' description of matter and the quantum mechanical 'wave-like' description of matter is encapsulated in the measurement problem [134]. In this chapter we detail how the respective Hamiltonians describing, the evolution of the wavefunction occupying two energetic modes, and the evolution of the wavefunction occupying two spatial modes, are directly related by a rotation.

In section 4.1 we outline briefly the history of, and highlight some of the literature related to, quantum tunneling. Here, the main goal is to relate the description of the wavefunction in the spatial and energetic mode basis. To tackle this problem we first propose that the spatial and energetic Hamiltonians are related via a rotation. We deduce (section 4.1) and compare (section 4.2) how the density evolves in each spatial region to arrive at a mapping between both Hamiltonians. The mappings are subsequently analysed in section 4.2.1 using the one dimensional harmonic oscillator potential. There remains some ambiguity as to the definition of the spatial mode kets. We discuss this issue in section 4.3 and offer a possible avenue toward a solution to this problem. Finally we discuss and summarise the major results of the chapter and conclude.

4.1 Quantum Tunneling

Quantum tunneling is a phenomenon central to many aspects of quantum theory [14, 15, 135–137]. First uncovered by Fredrich Hund [138], the concept of quantum tunneling was established in 1928 when Gamow used a semiclassical approach to describe the nature of alpha decay [139], and independently by Gurney and Condon [140]. The statistical nature of alpha decay could then be interpreted as the alpha particle's probability to penetrate a classically forbidden region, spanned by a potential barrier, separating two classically allowed regions. The use of the term tunneling is derived from the fact that from a classical point of view the particle is unable to traverse the energetic barrier.

Since its inception, quantum tunneling between spatially localised modes has proven to be a natural choice when describing the dynamics of many quantum mechanical systems [14, 15, 135–137]. The most common being multi-well potentials, in which different spatial regions are separated by potential barriers. An instructive and simplified model to study quantum tunneling is the quantum double well [141–145], a schematic of which is found in figure 4.1(a). In the early studies of alpha decay, the potential used was a type of double well with one bound region and a continuum. Today the applications of the double well model are broad, ranging from the inversion phenomenon of the ammonia molecule (NH_3) and the binding energies and transition times of valence electrons in molecules [12] to radioactive decay [139, 140], from the motion of the proton in a hydrogen bond [146] and proton transfer in DNA [147–149], to ion-molecule reactions [150], and from the theory of modern superconducting quantum interference devices (SQUIDs) [151] to the quantum dynamics of single ultracold atoms in optical lattices [152], and electron transfer in quantum dots [153].

The principle difficulty in applying the double well to model the dynamics of complex systems is in determining the correct shape of the potential. However, in the area of ultracold atoms the external potentials, can, and have been, engineered to high precision [38, 124, 125, 154–157]. Such experimental advances have allowed for detailed investigation into Josephson type effects [158–161] and tunneling of Bose-Einstein condensates in the mean field regime [17, 162, 163], where the inter-atomic interactions can suppress tunneling and lead to self trapping [130, 164–167].

The so-called 'tunneling matrix element', which describes the strength of the tunneling, can be calculated using a number of known semi-classical approximation techniques, such as for example the Wentzel-Kramers-Brillouin (WKB) method [14, 15, 135–137]. These results have been extensively used for the symmetric double well, in the limit where the (left and right) trap centers are far apart [160]. Recently the WKB method has been extended to resolve for the tunneling matrix element for asymmetric double

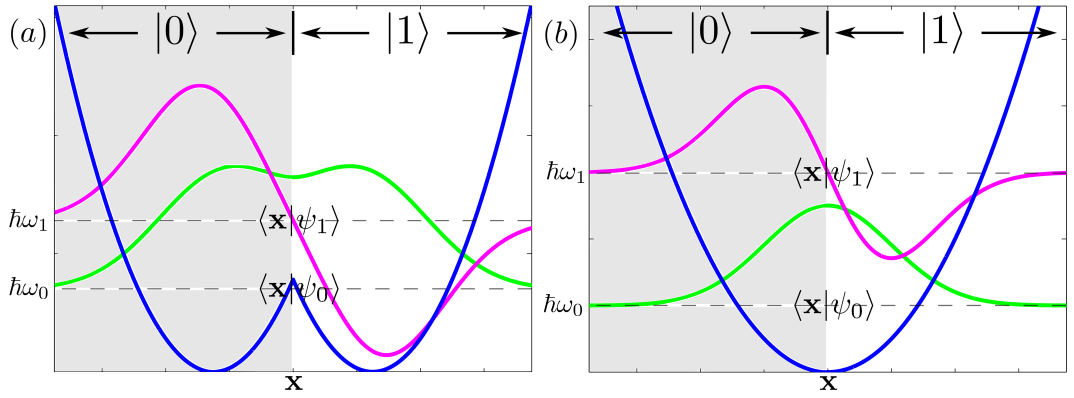


FIGURE 4.1: Schematic for (a) the double well and (b) the harmonic oscillator. Overlayed are the lowest lying symmetric $\langle \mathbf{x}|\psi_0\rangle$ and antisymmetric eigenfunctions $\langle \mathbf{x}|\psi_1\rangle$, and the spatial modes $|0\rangle$ and $|1\rangle$, with $x_b = 0$.

wells [168]. However, in order to fully describe the wavefunction in the spatial mode (or left-right) basis we are required to go beyond semi-classical approximation techniques. In this work we make a first step toward this goal by attending to the mapping between the (two-mode) spatial mode Hamiltonian, and energetic mode Hamiltonian, in terms of the overlap of the energy eigenfunctions in each spatial mode and the coefficients of the initial state.

For the double well, the 'potential barrier' is the area of the potential separating two spatial regions wherein the wavefunctions probability density may acquire local maximum. Here we use the term 'barrier' to define the separation point between two spatial regions, denoted x_b. In two dimensions the barrier is a line and in three dimensions a surface. Whilst for the double well the maximum value of the potential between its two minima is a natural choice for the barrier position x_b (as shown in figure 4.1(a)), we note that x_b can be chosen arbitrarily. Once the separation point has been chosen then it is possible to map the system into the usual left-right basis. A proper choice of the Hamiltonian in the new Hilbert space will give the same evolution of the probability densities on the left and right of x_b. Here we denote $|0\rangle$ for the left spatial mode and $|1\rangle$ for the right spatial mode.

4.1.1 Statement of the Tunneling Phenomenon

We consider a system where only the first two energetic modes $|\psi_0\rangle$ and $|\psi_1\rangle$ are occupied with energies $\hbar\omega_0$ and $\hbar\omega_1$ respectively, where $\omega_0 < \omega_1$. Our aim is to establish the relationship between the wavefunction in the energetic mode basis and the spatial mode, or the left-right $|0\rangle$-$|1\rangle$, basis that is synonymous with the double well potential. Both bases are illustrated in figure 4.1. We note that the left-right basis is not restricted to

the double well but can be applied to any potential; for example the harmonic oscillator with $x_b = 0$, shown in figure 4.1(b).

The wavefunction is expanded in the two mode energetic and spatial bases respectively as,

$$|\Psi(t)\rangle = c_0(t)|\psi_0\rangle + c_1(t)|\psi_1\rangle, \qquad \text{(Energetic Mode Basis)} \tag{4.1a}$$

$$|\Psi(t)\rangle_{\mathrm{R}} = b_0(t)|0\rangle + b_1(t)|1\rangle. \qquad \text{(Spatial Mode Basis)} \tag{4.1b}$$

where $c_\nu(t)$ and $b_\nu(t)$ are complex numbers which describe the evolution of the energetic and spatial modes respectively. The evolution of the wavefunction, in either representation, is determined by Hamiltonian of the considered basis. For the energetic basis we have $|\Psi(t)\rangle = \exp\left[-(\imath/\hbar)\mathbf{H}t\right]|\Psi(0)\rangle$, and for the spatial basis $|\Psi(t)\rangle_{\mathrm{R}} = \exp\left[-(\imath/\hbar)\mathbf{H}_{\mathrm{R}}t\right]|\Psi(0)\rangle_{\mathrm{R}}$. The subscript 'R' is used to denote the 'rotated' spatial mode basis. The energetic and spatial mode Hamiltonians are respectively given by,

$$\mathbf{H} = \begin{pmatrix} \omega_0 & 0 \\ 0 & \omega_1 \end{pmatrix}, \qquad \text{(Energetic Mode Hamiltonian Matrix)} \tag{4.2a}$$

$$\mathbf{H}_{\mathrm{R}} = \begin{pmatrix} \xi_0 & \Omega \\ \Omega & \xi_1 \end{pmatrix}. \qquad \text{(Spatial Mode Hamiltonian Matrix)} \tag{4.2b}$$

Here we note that any Hamiltonian matrix which is not diagonal can be diagonalised by rotating it into a dressed state picture and the discussion of this section applies.

The premise of this work is to establish the relationship between the energetic mode Hamiltonian (4.2a) and the spatial mode Hamiltonian (4.2b). We require to find a closed form solution for each of the matrix elements of the spatial mode Hamiltonian in terms of the known counterparts of the wavefunction in the energetic mode basis. To formally derive the mapping between the energetic and spatial Hamiltonians, it is first necessary that we determine how the density of the wavefunction evolves in both representations. We first consider the temporal density in the energetic basis (4.1a) in section 4.1.2 and then the density in the spatial basis (4.1b) in section 4.1.3.

4.1.2 Density Evolution in the Energetic Mode Basis

In Euler form the initial state is $c_\nu(0) = c_\nu e^{\imath\varphi_\nu}$. Without loss of generality we assume that our initial state is real valued up to a global phase $\varphi_1 - \varphi_0 = 0$. The time dependence

of the basis state coefficients are given by,

$$\begin{aligned} \mathbf{c}(t) &= \exp\left(-\frac{\imath}{\hbar}\mathbf{H}t\right)\mathbf{c}, \\ \begin{pmatrix} c_0(t) \\ c_1(t) \end{pmatrix} &= \exp\left(-\imath\begin{pmatrix} \omega_0 & 0 \\ 0 & \omega_1 \end{pmatrix}t\right)\begin{pmatrix} c_0 \\ c_1 \end{pmatrix}. \end{aligned} \tag{4.3}$$

Any quantum state that is not an eigenstate of the Hamiltonian exhibits a periodic modulation of its probability density in different spatial regions of the Hilbert space, which are a generalised form of the well known 'Rabi oscillations'. The rate of these Rabi oscillations depends on the difference between eigenfrequencies $\omega_1 - \omega_0$ of the occupied energetic modes. Their magnitude is dependent on both the size and location of the respective spatial regions and c_μ.

Here we focus on the mapping of the above system into the two-level spatial mode (or $|0\rangle$-$|1\rangle$) system. The probability for either of the two levels of the system to be occupied, is equal to the probability to find the atom on the left or on the right of a point x_b. In other words, at any time t, the probability for the wavefunction to be in the state $|0\rangle(|1\rangle)$ must be equal to the probability to find the atom in the corresponding spatial region $\eta = 0, 1$.

Presently of interest are the densities of the spatial regions as a function of time. We discretise the Hilbert space into two spatial modes which are allowed to have an arbitrary size which remains constant over time. If the volume of the η-th spatial region is represented by $\mathcal{V}_\eta$ ($\eta = 0, 1$), and the sum of the volume elements equal the total space, we can define the operator that projects on exactly one of these regions as,

$$\mathbf{P}_\eta = \int_{\mathcal{V}_\eta} d\mathbf{x}\, |\mathbf{x}\rangle\langle\mathbf{x}| = \sum_{\mu,\nu=0}^{\infty} \mathcal{D}^\eta_{\mu\nu} |\psi_\mu\rangle\langle\psi_\nu|, \tag{4.4}$$

where $\mathcal{D}^\eta_{\mu\nu}$ is a tensor whose elements are given by,

$$\mathcal{D}^\eta_{\mu\nu} \equiv \int_{\mathcal{V}_\eta} d\mathbf{x}\, \langle\psi_\mu|\mathbf{x}\rangle\langle\mathbf{x}|\psi_\nu\rangle. \tag{4.5}$$

By exploiting the completeness relations of the eigenfunctions $\{\psi_\mu\}$ and the fact that $\sum_\eta \mathbf{P}_\eta = \mathbb{1}$, it is easy to prove that $\mathcal{D}^\eta_{\mu\nu} = \mathcal{D}^\eta_{\nu\mu}$ and $\sum_\eta \mathcal{D}^\eta_{\mu\nu} = \delta_{\mu\nu}$, for all μ, ν. The temporal density of the quantum state (4.1a) in the spatial regions is given by $\rho_\eta(t) = \langle\Psi(t)|\mathbf{P}_\eta|\Psi(t)\rangle$ which can be written as:

$$\rho_\eta(t) = \sum_{\mu,\nu=0}^{\infty} c^*_\mu(t) c_\nu(t)\, \mathcal{D}^\eta_{\mu\nu}, \qquad \rho_\eta(t) = \mathcal{M}_\eta + \mathcal{N}_\eta \cos(\omega^-_{10} t). \tag{4.6}$$

For brevity we have defined,

$$\omega_{10}^{\pm} \equiv \omega_1 \pm \omega_0. \tag{4.7}$$

Since only c_0 and c_1 have finite values (and $c_\mu = 0$ for $\mu \geq 2$) we have defined,

$$\mathcal{M}_\eta \equiv c_0^2 \mathcal{D}_{00}^\eta + c_1^2 \mathcal{D}_{11}^\eta, \qquad \mathcal{N}_\eta \equiv 2\, c_0 c_1 \mathcal{D}_{10}^\eta. \tag{4.8}$$

Here we note $\mathcal{N}_0 = -\mathcal{N}_1$.

4.1.3 Density Evolution in the Spatial Mode Basis

As the energetic modes of the wavefunction evolve in time (according to (4.10)), the phase and amplitude of each spatial mode also evolve in time, which are described by the spatial mode coefficients $b_\eta(t)$. In the following we wish to map the temporal evolution of the system in the energy eigenbasis ($|\psi_\nu\rangle$) to the dynamics of a two level system ($|\eta\rangle$), the so-called spatial modes. The state of the latter is given by

$$|\Psi(t)\rangle_{\mathrm{R}} = b_0(t)|0\rangle + b_1(t)|1\rangle. \tag{4.9}$$

The spatial mode kets $|0\rangle$ and $|1\rangle$ are assumed to represent two non overlapping spatial regions which satisfy $\langle\eta|\eta'\rangle = \delta_{\eta\eta'}$. Presently we are not concerned with a strict definition of these kets, and we reserve a discussion of these for section 4.3. We are currently interested in the Hamiltonian $\mathbf{H}_{\mathrm{R}}$ that describes correctly the phase and amplitude evolution of the coefficients of the spatial modes $b_\eta(t)$,

$$\begin{aligned} \mathbf{b}(t) &= \exp\left(-\frac{\imath}{\hbar}\mathbf{H}_{\mathrm{R}} t\right)\mathbf{b}, \\ \begin{pmatrix} b_0(t) \\ b_1(t) \end{pmatrix} &= \exp\left(-\imath \begin{pmatrix} \xi_0 & \Omega \\ \Omega & \xi_1 \end{pmatrix} t\right) \begin{pmatrix} b_0 \\ b_1 \end{pmatrix}. \end{aligned} \tag{4.10}$$

The premise of this work is to recover a closed form solution for each of the matrix elements of the spatial mode Hamiltonian $\mathbf{H}_{\mathrm{R}}$ such that $\rho_\eta(t) = |b_\eta(t)|^2$. The frequency at which the density of the spatial modes oscillate is ω_{10}^-. Therefore it is crucial that the difference between the Hamiltonian's eigenvalues are the same in both representations. In this manner the density oscillates with the same frequency in both representations.[2]

[2] In this chapter we do not impose that energy is conserved by the rotation to the spatial representation. However, this can be easily achieved by rescaling the spatial mode Hamiltonian as, $\mathbf{H}'_{\mathrm{R}} = \mathbf{H}_{\mathrm{R}} - a\mathbb{1}$, where a is some constant equal to the energy difference of the wavefunction in both representations. In most cases, when the wavefunction is rescaled the eigenvalues of the 'new' spatial mode Hamiltonian are less than the eigenvalues of the energetic mode Hamiltonian. However, the difference between the eigenvalues remains the same, and the density dynamics are also described correctly. As the procedure is rather straightforward and of no immediate significance, we omit to detail it here.

This is easily achieved by making use of the Euler rotation matrix,

$$\mathbf{R} \;=\; \begin{pmatrix} \cos(\frac{\theta}{2}) & \sin(\frac{\theta}{2}) \\ -\sin(\frac{\theta}{2}) & \cos(\frac{\theta}{2}) \end{pmatrix}. \tag{4.11}$$

Subsequently the spatial mode Hamiltonian matrix is given by $\mathbf{H}_{\mathrm{R}} = \mathbf{R}\mathbf{H}\mathbf{R}^{\mathrm{T}}$. In addition this preserves the unitarity of the evolution in the spatial basis.

It is easy to show that the elements of the spatial mode Hamiltonian $\mathbf{H}_{\mathrm{R}}$ are given by,

$$\begin{aligned} \hbar\xi_0 \;&=\; \frac{\hbar\omega_{10}^{+}}{2} - \frac{\hbar\omega_{10}^{-}}{2}\cos(\theta), \\ \hbar\xi_1 \;&=\; \frac{\hbar\omega_{10}^{+}}{2} + \frac{\hbar\omega_{10}^{-}}{2}\cos(\theta), \\ \hbar\Omega \;&=\; \frac{\hbar\omega_{10}^{-}}{2}\sin(\theta). \end{aligned} \tag{4.12}$$

Herein we wish to resolve for those values of θ that recover the correct temporal density dynamics of the spatial regions, i.e. $|b_\eta(t)|^2 = \rho_\eta(t)$. From equations (4.10) and (4.12), the densities of the spatial modes are given by,

$$|b_0(t)|^2 \;=\; \frac{b_0^2 + (b_0\cos(\theta) - b_1\sin(\theta))^2}{2} + \frac{(b_0^2 - b_1^2)^2\sin^2(\theta) + b_0 b_1\sin(2\theta)}{2}\cos\left(\omega_{10}^{-}t\right), \tag{4.13a}$$

$$|b_1(t)|^2 \;=\; \frac{b_0^2 + (b_1\cos(\theta) + b_0\sin(\theta))^2}{2} - \frac{(b_0^2 - b_1^2)^2\sin^2(\theta) + b_0 b_1\sin(2\theta)}{2}\cos\left(\omega_{10}^{-}t\right). \tag{4.13b}$$

In the next section we compare the temporal densities of (4.6) and (4.13) to derive the formal solutions to the matrix elements of the spatial mode Hamiltonian.

4.2 Mapping the Spatial and Energetic Hamiltonians

Equating the temporal density in both pictures (equations (4.6) and (4.13)) at $t = 0$ we recover the initial densities of the state, $b_\eta^2 = \mathcal{M}_\eta + \mathcal{N}_\eta$. For all other values of t we recover a relation for the angles of rotation. As an example we compare the densities at $t = \pi/\omega_{10}^{-}$, thereby relating $|b_\eta(\pi/\omega_{10}^{-})|^2 = \rho_\eta(\pi/\omega_{10}^{-})$. From (4.10) we recover the following relation,

$$b_0\cos(\theta) + b_1\sin(\theta) \;=\; \sqrt{\mathcal{M}_0 - \mathcal{N}_0}. \tag{4.14}$$

As the angle of rotation θ may vary between 0 and 2π we solve the above equation for $\cos(\theta)$ and $\sin(\theta)$ separately. As we are equating densities we recover two independent solutions. From here we refer to them as Map A and Map B respectively.

Map A:

$$\begin{aligned}\cos(\theta) &= \pm\left(\sqrt{\mathcal{M}_1^2-\mathcal{N}_1^2}-\sqrt{\mathcal{M}_0^2-\mathcal{N}_0^2}\right),\\ \sin(\theta) &= \pm\left(\sqrt{(\mathcal{M}_0+\mathcal{N}_0)(\mathcal{M}_1-\mathcal{N}_1)}+\sqrt{(\mathcal{M}_0-\mathcal{N}_0)(\mathcal{M}_1+\mathcal{N}_1)}\right).\end{aligned} \tag{4.15}$$

Map B:

$$\begin{aligned}\cos(\theta) &= \pm\left(\sqrt{\mathcal{M}_1^2-\mathcal{N}_1^2}+\sqrt{\mathcal{M}_0^2-\mathcal{N}_0^2}\right),\\ \sin(\theta) &= \pm\left(\sqrt{(\mathcal{M}_0+\mathcal{N}_0)(\mathcal{M}_1-\mathcal{N}_1)}-\sqrt{(\mathcal{M}_0-\mathcal{N}_0)(\mathcal{M}_1+\mathcal{N}_1)}\right).\end{aligned} \tag{4.16}$$

These solutions for the angles of rotation, combined with the correctly initialised state, allow to recover the proper density dynamics for each spatial region. It is perhaps a little disconcerting that there are four solutions for the mapping of energetic and spatial Hamiltonian matrices. More correctly there are two independent sets of (two $\pm$) solutions. From studying elementary ballistics, one often finds two solutions to a problem. In certain cases there is only one physical solution and the other may be easily discarded as it is non-physical. In the following section we analyse both maps in an attempt to determine whether there are two physical solutions or just one.

4.2.1 Analysis

In what follows we analyse both sets to help to clarify whether it is plausible to discard one of the maps as non-physical and subsequently arrive at one correct mapping for the spatial and energetic modes.

From our derived solutions (4.15) and (4.16) it is obvious that there is no constraint that demands where the barrier is located. As no 'potential barrier' is necessary, and we are free to choose the barrier position 'x_b', it is convenient to use a potential whose energy eigenfunctions are known analytically. From this point of view, the one-dimensional harmonic oscillator is a natural starting point to study the matrix elements of the spatial mode Hamiltonian. This reduces the analysis as we may avoid to consider degenerate states and unusual barrier shapes in higher dimensions.

The most general state of the system is a linear superposition of the ground and first excited energy eigenstates (4.1a) where,

$$c_0 \;=\; \cos(\alpha), \qquad c_1 \;=\; \sin(\alpha). \tag{4.17}$$

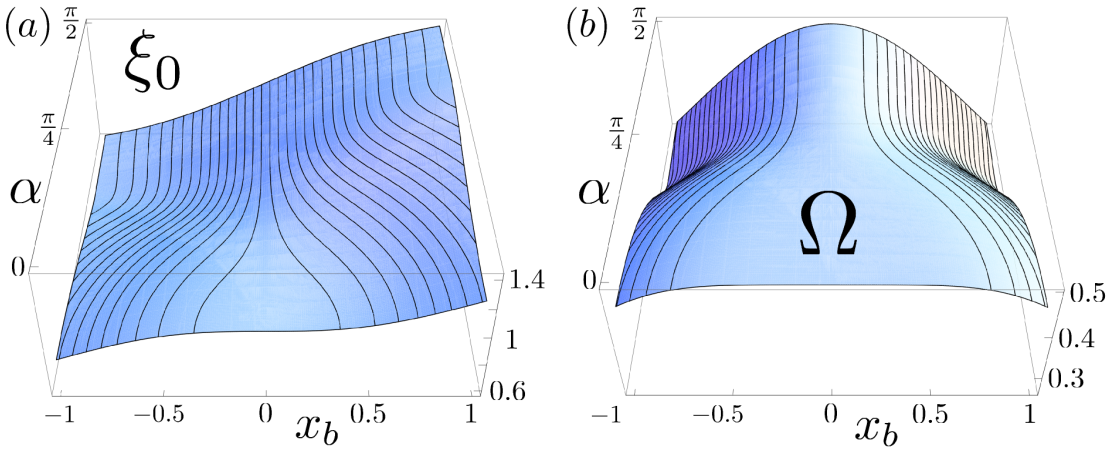


FIGURE 4.2: Map A (4.15): The matrix elements (a) ξ_0, and (b) Ω, as a function of α and x_b, in the one dimensional harmonic oscillator.

Here we are interested in how the matrix elements of $\mathbf{H}_{\mathrm{R}}$ change with respect to the choice of the initial state (4.17) and the barrier position x_b. Accordingly we allow x_b to vary between -1 and 1 (in harmonic oscillator units $\sqrt{\hbar/m\omega}$), and α to vary between 0 and $\pi/2$.

Map A

The values characterising the Hamiltonian elements ξ_0 and Ω according to Map A (equation (4.15)) are shown in figure 4.2(a) and (b) respectively, as a function of the angle α and the barrier position x_b.

The one dimensional harmonic potential in figure 4.1(b) is symmetric about the origin. A reassuring consequence of Map A (positive argument) is that when the barrier is located at the origin, $x_b = 0$, the local frequencies, ξ_0 and ξ_1 of the $|0\rangle$ and $|1\rangle$ spatial modes, are equal for all initial states (since $\xi_0 + \xi_1 = \omega_0 + \omega_1$). As x_b is moved from $-1 \to 1$ the local frequency ξ_0 increases as the 'volume' $\mathcal{V}_0$ is increased. Careful examination of (4.15) indicates that the sign of $\cos(\theta)$ changes from positive to negative with the barrier position when $\sqrt{\mathcal{M}_0^2 - \mathcal{N}_0^2} > \sqrt{\mathcal{M}_1^2 - \mathcal{N}_1^2}$. This result is agreeable as it makes sense that the local frequency should change in accordance with the size of the spatial mode spanned. However, for an asymmetric potential this is not necessarily true. Consequently, we may disregard the negative argument of Map A since $\xi_0 > \xi_1$ when $x_b < 0$ for the one dimensional harmonic oscillator.

The spatial mode coupling frequency Ω (or Rabi frequency) is positive for all values of the initial state and barrier position (figure 4.2(b)) but asymptotically approaches zero in the limit $x_b \to \pm\infty$. It is worth noting here that the sign of $\mathcal{D}_{10}^0$ does not effect the sign of the coupling frequency. This infers that when there is a phase difference between

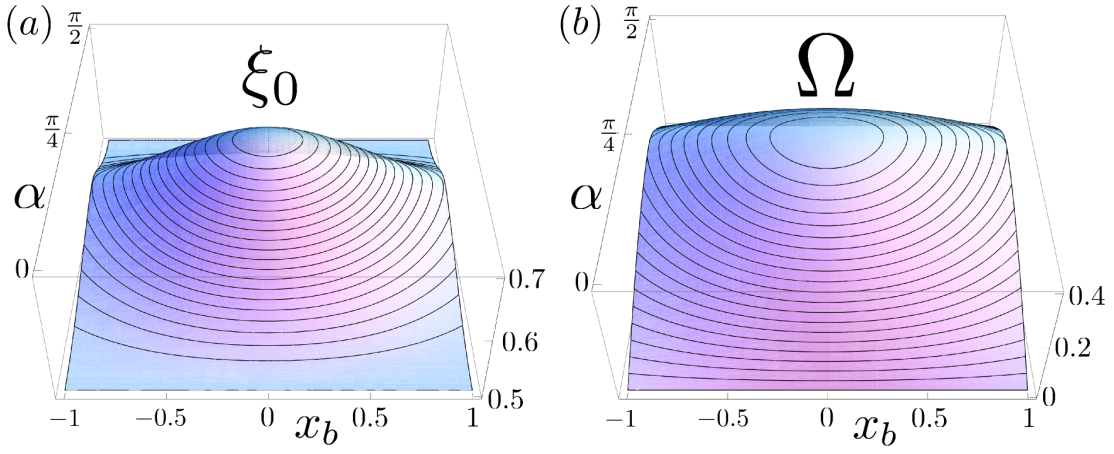


FIGURE 4.3: Map B (4.16): The matrix elements (a) ξ_0, and (b) Ω, as a function of α and x_b, in the one dimensional harmonic oscillator.

the energetic modes of $n\pi$, with $n = 0, 1, 2, \ldots$, there is no phase difference between the spatial modes.

Map B

The values characterising the Hamiltonian elements ξ_0 and Ω according to Map B (equation (4.16)) are shown in figure 4.3(a) and (b) respectively, as a function of the angle α and the barrier position x_b.

Whilst both maps recover the correct temporal density of the spatial modes, Map B exhibits some conflicts with respect to what may be expected from the properties of the spatial mode Hamiltonian matrix. We recognise that when only one energy eigenstate $|\psi_\mu\rangle$ is occupied, the solution for $\cos(\theta)$ from (4.16) becomes $\cos(\theta) = \mathcal{M}_0 + \mathcal{M}_1 = 1$, giving no coupling between the spatial modes. As only one energetic eigenstate is occupied, the density should not oscillate at all and it is therefore reasonable to expect that no coupling exists between the spatial modes. However for this to be satisfied, the matrix elements in this rotated basis assume the same values as that in the energetic mode basis. In other words, when $\alpha = 0, \pi/2$, the coupling terms are zero and we find, $\xi_0 = \omega_0$ and $\xi_1 = \omega_1$, for all values of x_b. Intuitively we expect that for the harmonic oscillator with $x_b = 0$, the two equally sized spatial modes have the same frequency value ($\xi_0 = \xi_1$ as found for Map A) rather than the energetic values of the energetic modes. For values of $\alpha \neq 0, \pi/2$, the spatial modes $|0\rangle$ and $|1\rangle$ are coupled.

Careful examination of (4.16) shows that when $\mathcal{D}^0_{10} > 0$, $\sin(\theta) > 0$ is positive (when we take the positive argument). Changing the sign of $\mathcal{D}^0_{10}$ is equivalent to imposing a π phase change to one of the energetic modes. If we wish to demand that the coupling frequency Ω to be always positive we need only initialise the state vector correctly.

When the sign of (4.16) is negative, we may take its positive value in the spatial mode Hamiltonian matrix and impose a π phase difference between the spatial modes.

The spatial modes, $|0\rangle$ and $|1\rangle$, are coupled for values of $\alpha \neq 0, \pi/2$. The difference between the local frequency terms $|\xi_1 - \xi_0|$ reaches a minimum for $\alpha = \pi/4$ and $x_b = 0$, whilst the coupling frequency Ω reaches a maximum. A slight asymmetry exists about $\alpha = \pi/4$ when $x_b \neq 0$, causing the point of maximum coupling to occur at values of $\alpha > \pi/4$.

4.2.2 Remarks

All elements of the Hamiltonian in the spatial mode basis depend on the barrier position x_b and the initial state distribution through α. One can interpret the initial state dependency by realising that α characterises its energy, which in the traditional picture of tunneling is an important factor as well. As α changes, the local frequencies of each spatial mode ξ_μ and their interaction frequency Ω change accordingly.

Map B may be considered physically less viable than Map A as the spatial modes are decoupled when only one energy eigenstate is occupied. Furthermore the local frequencies of the spatial modes assume the frequency values of the energy eigenstates. This is less than desirable as one expects two equally sized symmetric spatial modes to have the same local frequency, as found for Map A. Whilst Map B satisfies the demands of reproducing the density dynamics of the spatial modes, the above arguments suggest that Map B is an unphysical solution and (potentially) should be discarded.

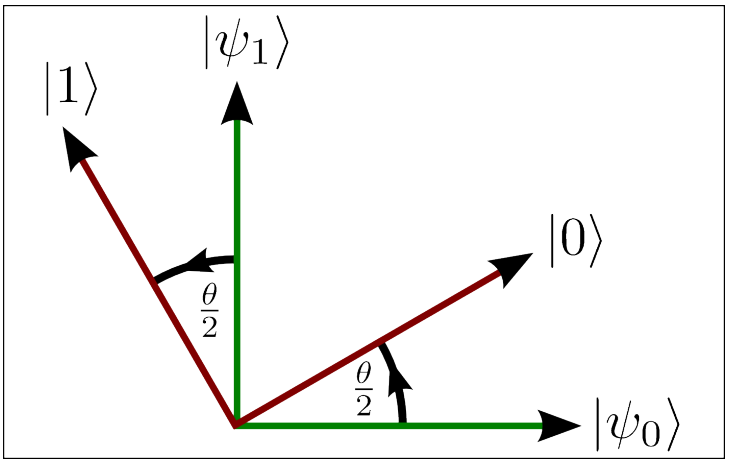


FIGURE 4.4: An angle of $\frac{\theta}{2}$ between the $\{|\psi_0\rangle, |\psi_1\rangle\}$ and $\{|0\rangle, |1\rangle\}$ coordinate systems.

4.3 The Spatial Mode Kets

A reasonable first approximation for the definition of the $|0\rangle$ and $|1\rangle$ spatial mode kets, is to expand them in terms of the energy eigenfunctions as (see figure 4.4),

$$|0\rangle = \cos(\tfrac{\theta}{2})|\psi_0\rangle + \sin(\tfrac{\theta}{2})|\psi_1\rangle, \tag{4.18a}$$

$$|1\rangle = -\sin(\tfrac{\theta}{2})|\psi_0\rangle + \cos(\tfrac{\theta}{2})|\psi_1\rangle. \tag{4.18b}$$

These kets satisfy the usual orthogonality condition $\langle\eta|\eta'\rangle = \delta_{\eta\eta'}$.

For the remainder of this chapter we explore the inherent difficulties involved with attempting to establish a strict definition of the spatial mode kets. To begin we first show how definition (4.18) is unsatisfactory. Thereafter we propose an alternative definition of the spatial mode ket and three requirements that this definition needs to satisfy so that the spatial mode ket can be considered properly defined. Whilst we can show that our alternative definition satisfies the necessary requirements, further complications exist which prevent the recovery of the spatial mode Hamiltonian. We discuss these points and then conclude.

From (4.18) we can construct a spatial mode projector $|\eta\rangle\langle\eta|$ with $\eta = 0,\ 1$. The density of the $|0\rangle$ and $|1\rangle$ spatial regions are then given by,

$$\rho_0(t) = \langle\Psi(t)|0\rangle\langle 0|\Psi(t)\rangle, \qquad \rho_1(t) = \langle\Psi(t)|1\rangle\langle 1|\Psi(t)\rangle, \tag{4.19}$$

where $|\Psi(t)\rangle$ is the two-mode quantum state (4.1a). Explicitly the densities of the spatial modes are,

$$\begin{aligned}\rho_0(t) &= c_0^2\cos^2(\tfrac{\theta}{2}) + c_1^2\sin^2(\tfrac{\theta}{2}) + 2c_0c_1\cos(\tfrac{\theta}{2})\sin(\tfrac{\theta}{2})\cos(\omega_{10}^{-}t),\\ \rho_1(t) &= c_0^2\sin^2(\tfrac{\theta}{2}) + c_1^2\cos^2(\tfrac{\theta}{2}) - 2c_0c_1\cos(\tfrac{\theta}{2})\sin(\tfrac{\theta}{2})\cos(\omega_{10}^{-}t).\end{aligned} \tag{4.20}$$

We now recall that according to equation (4.6) the densities of the spatial modes are,

$$\begin{aligned}\rho_0(t) &= c_0^2\mathcal{D}_{00}^0 + c_1^2\mathcal{D}_{11}^0 + 2c_0c_1\mathcal{D}_{10}^0\cos(\omega_{10}^{-}t),\\ \rho_1(t) &= c_0^2\mathcal{D}_{00}^1 + c_1^2\mathcal{D}_{11}^1 + 2c_0c_1\mathcal{D}_{10}^1\cos(\omega_{10}^{-}t).\end{aligned} \tag{4.21}$$

Initially one may think that a direct comparison of (4.20) and (4.21) should give the solutions for the angle of rotation. However, this is not the case, as the resulting solutions are in conflict with each other. We find,

$$\mathcal{D}_{00}^0 = \mathcal{D}_{11}^1 = \cos^2(\tfrac{\theta}{2}), \tag{4.22a}$$

$$\mathcal{D}_{11}^0 = \mathcal{D}_{00}^1 = \sin^2(\tfrac{\theta}{2}), \tag{4.22b}$$

$$-\mathcal{D}_{10}^1 = \mathcal{D}_{10}^0 = \cos(\tfrac{\theta}{2})\sin(\tfrac{\theta}{2}). \tag{4.22c}$$

The first relation claims that $\mathcal{D}_{00}^0 = \mathcal{D}_{11}^1$, which is in general not true, and similarly $\mathcal{D}_{11}^0 = \mathcal{D}_{00}^1$ is not generally correct. The above three relations together infer that,

$$\left(-\mathcal{D}_{10}^1\right)^2 = \left(\mathcal{D}_{10}^0\right)^2 = \mathcal{D}_{00}^0\mathcal{D}_{11}^0 = \mathcal{D}_{00}^1\mathcal{D}_{11}^1 = \mathcal{D}_{00}^0\mathcal{D}_{00}^1 = \mathcal{D}_{11}^0\mathcal{D}_{11}^1. \tag{4.23}$$

In all but some special cases the above is not satisfied. A particular case of interest is the symmetric double well, with the barrier position located at the midpoint between the trap centers. In the asymptotic limit, (i.e. when the trap centers have a large separation) we indeed find this relation to be satisfied. Each of the above terms approaches $\frac{1}{4}$, and we find that, $\cos(\frac{\theta}{2}) = \sin(\frac{\theta}{2}) = \frac{1}{\sqrt{2}}$, which is the usual value assumed for the spatial mode kets in equation (4.18).

On The Definition Of The Spatial Mode Kets

Whilst the definition of the two-mode spatial ket according to (4.18) certainly satisfies the orthogonality constraints $\langle\eta|\eta'\rangle = \delta_{\eta\eta'}$, further examination reveals that (4.18) fails to recover the correct density dynamics of the quantum state, in the said spatial modes. In this section we take a moment to address the question as to 'what requirements the spatial mode ket must satisfy, such that it can be considered sufficiently defined?'. We propose the following answer to this question. The spatial mode ket is considered sufficiently defined when the following three stipulations are satisfied:

1. The spatial mode ket should obey the usual orthogonality condition $\langle\eta|\kappa\rangle = \delta_{\eta\kappa}$.
2. The spatial mode ket should allow to define a spatial projector $\mathbf{P}_\eta = |\eta\rangle\langle\eta|$, which satisfies $(\mathbf{P}_\eta)^n = \mathbf{P}_\eta$ and $\sum_\eta \mathbf{P}_\eta = \mathbb{1}$.
3. The spatial projector should recover the density of the spatial modes as, $\rho_\eta(t) = \langle\Psi(t)|\mathbf{P}_\eta|\Psi(t)\rangle$.

Immediately we can see that the first condition is satisfied by the spatial mode ket definition (4.18). Whilst (4.18) also satisfies condition 2 above, we have already shown that condition 3 is unfulfilled. Therefore we assert that, according to the above requirements, the definition of the spatial mode ket (4.18) is insufficient.

To find an alternative closed form expression for the spatial mode kets, we first examine the definition of the spatial projector,

$$\mathbf{P}_\eta \;=\; \int_{\mathcal{V}_\eta} d\mathbf{x}\; |\mathbf{x}\rangle\langle\mathbf{x}| \;=\; \sum_{\mu,\nu=0}^{\infty} \mathcal{D}^\eta_{\mu\nu} |\psi_\mu\rangle\langle\psi_\nu| \;=\; |\eta\rangle\langle\eta|. \tag{4.24}$$

We recognise that the above definition does indeed satisfy the third requirement since, according to (4.6), the density dynamics of the spatial modes are correctly accounted for. What we aspire to achieve is to factorize the spatial ket $|\eta\rangle$ from the term on the right hand side of the above. This is a non trivial exercise, as we recognise that the second last term offers no obvious means of factorisation. There is however an alternative means by which we can attempt to achieve this. To begin, let us first check if the definition of the spatial projector satisfies the second requirement. If we can demonstrate that $(\mathbf{P}_\eta)^2 = \mathbf{P}_\eta$, then it is easily shown by induction that $(\mathbf{P}_\eta)^n = \mathbf{P}_\eta$. Continuing along these lines we have,

$$(\mathbf{P}_\eta)^2 \;=\; \left(\sum_{\mu,\nu=0}^{\infty} \mathcal{D}^\eta_{\mu\nu} |\psi_\mu\rangle\langle\psi_\nu|\right)\left(\sum_{q,p=0}^{\infty} \mathcal{D}^\eta_{qp} |\psi_q\rangle\langle\psi_p|\right). \tag{4.25}$$

Taking the inner product $\langle\psi_\nu|\psi_q\rangle = \delta_{\nu q}$, we find

$$(\mathbf{P}_\eta)^2 \;=\; \sum_{\mu,\nu,p=0}^{\infty} \mathcal{D}^\eta_{\mu\nu}\mathcal{D}^\eta_{\nu p} |\psi_\mu\rangle\langle\psi_p|. \tag{4.26}$$

Explicitly we have,

$$(\mathbf{P}_\eta)^2 \;=\; \sum_{\mu,\nu,p=0}^{\infty} \left(\int_{\mathcal{V}_\eta} d\mathbf{x}\; \langle\psi_\mu|\mathbf{x}\rangle\langle\mathbf{x}|\psi_\nu\rangle \int_{\mathcal{V}_\eta} d\mathbf{x}'\; \langle\psi_\nu|\mathbf{x}'\rangle\langle\mathbf{x}'|\psi_p\rangle\right) |\psi_\mu\rangle\langle\psi_p|. \tag{4.27}$$

We rearrange the integrals as,

$$(\mathbf{P}_\eta)^2 \;=\; \sum_{\mu,p=0}^{\infty}\left(\int_{\mathcal{V}_\eta} d\mathbf{x}\int_{\mathcal{V}_\eta} d\mathbf{x}'\;\langle\psi_\mu|\mathbf{x}\rangle\langle\mathbf{x}|\left[\sum_{\nu=0}^{\infty}|\psi_\nu\rangle\langle\psi_\nu|\right]|\mathbf{x}'\rangle\langle\mathbf{x}'|\psi_p\rangle\right)|\psi_\mu\rangle\langle\psi_p|. \quad (4.28)$$

Since the summation in square brackets is simply the identity we find,

$$(\mathbf{P}_\eta)^2 \;=\; \sum_{\mu,p=0}^{\infty}\left(\int_{\mathcal{V}_\eta} d\mathbf{x}\int_{\mathcal{V}_\eta} d\mathbf{x}'\;\langle\psi_\mu|\mathbf{x}\rangle\langle\mathbf{x}|\mathbf{x}'\rangle\langle\mathbf{x}'|\psi_p\rangle\right)|\psi_\mu\rangle\langle\psi_p|. \quad (4.29)$$

Here we recognise that the inner product $\langle\mathbf{x}|\mathbf{x}'\rangle$ is just another way of writing the delta function $\delta(\mathbf{x}-\mathbf{x}')$.[3] Finally we have,

$$(\mathbf{P}_\eta)^2 \;=\; \sum_{\mu,p=0}^{\infty}\left(\int_{\mathcal{V}_\eta} d\mathbf{x}\;\langle\psi_\mu|\mathbf{x}\rangle\langle\mathbf{x}|\psi_p\rangle\right)|\psi_\mu\rangle\langle\psi_p| \;=\; \sum_{\mu,p=0}^{\infty}\mathcal{D}^\eta_{\mu p}|\psi_\mu\rangle\langle\psi_p|. \quad (4.30)$$

Therefore $(\mathbf{P}_\eta)^2 = \mathbf{P}_\eta$ and by induction $(\mathbf{P}_\eta)^n = \mathbf{P}_\eta$. It can be easily shown that the sum over the spatial modes is the identity. We have,

$$\sum_\eta \mathbf{P}_\eta \;=\; \sum_{\mu,\nu=0}^{\infty}\sum_\eta \mathcal{D}^\eta_{\mu\nu}|\psi_\mu\rangle\langle\psi_\nu| \;=\; \sum_{\mu,\nu=0}^{\infty}\delta_{\mu\nu}|\psi_\mu\rangle\langle\psi_\nu| \;=\; \sum_{\mu=0}^{\infty}|\psi_\mu\rangle\langle\psi_\mu| \;=\; \mathbb{1}. \quad (4.31)$$

Hence the second requirement is satisfied. In proving that this requirement is satisfied we have found a new identity (see footnote 3),

$$\sum_{\nu=0}^{\infty}\mathcal{D}^\eta_{\mu\nu}\mathcal{D}^\kappa_{\nu p} \;=\; \mathcal{D}^\eta_{\mu p}\,\delta_{\eta\kappa}. \quad (4.32)$$

The Spatial Mode Ket

At this point we may proceed to attempt to define the spatial mode ket. To do so, we argue that the spatial ket is the normalised projector on the quantum state at $t = 0$. Explicitly we have,

$$\langle\eta|\eta\rangle \;=\; \langle\Psi(0)|\frac{\mathbf{P}_\eta}{\rho_\eta(0)}|\Psi(0)\rangle \;=\; \left(\langle\Psi(0)|\frac{\mathbf{P}_\eta}{\sqrt{\rho_\eta(0)}}\right)\left(\frac{\mathbf{P}_\eta}{\sqrt{\rho_\eta(0)}}|\Psi(0)\rangle\right). \quad (4.33)$$

where $\rho_\eta(0)$ is the density of the spatial mode at $t = 0$, according to (4.6), and we made use of the property $(\mathbf{P}_\eta)^n = \mathbf{P}_\eta$. Our initial state is expanded in terms of the energy

[3] For the case when the limits of the two integrals are $\mathcal{V}_\eta$ and $\mathcal{V}_\kappa$ respectively, we must consider that the volume elements can be non-overlapping. In that case, if $\mathbf{x}$ is an element of $\mathcal{V}_\eta$ it is not an element of $\mathcal{V}_\kappa$, and vise-versa for $\mathbf{x}'$. It then follows that by taking the inner product $\langle\mathbf{x}|\mathbf{x}'\rangle$ we obtain the delta function $\delta_{\eta\kappa}$.

eigenmodes as, [4]

$$|\Psi(0)\rangle \;=\; \sum_{\nu=0}^{\infty} c_\nu(0)|\psi_\nu\rangle. \tag{4.34}$$

From (4.24) and (4.34), we find that the spatial mode ket is defined as,

$$|\eta\rangle \;\equiv\; \frac{1}{\sqrt{\rho_\eta(0)}} \sum_{\mu,\nu=0}^{\infty} c_\mu(0)\mathcal{D}^\eta_{\mu\nu}|\psi_\nu\rangle. \tag{4.35}$$

Let us proceed to check is this definition satisfies the first requirement $\langle\eta|\kappa\rangle = \delta_{\eta\kappa}$. From the above, the inner product is given by,

$$\begin{aligned}
\langle\eta|\kappa\rangle \;&=\; \frac{1}{\sqrt{\rho_\eta(0)}} \sum_{\mu,\nu=0}^{\infty} c^*_\mu(0)\mathcal{D}^\eta_{\mu\nu}\langle\psi_\nu| \; \frac{1}{\sqrt{\rho_\kappa(0)}} \sum_{\alpha,\beta=0}^{\infty} c_\beta(0)\mathcal{D}^\kappa_{\alpha\beta}|\psi_\alpha\rangle, \\
\langle\eta|\kappa\rangle \;&=\; \frac{1}{\sqrt{\rho_\eta(0)\rho_\kappa(0)}} \sum_{\mu,\nu,\beta=0}^{\infty} c^*_\mu(0)c_\beta(0)\mathcal{D}^\eta_{\mu\nu}\mathcal{D}^\kappa_{\nu\beta}.
\end{aligned} \tag{4.36}$$

From the identity (4.32) and (4.6) we find,

$$\langle\eta|\kappa\rangle \;=\; \frac{1}{\rho_\eta(0)} \sum_{\mu,\beta=0}^{\infty} c^*_\mu(0)c_\beta(0)\mathcal{D}^\eta_{\mu\beta}\,\delta_{\eta\kappa} \;=\; \delta_{\eta\kappa}. \tag{4.37}$$

Hence the first requirement is satisfied. What remains to be done is to check whether the definition of the spatial ket (4.35) allows us to recover the spatial projector (4.24). We find,

$$\mathbf{P}_\eta \;=\; |\eta\rangle\langle\eta| \;=\; \frac{1}{\rho_\eta(0)} \sum_{p,q,r,s=0}^{\infty} c_p(0)c^*_r(0)\mathcal{D}^\eta_{pq}\mathcal{D}^\eta_{rs}|\psi_q\rangle\langle\psi_s|. \tag{4.38}$$

From a direct comparison between the spatial projector (4.24) and (4.38) above it is clear that both relations are not equivalent. In order for both relations to be equal, the following stipulation must be satisfied;

$$\sum_{p,r=0}^{\infty} c_p(0)c^*_r(0)\mathcal{D}^\eta_{pq}\mathcal{D}^\eta_{rs} \;=\; \sum_{p,r=0}^{\infty} c_p(0)c^*_r(0)\mathcal{D}^\eta_{pr}\mathcal{D}^\eta_{qs}. \tag{4.39}$$

This is not true in general. However, in the interest of progressing with the calculation, let us assume that for a given state we can choose the barrier location(s) so that the above is upheld. In so doing we find,

$$\mathbf{P}_\eta \;=\; \frac{1}{\rho_\eta(0)} \left(\sum_{p,r=0}^{\infty} c_p(0)c^*_r(0)\mathcal{D}^\eta_{pr} \right) \left(\sum_{q,s=0}^{\infty} \mathcal{D}^\eta_{qs}|\psi_q\rangle\langle\psi_s| \right). \tag{4.40}$$

[4] Here and in the following we are no longer making use of Euler notation.

From the definition of the spatial mode density (4.6) at $t = 0$, we are left with,

$$\mathbf{P}_\eta \;=\; \sum_{q,s=0}^{\infty} \mathcal{D}^{\eta}_{qs} |\psi_q\rangle\langle\psi_s|. \tag{4.41}$$

This exercise has shown us that only under the strict condition of (4.39), are the spatial kets allowed to be defined. It follows that if (4.39) is satisfied, the wavefunction and the Hamiltonian in the spatial basis can be described for an arbitrary number of spatial-energetic modes. We detail this calculation in appendix A.6.

4.4 Discussion

The principle results of this chapter is the mapping of the Hamiltonian between the spatial and energetic bases, (4.15) and (4.16) respectively. We showed that the Hamiltonian in both representations is related by a rotation. Each element of the spatial mode Hamiltonian matrix exhibits contributions from the quantum state's energetic mode coefficients, and the overlap of the energy eigenfunctions in the spatial regions. We showed that there is two unique mappings between the spatial and energetic representations, of which one mapping displays the expected characteristics of the spatial mode Hamiltonian matrix.

Whilst the Hamiltonian matrices can be easily related in both representations, the same cannot be said for the spatial and energetic coordinate system of the wavefunction (figure 4.4). Due to a difficulty in factorising the spatial mode projector $\mathbf{P}_\eta = |\eta\rangle\langle\eta|$, the definition of the spatial mode ket in terms of the energy eigenkets cannot be achieved.

The work contained in this chapter is a closed form mapping that relates the spatial and energetic dynamics of a wavefunction occupying two spatial and energetic modes. An off diagonal 'interaction' term can easily be added by hand to the energetic mode Hamiltonian matrix. For such operators, the phenomenon of self-trapping can be formally demonstrated by increasing the value of the off diagonal term (see Appendix A.7). As the interaction term increases, the 'self-trapping' becomes more pronounced. Relating this off diagonal term to physical systems is the focus of immediate developments to the work contained in this chapter. One avenue of potential exploration is a non-interacting BEC, coupled to an appropriate arrangement of laser fields, that supply the necessary momentum for the transition between the two lowest modes of the double well. Future work in this direction will help to unveil the nature of self trapping for the light-matter interaction, thereby shedding further insight as to the nature of self-trapping for the matter-matter interaction.

Chapter 5

Three Level Atom Optics via the Tunneling Interaction - Revisited

Fundamental to optical processes such as Stimulated Raman Adiabatic Passage (STIRAP) [46], coherent population trapping [169], electromagnetically induced transparency [55], laser cooling [38] and beyond, is the interaction between light and matter [13]. The transport of matter waves is made possible for the same phenomenological reasons as STIRAP, albeit in the absence of the usual light matter interaction, as outlined in chapter 3. Whilst STIRAP and subsequently spatial adiabatic passage (SAP) are considered well understood, authors have highlighted conceptual pitfalls, such as the appearance of apparent super-luminal velocities when SAP is analised using Bohmian mechanics [44]. The number of works focused on understanding the physics underpinning the mechanisms of coherent matter wave transport [39, 170] remain few. With the insight gained from chapter 4 on the nature of the tunneling interaction, here we decompose an original work on SAP [56] with an aim to establish a more fundamental understanding of matter wave transport.

In SAP processes, the tunneling interaction between localised spatial modes replaces the Rabi coupling interaction between an atom's internal electronic states generated by an applied laser field. Absent from the literature of matter wave transport, is an exact model describing the quantum tunneling interaction between spatial modes. The relationship between the spatial and energetic mode description of the wavefunction, detailed in chapter 4, has added insight into the nature of quantum tunneling, albeit for two spatial-energetic modes. An elegant way of generalising that work to N spatial-energetic modes (and furthermore to the time dependent regime) is currently not obvious, but highly desirable for multi-mode spatial systems. For three mode SAP processes, it is

typical in the literature to find the usual 3×3 model Hamiltonian presented for pedagogical reasons in combination with a full numerical integration of Schrödinger's equation (Appendix B.1). We followed this approach with our two experimental proposals for observing spatial adiabatic passage (SAP) of single atoms (and a weakly interacting BEC) using a triple waveguide atom chip structure [116] (section 3.3) and time-dependent radio-frequency potentials [171] (section 3.4) respectively. Probing the relationship between the time dependent Schrödinger equation and the dynamics of the wavefunction in the spatial mode basis offers the potential of uncovering the link between the matrix mechanics of condensed matter physics and quantum optics [39].

In this chapter we revisit the novel scheme proposed by Eckert *et al.* [56] which they showed to be the atom optical analogue of STIRAP. Using the foundational work of chapter 4 as a starting point of reference, we dissect in detail their proposed SAP model. The aim of which is to develop the theoretical understanding of SAP processes by bridging the gap between the spatial and energetic dynamics of the system, described via the spatial mode Hamiltonian matrix and the time dependent Schrödinger equation. We demonstrate that the correct 3×3 spatial mode Hamiltonian assumes tunneling interaction contributions from both nearest neighbour, and next nearest neighbour spatial regions. In addition the local energetic values of the spatial regions change in time. We present an alternative approach for integrating the time dependent Schrödinger equation which allows for an easy comparison with the spatial mode counterpart. Subsequently we show that both representations are equivalent and that matter wave transport in SAP processes is a result of a geometric phase acquired from the cyclical evolution.

In section 5.1 we present the SAP model. The eigenvalues and eigenfunctions of the system's time dependent potential can be solved for analytically, which is outlined in section 5.1.3. The complete spatial mode Hamiltonian can be recovered, to a very good approximation, by defining a basis for each potential region, detailed in section 5.2.1. Following the analysis of the system in the spatial basis picture, we move to the energetic basis in section 5.3 and demonstrate that both representations are equivalent. We outline a methodology to time evolve SAP in the non-interacting regime, which is an alternative to the usual split operator approach, section 5.3. This technique allows for a deeper understanding of the temporal dynamics of the system, uncovering the importance of the delay between the motion of the trap centers, how this delay affects the necessary constraints of adiabaticity and why the 'counter-intuitive' trap motions facilitates the transport of the matter wave. In addition this approach unveils how the SAP technique imposes a π change of phase to one of the wavefunction's basis states due to the geometry of the evolution covered in sections 5.3.1 and 5.3.2. We discuss how SAP itself is a consequence (and example of) a geometric phase, which exists for both the traditional 'counter-intuitive' and the 'intuitive' trap motions. Finally we discuss

the technique of fraction SAP in section 5.4. This technique allows for the creation of arbitrary superposition states between the outer traps, which is also independent of the total time taken for the evolution and thus geometric in nature.

5.1 Spatial Adiabatic Passage: Model

To maintain the generality of this work we scale the spatial co-ordinates $\mathbf{x}$ with respect to the length $\sqrt{\hbar/m\omega}$, where m is the mass of the atom, ω is the trapping frequency of the harmonic oscillator and $\hbar$ is Planck's constant divided by 2π.

For our numerical purposes we deal with the time dependent SAP Hamiltonian by discretising the total time taken for the evolution into $N+1$ points in time. We identify the Hamiltonian at each time step by its time co-ordinate t_n where $n = 0, 1, 2, \ldots, N$. Each of these points *in* time is separated by equal distances *of* time Δt, where $t_{n+1} - t_n = \Delta t$. The total time for the process is then $N\Delta t$. As the time for the stationary interval Δt increases, the total time taken for the process also increases. At each time step t_n the wavefunction evolves according to the Hamiltonian $\mathbf{H}(t_n)$ for an increment of time Δt followed by an instantaneous change of the Hamiltonian at the following point in time. The evolved wavefunction then assumes a linear combination of the Hilbert space basis states at the following time step $t = t_{n+1}$. The discretisation of the time spectrum in this way allows for the simulation of adiabatic evolution according to the time dependent Hamiltonian. This is further detailed in section 5.3.

5.1.1 The Hamiltonian And The Time Dependent Potential

Proposed in [56] is a novel scheme to actualise the high fidelity transport of a neutral atom in an array of optical dipole traps. The system is modeled using a one dimensional linear arrangement of three truncated piecewise harmonic potentials of equal trapping frequency (see figure 5.1). Each harmonic potential is centered on the position x_η where $\eta = 0, 1, 2$ refers to the left, middle and right harmonic potential respectively. Subsequently the spatial region spanned by each potential well is denoted $|\eta\rangle = |0\rangle, |1\rangle, |2\rangle$. A 'counter-intuitive' motion of the trap centers transports a matter wave from $|0\rangle \rightarrow |2\rangle$. The form of the potential $\mathbf{V}(\mathbf{x}, t_n)$ is determined by the position of each trap center $x_\eta(t_n)$. In scaled units,

$$\mathbf{V}(\mathbf{x}, t_n) \;=\; \frac{1}{2} \min \left[\sum_{\eta=0}^{2} \big(\mathbf{x} + x_\eta(t_n)\big)^2 \right]. \tag{5.1}$$

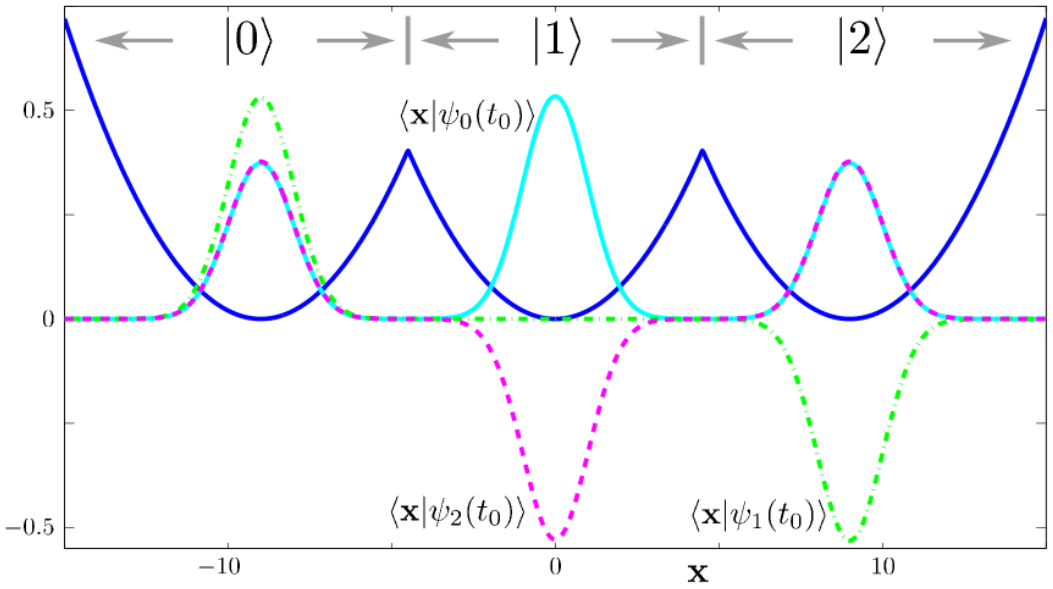


FIGURE 5.1: In blue is the scaled potential $\mathbf{V}(\mathbf{x}, t_n)/25$. Overlayed are the *gs*-triplet eigenfunctions. In solid cyan, dash-dot green and dashed magenta are; $\langle \mathbf{x}|\psi_0(t_0)\rangle$, $\langle \mathbf{x}|\psi_1(t_0)\rangle$ and $\langle \mathbf{x}|\psi_2(t_0)\rangle$ respectively. The spatial regions spanned by the traps are labeled $|1\rangle$, $|2\rangle$ and $|3\rangle$ for the left, middle and right harmonic potentials respectively.

The scaled Hamiltonian is,

$$\mathbf{H}(t_n) \;=\; \hbar\omega \left(-\frac{\partial^2}{\partial \mathbf{x}^2} \;+\; \mathbf{V}(\mathbf{x}, t_n) \right). \tag{5.2}$$

At each time step the eigenfunctions $|\psi_\mu(t_n)\rangle$ of (5.2) can be solved for by both numerical techniques [172] (i.e. via the finite difference method, appendix B.2) and analytical means. We detail how to solve for the eigenfunctions analytically in section 5.1.3. As usual the operation of the Hamiltonian (at each t_n) on the eigenfunctions of the potential returns their (scaled) eigenenergy as $\mathbf{H}(t_n)|\psi_\mu(t_n)\rangle = \hbar\omega_\mu(t_n)|\psi_\mu(t_n)\rangle$. Shown in figure 5.1 is the scaled potential and the three lowest eigenfunctions $\langle \mathbf{x}|\psi_\nu(t_0)\rangle$, with $\nu = 0, 1, 2$. These three eigenfunctions are asymptotically degenerate in the limit of large trap separations, and their scaled eigenenergies approach $\hbar\omega/2$. In the following, we refer to these eigenfunctions as the ground state triplet (*gs*-triplet).

The potential, the spatial modes $|0\rangle, |1\rangle, |2\rangle$ and the three lowest eigenfunctions are illustrated in figure 5.1. Here we have made a deliberate change to the previous notation used for the spatial modes, $|0\rangle_{L,M,R}$, from chapter 3, sections 3.3 and 3.4. We have adapted this notation as the latter infers that each spatial mode has it own energy spectrum. From the work of chapter 4 we know that the 'local energy' of each spatial mode depends on the occupied energetic modes of the wavefunction. Therefore for a given wavefunction, the possible energetic values of the spatial mode are not of interest, and we resort to the simpler $|0\rangle, |1\rangle, |2\rangle$ notation.

5.1.2 The Trap Motions

STIRAP has been thoroughly outlined in chapter 3 but for ease of reading we re-hash the basic principles here. A key feature of the STIRAP process is the time dependent Stokes laser pulse $\Omega_s(t)$ (coupling the *unoccupied* electronic states $|1\rangle$ and $|2\rangle$) which is applied first, followed by the pump laser pulse $\Omega_p(t)$ (coupling states $|0\rangle$ and $|1\rangle$), with an appropriate delay. This is reproduced in this matter wave setting by firstly decreasing the distance between traps $|1\rangle$ and $|2\rangle$ followed by decreasing the distance between traps $|0\rangle$ and $|1\rangle$. As the outer traps approach the center trap, it causes a splitting in the eigenenergies $\hbar\omega_\nu(t_n)$ of the basis states $|\psi_\nu(t_n)\rangle$. In turn this increases the Rabi *'tunneling'* interaction between the spatial regions spanned by the traps in a manner analogous to the optical case.

The outer traps are initially separated a distance $d_{\max}$ from the center trap, which is located at the origin. Throughout the SAP evolution they move from this maximum separation distance from the center trap to a minimum separation $d_{\min}$. The total time taken for the evolution is discretised into N time steps. The delay between the motion of the outer trap centers is allowed to take a total of length δ time steps, where $\delta = (0.1)N$. The 'counter-intuitive' paths of the left $(x_0(t_n))$ and right $(x_2(t_n))$ trap centers are subsequently given by,

$$x_0(t_n) = \Theta(n-\delta-1)\left\{\tfrac{d_{\max}-d_{\min}}{2}\left[\cos\left(\tfrac{2\pi(n-\delta)}{N-\delta}\right)+1\right]+d_{\min}\right\}+\Theta(\delta-n)d_{\max}, \quad (5.3a)$$

$$x_2(t_n) = -\Theta(N-\delta-n-1)\left\{\tfrac{d_{\max}-d_{\min}}{2}\left[\cos\left(\tfrac{2\pi n}{N-\delta}\right)+1\right]+d_{\min}\right\} - \Theta(n+\delta-N)d_{\max}, \quad (5.3b)$$

where $\Theta(z)$ is the Heaviside step function, $\Theta(z) = 0$ ($\Theta(z) = 1$) when $z < 0$ ($z \geq 0$) and $n = 0, 1, 2, \ldots, N$.

5.1.3 The Energy Eigensystem

Conducive to developing a complete illustration of the SAP procedure for this piecewise triple harmonic oscillator, an analytical means of determining the eigensystem of (5.2) is necessary. A technique to recover the energy eigensystem for two piecewise harmonic oscillators is found in Razavy *'Quantum Theory of Tunneling'* [14], which we extend here for an arbitrary arrangement of three piecewise harmonic oscillators. In doing so we impose that each trap has the same trapping frequency but the procedure detailed can be easily generalised to account for traps with unequal trapping frequencies.

To arrive at a general solution for the whole three trap potential, we must solve for each individual potential separately and afterwards ensure that these solutions are continuous over the whole potential. To do so we define the point of intersection between the left and middle trap as a_l, and the point of intersection between the middle and right trap as a_r. The scaled potential at each time step t_n is thus given (from section 5.1.1) by,

$$\mathbf{V}(\mathbf{x},t_n)=\begin{cases}\big(\mathbf{x}+x_0(t_n)\big)^2/2, & \text{for} \quad -\infty<\mathbf{x}\leq a_l,\\ \big(\mathbf{x}+x_1(t_n)\big)^2/2, & \text{for} \quad a_l\leq\mathbf{x}\leq a_r,\\ \big(\mathbf{x}+x_2(t_n)\big)^2/2, & \text{for} \quad a_r\leq\mathbf{x}<\infty.\end{cases} \tag{5.4}$$

The middle trap center $x_1(t_n)$ is stationary and is located on the origin. For resonant harmonic traps the intersection points are $a_l=-x_0(t_n)/2$ and $a_r=-x_2(t_n)/2$, with the position of the trap centers defined by (5.3).

Schrödinger's equation must be solved within the boundaries of each trap. Furthermore the logarithmic derivatives of neighbouring solutions must be equal at each boundary. The procedure is as follows. Firstly we write (5.2) for each potential well in scaled units,

$$\left(\frac{d^2}{d\mathbf{x}^2}-\frac{\big(\mathbf{x}+x_0(t_n)\big)^2}{2}+\left(\upsilon+\frac{1}{2}\right)\right)\phi_\upsilon^0(\mathbf{x},t_n)=0, \quad \text{for} \quad -\infty<\mathbf{x}\leq a_l, \tag{5.5a}$$

$$\left(\frac{d^2}{d\mathbf{x}^2}-\frac{\big(\mathbf{x}+x_1(t_n)\big)^2}{2}+\left(\upsilon+\frac{1}{2}\right)\right)\phi_\upsilon^1(\mathbf{x},t_n)=0, \quad \text{for} \quad a_l<\mathbf{x}\leq a_r, \tag{5.5b}$$

$$\left(\frac{d^2}{d\mathbf{x}^2}-\frac{\big(\mathbf{x}+x_2(t_n)\big)^2}{2}+\left(\upsilon+\frac{1}{2}\right)\right)\phi_\upsilon^2(\mathbf{x},t_n)=0, \quad \text{for} \quad a_r<\mathbf{x}<\infty. \tag{5.5c}$$

The eigenenergies of the eigenfunctions for each spatial region must be equal as, $\mathbf{H}^\eta\phi_\upsilon^\eta(\mathbf{x},t_n)=\hbar\omega_\upsilon\phi_\upsilon^\eta(\mathbf{x},t_n)$ where $\hbar\omega_\upsilon=\hbar\omega(\upsilon+\frac{1}{2})$ and $\mathbf{H}^\eta$ is the operator within the bounds of the η spatial region. Changing the position of the trap centers does not change the functional form of the eigenfunctions in each spatial region but, as we will momentarily show, it changes the relative contribution each spatial mode solution contributes to the eigenfunctions of the whole potential.[1]

The solutions of the dimensionless equations (5.5) are the parabolic cylinder functions, $\phi_\upsilon^\eta(\mathbf{x},t_n)=D_\upsilon(\sqrt{2}(\mathbf{x}+x_\eta(t_n)))$ [31]. We can expect that the quantum number υ

[1] For the case when the three traps have unequal trapping frequencies, we note here that changing the trapping frequency of each harmonic potential changes the functional form of the eigenfunctions for each spatial region. The condition that their energies are the same in each spatial region, must still be satisfied. For harmonic traps of unequal trapping frequencies, i.e. $\omega_l,\omega_m,\omega_r$, the quantum number associated with the solution of each spatial region is different $\upsilon_l,\upsilon_m,\upsilon_r$. For such a non-trivial case it helps to proceed in terms of a single quantum number υ_m. This is achieved by relating the υ_l and υ_r quantum numbers to υ_m as, $\upsilon_l=(\omega_m-\omega_l+2\omega_m\upsilon_m)/(2\omega_l)$, and $\upsilon_r=(\omega_m-\omega_r+2\omega_m\upsilon_m)/(2\omega_r)$, where ω_{lmr} is the trapping frequencies of the left, middle and right potential respectively. Similarly the intersection points are changed as $a_l=-x_0(t_n)\omega_m/(\omega_m+\omega_l)$ and $a_r=-x_2(t_n)\omega_m/(\omega_m+\omega_r)$.

associated with the eigenenergies of the system is non-integer. Therefore the parabolic cylinder functions vanish for $\mathbf{x} \to \infty$ but will diverge for $\mathbf{x} \to -\infty$. With this in mind we may first construct the solutions to the left and right traps such that the argument of the function is always positive within the bounds of the traps, i.e. $\phi_\upsilon^0(\mathbf{x}, t_n) = D_\upsilon(-\sqrt{2}(\mathbf{x} + x_0(t_n)))$ and $\phi_\upsilon^2(\mathbf{x}, t_n) = D_\upsilon(\sqrt{2}(\mathbf{x} + x_2(t_n)))$.

The solution for the middle trap presents a small problem since it is bounded by both the left and right traps. If we were solving for the middle and left boundary, or the middle and right boundary alone, it would be rather straightforward. The issue is that we require a solution that satisfies logarithmic derivative condition at both bounds and does not diverge to infinity at either. In order to resolve this we write the solution of the middle trap as a superposition of the solutions on both the left and right sides. To put it more straightforwardly this means,

$$\phi_\upsilon^0(\mathbf{x}, t_n) = D_\upsilon(-\sqrt{2}(\mathbf{x} + x_0(t_n))), \tag{5.6a}$$

$$\phi_\upsilon^1(\mathbf{x}, t_n) = \alpha D_\upsilon(\sqrt{2}\,\mathbf{x}) + D_\upsilon(-\sqrt{2}\,\mathbf{x}), \tag{5.6b}$$

$$\phi_\upsilon^2(\mathbf{x}, t_n) = D_\upsilon(\sqrt{2}(\mathbf{x} + x_2(t_n))), \tag{5.6c}$$

To simplify we have let $x_1(t_n) = 0$.

In the usual way we may connect the solutions of adjacent traps by requiring that they satisfy the logarithmic derivatives at the boundaries,

$$\left(\frac{\phi_\upsilon^0(\mathbf{x}, t_n)'}{\phi_\upsilon^0(\mathbf{x}, t_n)}\right)_{a_l} = \left(\frac{\phi_\upsilon^1(\mathbf{x}, t_n)'}{\phi_\upsilon^1(\mathbf{x}, t_n)}\right)_{a_l}, \tag{5.7a}$$

$$\left(\frac{\phi_\upsilon^2(\mathbf{x}, t_n)'}{\phi_\upsilon^2(\mathbf{x}, t_n)}\right)_{a_r} = \left(\frac{\phi_\upsilon^1(\mathbf{x}, t_n)'}{\phi_\upsilon^1(\mathbf{x}, t_n)}\right)_{a_r}. \tag{5.7b}$$

The prime $'$ indicates the derivative with respect to $\mathbf{x}$. The simultaneous equations of (5.7) are a function of both α (the coefficient of the middle trap solution) and υ (the quantum number of the energy eigenfunction).

The parabolic cylinder functions satisfy the recurrence relations,

$$\begin{aligned} D_{\upsilon+1}(\mathbf{x}) - \mathbf{x}\, D_\upsilon(\mathbf{x}) + \upsilon D_{\upsilon-1}(\mathbf{x}) &= 0, \\ D'_\upsilon(\mathbf{x}) + \frac{\mathbf{x}}{2} D_\upsilon(\mathbf{x}) - \upsilon D_{\upsilon-1}(\mathbf{x}) &= 0, \end{aligned}$$

which can be used in the explicit evaluation of (5.7).

In order to resolve for υ it helps to first rearrange equations (5.7) in terms of α. We note for resonant harmonic traps $a_l = -x_0(t_n)/2$ and $a_r = -x_2(t_n)/2$ and to abbreviate

we define $x_0 \equiv x_0(t_n)$ and $x_2 \equiv x_2(t_n)$.

$$\alpha = \frac{\sqrt{2}D_\upsilon\big(\frac{-x_0}{\sqrt{2}}\big)D_{\upsilon+1}\big(\frac{x_0}{\sqrt{2}}\big) - D_\upsilon\big(\frac{x_0}{\sqrt{2}}\big)\Big[\sqrt{2}D_{\upsilon+1}\big(\frac{-x_0}{\sqrt{2}}\big) + x_0 D_\upsilon\big(\frac{-x_0}{\sqrt{2}}\big)\Big]}{D_\upsilon\big(\frac{-x_0}{\sqrt{2}}\big)\Big[2\sqrt{2}D_{\upsilon+1}\big(\frac{-x_0}{\sqrt{2}}\big) + x_0 D_\upsilon\big(\frac{-x_0}{\sqrt{2}}\big)\Big]}, \tag{5.8a}$$

$$\alpha = \frac{D_\upsilon\big(\frac{x_2}{\sqrt{2}}\big)\Big[2\sqrt{2}D_{\upsilon+1}\big(\frac{x_2}{\sqrt{2}}\big) - x_2 D_\upsilon\big(\frac{x_2}{\sqrt{2}}\big)\Big]}{D_\upsilon\big(\frac{x_2}{\sqrt{2}}\big)\Big[\sqrt{2}D_{\upsilon+1}\big(\frac{-x_2}{\sqrt{2}}\big) + x_2 D_\upsilon\big(\frac{-x_2}{\sqrt{2}}\big)\Big] - \sqrt{2}D_\upsilon\big(\frac{-x_2}{\sqrt{2}}\big)D_{\upsilon+1}\left(\frac{x_2}{\sqrt{2}}\right)}, \tag{5.8b}$$

In practice making use of a software program such as Mathematica allows an easy progression from equation (5.7) to equation (5.8).

For a known value of υ we can find α. To find the values of υ we construct a function $\mathcal{F}(\upsilon)$, by subtracting the right hand sides of both the above equations. We have,

$$\begin{aligned}\mathcal{F}(\upsilon) \;=\; & \frac{\sqrt{2}D_\upsilon\big(\frac{-x_0}{\sqrt{2}}\big)D_{\upsilon+1}\big(\frac{x_0}{\sqrt{2}}\big) - D_\upsilon\big(\frac{x_0}{\sqrt{2}}\big)\Big[\sqrt{2}D_{\upsilon+1}\big(\frac{-x_0}{\sqrt{2}}\big) + x_0 D_\upsilon\big(\frac{-x_0}{\sqrt{2}}\big)\Big]}{D_\upsilon\big(\frac{-x_0}{\sqrt{2}}\big)\Big[2\sqrt{2}D_{\upsilon+1}\big(\frac{-x_0}{\sqrt{2}}\big) + x_0 D_\upsilon\big(\frac{-x_0}{\sqrt{2}}\big)\Big]} \\ & - \frac{D_\upsilon\big(\frac{x_2}{\sqrt{2}}\big)\Big[2\sqrt{2}D_{\upsilon+1}\big(\frac{x_2}{\sqrt{2}}\big) - x_2 D_\upsilon\big(\frac{x_2}{\sqrt{2}}\big)\Big]}{D_\upsilon\big(\frac{x_2}{\sqrt{2}}\big)\Big[\sqrt{2}D_{\upsilon+1}\big(\frac{-x_2}{\sqrt{2}}\big) + x_2 D_\upsilon\big(\frac{-x_2}{\sqrt{2}}\big)\Big] - \sqrt{2}D_\upsilon\big(\frac{-x_2}{\sqrt{2}}\big)D_{\upsilon+1}\left(\frac{x_2}{\sqrt{2}}\right)}.\end{aligned} \tag{5.9}$$

The roots of $\mathcal{F}(\upsilon) = 0$ are the allowed values of υ. For each value of υ the corresponding value of α is found from either of equations (5.8).

The non-normalised eigenfunctions are given by equation (5.6). In order to preserve continuity, we rewrite the solutions to each region of the triple well as,

$$\phi_\upsilon^0(\mathbf{x}, t_n) \;=\; k_0\, D_\upsilon(-\sqrt{2}(\mathbf{x} + x_0(t_n))), \qquad \text{for} \qquad -\infty < \mathbf{x} \le a_l, \tag{5.10a}$$

$$\phi_\upsilon^1(\mathbf{x}, t_n) \;=\; k_1\, \big[\alpha D_\upsilon(\sqrt{2}\,\mathbf{x}) + D_\upsilon(-\sqrt{2}\,\mathbf{x})\big], \qquad \text{for} \qquad a_l \le \mathbf{x} \le a_r, \tag{5.10b}$$

$$\phi_\upsilon^2(\mathbf{x}, t_n) \;=\; k_2\, D_\upsilon(\sqrt{2}(\mathbf{x} + x_2(t_n))), \qquad \text{for} \qquad a_r \le \mathbf{x} < \infty. \tag{5.10c}$$

where,

$$\begin{aligned} k_0 \;&=\; 1, \\ k_1 \;&=\; D_\upsilon(-x_0(t_n)/\sqrt{2})/\Big(\alpha D_\upsilon(-x_0(t_n)/\sqrt{2}) + D_\upsilon(x_0(t_n)/\sqrt{2})\Big), \\ k_2 \;&=\; \operatorname{sign}\Big[\alpha D_\upsilon(-x_2(t_n)/\sqrt{2}) + D_\upsilon(x_2(t_n)/\sqrt{2})\Big]\, \operatorname{sign}\Big[D_\upsilon(x_2(t_n)/\sqrt{2})\Big]. \end{aligned}$$

From these relations we may construct the normalised eigenfunctions.

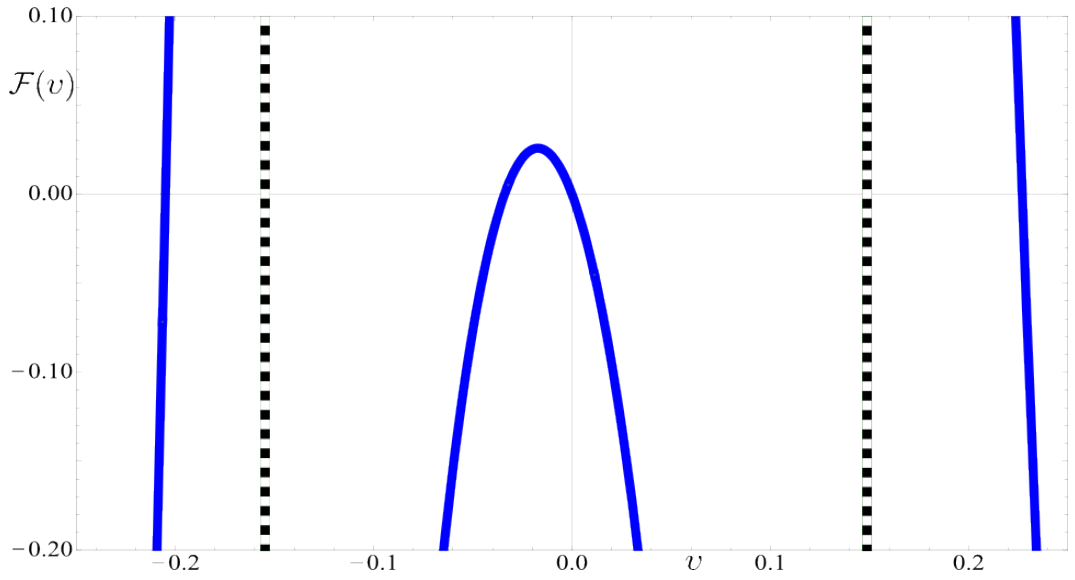


FIGURE 5.2: A plot of the function $\mathcal{F}(\upsilon)$ recovered from equation (5.9). The vertical lines indicated the position of the poles.

To do so we first abbreviate $\phi_\upsilon^\eta \equiv \phi_\upsilon^\eta(\mathbf{x}, t_n)$. We make use of the Heaviside step function $\Theta(z)$ and let $\mathcal{V}_\eta$ represent the spatial region spanned by the $|\eta\rangle$ harmonic trap. The normalised eigenfunctions of the triple well potential are thus given by,

$$\psi_\upsilon(\mathbf{x}, t_n) \;=\; \frac{\Theta(-\mathbf{x}-a_l)\phi_\upsilon^0 - \big[\Theta(\mathbf{x}+a_l)-\Theta(\mathbf{x}+a_r)\big]\phi_\upsilon^1 + \Theta(\mathbf{x}+a_r)\phi_\upsilon^2}{\sqrt{\int_{\mathcal{V}_0} d\mathbf{x}\,|\phi_\upsilon^0|^2 + \int_{\mathcal{V}_1} d\mathbf{x}\,|\phi_\upsilon^1|^2 + \int_{\mathcal{V}_2} d\mathbf{x}\,|\phi_\upsilon^2|^2}}. \tag{5.12}$$

The notation for the energy eigenfunctions may be interchanged with the Dirac notation as, $\psi_\upsilon(\mathbf{x}, t_n) = \langle \mathbf{x}|\psi_\upsilon(t_n)\rangle$.

Numerical Example

In our units the eigenvalues of the triple well harmonic oscillator are,

$$E_\upsilon \;=\; \hbar\omega\left(\upsilon + \frac{1}{2}\right). \tag{5.13}$$

For the usual one dimensional harmonic oscillator the ground state is $\hbar\omega/2$ and the quantum number υ is an integer, $\upsilon = 0, 1, 2, \ldots$. For this triple well harmonic oscillator the quantum number υ associated with the eigenfunctions $|\psi_\upsilon(t_n)\rangle$, is non-integer.

For the purposes of clarity and completeness we momentarily consider a numerical example; we choose a particular case when the 'potential barrier' between the spatial modes is small. We let $(x_0(t_n), x_1(t_n), x_2(t_n)) = (2.4527, 0, -2.4551)$ and all harmonic traps have the same trapping frequency. When the trap centers are in close proximity (as is the case here) the eigenspectrum of each spatial mode cannot be approximated by harmonic

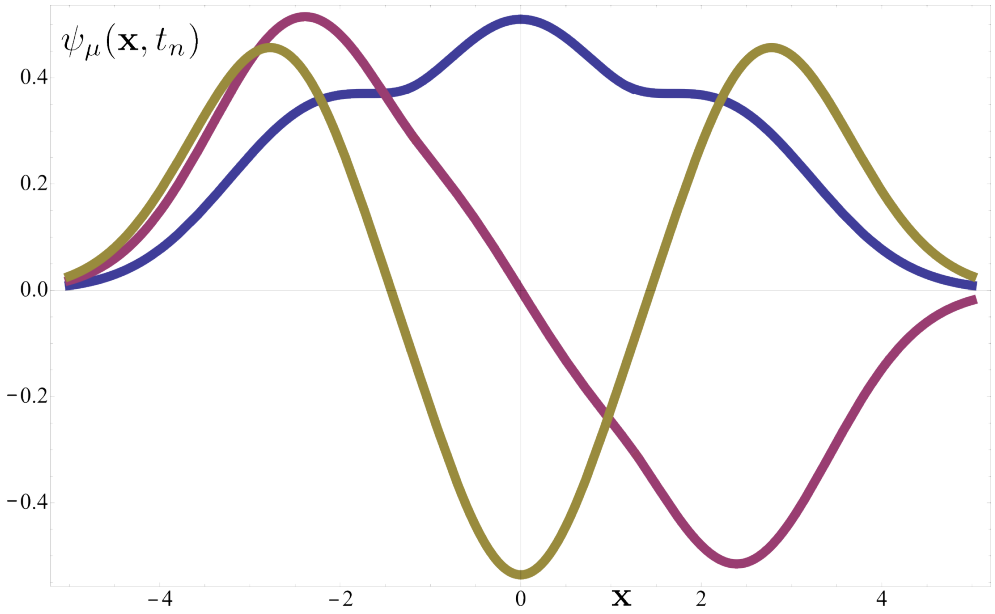


FIGURE 5.3: The *gs*-triplet eigenfunctions $\psi_\mu(\mathbf{x}, t_n)$, (for $\mu = 0, 1, 2$) of the piecewise triple harmonic oscillator potential. The trap centers are $(x_0(t_n), x_1(t_n), x_2(t_n)) = (2.4527, 0, -2.4551)$.

oscillator states. Furthermore a state localised in any spatial mode has a short lifetime as it is in the strong coupling or the high frequency tunneling regime.

The roots of $\mathcal{F}(\upsilon)$ allow us to recover the quantum number υ associated with each eigenfunction. In figure 5.2 we show the function $\mathcal{F}(\upsilon)$ for our chosen parameters, where the poles are indicated by the position of the vertical dashed lines. The three roots which are the solutions for the eigenfunctions are the non-integer roots. Note there is an 'extra' root that lies on the origin which is not a solution for the eigenfunctions of the potential and is therefore neglected. There are similar 'extra' roots at all integer values of υ which are neglected as they do not recover the correct eigenfunctions of the potential.

We find that the quantum numbers associated with the ground, first and second excited eigenfunctions are, $(\upsilon_0, \upsilon_1, \upsilon_2) = (-0.20491, -0.03398, 0.22687)$. The value of α corresponding to each of these numbers is found from (5.8). The related eigenfunctions for these three quantum numbers are constructed from (5.12) and found plotted in figure 5.3. These eigenfunctions can be readily compared to a situation close to the asymptotic limit, as in figure 5.1, and the asymmetric case in figure 5.5. The eigenfunctions $|\psi_\nu\rangle$ for $\nu = 0, 1, 2$ for each magnitude of the trap separations can be identified by their functional form or, to be precise, by the number of nodes.

At this point we note that as the trap centers are moved throughout the SAP evolution, the energy of each eigenfunction $|\psi_\upsilon(t_n)\rangle$ changes as the scaling of the quantum number υ changes (see (5.13)). Keeping track of the each eigenfunction (ground, first or second

excited) using these non-integer numbers is not practical. However the ground, first and second excited eigenfunctions are identifiable (for all t_n) in SAP processes from their functional form. For the purposes of clarity we shall, from here on, refer to the ground first and second excited eigenfunction using the labels $\nu = 0, 1, 2$ respectively. Equation 5.13 becomes,

$$E_\nu \;=\; \hbar\omega\left(\upsilon_\nu + \frac{1}{2}\right) \;=\; \hbar\omega_\nu. \tag{5.14}$$

The properties of the eigenfunctions of (5.12) exhibit a trait similar to those of the three square wells potential studied in [39], in that they form groups of three or triplets. Herein we refer to the three lowest eigenfunctions $|\psi_\nu(t_0)\rangle$, for $\nu = 0, 1, 2$, as the ground state triplet (*gs*-triplet), and examples are found plotted in both figures 5.3 and 5.1. In the limit of large separation between the traps the eigenenergies $\hbar\omega_\upsilon(t_n) = \hbar\omega(\upsilon + 1/2)$ of the *gs*-triplet asymptotically approach $\hbar\omega/2$, for $\nu = 0, 1, 2$. Similarly for the first excited triplet, their eigenenergies asymptotically approach $3\hbar\omega/2$, for $\nu = 3, 4, 5$, and so on.

5.2 SAP in the Spatial Mode Basis

Chapter 4 showed that the Hamiltonian operator in the spatial basis is related to the operator in the energy basis by a rotation, made possible via the Euler rotation matrices. When two energetic modes are occupied, this rotation matrix consists of one angle of rotation which determines the phase and amplitude evolution of two spatial modes.

When (for instance) the three lowest energetic modes are occupied $|\psi_0\rangle, |\psi_1\rangle$ and $|\psi_2\rangle$, the corresponding rotation matrix consists of three angles of rotation. These angles θ_{10}, θ_{21} and θ_{20} depend on the frequency difference between the energetic modes, ω_{10}^-, ω_{21}^- and ω_{20}^-, and the overlap of the energy eigenfunctions in the different spatial regions $\mathcal{D}_{\mu\nu}^\eta$. The spatial mode Hamiltonian matrix is related to the energetic mode Hamiltonian matrix by the rotation $\mathbf{H}_\mathrm{R} = \mathbf{R}\mathbf{H}\mathbf{R}^\dagger$, where the rotation matrix $\mathbf{R} = \mathbf{R}_x\mathbf{R}_y\mathbf{R}_z$ and,

$$\begin{aligned}
\mathbf{R}_x \;&=\; \begin{pmatrix} \cos\theta_{10} & \sin\theta_{10} & 0 \\ -\sin\theta_{10} & \cos\theta_{10} & 0 \\ 0 & 0 & 1 \end{pmatrix}; \qquad \mathbf{R}_y \;=\; \begin{pmatrix} \cos\theta_{21} & 0 & \sin\theta_{21} \\ 0 & 1 & 0 \\ -\sin\theta_{21} & 0 & \cos\theta_{21} \end{pmatrix}; \\
\mathbf{R}_z \;&=\; \begin{pmatrix} 1 & 0 & 0 \\ 0 & \cos\theta_{20} & \sin\theta_{20} \\ 0 & -\sin\theta_{20} & \cos\theta_{20} \end{pmatrix}; \qquad \mathbf{H} \;=\; \hbar\begin{pmatrix} \omega_0 & 0 & 0 \\ 0 & \omega_1 & 0 \\ 0 & 0 & \omega_2 \end{pmatrix}.
\end{aligned} \tag{5.15}$$

Resolving for a closed form solution for each of these angles, using a method analogous to that of chapter 4, is a cumbersome task. Evaluating the density evolution in both

representations, using these three angles, results in equations that are far too big to work with in any type of reasonable fashion. For the purposes of this work we assert that an exact solution for each of these angles is not necessary. Until the correct spatial-energetic map is available, for three (or N) spatial-energetic modes, we present in the following a means of approximating the rotation matrix $\mathbf{R}$.

5.2.1 The Trap Basis Approximation

In general it is not possible to construct a basis to represent a spatial region of an arbitrary potential, e.g. a 1-D harmonic trap. However, potentials wherein the density of a wavefunction (which is some linear superposition of the basis states) may assume a local maximum in a spatial region, whilst having a negligible density in the other spatial regions, do offer the possibility to construct a basis to represent each spatial region. The functional form of this triple well harmonic potential is an example of such a potential and subsequently we may define a basis for the spatial regions spanned by the traps [70]. The 'ground state' of each harmonic trap may be expanded as a linear combination of the ground state triplet eigenfunctions $|\psi_\nu(t_n)\rangle$, for $\nu = 0, 1, 2$. In the adiabatic limit the evolution of the wavefunction is completely confined to the *gs*-triplet eigenfunctions. Therefore we are justified in constructing this basis using only these three eigenfunctions. This 'trap basis' can be used to recover an approximate form of the rotation matrix $\mathbf{R}$. Thereafter the spatial Hamiltonian matrix $\mathbf{H}_{\mathrm{R}}$ may be recovered to a good approximation.

In our dimensionless units, the 'ground state' of each harmonic trap is a gaussian located on each trap center,

$$\langle \mathbf{x}|\vartheta_\eta(t_n)\rangle = \exp\big(-(\mathbf{x} + x_\eta(t_n))^2\big). \tag{5.16}$$

The 'trap basis' for $|\eta\rangle$ is a normalised linear combination of the *gs*-triplet eigenfunctions, which is the projection of $|\vartheta_\eta(t_n)\rangle$ on the sum of the basis states $|\psi_\nu(t_n)\rangle$. The ket $|\eta\rangle$ may be defined as,

$$|\eta\rangle \;=\; \sum_{\nu=0}^{2} R_{\eta\nu}(t_n)|\psi_\nu(t_n)\rangle. \tag{5.17}$$

For brevity we omit to include the time coordinate, t_n, in the spatial mode ket. The elements $R_{\eta\nu}$ are defined by,

$$\begin{aligned} r_{\eta\nu}(t_n) \;&=\; \int d\mathbf{x}\, \langle \vartheta_\eta(t_n)|\mathbf{x}\rangle\langle \mathbf{x}|\psi_\nu(t_n)\rangle, \\ R_{\eta\nu}(t_n) \;&=\; r_{\eta\nu}(t_n)/\sqrt{\sum_{\mu=0}^{2} r_{\eta\mu}(t_n)}. \end{aligned} \tag{5.18}$$

Here we make use of $R_{\eta\nu}$ to construct a rotation matrix $\mathbf{R}$ which acts to rotate the usual energetic Hamiltonian matrix $\mathbf{H}$, to approximate the equivalent spatial Hamiltonian matrix $\mathbf{H}_{\mathrm{R}}$.

$$\mathbf{H}_{\mathrm{R}}(t_n) \;=\; \mathbf{R}(t_n)\mathbf{H}(t_n)\mathbf{R}^{-1}(t_n). \tag{5.19}$$

where the elements of $\mathbf{R}(t_n)$ are given by (5.18) and $\mathbf{H}(t_n)$ is a diagonal matrix whose diagonal elements, $\hbar\omega_0(t_n)$, $\hbar\omega_1(t_n)$ and $\hbar\omega_2(t_n)$, are the eigenenergies of the *gs*-triplet eigenfunctions.

The spatial modes, as defined per the 'trap basis' approximation, do not form an orthonormal basis. As a result we are forced to make use of the inverse of the rotation matrix $\mathbf{R}(t_n)$, rather than its hermitian conjugate, when rotating to the spatial mode Hamiltonian matrix. The principle downfall of the trap basis approach is that the resulting approximation to the spatial mode Hamiltonian is non-hermitian, which is an artifact of having to use the inverse of $\mathbf{R}(t_n)$ when rotating between both bases.

The explicit form of the spatial Hamiltonian matrix of (5.19) is,

$$\mathbf{H}_{\mathrm{R}}(t_n) \;=\; \hbar \begin{pmatrix} \xi_0(t_n) & \Omega_{01}(t_n) & \Omega_{02}(t_n) \\ \Omega_{10}(t_n) & \xi_1(t_n) & \Omega_{12}(t_n) \\ \Omega_{20}(t_n) & \Omega_{21}(t_n) & \xi_2(t_n) \end{pmatrix}. \tag{5.20}$$

The degree of how non-hermitian $\mathbf{H}_{\mathrm{R}}(t_n)$ becomes during the SAP process is related to the minimum approach distance d_{min}. Naturally the correct spatial Hamiltonian matrix is hermitian and can found by making use of the Euler rotation matrices (5.15) and employing a related, but more sophisticated, approach as that of chapter 4. The trap basis approximation is more than sufficient for our purposes.

5.2.2 Temporal Evolution of the Spatial Modes

At each time step the wavefunction is expanded in the Schrödinger picture as a linear combination of the energetic modes and in the spatial basis, as a direct sum of the spatial modes. Respectively we have,

$$|\Psi(t_n)\rangle \;=\; c_0(t_n)|\psi_0(t_n)\rangle + c_1(t_n)|\psi_1(t_n)\rangle + c_2(t_n)|\psi_2(t_n)\rangle, \tag{5.21a}$$

$$|\Psi(t_n)\rangle_{\mathrm{R}} \;=\; b_0(t_n)|0\rangle + b_1(t_n)|1\rangle + b_2(t_n)|2\rangle. \tag{5.21b}$$

Whilst the spatial mode kets also depend on t_n, here we omit this detail for the purposes of abbreviation. In section 5.3 we discuss the phase evolution of the wavefunction in the

energetic basis. In the spatial representation the wave equation reads,

$$\begin{aligned} \imath\hbar\frac{d}{dt}|\Psi(t_n)\rangle_{\mathrm{R}} &= \mathbf{H}_{\mathrm{R}}(t_n)\ |\Psi(t_n)\rangle_{\mathrm{R}}, \\ \int_{|\Psi(t_n)\rangle_{\mathrm{R}}}^{|\Psi(t_{n+1})\rangle_{\mathrm{R}}} \frac{d|\Psi(t_n)\rangle_{\mathrm{R}}}{|\Psi(t_n)\rangle_{\mathrm{R}}} &= -\frac{\imath}{\hbar}\int_{t_n}^{t_{n+1}} \mathbf{H}_{\mathrm{R}}(t_n)\ dt. \end{aligned} \tag{5.22}$$

The distance between any two points in time is a constant value, $t_{n+1} - t_n = \Delta t$, and it follows that the evolved wavefunction at t_{n+1} is given by,

$$|\Psi(t_{n+1})\rangle_{\mathrm{R}} = \exp\Big(-\frac{\imath}{\hbar}\,\mathbf{H}_{\mathrm{R}}(t_n)\ \Delta t\Big)\,|\Psi(t_n)\rangle_{\mathrm{R}}. \tag{5.23}$$

From this relation the wavefunction may be iteratively time evolved from some initial state at $t = t_0$ to its final state at $t = t_N$. The initial spatial mode state vector, $\mathbf{b}(t_0) = (b_0(t_0), b_1(t_0), b_2(t_0))^{\mathrm{T}}$, is given by the square root of the densities of the wavefunction in each spatial mode.

$$b_\eta(t_0) = \sqrt{\rho_\eta(t_0)}, \tag{5.24}$$

where,

$$\rho_\eta(t_n) = \sum_{\mu,\nu=0}^{2} c_\mu^*(t_n)c_\nu(t_n)\mathcal{D}_{\mu\nu}^{\eta}(t_n); \qquad \mathcal{D}_{\mu\nu}^{\eta}(t_n) = \int_{\mathcal{V}_\eta} d\mathbf{x}\ \langle\psi_\mu(t_n)|\mathbf{x}\rangle\langle\mathbf{x}|\psi_\nu(t_n)\rangle. \tag{5.25}$$

When the initial state coefficients $c_\nu(t_0)$ in the Schrödinger picture are all real valued there is no phase difference between the spatial modes at t_0 and (5.24) is the correct initial state in the spatial basis. The work of chapter 4 has demonstrated this principle for two spatial and energetic modes.

5.2.3 Numerical Calculations

We require the initial state to be localised in $|0\rangle$, such that $(b_0(t_0), b_1(t_0), b_2(t_0))^{\mathrm{T}} \approx (1, 0, 0)^{\mathrm{T}}$. Therefore we choose the energetic mode amplitudes to be $(c_0(t_0), c_1(t_0), c_2(t_0))^{\mathrm{T}} = \big(\sqrt{0.25}, \sqrt{0.5}, \sqrt{0.25}\big)^{\mathrm{T}}$. As the eigenenergies of the basis states are close in value at t_0 (i.e. $d_{\max}$ large), the localised probability density of this initial state is long lived.

For our numerical work the maximum and minimum allowed distances between the outer and central wells (in dimensionless units) are $d_{\max} = 9$ and $d_{\min} = 2.25$. The time scale is discretised into $N + 1$ time steps with $N = 4 \times 10^4$, and the time step $\Delta t = 0.0375$, giving a total time of $t_N = 1500$. We show in section 5.3.1 that these parameters are in the adiabatic regime. The 'counter-intuitive' paths of the $\eta = 0, 2$ trap centers are given by (5.3).

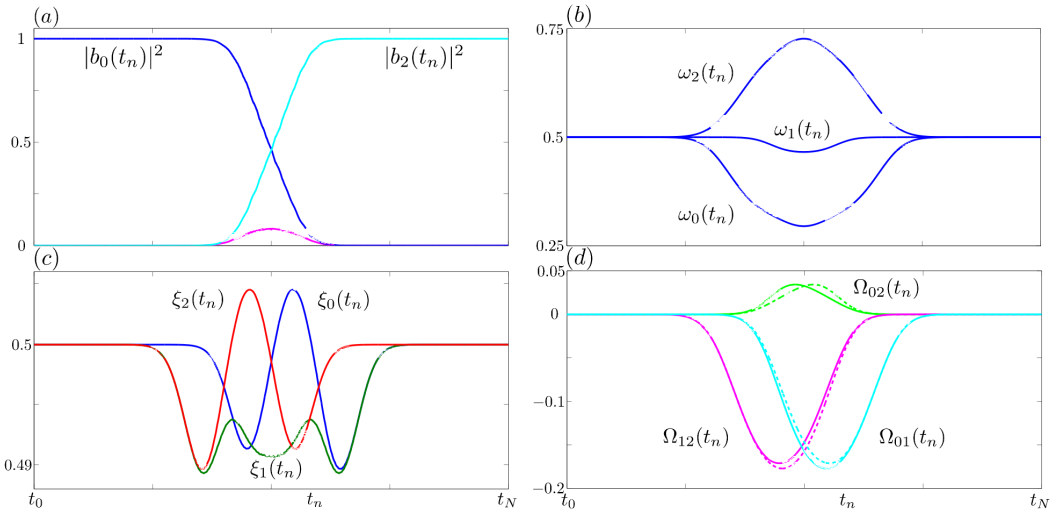


FIGURE 5.4: (a) The absolute value of the spatial mode coefficients (b) The eigenfrequencies of the triple well harmonic oscillator (c) The local frequency terms of the spatial modes (d) The interaction frequency between the spatial modes. The solid (dashed) lines are the upper (lower) matrix elements of $\mathbf{H}_{\mathrm{R}}(t_n)$.

In vector form (5.23) becomes,

$$\begin{pmatrix} b_0(t_{n+1}) \\ b_1(t_{n+1}) \\ b_2(t_{n+1}) \end{pmatrix} = \exp\left[-\imath \begin{pmatrix} \xi_0(t_n) & \Omega_{01}(t_n) & \Omega_{02}(t_n) \\ \Omega_{10}(t_n) & \xi_1(t_n) & \Omega_{12}(t_n) \\ \Omega_{20}(t_n) & \Omega_{21}(t_n) & \xi_2(t_n) \end{pmatrix} \Delta t\right] \begin{pmatrix} b_0(t_n) \\ b_1(t_n) \\ b_2(t_n) \end{pmatrix}. \tag{5.26}$$

This relation is used to iteratively time evolve the initial state vector from $t = t_0 \to t_N$. The matrix elements for each time step are calculated using the trap basis approach of section 5.2.1.

In figure 5.4 (a) we show the probability densities of the spatial mode coefficients throughout the evolution. As expected the 'counter-intuitive' motion of the trap centers has shown complete transfer of probability density from $|0\rangle \to |2\rangle$. In (b) is the frequency spectrum of the *gs*-triplet eigenfunctions, which is equivalent to the eigenfrequencies of $\mathbf{H}_{\mathrm{R}}/\hbar$. The eigenenergy $\hbar\omega_1(t_n)$ corresponds to the eigenvalue of the usual dark state eigenvector, discussed in chapter 3. The dark state eigenenergy remains effectively constant throughout the evolution, i.e. at all t_n it is $\approx 0.5\hbar\omega$.

As the trap centers move there is a splitting of the eigenspectrum and a 'reshuffling' of the probability density of the eigenfunctions between the spatial regions spanned by the traps. This reshuffling (addressed in further detail in sections 5.3.2 and 5.3.3) in turn changes the values of the matrix elements of $\mathbf{H}_{\mathrm{R}}(t_n)$. In figure 5.4 (c) and (d) are the matrix elements of $\mathbf{H}_{\mathrm{R}}(t_n)/\hbar$. In (c) are the local frequencies of the spatial modes. For the majority of the evolution $\xi_0 = \xi_1 = \xi_2 = 0.5$, but around its midpoint these values change slightly. The timescale over which these slight changes are happening corresponds

to the times when the dark state's energy eigenvalue differs from 0.5 in (b). At all times the trace of the Hamiltonian matrix is equivalent in both bases, $\mathrm{Tr}\big(\mathbf{H}_{\mathrm{R}}\big) = \mathrm{Tr}\big(\mathbf{H}\big)$.

In (d) we show the interaction frequencies between the spatial modes. The upper (lower) matrix elements are the solid (dashed) lines. The trap basis approach has recovered (albeit non-hermitian) the familiar characteristic form of the SAP 'counter-intuitive' tunnel coupling between the spatial modes. The tunneling interaction between the unoccupied spatial modes $\Omega_{12}(t_n)$ increases first (reminiscent of the Stokes pulse in STIRAP), followed in-situ by $\Omega_{01}(t_n)$ (the pump pulse in STIRAP). The trap basis approximation has also uncovered the existence of an interaction frequency between the outer traps, $\Omega_{02}(t_n)$. To date this interaction frequency has always been assumed negligible for SAP processes. Obvious from figure 5.4 (d), this interaction frequency reaches a significant magnitude at the midpoint of the evolution. The sign of $\Omega_{02}(t_n)$ is opposite that of the nearest neighbour trap interaction frequencies; at present we are unaware of any obvious physical interpretation for this artifact. Whilst this interaction term may certainly be neglected without significant error, as is usual in the literature, when it is omitted the eigenvalues of the Hamiltonian matrix in the spatial and energetic bases are no longer equal.

The most significant insight the trap basis approximation offers is illuminating the direct relationship between the Hamiltonian matrix in the energetic and spatial bases. It follows that the interaction terms between the spatial modes may be derived analytically from an arbitrary potential of interest. The extension of the work outlined in chapter 4 to three spatial and energetic modes would provide a means of analytically determining the exact spatial dynamics of the wavefunction in the spatial basis.

5.3 SAP in the Energetic Basis

Schrödinger's equation reads,

$$\imath\hbar\frac{d}{dt}|\Psi(t_n)\rangle \;=\; \mathbf{H}(t_n)\;|\Psi(t_n)\rangle. \tag{5.27}$$

With expansion (5.21a), we make use of the chain rule and project on the left hand side with $\int d\mathbf{x}\;\langle\psi_\mu|\mathbf{x}\rangle\langle\mathbf{x}|$. This allows us to recover a differential equation for each coefficient,

$$\dot{c}_\mu(t_n) \;=\; -\imath\sum_{\nu=0}^{2}\big(\omega_\nu(t_n)\delta_{\mu\nu} - \dot{\gamma}_{\mu\nu}(t_n)\big)\;c_\nu(t_n), \tag{5.28}$$

where,

$$\dot{\gamma}_{\mu\nu}(t_n) \;=\; \imath\int d\mathbf{x}\;\langle\psi_\mu(t_n)|\mathbf{x}\rangle\langle\mathbf{x}|\dot{\psi}_\nu(t_n)\rangle. \tag{5.29}$$

This term preserves the unitarity of the evolution whilst coupling the dynamical evolution of the basis states. It follows that the phase evolution of the energetic mode coefficients are iteratively time evolved as,

$$\mathbf{c}(t_{n+1}) \;=\; \mathbf{U}(t_n)\,\mathbf{c}(t_n). \tag{5.30}$$

The time evolution operator is given by,

$$\mathbf{U}(t_n) = \exp\left[-\imath\begin{pmatrix} \omega_0(t_n) - \dot{\gamma}_{00}(t_n) & -\dot{\gamma}_{10}(t_n) & -\dot{\gamma}_{20}(t_n) \\ -\dot{\gamma}_{01}(t_n) & \omega_1(t_n) - \dot{\gamma}_{11}(t_n) & -\dot{\gamma}_{21}(t_n) \\ -\dot{\gamma}_{02}(t_n) & -\dot{\gamma}_{12}(t_n) & \omega_2(t_n) - \dot{\gamma}_{22}(t_n) \end{pmatrix}\Delta t\right]. \tag{5.31}$$

For a time independent Hamiltonian the geometric component $\dot{\gamma}_{\mu\nu}(t_n) = 0$ for all $\mu,\ \nu$ and we observe the usual dynamical evolution of the basis states. For the time dependent Hamiltonian, the geometric component acts to decay the usual dynamical evolution whilst coupling the basis states. As can be seen from (5.29), $\imath/\hbar\dot{\gamma}_{\mu\nu}(t_n)$ is real valued. Noted in [173], this phase factor is non-integrable as the phase evolution of the coefficients is interdependent, since we now have off diagonal terms in the energetic Hamiltonian matrix.

Presently we diverge from the usual form of the time evolution operator (5.31) and derive an analogous expression that helps to shed some light on the coupling of the energetic modes for time dependent processes. Analogous to (5.23) the phase evolution of the basis states in the energy eigenbasis reads,

$$|\Psi(t_{n+1})\rangle \;=\; \exp\left(-\frac{\imath}{\hbar}\,\mathbf{H}(t_n)\,\Delta t\right)|\Psi(t_n)\rangle. \tag{5.32}$$

At each time step the state ket is expanded as a linear superposition of the energetic modes as,

$$|\Psi(t_n)\rangle \;=\; \sum_{\nu=0}^{2} c_\nu(t_n)|\psi_\nu(t_n)\rangle. \tag{5.33}$$

Projecting on the left of (5.32) with $\langle\Psi(t_{n+1})|$ we find the time evolution operator of (5.30) may also we expressed as,

$$\mathbf{U}(t_n) = \begin{pmatrix} e^{-\imath\omega_0(t_n)\Delta t}\cos\,\theta_{00}(t_n) & e^{-\imath\omega_1(t_n)\Delta t}\cos\,\theta_{01}(t_n) & e^{-\imath\omega_2(t_n)\Delta t}\cos\,\theta_{02}(t_n) \\ e^{-\imath\omega_0(t_n)\Delta t}\cos\,\theta_{10}(t_n) & e^{-\imath\omega_1(t_n)\Delta t}\cos\,\theta_{11}(t_n) & e^{-\imath\omega_2(t_n)\Delta t}\cos\,\theta_{12}(t_n) \\ e^{-\imath\omega_0(t_n)\Delta t}\cos\,\theta_{20}(t_n) & e^{-\imath\omega_1(t_n)\Delta t}\cos\,\theta_{21}(t_n) & e^{-\imath\omega_2(t_n)\Delta t}\cos\,\theta_{22}(t_n) \end{pmatrix}. \tag{5.34}$$

The angle $\theta_{\mu\nu}(t_n)$ is a measure of the rotation of the Hilbert space which is the projection of the basis states between the times t_n and t_{n+1} as,

$$\cos\,\theta_{\mu\nu}(t_n) \;=\; \int d\mathbf{x}\;\langle\psi_\mu(t_{n+1})|\mathbf{x}\rangle\langle\mathbf{x}|\psi_\nu(t_n)\rangle. \tag{5.35}$$

For a time independent Hamiltonian, we find that $\cos\,\theta_{\mu\nu}(t_n) = \delta_{\mu\nu}$, and there is no longer any need for the discretised time notation. However, for the time dependent case this matrix is not diagonal and the angle $\theta_{\mu\nu}(t_n)$ becomes an important measure, which acts to couple the occupied eigenfunctions so that their phase evolution becomes interdependent. The elements of the rotation matrix, $\cos\,\theta_{\mu\nu}(t_n)$, in general exhibit a non-hermitian character. As the eigenspectrum changes in time, $\hbar\omega_\mu(t_{n+1}) - \hbar\omega_\nu(t_n)$ is not necessarily equal to $\hbar\omega_\nu(t_{n+1}) - \hbar\omega_\mu(t_n)$, for $\mu \neq \nu$. For our numerical work we find the time evolution operator according to (5.34) a more natural tool for determining the phase evolution of the energetic mode coefficients.

5.3.1 SAP: Adiabaticity And The Geometric Phase

For the numerical work in this section we use the same parameters as those outlined in section 5.2.3. Our initial state $\mathbf{c}(t_0) = (\sqrt{0.25}, \sqrt{0.5}, \sqrt{0.25})^{\mathrm{T}}$ localises the matter wave in $|0\rangle$. The 'counter-intuitive' motion of the trap centers (equation (5.3)) determines how the potential and eigenspectrum changes in time (section 5.1.3). The time evolution of the wavefunction is determined via equation (5.30), where the time evolution operator is given by equation (5.34). Here we allow the length of the stationary period Δt to vary between $0 \rightarrow 0.02$.

A working interpretation of the adiabatic criterion is that the system's evolution has to be slow enough that additional eigenfunctions of the Hilbert space are not excited. For the purposes of this work, we wish to remain confined to the *gs*-triplet, therefore the process is considered adiabatic as long as higher order eigenfunctions are not occupied at any intermediate time t_n. Typical values of t_N for this time dependent process are $t_N > 1000$.

If each incremental change in the eigenfrequencies $\Delta\omega_\nu(t_n) = \omega_\nu(t_{n+1}) - \omega_\nu(t_n)$ for the basis states is sufficiently small (for our purposes this change is less than 10^{-3}), and the 'continuous time' increment Δt is sufficiently large, the process as a whole is smoothly varying. When these conditions are satisfied the chosen quantum state evolves adiabatically. In the limit where $\Delta t \rightarrow 0$ the functional form of the initial wavefunction will not change throughout the whole evolution. To maintain its initial form, the quantum state assumes contributions from the higher order eigenfunctions. Toward the midpoint

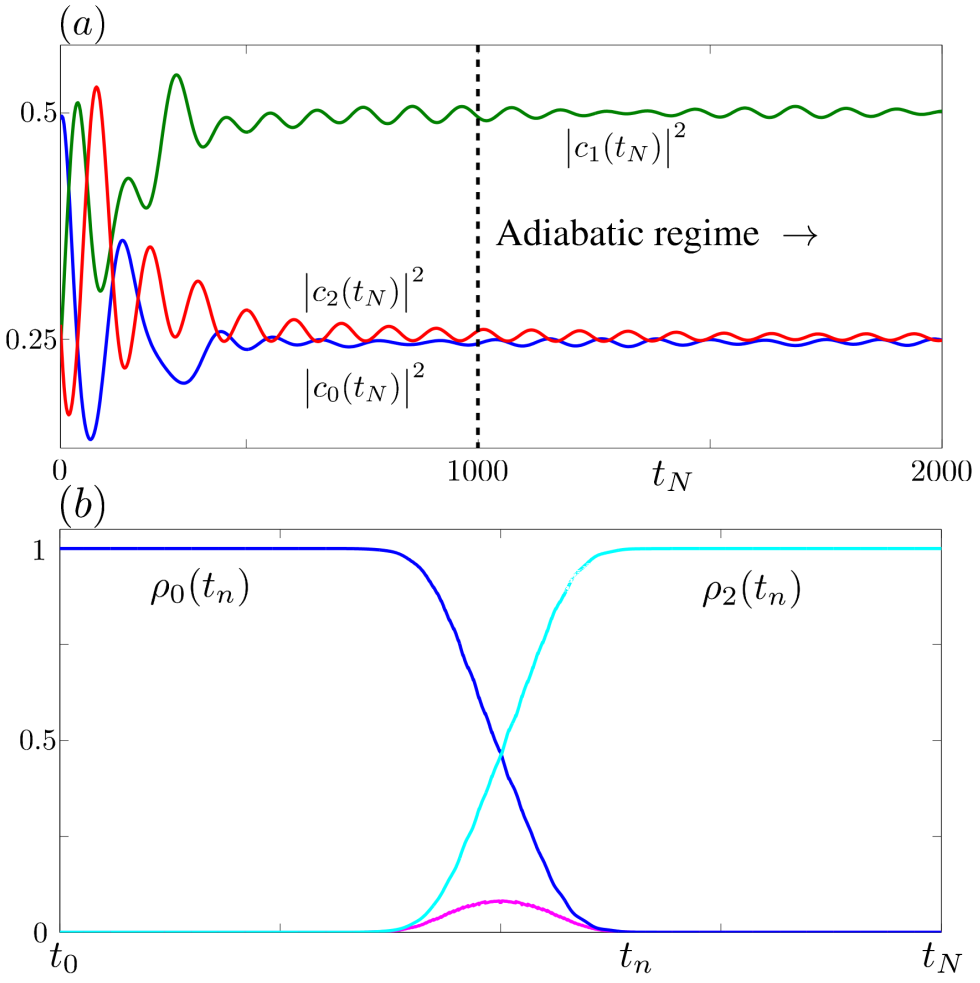


FIGURE 5.5: Counter-intuitive trap paths. (a) The final densities of the energetic mode coefficients as a function of the total time t_N. (b) The probability density of the wavefunction in the traps $|1\rangle$ (dark blue), $|2\rangle$ (pink) and $|3\rangle$ (light blue), with $t_N = 1500$.

of the process the potential and basis states differs most significantly (from their initialised values) and consequently the quantum state will assume a large contribution from higher order eigenfunctions. Increasing the value of the stationary interval Δt adequately allows the quantum state to smoothly evolve into the basis states at each time step.

In figure 5.5(a) we show these probability densities at the end of the evolution for different durations of the process, $t_N = N\Delta t$. For $t_N < 1000$ there is an erratic pattern in the densities of the final state corresponding to diabatic evolution. However for $t_N > 1000$ the probability densities maintain a small amplitude (indicated in figure). Close examination of the oscillation amplitude shows that it is not actually constant, but rather exhibits a repetitious pattern, and we are in the adiabatic regime. In figure 5.5(b) are the densities of the spatial modes ($\eta = 0, 1, 2$) throughout the SAP process with $\Delta t = 0.0375$, calculated via equation (5.25).

The initial state $\mathbf{c}(t_0) = \left(\sqrt{0.25}, \sqrt{0.5}, \sqrt{0.25}\right)^{\mathrm{T}}$ is localised in $|0\rangle$. Conversely, the final state $\mathbf{c}(t_N) \approx e^{i\varphi}\left(\sqrt{0.25}, e^{i\pi}\sqrt{0.5}, \sqrt{0.25}\right)^{\mathrm{T}}$ is localised in $|2\rangle$, where φ is a global phase. The first excited eigenfunction $|\psi_1(t_N)\rangle$ has acquired a π phase from this cyclical process. This acquired phase is detectable/measurable as the probability density of the wavefunction has been transported from $|0\rangle \rightarrow |2\rangle$. This evidently alludes that SAP is a consequence of, and example of, a geometric phase. To explore the nature of this phase factor we consider the temporal evolution of the wavefunction for both the 'counter-intuitive' and 'intuitive' trap motions.

5.3.2 SAP: Counter-Intuitive Trap Paths

Synonymous with matter wave transport in SAP processes is the so-called 'spatial dark state'. Here we look at the occupation of the energy eigenfunctions throughout the SAP evolution according to Schrödinger equation. In figure 5.6(a) are the amplitudes of the basis states $|c_\nu(t_n)|^2$ when $t_N = 1500$. Visible from the plot is a rapid exchange of probability density at the beginning (and end) of the evolution, whereby the wavefunction obtains (loses) complete occupation of the first excited eigenfunction $|\psi_1(t_n)\rangle$. The rapid change at the beginning (and end) is due to the breaking of the symmetry. Initially the interaction terms are all zero, thus the initial state has contributions from all eigenvectors. When the trap motions begin, the interaction terms assume values which result in the complete occupation of $|\psi_1(t_n)\rangle$. Following a complete cyclical evolution, all interaction terms return to zero and the π phase acquired by $|\psi_1(t_n)\rangle$ localises the matter wave in $|2\rangle$. The $|\psi_1(t_n)\rangle$ energy eigenfunction corresponds to the 'spatial dark state' of the spatial Hamiltonian matrix in section 5.2.1.

At $t_n = t_{4\times10^3}$ the matter wave has assumed complete occupation of $|\psi_1(t_n)\rangle$, indicated by the vertical dashed line in figure 5.6(a). The underlying reason for this transition can be understood by looking at the change in the functional form of the basis states between $t_n = t_0$ and $t_n = t_{4\times10^3}$. In figure 5.1 are the eigenfunctions of the *gs*-triplet at $t_n = t_0$, and in figure 5.6(b) are the eigenfunctions at $t_n = t_{4\times10^3}$. The 'counter-intuitive' motion of the $|2\rangle$ trap center localises $\langle\mathbf{x}|\psi_1(t_n)\rangle$ in $|0\rangle$, whereas the ground and second excited eigenfunctions ($\langle\mathbf{x}|\psi_0(t_n)\rangle$ and $\langle\mathbf{x}|\psi_2(t_n)\rangle$) have significant densities only in the $|1\rangle$ and $|2\rangle$ spatial regions. As the eigenspectrum of the *gs*-triplet is initially very close in value, transitions between these states readily occurs. An adiabatic motion of the trap centers prohibits excitation of the wavefunction to higher lying triplets and allows the wavefunction to assume complete occupation of $|\psi_1(t_n)\rangle$.

As we pass the mid-point of the evolution the relative distances of the outer traps to the central one are reversed. As a result the densities of the eigenfunctions in the

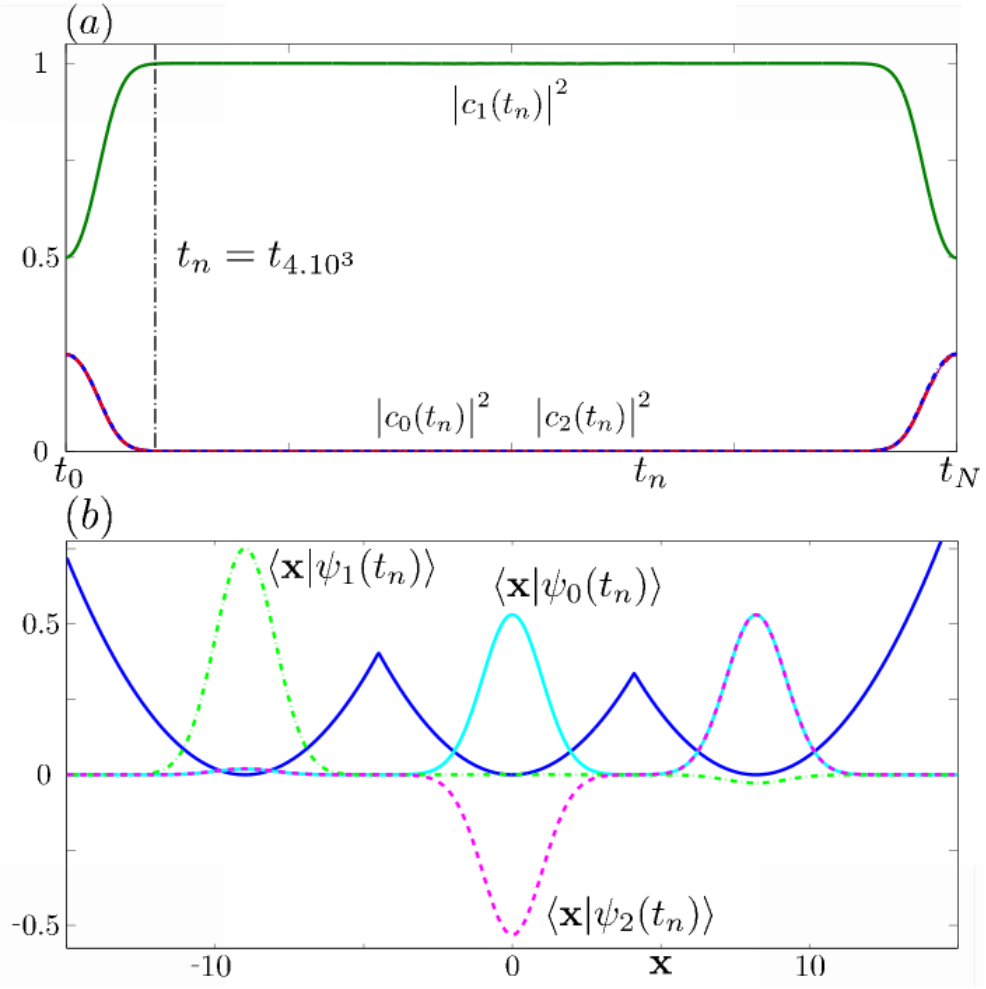


FIGURE 5.6: (a) The probability densities $|c_\nu(t_n)|^2$ for the 'counter-intuitive' trap motions, where $\nu = 0$ dash-dot blue, $\nu = 1$ in green and $\nu = 2$ is in red. (b) In solid blue is the scaled potential $\mathbf{V}(t_n)/25$. Overlayed are the *gs*-triplet eigenfunctions at $t_n = t_{4\times10^3}$.

respective spatial regions are reversed. $|\psi_1(t_n)\rangle$ is now localised in $|2\rangle$ and the remaining eigenfunctions have significant densities only in $|0\rangle$ and $|1\rangle$. During this exchange there is a large spatial overlap of the energetic modes. Since the eigenspectrum is broadly separated (see figure 5.4(d)), and the motion is adiabatic, transitions between the basis states are inhibited and the wavefunction remains in $|\psi_1(t_n)\rangle$. At $t_n = t_N$ the potential returns to its symmetric form and the wavefunction assumes the state $\mathbf{c}(t_N) \approx e^{i\varphi}\left(\sqrt{0.25}, e^{i\pi}\sqrt{0.5}, \sqrt{0.25}\right)^{\mathrm{T}}$. The phase difference present in the wavefunction between at the initial and final times is evidenced by the fact that the probability density is now localised in $|2\rangle$.

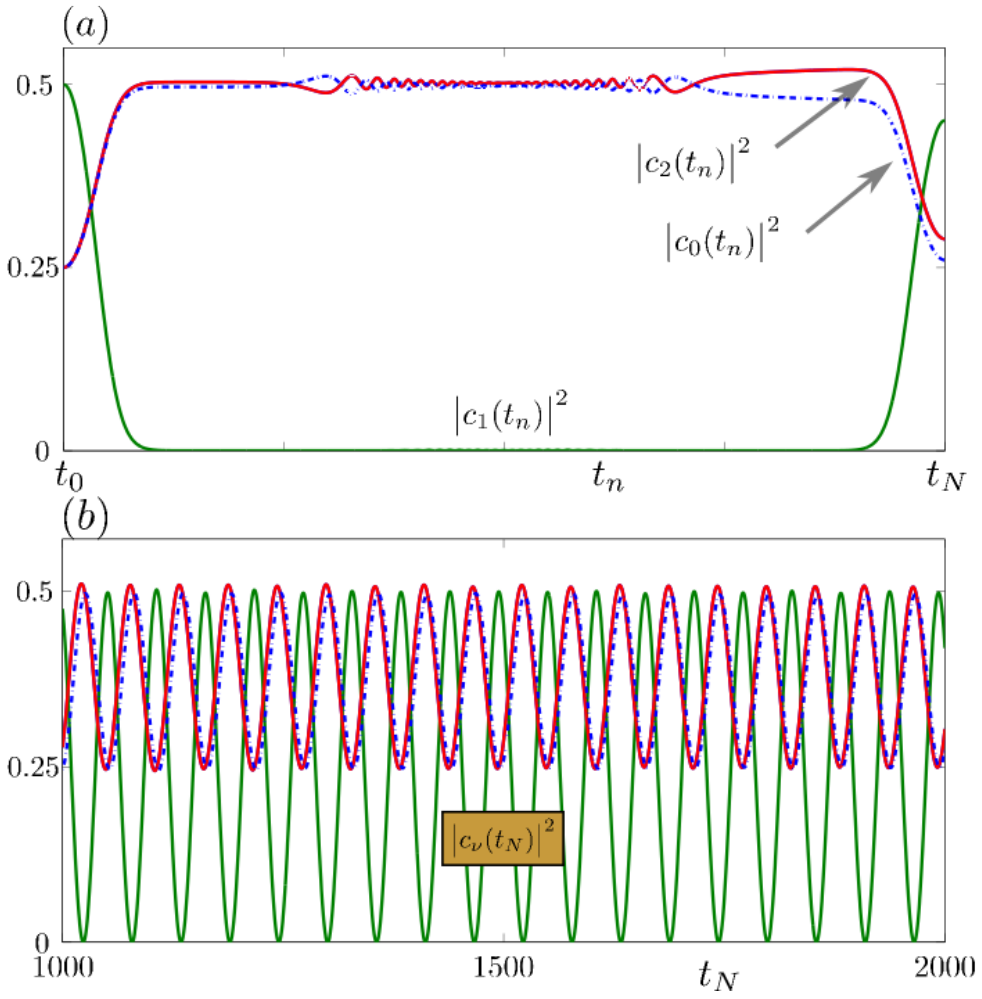


FIGURE 5.7: Intuitive trap paths. (a) Temporal density of the energetic mode coefficients. (b) Final densities of the energetic mode coefficients as a function of the total time t_N.

5.3.3 SAP: Intuitive Trap Paths

The motion of the trap centers given by (5.3) describes the 'counter-intuitive' case. Simply by interchanging the relations provided we have the 'intuitive' trap motions for the wavefunction $\mathbf{c}(t_0) \approx \left(\sqrt{0.25}, \sqrt{0.5}, \sqrt{0.25}\right)^{\mathrm{T}}$ localised in $|0\rangle$. In figure 5.7(a) are the densities of the energetic coefficients throughout the evolution with $t_N = 1500$. In contrast to the 'counter-intuitive' case, the initial delay between the motion of the $|0\rangle$ and $|2\rangle$ trap centers extinguishes the density of $\langle \mathbf{x}|\psi_1(t_n)\rangle$ in $|0\rangle$, whilst the $\langle \mathbf{x}|\psi_0(t_n)\rangle$ and $\langle \mathbf{x}|\psi_2(t_n)\rangle$ energetic modes have densities in $|0\rangle$ and $|1\rangle$ exclusively. As a consequence, the wavefunction assumes a linear superposition of $|\psi_0(t_n)\rangle$ and $|\psi_2(t_n)\rangle$. Throughout the evolution transitions readily occur between these two states as they are close in energy and have a large spatial overlap. Toward the midpoint of the process, transitions between $|\psi_0(t_n)\rangle$ and $|\psi_2(t_n)\rangle$ are reduced due to the splitting of the eigenspectrum but still occur since their densities span overlapping spatial regions. Numerically it can be

shown that if the delay between the trap paths is too large the eigenspectrum becomes narrow at the midpoint of the evolution and transitions to the $|\psi_0(t_n)\rangle$ and $|\psi_2(t_n)\rangle$ basis states readily occur, and consequently leakage into $|1\rangle$ is observed.

When the traps return to their initial positions the final state is somewhat unpredictable as the amplitude of the energetic modes at the end of the process depends on t_N. Illustrated in figure 5.7(b) is the dependency of the final energetic mode densities as a function of the total time t_N. The oscillatory pattern visible in the plot continues ad-infinitum as $t_N \to \infty$.

If the phase difference between the basis states at t_N were random, we would certainly observe a random distribution of density between all spatial modes, however this is not the case. Since $|\psi_0(t_n)\rangle$ and $|\psi_2(t_n)\rangle$, which facilitated the transport of state, have densities only in only the $|1\rangle$ and $|2\rangle$ spatial regions (past the midpoint of the evolution), similarly the final state has densities in only the $|1\rangle$ and $|2\rangle$ spatial regions. The weighting of the densities in these regions is dependent on the total time t_N. We may infer that the reason densities exist only in $|1\rangle$ and $|2\rangle$ is due the phase difference between the basis states (at t_N) acquired from the cyclical evolution. Therefore, similar to the 'counter-intuitive' scheme there is a geometric phase present in the 'intuitive' scheme, albeit less obvious or appealing. A consequence of the geometric phase for the 'intuitive' procedure is that the wavefunction becomes 'localised' in (some weighted combination of) $|1\rangle$ and $|2\rangle$.

5.4 Fractional SAP

In what has now become referred to as fractional SAP (or fractional CTAP [79]), an appropriate adjustment of the trap paths allows for the creation of an even superposition state between the outer traps, originally shown in [70, 174]. Additionally an arbitrary superposition state between the outer traps can be created. In the adiabatic regime, this superposition state is independent of the total time taken for the process and is therefore geometric in origin. Here we detail, and offer an intuitive explanation for, the f-SAP (fractional SAP) process.

For the numerical work in this section, we discretise the time evolution into $N+1$ time steps, with $N = 4.4 \times 10^4$. The stationary period is $\Delta t = 0.1s$, so the total time for the process is $t_N = 4.4 \times 10^3 s$. The maximum and minimum distances of the outer traps, with respect to the center trap, are $d_{\max}$ and $d_{\min}$ respectively. The f-SAP process is invoked by adjusting the motion of the target trap $x_2(t_n)$, whilst the initial trap maintains the usual trajectory used in SAP processes.

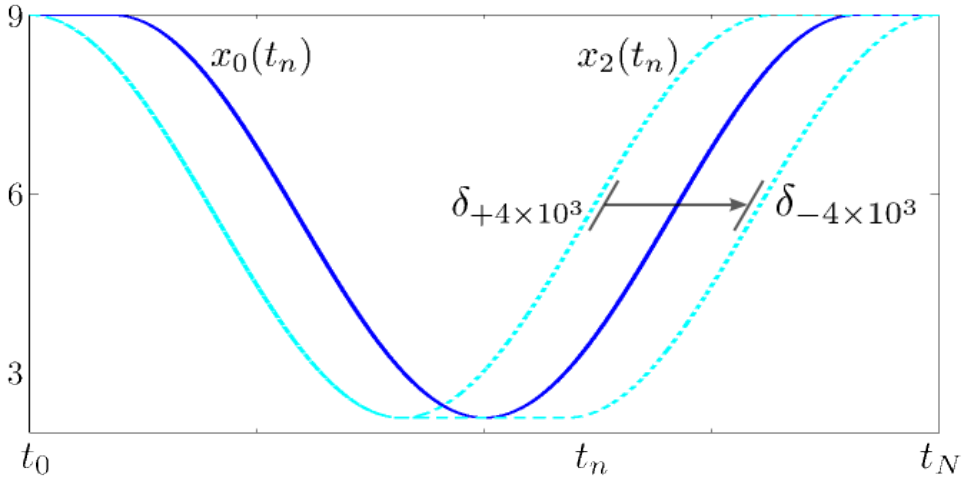


FIGURE 5.8: The trap paths as a function of the delay parameter δ. In solid blue is $x_0(t_n)$, and in dashed cyan is $x_2(t_n)$ according to (5.36) and (5.37) respectively. The chosen values of $\delta = 4 \times 10^3$, and $\delta = -4 \times 10^3$, are indicated in the figure.

Visible from figure 5.8, the $|0\rangle$ trap is initially stationary, $x_0(t_n) = d_{\max}$, for a period of $\frac{1}{11}N$ time steps. It then follows the approach and return sequence, reaching a minimum distance $d_{\min}$, for the following $\frac{9}{11}N$ time steps. For the final $\frac{1}{11}N$ time steps, the $|0\rangle$ trap is stationary, $x_0(t_n) = d_{\max}$. Numerically this is expressed as,

$$\begin{aligned} x_0(t_n) = \Theta\left(\tfrac{9}{11}N - n - 1\right)\left\{\tfrac{d_{\max}-d_{\min}}{2}\left[\cos\left(\frac{2\pi\left(n-\frac{1}{11}N\right)}{\frac{9}{11}N}\right)+1\right]+d_{\min}\right\} \\ + \Theta\left(\tfrac{1}{11}N - n\right)d_{\max} + \Theta\left(n - \tfrac{10}{11}N - 1\right)d_{\max}, \end{aligned} \tag{5.36}$$

where $\Theta(z)$ is the Heaviside step function.

The target trap begins its approach sequence, as is usual for the f-SAP procedure. However, once it reaches the minimum distance $d_{\min}$, the target trap remains stationary for a certain time interval before completing its return sequence. Once it has reached the maximum separation $d_{\max}$, it then remains stationary until the process is completed. Numerically we let the variable δ determine the length of the stationary period. For $\delta = 4\times10^3$, we have the usual SAP process, as the stationary period is zero. When $\delta = 0$, the initial and target traps both return to their maximum separation points in sync. When this occurs, we obtain the even superposition between the outer traps [70, 174]. For other values of the delay parameter, we obtain a range of superposition states. To demonstrate, we let δ vary from $\delta = 4 \times 10^3$ to $\delta = -4 \times 10^3$ (i.e. $\delta = \frac{N}{11} \to -\frac{N}{11}$). The path of the $|0\rangle$ trap for both of these parameters is shown in figure 5.8. Numerically the

path of the initial trap, as a function of the delay δ is written,

$$\begin{aligned} x_2(t_n) \;=\; & -\Theta\left(\tfrac{4.5}{11}N-n-1\right)\left\{\tfrac{d_{\max}-d_{\min}}{2}\left[\cos\left(\tfrac{2\pi n}{\frac{9}{11}N}\right)+1\right]+d_{\min}\right\} \\ & -\left(\Theta\left(n-\tfrac{4.5}{11}N-1\right)-\Theta\left(n-\tfrac{5.5}{11}N+\delta-1\right)\right)d_{\min} \\ & -\left(\Theta\left(n-\tfrac{5.5}{11}N+\delta\right)-\Theta\left(n-\tfrac{10}{11}N+\delta\right)\right)\times \\ & \qquad \times\left\{\tfrac{d_{\max}-d_{\min}}{2}\left[\cos\left(\tfrac{2\pi\left(n-\frac{1}{11}N+\delta\right)}{\frac{9}{11}N}\right)+1\right]+d_{\min}\right\} \\ & -\Theta(n-\frac{10}{11}N+\delta)d_{\max}. \end{aligned} \tag{5.37}$$

The initial state $\mathbf{c}(t_0)=(1/2,1/\sqrt{2},1/2)^{\mathrm{T}}$ is localised in the $|0\rangle$ spatial mode. The time dependent Hamiltonian changes according to the trap motions (5.36) and (5.37), and the quantum state evolves via $\mathbf{c}(t_{n+1})=\mathbf{U}(t_n)\mathbf{c}(t_n)$, where $\mathbf{U}(t_n)$ is given by (5.34).

In figure 5.9(a) we show the densities of the final state in the $\eta=0,2$ spatial modes at the end of the f-SAP process, with $\rho_0(t_N)$ and $\rho_2(t_N)$ given by (5.25). We note here that when $\delta=4\times10^3$ we have the traditional SAP process, and the final quantum state is localised in the $\eta=2$ spatial mode. Close examination of figure 5.9(b) shows that the final state is $\mathbf{c}(t_N)\approx e^{\imath\varphi}\left(\sqrt{0.25},e^{i\pi}\sqrt{0.5},\sqrt{0.25}\right)^{\mathrm{T}}$. Conversely when $\delta=-4\times10^3$, the matter wave is not transported to $|2\rangle$, and the final state is localised in the $\eta=0$ spatial mode. From figure 5.9(b) we may infer that the final state is $\mathbf{c}(t_N)\approx e^{\imath\varphi}\left(\sqrt{0.25},\sqrt{0.5},\sqrt{0.25}\right)^{\mathrm{T}}$. For all other values of the delay parameter, δ, the final state is in some weighted spatial superposition between the outer traps.

When $\delta=0$, the traps return to their initial positions in sync and the final state is distributed evenly between the $\eta=0,2$ spatial modes, shown in figure 5.9(a). From (b) we acknowledge that in this case $|\psi_1\rangle$ is the only energetic mode occupied at the end of the (even) f-SAP evolution. To help interpret this result we first recognise that there is not one, but a set of quantum states that may occupy an even superposition between the $\eta=0,2$ spatial modes. From figure 5.1 we can see that the quantum state in the energetic representation $\mathbf{c}=(1/\sqrt{2},0,1/\sqrt{2})^{\mathrm{T}}$, corresponds to the quantum state in the spatial representation $\mathbf{b}=(1/\sqrt{2},0,1/\sqrt{2})^{\mathrm{T}}$, i.e. an even superposition between the outer traps. Our work from chapter 4 has shown that when there is no phase difference between the energetic modes, there is also no phase difference between the spatial modes.

Here we wish to establish how a phase difference between the spatial modes, relates to the quantum state in the energetic representation. To do so, let us consider the spatial state $\mathbf{b}=(1/\sqrt{2},0,e^{\imath\phi_s}/\sqrt{2})^{\mathrm{T}}$, where $0\leq\phi_s\leq2\pi$. In the spatial representation, it is a trivial exercise to apply the phase difference between the spatial modes. However, to apply the phase ϕ_s to the quantum state in the energetic representation, we first expand

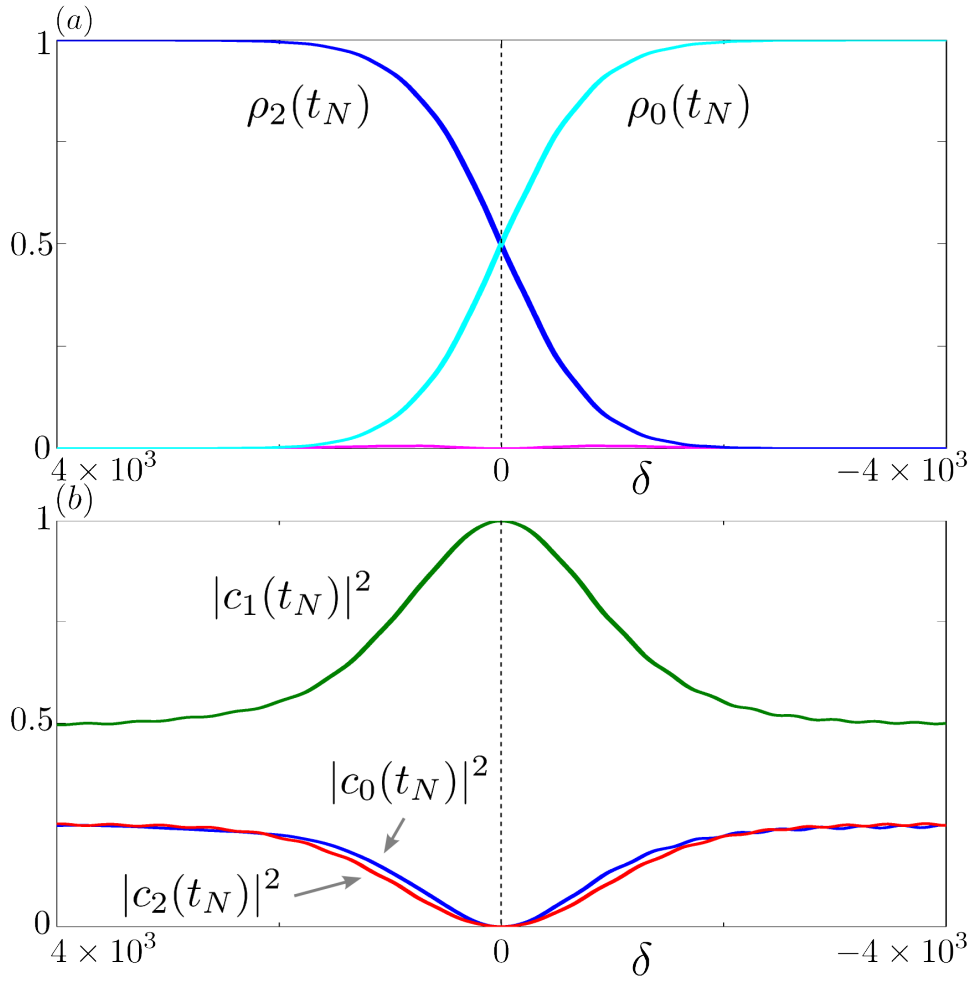


FIGURE 5.9: (*a*) The density of the spatial modes $|0\rangle$ and $|2\rangle$, at the end of the f-SAP process, as a function of the delay parameter δ. Note that when $\delta = 0$ the traps return to their initial positions in sync and we obtain an even superposition between the outer traps. (*b*) The densities of the energetic modes at $t_n = t_N$, as a function of δ.

the state in terms of the energy eigenfunctions as,

$$\langle \mathbf{x}|\Psi_{\text{init}}\rangle = \tilde{c}_0\langle \mathbf{x}|\psi_0\rangle + \tilde{c}_1\langle \mathbf{x}|\psi_1\rangle + \tilde{c}_2\langle \mathbf{x}|\psi_2\rangle. \tag{5.38}$$

where the amplitudes of the even superposition state are $(\tilde{c}_0, \tilde{c}_1, \tilde{c}_2)^{\mathrm{T}} = (1/\sqrt{2}, 0, 1/\sqrt{2})^{\mathrm{T}}$. Thereafter we separate the state into its components in the different spatial modes, $\eta = 0, 1, 2$ and multiply the component in the $\eta = 2$ spatial mode by the desired phase factor. We have,

$$\langle \mathbf{x}|\Psi_{\text{new}}\rangle = \langle \mathbf{x}|\Psi_{\text{init}}\rangle_{\mathcal{V}_0} + \langle \mathbf{x}|\Psi_{\text{init}}\rangle_{\mathcal{V}_1} + e^{\imath\phi_s}\langle \mathbf{x}|\Psi_{\text{init}}\rangle_{\mathcal{V}_2} \tag{5.39}$$

It follows that the 'new' energetic mode coefficients are given by,

$$c_\nu \;=\; \int d\mathbf{x}\; \langle \psi_\nu|\mathbf{x}\rangle\langle \mathbf{x}|\Psi_{\text{new}}\rangle. \tag{5.40}$$

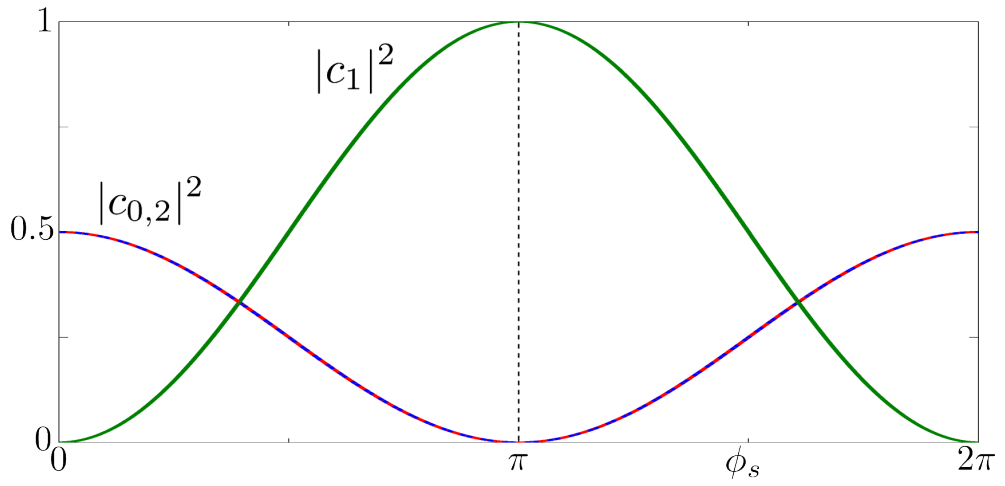


FIGURE 5.10: A quantum state, $\mathbf{c} = (c_0, c_1, c_2)^{\mathrm{T}}$, evenly distributed between the $\eta = 0, 2$ spatial modes. Plotted are the densities of the energetic modes $|c_\nu|^2$ for $\nu = 1$ green, and $\nu = 0, 2$ blue, dash-dot red, as a function of the phase difference ϕ_s between $\eta = 0, 2$ spatial modes. See text for details.

In figure 5.10 we show the densities of the energetic mode coefficients $|c_\nu|^2$, for $\nu = 0, 1, 2$ as a function of the phase difference, ϕ_s, between the $\eta = 0, 2$ spatial modes. Obvious from the figure is that when the phase difference between the spatial modes is, $\phi_s = \pi$, the only energy eigenfunction occupied is $|\psi_1\rangle$. Here we recall that the functional form of $\langle \mathbf{x}|\psi_1\rangle$, shown in figure 5.1, is antisymmetric. It therefore makes sense that there is a π phase difference between the spatial modes, when $|\psi_1\rangle$ is the only occupied energetic mode. We may now affirm that the f-SAP protocol, which produces an even superposition state between the $\eta = 0, 2$ spatial modes, imposes a π phase on the quantum state in the spatial representation. The acquired phase is independent of the total time taken for the evolution and is (once again) geometric in origin.

Returning to figure 5.9(b) we note that for the traditional SAP process ($\delta = 4 \times 10^3$), the π phase acquired from the cyclical evolution is manifest in the energetic modes. Since only one spatial mode is occupied ($|2\rangle$), there can be no phase difference between the spatial modes. Conversely, for the even f-SAP process ($\delta = 0$), the π phase acquired from the cyclical evolution is manifest in the spatial modes. Here, only one energy eigenfunction is occupied ($|\psi_1\rangle$), thus there can be no phase difference between the energetic modes. Varying the delay parameter from $\delta = 4 \times 10^3 \to 0$, distributes the π phase between both the spatial and energetic representations, thereby creating a range of spatial superposition states between $|0\rangle$ and $|2\rangle$ which is independent of the total time t_N.

From figure 5.9(b) we see that when $\delta = -4 \times 10^3$, the final state is localised in $|0\rangle$, and there is no phase difference between the energetic modes. Tuning the delay parameter from $\delta = 0 \to -4 \times 10^3$, extinguishes the phase acquired from the f-SAP evolution from

$\pi \rightarrow 0$. Consequently the range of spatial superposition states created, between $|0\rangle$ and $|2\rangle$, is the inverse of those created when the delay is varied from $\delta = 4 \times 10^3 \rightarrow 0$. Thus it is revealed that tuning the delay parameter allows for the creation of an arbitrary spatial superposition state between $|0\rangle$ and $|2\rangle$, which is independent of t_N and therefore geometric in origin.

5.5 Discussion

We have shown in this chapter a means of relating the evolution of the wavefunction in the spatial and energetic basis. Using the trap basis approximation an intuitive relationship between the phase evolution of the spatial and energetic modes becomes obvious. The interaction frequency between nearest neighbour, and next nearest neighbour spatial modes, is uncovered using this approach. This demonstrates that interaction frequency between any two modes must be resolved as a component of the interaction between all spatial modes. A distinct advantage of using the trap basis approach, is that the matrix elements of the spatial mode Hamiltonian do not depend on the state of the wavefunction in the energetic representation, as was found in chapter 4.

Here we have shown that SAP acts to impose a π phase on the $|\psi_1(t_n)\rangle$ eigenfunction due to the geometry of the cyclical evolution. The nature of this type of quantum geometric phase is such to impose a phase on the internal energetic modes of the quantum state. The signature of the acquired phase in three level SAP processes, is the transport of a localised matter wave from $|0\rangle \rightarrow |2\rangle$. We further showed how this phase is present in f-SAP processes, which permits the creation of spatial superposition states between the outer spatial modes.

The form of the geometric phase acquired from a quantum state in SAP processes differs from, for instance, the classical geometric phase acquired by Foucault's pendulum [175]. Following a full rotation of the earth, the plane through which Foucault's pendulum oscillates is rotated by an angle which is determined by the solid angle it traces out during the rotation of the earth. A classical geometric phase of this type imposes a global geometric phase to the whole system whereas the geometric phase associated with SAP and STIRAP processes acts to impose a phase on an internal state of the system.

Traditionally the dark state eigenvector in the spatial representation, is considered the reason for the transport of the matter wave. Here we examined the mechanism of the SAP process via the dark state in the energetic representation. Viewing the transport of the wavefunction in the energetic basis shows that SAP is a consequence of a geometric

phase acquired from the cyclical evolution. Extending the usual three trap potential to multiwell potentials offers exciting possibilities for the creation of spatial qubit and qutrit states.

Chapter 6

SAP In Four Mode Systems - Qubit and Qutrit States

Controlling the dynamics of single quantum particles is one of the holy grails in the area of quantum engineering. While for charged particles strong coupling to electrodynamical fields can be used, for neutral atoms only recently microtraps based on optical and magnetic fields have been developed [176]. Numerous experimental setups have been suggested and demonstrated which show great promise for, the production, control and study of nano scale devices. Today experimental advances have shown a high degree of control over the manipulation and storage of single atoms using optical dipole traps [154], tightly focused laser beams [177] and electro-optical nanotraps for single atoms [178]. Site resolved images of single atoms on optical lattices have been achieved [179] and the coherent splitting of BECs using active optical elements with programmable phase gratings [180]. Recently it has been pointed out that many of the adiabatic techniques in optics (in particular STIRAP processes [46, 47, 59, 181]) have an analogon with atoms in trapped microscopic potentials. These include the transfer of neutral atoms between optical dipole traps [43, 56] and radio frequency potentials [171], electrons in arrays of quantum dots [40, 57, 64, 67, 77, 78], the transfer of a classical light source [81, 82] and neutral atoms in waveguide arrays [70, 116] and nanocircuits [63]. With the rate of modern experimental development the realisation of these systems looks promising and the testing of the underlying theoretical models an exciting prospect. Here we explore the potentiality of multi-mode Spatial Adiabatic Passage (SAP) systems for the engineering of spatial qubit and qutrit states.

For three level SAP (and STIRAP) systems there is a single population trapping state, known as the 'dark state' in the spatial mode basis, which corresponds to the first excited eigenfunction in the energetic mode basis. Extensions of this model to four level

systems and beyond, allows for an exploration of a much richer phenomenology. For four level systems in particular there are two population trapping states. The dynamics of these population trapping states allows for the creation of superposition states between localised spatial modes, and was originally explored in optical systems by Unanyan *et al.* [182]. As we have already shown there is a distinct advantage attributed to the study of of these adiabatic processes in the matter wave setting. The dynamics of the systems under study may be explored from not only the traditional quantum optics viewpoint but also in the energy eigenbasis. Moreover, in the matter wave setting, the spatial mode Hamiltonian shows significant and non-negligible cross coupling between all localised spatial modes. When four localised spatial modes are considered, the SAP process can be used to create superposition states between two target spatial modes, which is the focus of this chapter. Here we show that all elements of the spatial mode Hamiltonian matrix contribute to the SAP process, which can be used to measure an existing phase difference in an even 'spatial mode' superposition quantum state.

The content of this chapter is essentially a marriage of two papers, the first by Eckert *et al.* [56] and the second by Unanyan *et al.* [182], made possible from the theoretical grounding of the SAP process established in chapter 5. The former bridged the gap between three-level optical and three-level atom-optical STIRAP, now known by the acronym SAP. Whereas the latter studied non-abelian geometrical phase factors of a four level atom which are present in a STIRAP-type evolution. Unanyan *et al.* showed that in systems with more than one population trapping state, possible in four or more level systems, a *non*-Abelian transformation can take place, which changes the expectation value of a physical observable. In our case this is the trap occupation probability. In section 6.1 we present the time dependent potential, the related Hamiltonian and the energy eigensystem. The time evolution of the system in the spatial basis is outlined in section 6.2.1 and in the energetic basis in section 6.2.2. We perform numerical calculations to show that these systems readily produce an even superposition state between the target spatial modes in section 6.2.2. We demonstrate that this procedure can be implemented to measure any existing phase difference between the spatial modes in section 6.3. In turn this facilitates the creation of superposition states between the spatial modes. The control of the phase of the spatial modes allows for the creation of arbitrary qubit and qutrit states. In section 6.5 we discuss the results and conclude.

6.1 The Hamiltonian And The Time Dependent Potential

As in chapter 5, we discretise the time spectrum into $N+1$ points in time, where each time coordinate is identified by t_n where $n = 0, 1, 2, \ldots, N$, and $t_{n+1} - t_n = \Delta t$. At each

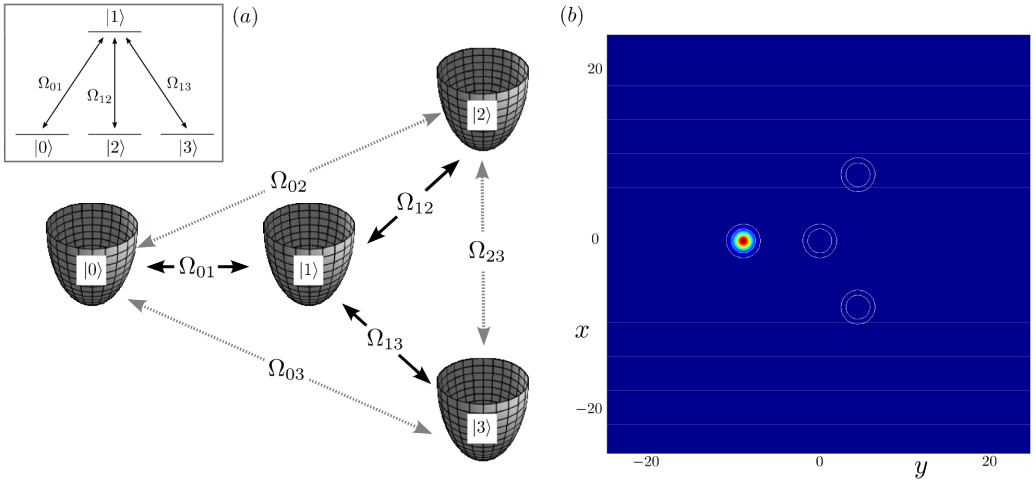


FIGURE 6.1: (a) Schematic consisting of the four spatial modes $|0\rangle$, $|1\rangle$, $|2\rangle$ and $|3\rangle$ spanned by resonant harmonic traps. Overlayed are in interaction frequencies between the spatial modes. Inset is the related optical scheme. (b) The numerical grid used for the numerical calculations. The contour lines show the position of the traps.

time step t_n the wavefunction evolves according to the Hamiltonian $\mathbf{H}(t_n)$ for a stationary increment of time Δt followed by an instantaneous change of the Hamiltonian at the following point in time. The evolved wavefunction then assumes a linear combination of the Hilbert space basis states at the following time step $t = t_{n+1}$.

The system we consider consists of four piecewise harmonic potentials arranged in a Y-shaped structure on a two dimensional plane as shown in fig. 6.1(a). Each harmonic potential is centered on the position (x_η, y_η) where $\eta = 0, 1, 2, 3$ refers to the trap centers of the related harmonic traps. The trapping frequency in the $\hat{x}$ and $\hat{y}$ directions are equal $\omega_x = \omega_y = \omega$, and each harmonic trap has the same trapping frequency. The spatial modes $|\eta\rangle = |0\rangle,\ |1\rangle,\ |2\rangle,\ |3\rangle$ are the spatial regions spanned by each trap. This potential is made time dependent by allowing the outer traps to move along the lines indicated by $\Omega_{01},\ \Omega_{12}$ and Ω_{13}, whilst the center trap $|1\rangle$ remains stationary at all times. The two dimensional time dependent potential is defined at each t_n by,

$$\mathbf{V}(\mathbf{x}, t_n) \;=\; \frac{1}{2}\,\min \sum_{\eta=0}^{3} \Big[\big(x + x_\eta(t_n)\big)^2 + \big(y + y_\eta(t_n)\big)^2 \Big]\,. \tag{6.1}$$

where $\mathbf{x} = (x, y)$, and the all lengths have been scaled by $\sqrt{\hbar/m\omega}$. The scaled Hamiltonian is,

$$\mathbf{H}(t_n) \;=\; \hbar\omega \left(-\frac{\partial^2}{\partial \mathbf{x}^2} \;+\; \mathbf{V}(\mathbf{x}, t_n) \right). \tag{6.2}$$

At present there is no obvious way to determine, by analytic means, the related eigensystem of this two dimensional Hamiltonian. It is possible however to obtain the related eigensystem by using numerical techniques. This essentially reduces to a two dimensional

eigenvalue and eigenvector problem, solvable using the technique of finite differences [183]. The procedure involved is outlined in section 6.1.2.

6.1.1 The Trap Motions

This arrangement of four harmonic traps offers a wealth of different ways to perform a cyclical evolution. As this a first exploration of this type of potential we consider a simple form of the time dependence. The harmonic traps all have the same trapping frequency $\omega_x = \omega_y = \omega$, and the center trap $|1\rangle$ remains stationary at all times $(x_1(t_n), y_1(t_n)) = (0, 0)$. We shall consider an initial state localised in the $|0\rangle$ trap and the $|2\rangle$ and $|3\rangle$ traps take the form of the target traps, similar to the single target spatial mode in the usual three mode SAP. The outer traps approach the center trap along the axis joining the trap centers, whilst maintaining a constant angle of $2\pi/3$ between all outer traps, as illustrated in figure 6.1. We impose the "counter-intuitive" trap motions by allowing the $|2\rangle$ and $|3\rangle$ trap centers to first approach the center $|1\rangle$ trap, followed by the $|0\rangle$ trap with an appropriate delay. The delay between the motion of the trap centers is taken to be $\delta = (0.1)N$ time steps. All traps are initially separated a distance $d_{\max}$ and reach a minimum distance $d_{\min}$ from the center trap.

The path of the $\eta = 0, 2, 3$ trap centers are then,

$$x_0(t_n) = 0, \tag{6.3a}$$
$$y_0(t_n) = \Theta(\alpha_0)\left\{\tfrac{d_{\max}-d_{\min}}{2}\left[\cos(\theta_0)+1\right] + d_{\min}\right\} + \Theta(\beta_0)d_{\max}, \tag{6.3b}$$

$$x_2(t_n) = -\cos(\tfrac{\pi}{3})\left(\Theta(\alpha_2)\left\{\tfrac{d_{\max}-d_{\min}}{2}\left[\cos(\theta_2)+1\right] + d_{\min}\right\} + \Theta(\beta_2)d_{\max}\right), \tag{6.4a}$$
$$y_2(t_n) = -\sin(\tfrac{\pi}{3})\left(\Theta(\alpha_2)\left\{\tfrac{d_{\max}-d_{\min}}{2}\left[\cos(\theta_2)+1\right] + d_{\min}\right\} + \Theta(\beta_2)d_{\max}\right), \tag{6.4b}$$

$$x_3(t_n) = \cos(\tfrac{\pi}{3})\left(\Theta(\alpha_3)\left\{\tfrac{d_{\max}-d_{\min}}{2}\left[\cos(\theta_3)+1\right] + d_{\min}\right\} + \Theta(\beta_3)d_{\max}\right), \tag{6.5a}$$
$$y_3(t_n) = -\sin(\tfrac{\pi}{3})\left(\Theta(\alpha_3)\left\{\tfrac{d_{\max}-d_{\min}}{2}\left[\cos(\theta_3)+1\right] + d_{\min}\right\} + \Theta(\beta_3)d_{\max}\right), \tag{6.5b}$$

where $\Theta(z)$ is the Heaviside step function, and $n = 0, 1, 2, \ldots, N$. The usual counter-intuitive motion of the trap centers is employed when $(\alpha_0, \beta_0, \theta_0) = (n-\delta-1, \delta-n, 2\pi(n-\delta)/(N-\delta))$, and $(\alpha_2, \beta_2, \theta_2) = (\alpha_3, \beta_3, \theta_3) = (N-n-\delta-1, n+\delta-N, 2\pi n/(N-\delta))$.

6.1.2 The Finite Difference Method

A prerequisite to properly time evolving this time dependent system is a means of correctly deriving the eigenvalues and eigenfunctions of the potential at each time step. Presently an analytical means of finding the eigensystem is beyond our current capacity, but what we can do is make use of the numerical technique known as the finite difference method to approximate the eigensystem, which is the focus of this section.[1]

We aim to construct a computer code that can numerically compute the eigenvalues and two dimensional eigenfunctions of,

$$\left(-\frac{1}{2}\frac{\partial^2}{\partial x^2} - \frac{1}{2}\frac{\partial^2}{\partial y^2} + \mathbf{V}(x,y)\right)\psi(x,y) \;=\; E\psi(x,y), \tag{6.6}$$

for a potential $\mathbf{V}(x,y)$ with an energy eigenvalue E. For abbreviation purposes we have omitted to include the time step t_n.

Our potential (6.1) is represented on a square numerical grid, with the total number of points along the $\hat{x}$ and $\hat{y}$ axes of $N_x = N_y = 2^7$. A schematic of our grid is found in figure 6.1(b). This is our computational domain, consisting of a total of $N_x \times N_y$ nodes, at the locations (x,y). The distance between each node in the $\hat{x}$ and $\hat{y}$ directions are equal, $\Delta x = \Delta y$, seen in fig. 6.2(a). An array of nodes is generated by evaluating the Cartesian product of the x and y locations. The result is a grid of points, shown in figure 6.2(b), with the grid nodes labeled (x_p, y_q) respectively, with a total of $N_x = P$ nodes in the $\hat{x}$ direction and $N_y = Q$ nodes in the $\hat{y}$ direction. The labeling of the nodes in this manner is important in building a set of linear equations whose solution determines the numerical approximation. The grid shown in figure 6.2(b) is that on which the numerical solution to (6.6) is to be determined. Therefore to solve equation (6.6) using finite differences, an eigenvalue problem of size $N_x \times N_y$ must be solved.

The procedure for solving (6.6) using finite differences is as follows; Each node is identifiable by its label, (x_p, y_q), which is referred to as local numbering. The corresponding number of the node in the mesh is called the global number of the node. Therefore for a node of local numbering (p,q), the corresponding global number is $r = (p-1)N_x + q$, when the nodes are set up as in figure 6.2. The global number corresponds to the row and column indices of the matrix whose eigenvalues determine the numerical solution.

[1] We acknowledge insightful discussions with Robert Sheehan for the clarification of the theory contained in this section.

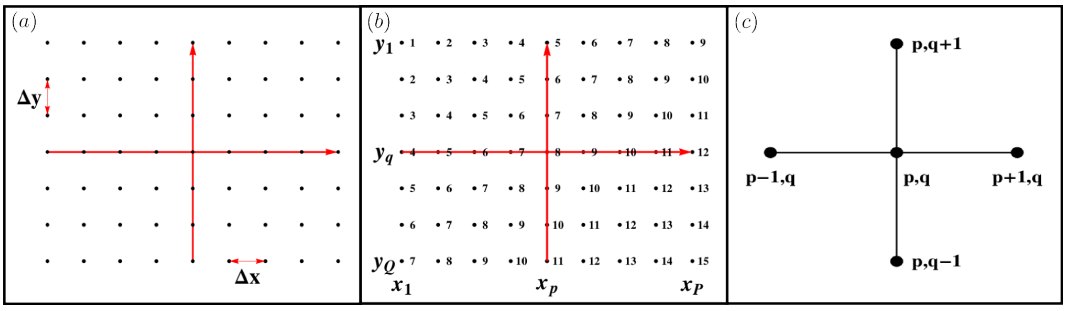


FIGURE 6.2: (a) Finite Difference Nodes, (b) Finite Difference Node Numbering and (c) the Grid spacing around the point (x_p, y_q).

An important consideration is how the global numbering of a node corresponds to its location (x_p, y_q) on the mesh. Inverting the formula for the global numbering we obtain,

$$(p,q) = \left(\left\lfloor \frac{r-1}{N_x} \right\rfloor + 1, r - N_x \left\lfloor \frac{r-1}{N_x} \right\rfloor \right). \tag{6.7}$$

where $\lfloor x \rfloor$ is the floor function, i.e. the smallest integer less than or equal to x. From this formula the necessary matrices can be constructed and the value of the function $\psi_\nu(x,y)$ can be assigned to each node correctly.

The numerical solution to (6.6) is evaluated using the finite difference technique by replacing the partial derivatives in (6.6) with the equivalent derivatives using finite differences. To proceed we define the value of the function at the node (x_p, y_q) as $\psi(x_p, y_q) \equiv \psi_{p,q}$. The second order partial derivatives of the function is then given by,

$$\frac{\partial^2}{\partial x^2}\psi_{p,q} \approx \frac{\psi_{p-1,q} - 2\psi_{p,q} + \psi_{p+1,q}}{(\Delta x)^2}, \tag{6.8a}$$

$$\frac{\partial^2}{\partial y^2}\psi_{p,q} \approx \frac{\psi_{p,q-1} - 2\psi_{p,q} + \psi_{p,q+1}}{(\Delta y)^2}. \tag{6.8b}$$

A conceptual illustration of the relevant labeling is found in figure 6.2(c). Plugging the above into (6.6) results in,

$$-\frac{\psi_{p-1,q}}{2(\Delta x)^2} - \frac{\psi_{p+1,q}}{2(\Delta x)^2} + \frac{\psi_{p,q-1}}{2(\Delta y)^2} - \frac{\psi_{p,q+1}}{2(\Delta y)^2} + \left(V_{p,q} + \frac{1}{(\Delta x)^2} + \frac{1}{(\Delta x)^2} \right) \psi_{p,q} = E\psi_{p,q}. \tag{6.9}$$

In order to evaluate the related eigensystem the above equation needs to be converted to an eigenvalue problem. To do so we build a matrix from the information contained on the mesh, by converting the local index values into global index values. For a total number of N_x nodes in the $\hat{x}$-direction and N_y nodes in the $\hat{y}$-direction (with $N_x = N_y$), the global number of the node (x_p, y_q) is given by $r = (p-1)N_x + q$. It follows that,

$$(p,q) \to r, \qquad (p \pm 1, q) \to r \pm N_x, \qquad (p, q \pm 1) \to r \pm 1. \tag{6.10}$$

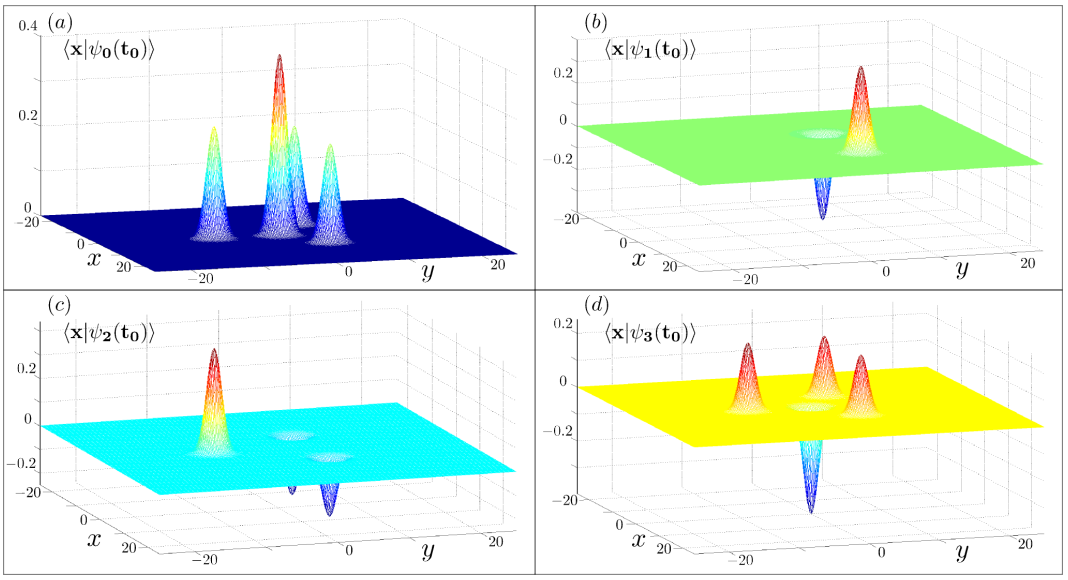


FIGURE 6.3: The functional form of the *gs*-quadruplet at $t = t_0$. In (a) is $\langle \mathbf{x}|\psi_0(t_0)\rangle$, (b) is $\langle \mathbf{x}|\psi_1(t_0)\rangle$, (c) is $\langle \mathbf{x}|\psi_2(t_0)\rangle$ and (d) is $\langle \mathbf{x}|\psi_3(t_0)\rangle$.

Rewriting (6.9) in terms of the global index r,

$$-\frac{\psi_{r-N_x}}{2(\Delta x)^2}-\frac{\psi_{r+N_x}}{2(\Delta x)^2}+\frac{\psi_{r-1}}{2(\Delta y)^2}-\frac{\psi_{r+1}}{2(\Delta y)^2}+\left(V_r+\frac{1}{(\Delta x)^2}+\frac{1}{(\Delta x)^2}\right)\psi_r \;=\; E\psi_r. \quad (6.11)$$

This relation allows us to build the necessary matrix from the mesh information. The matrix itself will be sparse and is best described as a tridiagonal matrix with wings. The diagonal terms in the matrix multiply ψ_r, the upper and lower diagonal terms multiply $\psi_{r\pm1}$, and the terms in the wings multiply $\psi_{r\pm N_x}$.

6.1.3 The Energy Eigensystem and Initialisation of the State Vector

The eigenfunctions of this four trap system are arranged in quadruplets. There are four eigenfunctions which form the ground state quadruplet (*gs*-quadruplet), four which form the first excited quadruplet and so on. In the limit of a large separation between the trap centers, the eigenenergies of the *gs*-quadruplet approach $\hbar\omega$, and the eigenenergies of the first excited quadruplet approach $2\hbar\omega$, and so on. Here we confine our analysis of this system to the *gs*-quadruplet. The state vector is prepared in some superposition of the *gs*-quadruplet and by maintaining an adiabatic evolution the wavefunction is not excited to occupy higher lying eigenfunctions.

Applying the finite difference outlined in section 6.1.2 we recover both the eigenenergies and eigenfunctions at each time step t_n. The eigenfunction of the *gs*-quadruplet $\langle \mathbf{x}|\psi_\nu(t_n)\rangle$, with $\nu = 0, 1, 2, 3$, at $t = t_0$ are plotted in figure 6.3. The eigenenergies of the *gs*-quadruplet are correspondingly labeled $\hbar\omega_\nu(t_n)$. Here we note that the first

excited eigenfunction $\langle \mathbf{x}|\psi_1(t_n)\rangle$ has no significant density contribution in the $|0\rangle$ and $|1\rangle$ spatial modes. As a result the initial state we choose, which is localised in $|0\rangle$, has no contribution from this eigenfunction. In section 6.2 we show that this eigenfunction remains unoccupied throughout the SAP process for the trap motions outlined in section 6.1.1.

In this section we wish to highlight the behaviour of the eigenenergies of (6.2) throughout the SAP evolution, according to the trap motions found in section 6.1.1. At each t_n, the related Hamiltonian matrix in the energetic basis is formally written,

$$\mathbf{H}(t_n) \;=\; \hbar \begin{pmatrix} \omega_0(t_n) & 0 & 0 & 0 \\ 0 & \omega_1(t_n) & 0 & 0 \\ 0 & 0 & \omega_2(t_n) & 0 \\ 0 & 0 & 0 & \omega_3(t_n) \end{pmatrix}. \tag{6.12}$$

In figure 6.4 we show the above eigenenergies as a function of time for the SAP process. Here we note an unusual behaviour, in that the eigenenergies of the $\nu = 1, 2$ energetic modes exhibit crossings as the process evolves in time. This trait is unique to these types of time dependent four mode 'resonant' potentials, and is not found in analogous two and three spatial mode potentials.[2]

6.2 Spatial Adiabatic Passage

The energetic and spatial Hamiltonian matrices have been shown to be related by a rotation. The exact mapping is derived in chapter 4 for two energetic and spatial modes. The trap basis approximation, which has been covered in detail in chapter 5, can be applied to our four spatial mode potential that is of interest presently, thereby allowing the recovery of the spatial mode Hamiltonian matrix.

In section 6.2.1 we outline the trap basis approximation and show the values of the time dependent spatial mode Hamiltonian matrix elements throughout the SAP process. Thereafter in section 6.2.2 we describe the phase evolution of the wavefunction in both the spatial and energetic bases and show that SAP in this four mode system can be easily used to produce an even superposition state between the $|2\rangle$ and $|3\rangle$ spatial modes.

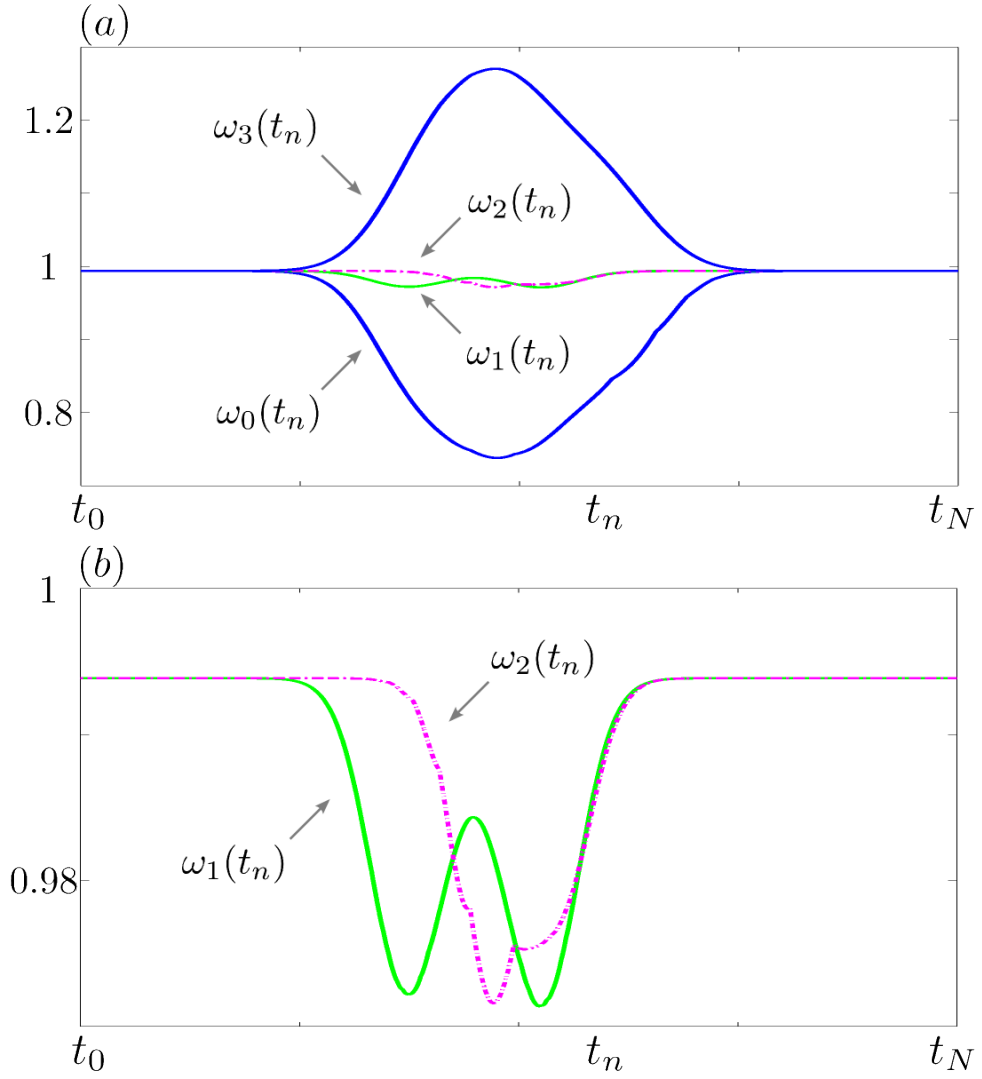


FIGURE 6.4: (*a*) The eigenfrequencies of the *gs*-quadruplet throughout the SAP evolution. (*b*) Detailed view of the crossing of the time dependent eigenfrequency spectrum exhibited by the ω_1 and ω_2 eigenfrequencies.

6.2.1 The Spatial Hamiltonian Matrix

For the purposes of continuity of reading and clarity we shall briefly outline the trap basis approximation in this section. The spatial mode Hamiltonian matrix $\mathbf{H}_{\mathrm{R}}(t_n)$ is given by a correct rotation of the energetic mode Hamiltonian matrix $\mathbf{H}(t_n)$ of equation (6.12).

[2]The phenomenon of avoided crossings in the *spatial* eigenenergy spectrum is well known [30], i.e. Landau-Zener potentials.

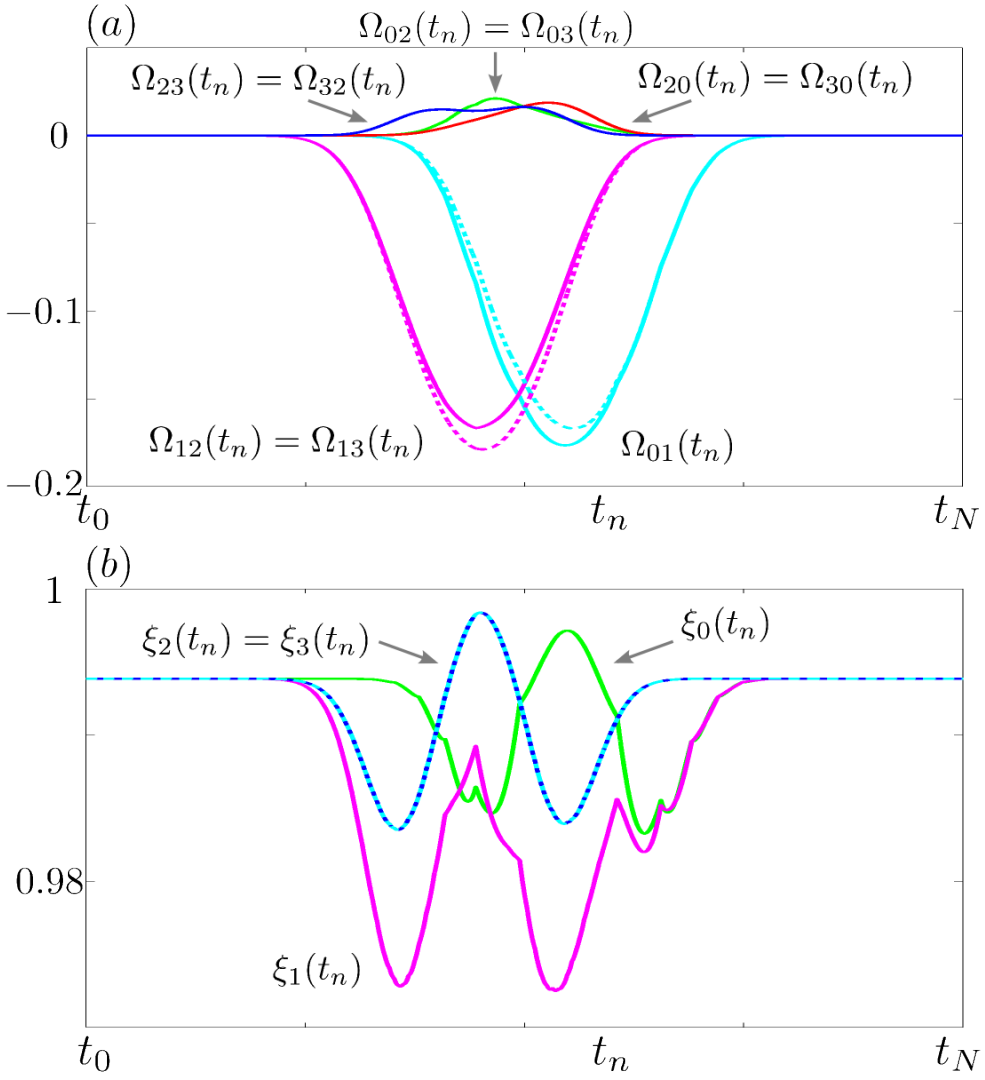


FIGURE 6.5: (*a*) The interaction frequencies of $\mathbf{H}_{\mathrm{R}}/\hbar$, the lower matrix elements are the dashed lines. In magenta are $\Omega_{12}(t_n)$, $\Omega_{13}(t_n)$; In cyan is $\Omega_{01}(t_n)$; In green are $\Omega_{02}(t_n)$, $\Omega_{03}(t_n)$; In blue are $\Omega_{23}(t_n)$, $\Omega_{32}(t_n)$; In red are $\Omega_{20}(t_n)$, $\Omega_{30}(t_n)$;. (*b*) The local spatial modes frequencies (diagonal elements of $\mathbf{H}_{\mathrm{R}}/\hbar$).

Here we approximate this as,

$$\begin{aligned}\mathbf{H}_{\mathrm{R}}(t_n) &= \mathbf{R}(t_n)\,\mathbf{H}(t_n)\,\mathbf{R}^{-1}(t_n),\\ \mathbf{H}_{\mathrm{R}}(t_n) &= \hbar\begin{pmatrix}\xi_0(t_n) & \Omega_{01}(t_n) & \Omega_{02}(t_n) & \Omega_{03}(t_n)\\ \Omega_{10}(t_n) & \xi_1(t_n) & \Omega_{12}(t_n) & \Omega_{13}(t_n)\\ \Omega_{20}(t_n) & \Omega_{21}(t_n) & \xi_2(t_n) & \Omega_{23}(t_n)\\ \Omega_{30}(t_n) & \Omega_{31}(t_n) & \Omega_{32}(t_n) & \xi_3(t_n)\end{pmatrix}.\end{aligned} \tag{6.13}$$

The elements of the rotation matrix $\mathbf{R}$, denoted $R_{\eta\nu}$, are given by,

$$R_{\eta\nu}(t_n) = r_{\eta\nu}(t_n)/\sqrt{\sum_{\mu=0}^{3} r_{\eta\mu}(t_n)}, \qquad r_{\eta\nu}(t_n) = \int d\mathbf{x}\,\langle\vartheta_\eta(t_n)|\mathbf{x}\rangle\langle\mathbf{x}|\psi_\nu(t_n)\rangle. \tag{6.14}$$

The function $\langle \mathbf{x}|\vartheta_\eta(t_n)\rangle$ is (in our scaled units) a gaussian located on each trap center,

$$\langle \mathbf{x}|\vartheta_\eta(t_n)\rangle = \exp\big(-(x+x_\eta(t_n))^2-(y+y_\eta(t_n))^2\big). \tag{6.15}$$

This gaussian assumes the same functional form as the ground state of each 'isolated' harmonic trap.

The contributions of the elements that characterise the spatial mode Hamiltonian matrix $\mathbf{H}_\mathrm{R}/\hbar$ are shown in figure 6.5, for the counter-intuitive trap paths in section 6.1.1. As we found in chapter 5, the operator in the spatial basis is non-hermitian, which is an artifact of having to use the inverse, rather than the transpose of $\mathbf{R}(t_n)$, to approximate the spatial mode Hamiltonian matrix (6.13). The interaction frequencies between the outer and center trap assume the expected form (shown in (a)) which is typical of the models used in the literature. The magnitude of the interaction frequencies between the outer traps is negligible by comparison, but nonetheless their inclusion is essential to ensure that the eigenvalues of the Hamiltonian matrices in both the spatial and energetic bases are equal at all t_n. In (b) are the local frequencies of the spatial modes. Their value is for all practical purposes constant throughout the evolution, and at all times, $\mathrm{Tr}\,(\mathbf{H}_\mathrm{R}(t_n)) = \mathrm{Tr}\,(\mathbf{H}(t_n))$.

6.2.2 Phase Evolution of the Wavefunction

Here we make use of the tools employed in chapter 5 to describe the phase evolution of the wavefunction in both the energetic and spatial basis. As we are confined to the *gs*-quadruplet, the wavefunction is expanded at the time t_n in a superposition of the *gs*-quadruplet energetic modes. Similarly the wavefunction in the spatial basis is expanded in a superposition of the four spatial modes at any time t_n. These are respectively,

$$|\Psi(t_n)\rangle = c_0(t_n)|\psi_0(t_n)\rangle + c_1(t_n)|\psi_1(t_n)\rangle + c_2(t_n)|\psi_2(t_n)\rangle + c_3(t_n)|\psi_3(t_n)\rangle, \tag{6.16a}$$

$$|\Psi(t_n)\rangle_\mathrm{R} = b_0(t_n)|0\rangle + b_1(t_n)|1\rangle + b_2(t_n)|2\rangle + b_3(t_n)|3\rangle. \tag{6.16b}$$

The phase evolution of the basis state coefficients are determined by the time evolution operators in the energetic and spatial bases respectively as,

$$\mathbf{c}(t_{n+1}) = \mathbf{U}(t_n)\mathbf{c}(t_n), \tag{6.17a}$$

$$\mathbf{b}(t_{n+1}) = \mathbf{U}_\mathrm{R}(t_n)\mathbf{b}(t_n). \tag{6.17b}$$

The time evolution operator in the spatial basis is quite simply given by $\mathbf{U}_\mathrm{R}(t_n) = \exp\big(-\frac{i}{\hbar}\mathbf{H}(t_n)\Delta t\big)$. The time evolution operator in the energetic basis was derived in

section 5.2.2 and is given by,

$$U_{\mu\nu}(t_n) \;=\; \int d\mathbf{x}\; \langle\psi_\mu(t_{n+1})|\mathbf{x}\rangle\langle\mathbf{x}|\psi_\nu(t_n)\rangle\, \exp\left(-\imath\omega_\nu(t_n)\Delta t\right). \tag{6.18}$$

For the SAP process we consider a quantum state initially localised in the $|0\rangle$ spatial mode. Therefore at $t = t_0$ we infer that the state vector of the *gs*-quadruplet is $\mathbf{c}(t_0) = (1/2, 0, 1/\sqrt{2}, 1/2)^{\mathrm{T}}$. Notably the is no contribution from the $\langle\mathbf{x}|\psi_1(t_n)\rangle$ energetic mode. The state vector in the spatial basis is subsequently initialised as $\mathbf{b}(t_0) = (\sqrt{\rho_0(t_0)}, \sqrt{\rho_1(t_0)}, \sqrt{\rho_2(t_0)}, \sqrt{\rho_3(t_0)})^{\mathrm{T}} \approx (1, 0, 0, 0)^{\mathrm{T}}$, where,

$$\rho_\eta(t_n) \;=\; \sum_{\mu,\nu=0}^{3} c^*_\mu(t_n)c_\nu(t_n)\mathcal{D}^\eta_{\mu\nu}(t_n); \qquad \mathcal{D}^\eta_{\mu\nu}(t_n) \;=\; \int_{\mathcal{V}_\eta} d\mathbf{x}\; \langle\psi_\mu(t_n)|\mathbf{x}\rangle\langle\mathbf{x}|\psi_\nu(t_n)\rangle. \tag{6.19}$$

The area spanned by each spatial mode $|\eta\rangle$ is labeled $\mathcal{V}_\eta$.

Due to the symmetry of the four mode potential, the first excited eigenfunction $|\psi_1(t_n)\rangle$ remains unoccupied throughout the whole SAP evolution. We consider ourselves in the adiabatic regime when the final occupation density of the energetic mode coefficients, maintain a small amplitude oscillatory pattern, about some constant value. In figure 6.6(a) we show $|c_\nu(t_N)|^2$ for $\nu = 0, 1, 2, 3$ for $t_N = 100 \to 5000$. As t_N is increased, the visible oscillatory pattern repeats. For the SAP evolution we use a total time for the evolution of $t_N = 3000$ as we are in the adiabatic regime.

The counter-intuitive trap motions diminishes the densities of the $|\psi_0(t_n)\rangle$ and $|\psi_3(t_n)\rangle$ energy eigenfunctions in the $|0\rangle$ spatial mode. Whereas the $|\psi_2(t_n)\rangle$ becomes localised in the $|0\rangle$ spatial mode, whilst the first excited eigenfunction $|\psi_1(t_n)\rangle$ remains confined to $|2\rangle$ and $|3\rangle$. As a result the wavefunction assumes complete occupation of $|\psi_2(t_n)\rangle$, shown in (b) for $t_N = 3000$. This continues until the end of the process, when the traps begin to return to their initial positions for $t_n > t_{N-\delta}$; at all times $|c_1(t_n)|^2 = 0$. At the end of the process the eigenfunctions assume their initial functional forms, as shown in figure 6.3. The final state of the wavefunction is then $\mathbf{c}(t_N) \approx e^{\imath\varphi}(1/2, 0, e^{\imath\pi}/\sqrt{2}, 1/2)^{\mathrm{T}}$. Similar to the three mode case (chapter 5) the cyclical evolution has imposed a π phase change on the $|\psi_2(t_n)\rangle$ eigenfunction and the density of the wavefunction has been transported from $|0\rangle \to |2\rangle, |3\rangle$. Since $|\psi_2(t_n)\rangle$ has equal densities in the $|2\rangle$ and $|3\rangle$ spatial modes the final state is an even superposition of $|2\rangle$ and $|3\rangle$. In figure 6.6(c) are the densities of the spatial modes $\rho_\eta(t_n)$ $\left(|b_\eta(t_n)|^2\right)$ in solid (dashed light) blue throughout the evolution.

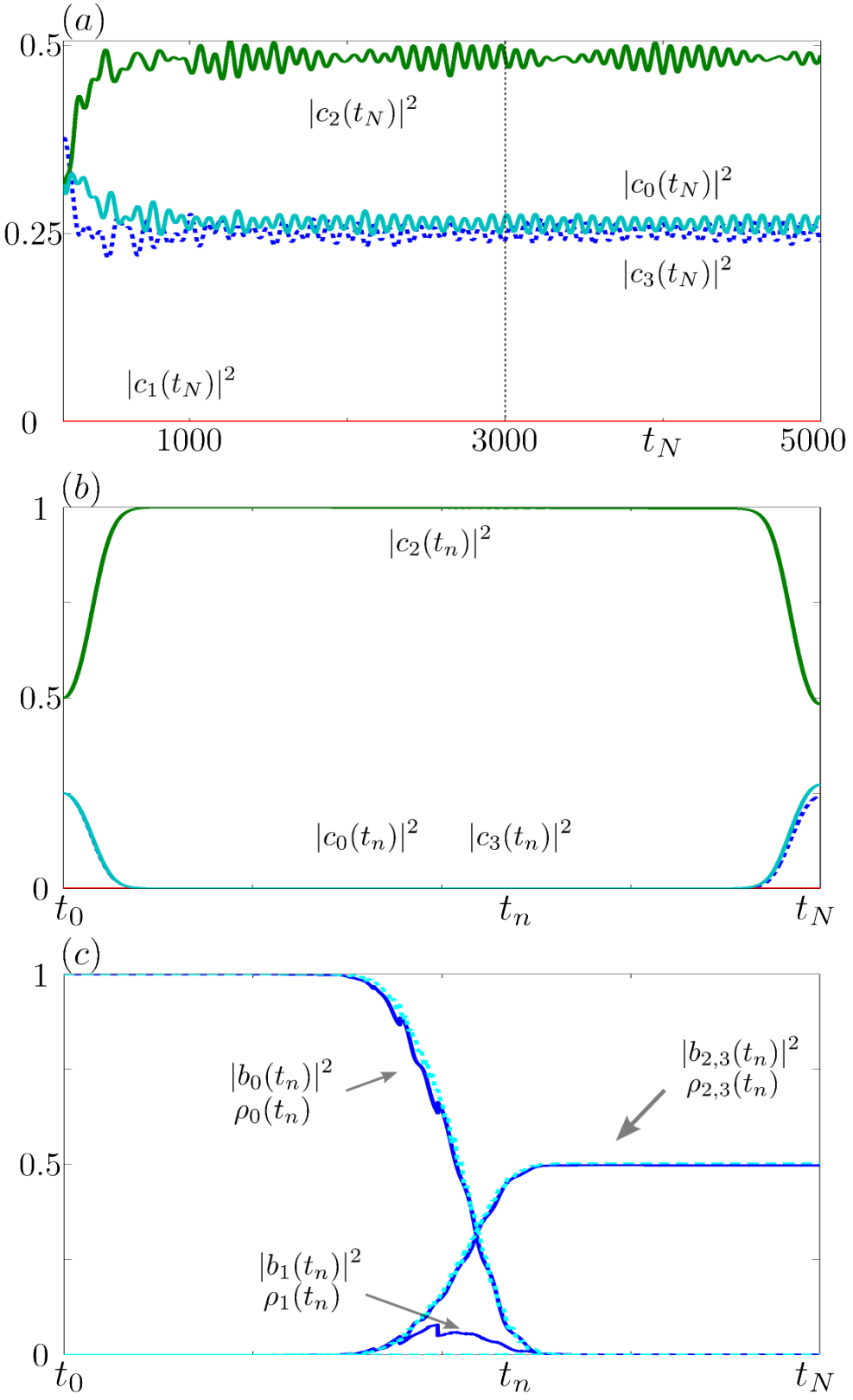


FIGURE 6.6: Counter-Intuitive trap motions. (a) The absolute value of the energetic mode coefficients at the end of the evolution as a function of the total time. (b) The absolute value of the energetic mode coefficients throughout the evolution for $t_N = 3000$. (c) The densities of the spatial mode coefficients $\rho_\eta(t_n)$ $\left(|b_\eta(t_n)|^2\right)$ in solid (dashed light) blue, with $t_N = 3000$ and $\eta = 0, 1, 2, 3$.

6.3 Spatial Mode Phase Imprinting

In this section we consider our initial state to be the even superposition between the $|2\rangle$ and $|3\rangle$ spatial modes. The target spatial mode is thus $|0\rangle$. We subsequently adapt the motion of the trap centers from section 6.1.1 so that the $|0\rangle$ approaches the $|1\rangle$ trap center followed by the $|2\rangle$ and $|3\rangle$ trap centers moving in sync. This motion is employed when $(\alpha_0, \beta_0, \theta_0) = (N-n-\delta-1, n+\delta-N, 2\pi n/(N-\delta))$, and $(\alpha_2, \beta_2, \theta_2) = (\alpha_3, \beta_3, \theta_3) = (n-\delta-1, \delta-n, 2\pi(n-\delta)/(N-\delta))$.

The initial state $\tilde{\mathbf{c}}(t_0) = (\sqrt{2/7}, 0, e^{\imath\pi}\sqrt{3/7}, \sqrt{2/7})^{\mathrm{T}}$ localises the wavefunction in an even superposition between the $|2\rangle$ and $|3\rangle$ spatial modes. In the spatial basis the initial coefficients are $b_\eta(t_0) = \sqrt{\rho_\eta(t_0)}$, therefore we find $\mathbf{b}(t_0) \approx (0, 0, 1/\sqrt{2}, 1/\sqrt{2})^{\mathrm{T}}$. In this section we explore the effect of imprinting a phase difference, of $e^{\imath\phi}$, between the $|2\rangle$ and $|3\rangle$ spatial modes. This can be achieved experimentally and is an involved process but nonetheless is possible. Numerically we will consider the phase imprinting in both the energetic and spatial bases. The initial state is expanded in terms of the energy eigenfunctions as,

$$\langle \mathbf{x}|\Psi_{\mathrm{init}}(t_0)\rangle = \tilde{c}_0\langle \mathbf{x}|\psi_0(t_0)\rangle + \tilde{c}_1\langle \mathbf{x}|\psi_1(t_0)\rangle + \tilde{c}_2\langle \mathbf{x}|\psi_2(t_0)\rangle + \tilde{c}_3\langle \mathbf{x}|\psi_3(t_0)\rangle, \tag{6.20}$$

where $(\tilde{c}_0, \tilde{c}_1, \tilde{c}_2, \tilde{c}_3)^{\mathrm{T}} = (\sqrt{2/7}, 0, e^{\imath\pi}\sqrt{3/7}, \sqrt{2/7})^{\mathrm{T}}$. In the energetic mode basis we apply the phase $e^{\imath\phi}$ on the $|2\rangle$ spatial mode. Numerically this is achieved by separating the initialised wavefunction $|\Psi_{\mathrm{init}}(t_0)\rangle$ into its components in each spatial mode, and multiplying the component in the $|2\rangle$ mode by the desired phase factor. We have,

$$\langle \mathbf{x}|\Psi_{\mathrm{new}}(t_0)\rangle = \langle \mathbf{x}|\Psi_{\mathrm{init}}(t_0)\rangle_{\mathcal{V}_0} + \langle \mathbf{x}|\Psi_{\mathrm{init}}(t_0)\rangle_{\mathcal{V}_1} + e^{\imath\phi}\langle \mathbf{x}|\Psi_{\mathrm{init}}(t_0)\rangle_{\mathcal{V}_2} + \langle \mathbf{x}|\Psi_{\mathrm{init}}(t_0)\rangle_{\mathcal{V}_3}. \tag{6.21}$$

The new initialised coefficients in the energetic basis are then given by,

$$c_\nu(t_0) = \int d\mathbf{x}\ \langle \psi_\nu(t_0)|\mathbf{x}\rangle\langle \mathbf{x}|\Psi_{\mathrm{new}}(t_0)\rangle, \tag{6.22}$$

with $\nu = 0, 1, 2, 3$. As we will momentarily show, the effect of this phase imprinting is to excite the wavefunction to occupy the population trapping state $|\psi_1(t_0)\rangle$. In the previous section we observed that the population of this state remains unchanged throughout the whole SAP evolution. In the spatial basis the imprinting of the phase is much more straight forward. For an applied phase $e^{\imath\phi}$, the initialised state vector in the spatial basis is given by $\mathbf{b}(t_0) = (0, 0, e^{\imath\phi}/\sqrt{2}, 1/\sqrt{2})^{\mathrm{T}}$.

In the following we compare the evolution of the state vector in both the energetic and spatial bases according to the time evolution operators (6.17) respectively, as we tune the applied phase from $\phi = 0 \to 2\pi$, in the adiabatic regime $t_N = 3000$. In figure 6.7(a)

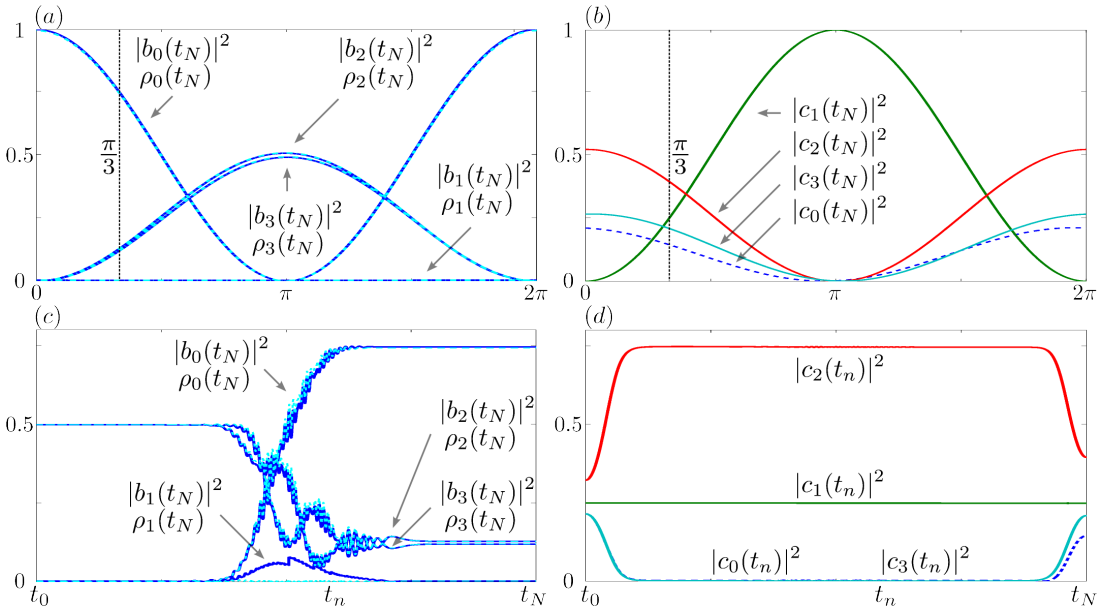


FIGURE 6.7: (*a*) The densities of the spatial modes at the end of the evolution, in solid (dashed light) blue is $\rho_\eta(t_N)$ ($|b_\eta(t_N)|^2$). (*b*) The densities of the energetic mode coefficients at the end of the SAP evolution. (*c*) The densities of the spatial modes at the end of the evolution, in solid (dashed light) blue is $\rho_\eta(t_N)$ ($|b_\eta(t_N)|^2$). (*d*) The densities of the energetic mode coefficients throughout the SAP evolution.

the densities of the spatial modes at the end of the SAP process for both time evolution operators are compared as a function of the applied phase. In solid (dashed light) blue is $\rho_\eta(t_N)$ ($|b_\eta(t_N)|^2$). We point out that for no applied phase the quantum state is transferred to the $|0\rangle$ spatial mode, as expected, and in the energetic basis the final state is differs from the initial state as the $|\psi_1(t_0)\rangle$ has acquired a π phase from the evolution.

When the applied phase, $e^{\imath\phi} = e^{\imath\pi}$, the population remains in the $|2\rangle$ and $|3\rangle$ spatial modes. For all other values of the applied phase we observe the creation of qutrit states, i.e. the final state is some superposition of the $|0\rangle$, $|2\rangle$ and $|3\rangle$ modes. These qutrit states are geometric in origin as the final state is independent of the total time taken for the SAP evolution. In figure 6.7(c) we show the densities of the spatial modes throughout the evolution when $e^{\imath\phi} = e^{\imath\pi/3}$. Here we note that for longer times the intermediate densities oscillate more rapidly, yet the final state is always the same.

In order to gain an insight into the creation of these qutrit states it is necessary to observe the role the applied phase plays in the evolution of the energetic modes. In figure 6.7(b) the densities of the energetic mode coefficients at the end of the evolution are shown. We note that when the applied phase $e^{\imath\phi} = e^{\imath\pi}$, the wavefunction assumes complete occupation of the population trapping state $|\psi_1(t_n)\rangle$. As the population of this state remains unchanged throughout the SAP evolution, the final densities remain confined to $|2\rangle$ and $|3\rangle$. For intermediate values of the applied phase $\phi = 0 \to 2\pi$, the

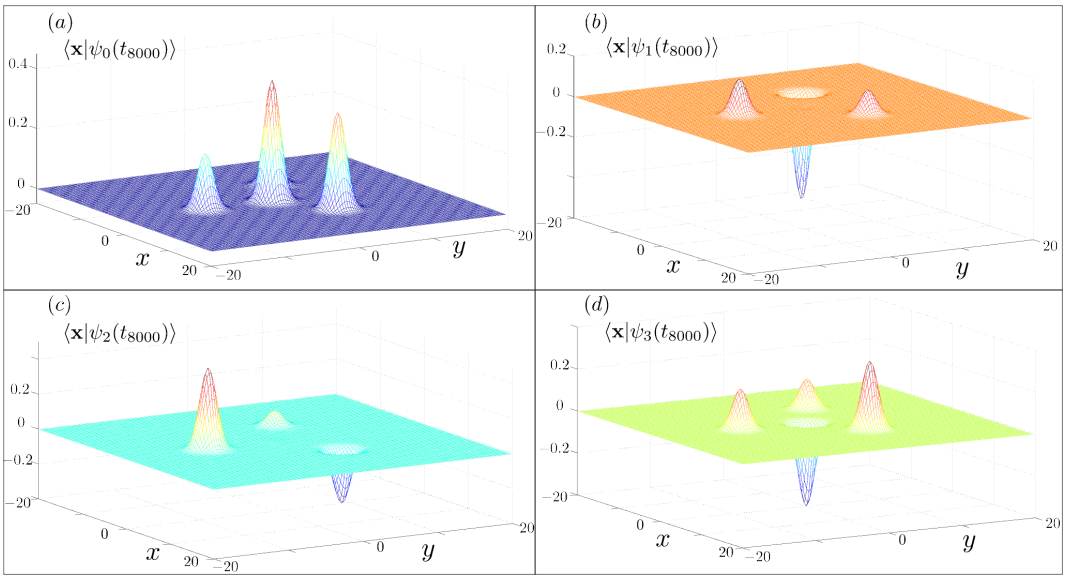


FIGURE 6.8: The *gs*-quadruplet eigenfunctions $\langle \mathbf{x}|\psi_\nu(t_n)\rangle$ for the asymmetric trap paths at $t_n = t_{8000}$, and $\nu = 0, 1, 2, 3$ inset.

excitation of the quantum state to occupy the population trapping state varies smoothly. Consequently the densities of the outer traps also vary smoothly. In figure 6.7(d) we show the densities of the energetic modes throughout the SAP process. Obvious from the plot the population of $|\psi_1(t_n)\rangle$ remains unchanged whilst the remaining basis states exhibit the usual exchange of densities.

6.4 Dynamic Phases in Four Mode SAP

We have shown thus far that due to the symmetry of this four SAP model the first excited eigenfunction $|\psi_1(t_n)\rangle$ plays no role in the population transfer process. Breaking the symmetry of the potential invokes the inclusion of $|\psi_1(t_n)\rangle$ during the temporal dynamics of the system. In the following we will show that when an asymmetry is present in the time dependent potential, non-adiabatic coupling occurs between the $|\psi_1(t_n)\rangle$ and $|\psi_2(t_n)\rangle$ eigenfunctions, and it follows that the final state is dependent on the total time allocated for the evolution.

There are many ways that the symmetry of the system may be broken. Two simple methods are to (a) reduce the relative minimum approach distance between the target traps and center trap, or (b) to change the relative delay between the target trap paths, i.e. they no longer approach the center trap in sync. Here we make use of the latter. We adapt the definition of the trap paths as outlined in section 6.1.1 as follows; The $|0\rangle$ and $|3\rangle$ trap centers maintain the same paths as before, whereas, the $|2\rangle$ trap center begins its approach and return sequence at the midpoint between the paths of the $|0\rangle$ and $|3\rangle$

traps. For this evolution we discretise the time spectrum finely by setting $N = 16 \times 10^4$. To show the effect of the non-adiabatic coupling between the $\nu = 1, 2$ energetic modes we let Δt range from $0.01875 \rightarrow 0.1875$, therefore the total time taken for the evolution ranges between $t_N = 3000 \rightarrow 30000$. The delay between the motion of the $|0\rangle$ and $|3\rangle$ trap centers is $\delta = (0.1)N = 16000$ time steps, and therefore the delay between the $|0\rangle$ and $|2\rangle$ trap centers is $\delta_2 = (0.05)N = 8000$ time steps. Consequently the symmetry of the potential is broken at $t_n = t_{8000}$. The functional form of the eigenfunctions at the time step $t_n = t_{7999}$ is effectively the same as that in figure 6.3. However at $t_n = t_{8000}$ the symmetry is broken and the $\nu = 1, 2$ energetic modes exhibit a large spatial overlap, see figure 6.8. These eigenfunctions share a large spatial overlap throughout the evolution, and since their eigenenergies are close in value throughout the process, non-adiabatic transitions readily occur between these two basis states. This non-adiabatic coupling continues until $t_n = t_{152000}$.

We further illustrate the effect of the non-adiabatic coupling between the $\nu = 1, 2$ basis states in figure 6.9. In (a) are the densities of the spatial modes at the end of the evolution as a function of the total time t_N, and in (b) are the densities of the energetic modes. Whilst a regular sinusoidal relationship exists for the final state in both the spatial and energetic bases, at present it is not obvious how to quantify this relationship. Whilst this four mode model may be used to generate qubit and qutrit states when the potential maintains a symmetry throughout the evolution, introducing asymmetry into the process adds extra complications and destroys the geometric nature of the final state of the system.

6.5 Discussion

In this chapter we have presented the spatial analogue of a well known four level optical system. This model can be extended to similar four level optical systems, such as [184], by making an appropriate arrangement of the traps and their paths. We applied the time dependent evolution of the wavefunction in the energetic basis and spatial basis via the trap basis approximation, from the work of chapter 5 to uncover the dynamics involved in this four level system.

It was shown that, as in the three mode SAP, a single population trapping state exists that transports the wavefunction from $|0\rangle$ to an even superposition between the $|2\rangle$ and $|3\rangle$ spatial modes, for the counter-intuitive motion of the trap centers. When the process is reversed, and the $|0\rangle$ mode takes the place of the target spatial mode, with an even superposition state initially between $|2\rangle$ and $|3\rangle$, the state is transport with the usual high fidelity associated with SAP processes. This approach was shown to be sensitive

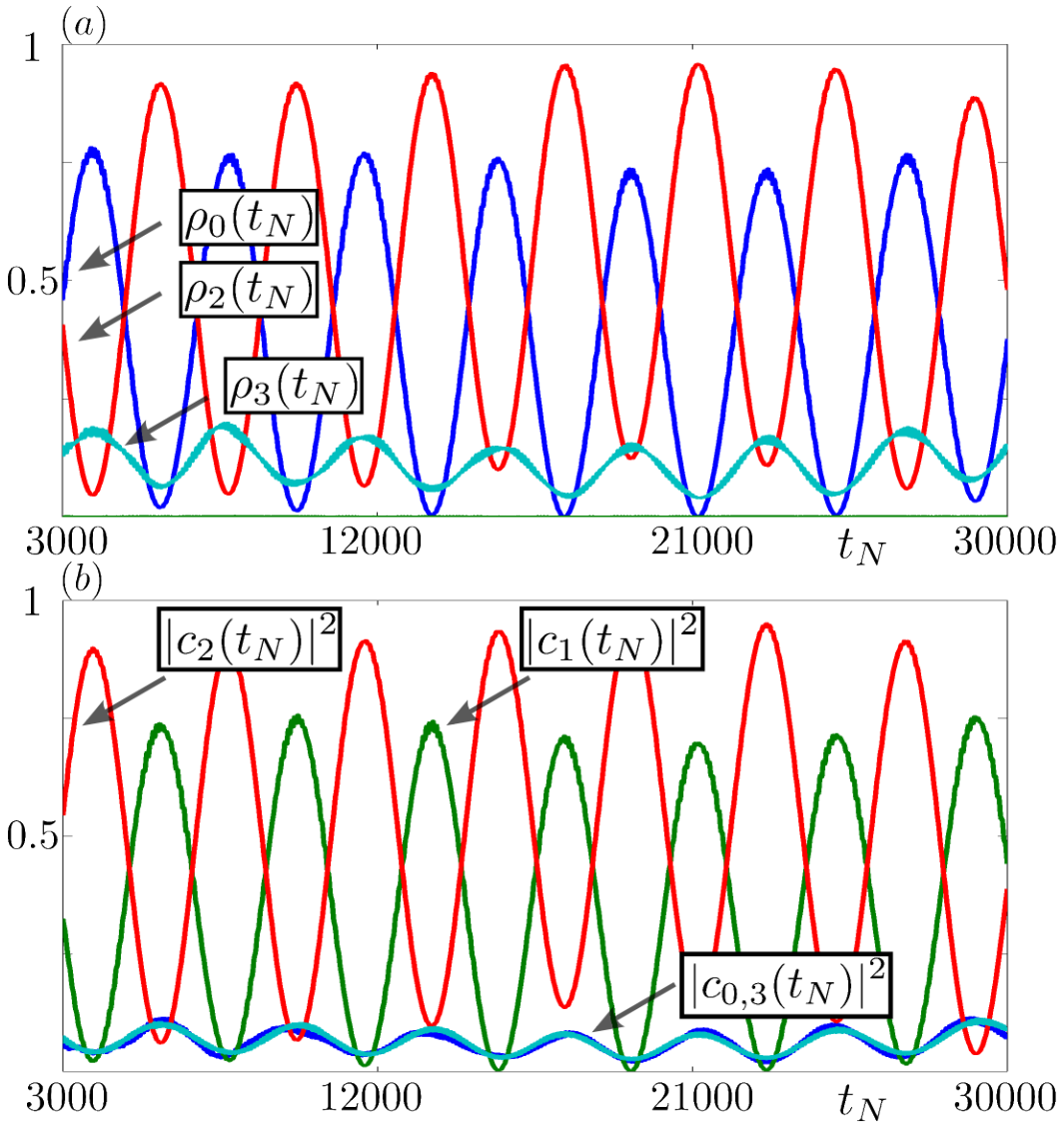


FIGURE 6.9: Asymmetric trap paths. (a) The densities of the spatial modes, at the end of the evolution, as a function of t_N. (b) The densities of the energetic modes, at the end of the evolution, as a function of t_N.

to any existing phase difference between $|2\rangle$ and $|3\rangle$, made possible via the population trapping state $|\psi_1(t_n)\rangle$.

We showed that this system is highly sensitive to any introduced asymmetry. Modifying the motion of the $|2\rangle$ and $|3\rangle$ trap centers produces two population trapping states whose eigenenergies are very close in value. In addition these state assume a large spatial overlap. This spatial overlap and their quasi-degenerate nature leads to highly non-adiabatic coupling which destroys the geometric SAP process. It follows that the system becomes sensitive to the total evolution time leading to a final state which, albeit sinusoidal with respect to t_N, is non-trivial to predict.

Chapter 7

Conclusion and Outlook

In this thesis we have investigated the relationship between the spatial and energetic mode dynamics of ultracold fermionic and bosonic systems. Our work on spontaneous emission in anisotropic Fermi seas has shed light two interesting aspects of ultracold Fermi gases; these are the degenerate shell structure of anisotropic harmonic trapping geometries, and the anisotropic spatial decay rate of excited fermions in the presence of an anisotropic ground state Fermi sea. This work offers a perspective with which to study directional photon scattering experiments performed on ultracold Fermi gases. The formulae for the degeneracies of the energetic levels of the three dimensional harmonic oscillator offer a deterministic solution to the number of bound momentum or energetic modes that exist as a function of the trap shape. We have shown that they are fundamental tool in the description of directional photon emission in ultracold Fermi gases, without the use of an optical cavity.

Spatial adiabatic passage (SAP) is a dynamic and growing field, albeit it has not yet enjoyed the same experimental success as its optical counterpart. Our two experimental proposals have given a strong indication for the feasibility of matter wave transport in both atom chips (waveguide settings) and radio frequency potentials. To take our work from the outlined theoretical analysis to experimental realisation is a formidable challenge from an engineering and fabrication point of view. Unforeseen obstacles that we have omitted to address, such as the roughness of wires on atom chips at the nanoscale and below and the strict confinement of the radio-frequency potentials along a one dimensional axis, are left to the enthusiastic experimentalist to tackle. The theory of SAP may be well rounded but the decision as to whether it is sufficient is at the mercy of an appropriate experiment. We hope that our investigations will help to guide a venture in this direction.

Our work on the the nature of the quantum tunneling interaction is a contribution to the fundamental understanding of spatial mode dynamics. In a general sense our derived mapping is of interest to all communities in quantum mechanics and optics that deal with the tunneling phenomenon, which are vast in both breath and number. Of particular appeal is extending the derived model to the time dependent case. We focused on the mapping between the energetic and spatial mode Hamiltonian when the energetic mode Hamiltonian is time independent and diagonal. Introducing a time dependent coupling term between the energetic modes offers a mechanism to study adiabatic time dependent processes, and moreover to study geometric phases in both representations.

With the insight as to the form of the spatial mode Hamiltonian of chapter 4 we examined a pioneering work on matter wave transport [56] via the SAP technique. We found that a means of extending the exact two mode model to approximate the three mode model of SAP was possible. For here it was shown that this approximation recovers the standard form of the 3×3 spatial mode Hamiltonian found in the literature for SAP processes. Two key components of the operator emerged; firstly that the eigenvalues in both the spatial and energetic representations are the same, and secondly it revealed the presence of a coupling term between the outer traps, which reaches a significant magnitude at the midpoint of the evolution. This coupling term has thus far been neglected in the literature (with no significant error) but is necessary to include so that the eigenvalues of the operator in both representations are the same. Moreover there is a direct relationship between the eigenvectors of the 3×3 spatial mode Hamiltonian matrix and the energy eigenfunctions. The latter is the coordinate space representation of the former. Thereafter we moved to the energetic mode representation where we showed that the SAP process imposes a π phase change to one of the internal energetic modes of the systems. A signature of this phase is the transport of the wavefunction from $|0\rangle \rightarrow |2\rangle$. We showed that the acquired phase is independent of the time taken for the cyclical process, and therefore geometric in origin. This geometric phase is also present in fractional SAP process, which afford the creation of spatial mode qubit state between the outer traps.

The final work of the thesis 'SAP In Four Mode Systems - Qubit and Qutrit States' demonstrated the feasibility of generating spatial qubit and qutrit states. Here the coupling interaction between the outer traps cannot be neglected, and as a result there is but one dark state, as opposed to two found in the optical case. We were able to find that the usual SAP process creates an even superposition state between the two target traps $|2\rangle$ and $|3\rangle$. We used this superposition state to explore the consequences of an applied phase difference between the spatial modes. Here we found that when the SAP process is reversed, with no phase difference, the state is transported to $|0\rangle$. However, the applied phase difference between the spatial modes inhibits the transfer process,

creating a qutrit state between $|0\rangle$, $|2\rangle$ and $|3\rangle$. The applied phase excites the system to occupy a population trapping state which is unique to this type of four mode system. We showed that the density of the final state in each spatial mode can be quantified as a function of the applied phase. Finally we revealed that when the symmetry of the evolution is broken (i.e. the target traps no longer move in sync but have different paths), that a qutrit state between the outer traps is once again created. However the final state of the system depends of the total time taken for the evolution and therefore is not completely geometric, i.e. there are dynamical contributions to the final state. At present there is no obvious way to quantify the dynamical and geometric phase contributions to the final state. Further work in this venture, with an aim to understand the dynamical and geometric phase factors, could lead to the possibility of applying techniques borrowed from Optimal Control to dampen the dynamical contributions and arrive at an all geometric means of producing arbitrary qutrit states.

Appendix A

Supplementary Calculations

A.1 Chapter 2: Transition Matrix

From (2.74) we have,

$$\langle m|\mathscr{T}^{\dagger}(\alpha)|n\rangle = e^{|\alpha|^2/2}\langle m|e^{\alpha^*\,\hat{a}}e^{\,-\alpha\,\hat{a}^{\dagger}}|n\rangle. \tag{A.1}$$

Expanding the exponential on the right hand side of (A.1) and using the identities (2.77) we find,

$$e^{\,-\alpha\,\hat{a}^{\dagger}}|n\rangle \;=\; \sum_{p=0}^{\infty}\frac{(-\alpha)^p}{p!}(\hat{a}^{\dagger})^p|n\rangle \;=\; \sum_{p=0}^{\infty}\frac{(-\alpha)^p}{p!}\sqrt{\frac{(n+p)!}{n!}}|n+p\rangle. \tag{A.2}$$

Similarly we consider the operation of $e^{\,\alpha^*\,\hat{a}}$ on the state ket $|n+p\rangle$ by expanding the exponential and using the identities (2.77),

$$e^{\,-\alpha^*\,\hat{a}}|n+p\rangle \;=\; \sum_{q=0}^{\infty}\frac{(\alpha^*)^q}{q!}\hat{a}^q|n+p\rangle \;=\; \sum_{q=0}^{n+p}\frac{(\alpha^*)^q}{q!}\sqrt{\frac{(n+p)!}{(n+p-q)!}}|n+p-q\rangle. \tag{A.3}$$

Plugging both these relations into (A.1) we find the r.h.s. reduces to,

$$e^{|\alpha|^2/2}\sum_{p=0}^{\infty}\frac{(-\alpha)^p}{p!}\sqrt{\frac{(n+p)!}{n!}}\sum_{q=0}^{n+p}\frac{(\alpha^*)^q}{q!}\sqrt{\frac{(n+p)!}{(n+p-q)!}}\langle m|n+p-q\rangle. \tag{A.4}$$

Since $\langle n|m+p-q\rangle \;=\; \delta_{n,m+p-q}$, we obtain the condition $q=n+p-m$, and that the outer sum must begin at $p=m$. Therefore (2.76) is given by,

$$\langle m|\mathscr{T}^{\dagger}(\alpha)|n\rangle = e^{|\alpha|^2/2}\frac{(\alpha^*)^{m-n}}{\sqrt{m!n!}}\sum_{p=m}^{\infty}\frac{\left(-|\alpha|^2\right)^p}{p!}\frac{(n+p)!}{(n+p-m)!}. \tag{A.5}$$

A.2 Chapter 2: Cigar Trap

We apply the Lamb-Dicke Parameter for the cigar trap as given by (2.99) to simplify (2.98) as,

$$\sum_{\boldsymbol{n}=0}^{\infty}|\langle\boldsymbol{n}|e^{\imath\mathbf{k}(\Omega)\cdot\mathbf{r}}|0\rangle|^2=\sum_{(n_x,n_y,n_z)=0}^{\infty}e^{-\frac{\eta^2}{\lambda}\left(\sin^2\theta\cos^2\vartheta+\sin^2\theta\sin^2\vartheta\right)-\eta^2\cos^2\theta}\,\frac{\left(\frac{\eta^2}{\lambda}\right)^{n_x+n_y}\left(\eta^2\right)^{n_z}}{n_x!\,n_y!\,n_z!}\times\left(\sin^2\theta\right)^{n_x+n_y}\left(\cos^2\vartheta\right)^{n_x}\left(\sin^2\vartheta\right)^{n_y}\left(\cos^2\theta\right)^{n_z}\tag{A.6}$$

To further reduce this expression, we make a change of variables, $N=n_x+n_y$, which allows us to rearrange the sums $\sum_{n_x=0}^{\infty}\sum_{n_y=0}^{\infty}\rightarrow\sum_{N=0}^{\infty}\sum_{n_x=0}^{N}$,

$$\sum_{\boldsymbol{n}=0}^{\infty}|\langle\boldsymbol{n}|e^{\imath\mathbf{k}(\Omega)\cdot\mathbf{r}}|0\rangle|^2=\sum_{N=0}^{\infty}\sum_{n_x=0}^{N}\sum_{n_z=0}^{\infty}e^{-\frac{\eta^2}{\lambda}\sin^2\theta+\eta^2\cos^2\theta}\frac{\eta^{2(N+n_z)}}{N!n_z!\lambda^N}(\sin^2\theta)^N(\cos^2\theta)^{n_z}\times\left(\sum_{n_x=0}^{N}\frac{N!}{n_x!(N-n_x!)}\left(\sin^2\vartheta\right)^{N-n_x}\left(\cos^2\vartheta\right)^{n_x}\right).\tag{A.7}$$

Using the identity,

$$\sum_{n_x=0}^{N}\frac{N!}{n_x!(N-n_x)!}\left(\sin^2\vartheta\right)^{N-n_x}\left(\cos^2\vartheta\right)^{n_x}=\left(1+\cot^2\vartheta\right)^N\left(\sin^2\vartheta\right)^N=1.\tag{A.8}$$

we reduce (A.7) to the following compact form,

$$\sum_{\boldsymbol{n}=0}^{\infty}|\langle\boldsymbol{n}|e^{\imath\mathbf{k}(\Omega)\cdot\mathbf{r}}|0\rangle|^2=e^{-\frac{\eta^2}{\lambda}\sin^2\theta-\eta^2\cos^2\theta}\sum_{N=0}^{\infty}\sum_{n_z=0}^{\infty}\frac{\left(\frac{\eta^2}{\lambda}\sin^2\theta\right)^N}{N!}\frac{\left(\eta^2\cos^2\theta\right)^{n_z}}{n_z!}.\tag{A.9}$$

A.3 Chapter 3: Laser Mode

We develop from equation (3.6),

$$\langle\alpha_l e^{-\imath\omega_l t}|\mathbf{E}(\mathbf{x})|\alpha_l e^{-\imath\omega_l t}\rangle\;=\;\boldsymbol{\epsilon}_l\sqrt{\frac{\hbar\omega_l}{2\epsilon_0 V}}\left(\langle\alpha_l e^{-\imath\omega_l t}|\hat{a}_l|\alpha_l e^{-\imath\omega_l t}\rangle+\langle\alpha_l e^{-\imath\omega_l t}|\hat{a}_l^\dagger|\alpha_l e^{-\imath\omega_l t}\rangle\right).\tag{A.10}$$

From the expansion of the coherent state as given by (3.5) the first and second terms of the above become respectively,

$$\langle\alpha_l e^{-\imath\omega_l t}|\hat{a}_l|\alpha_l e^{-\imath\omega_l t}\rangle\;=\;\exp\left[-|\alpha_l|^2\right]\langle 0_l|\exp\left[\alpha_l^* e^{\imath\omega_l t}\hat{a}_l\right]\hat{a}_l\,\exp\left[\alpha_l e^{-\imath\omega_l t}\hat{a}_l^\dagger\right]|0_l\rangle,\tag{A.11a}$$

$$\langle\alpha_l e^{-\imath\omega_l t}|\hat{a}_l^\dagger|\alpha_l e^{-\imath\omega_l t}\rangle\;=\;\exp\left[-|\alpha_l|^2\right]\langle 0_l|\exp\left[\alpha_l^* e^{\imath\omega_l t}\hat{a}_l\right]\hat{a}_l^\dagger\,\exp\left[\alpha_l e^{-\imath\omega_l t}\hat{a}_l^\dagger\right]|0_l\rangle.\tag{A.11b}$$

Of interest is the common term on the right hand side, $\exp\big[\alpha_l e^{-\imath\omega_l t}\hat{a}_l^\dagger\big]|0_l\rangle$. Expanding the exponential we have,

$$\exp\big[\alpha_l e^{-\imath\omega_l t}\hat{a}_l^\dagger\big]|0_l\rangle \;=\; \sum_{\mu=0}^{\infty}\frac{\alpha_l^\mu e^{-\imath\mu\omega_l t}}{\mu!}\left(\hat{a}_l^\dagger\right)^\mu|0_l\rangle. \tag{A.12}$$

At this point it is prudent to define the creation and annihilation operators $\hat{a}_l^\dagger, \hat{a}_l$.The vacuum state may be define as,

$$|vac\rangle \;=\; |0\rangle \;=\; |0_0, 0_1, 0_2, \ldots, 0_l, \ldots, 0_L\rangle, \tag{A.13}$$

where the notation $|n_l\rangle$ refers to n photons in the energetic mode l. For the purposes of abbreviation we write,

$$|n_l\rangle \;=\; |0_0, 0_1, 0_2, \ldots, n_l, \ldots, 0_L\rangle. \tag{A.14}$$

It follows that the creation and annihilation operators are defined by,

$$\left(\hat{a}_l^\dagger\right)^\mu|n_l\rangle \;=\; \sqrt{\frac{(n+\mu)!}{n!}}|(n+\mu)_l\rangle, \tag{A.15a}$$

$$(\hat{a}_l)^\mu|n_l\rangle \;=\; \sqrt{\frac{n!}{(n-\mu)!}}|(n-\mu)_l\rangle. \tag{A.15b}$$

Equation (A.12) becomes,

$$\exp\big[\alpha_l e^{-\imath\omega_l t}\hat{a}_l^\dagger\big]|0_l\rangle \;=\; \sum_{\mu=0}^{\infty}\frac{\alpha_l^\mu e^{-\imath\mu\omega_l t}}{\sqrt{\mu!}}\,|\mu_l\rangle. \tag{A.16}$$

Plugging the above into (A.11) we find,

$$\langle\alpha_l e^{-\imath\omega_l t}|\hat{a}_l|\alpha_l e^{-\imath\omega_l t}\rangle \;=\; e^{-|\alpha|^2}\sum_{\mu=0}^{\infty}\frac{\alpha_l^\mu e^{-\imath\mu\omega_l t}}{\sqrt{\mu!}}\sqrt{\mu}\,\langle 0_l|\exp\big[\alpha_l^* e^{\imath\omega_l t}\hat{a}_l\big]|(\mu-1)_l\rangle, \tag{A.17a}$$

$$\langle\alpha_l e^{-\imath\omega_l t}|\hat{a}_l^\dagger|\alpha_l e^{-\imath\omega_l t}\rangle \;=\; e^{-|\alpha|^2}\sum_{\mu=0}^{\infty}\frac{\alpha_l^\mu e^{-\imath\mu\omega_l t}}{\sqrt{\mu!}}\sqrt{\mu+1}\,\langle 0_l|\exp\big[\alpha_l^* e^{\imath\omega_l t}\hat{a}_l\big]|(\mu+1)_l\rangle. \tag{A.17b}$$

Expanding the exponentials once again (A.11) is expressed,

$$\langle \alpha_l e^{-\imath\omega_l t}|\hat{a}_l|\alpha_l e^{-\imath\omega_l t}\rangle = e^{-|\alpha|^2}\sum_{\mu,\nu=0}^{\infty}\frac{\alpha_l^{\mu}e^{-\imath\mu\omega_l t}}{\sqrt{\mu!}}\sqrt{\mu}\,\frac{(\alpha_l^*)^{\nu}\,e^{\imath\nu\omega_l t}}{\nu!}\langle 0_l|\,(\hat{a}_l)^{\nu}\,|(\mu-1)_l\rangle, \tag{A.18a}$$

$$\langle \alpha_l e^{-\imath\omega_l t}|\hat{a}_l^{\dagger}|\alpha_l e^{-\imath\omega_l t}\rangle = e^{-|\alpha|^2}\sum_{\mu,\nu=0}^{\infty}\frac{\alpha_l^{\mu}e^{-\imath\mu\omega_l t}}{\sqrt{\mu!}}\sqrt{\mu+1}\,\frac{(\alpha_l^*)^{\nu}\,e^{\imath\nu\omega_l t}}{\nu!}\langle 0_l|\,(\hat{a}_l)^{\nu}\,|(\mu+1)_l\rangle. \tag{A.18b}$$

Making use of (A.15) and tidying up,

$$\langle \alpha_l e^{-\imath\omega_l t}|\hat{a}_l|\alpha_l e^{-\imath\omega_l t}\rangle = e^{-|\alpha|^2}\sum_{\mu,\nu=0}^{\infty}\frac{\alpha_l^{\mu}\,(\alpha_l^*)^{\nu}\,e^{-\imath(\mu-\nu)\omega_l t}}{\nu!\sqrt{(\mu-1-\nu)!}}\langle 0_l|(\mu-1-\nu)_l\rangle, \tag{A.19a}$$

$$\langle \alpha_l e^{-\imath\omega_l t}|\hat{a}_l^{\dagger}|\alpha_l e^{-\imath\omega_l t}\rangle = e^{-|\alpha|^2}\sum_{\mu,\nu=0}^{\infty}\frac{\alpha_l^{\mu}\,(\alpha_l^*)^{\nu}\,e^{-\imath(\mu-\nu)\omega_l t}}{\nu!\sqrt{(\mu+1-\nu)!}}\,(\mu+1)\,\langle 0_l|(\mu+1-\nu)_l\rangle. \tag{A.19b}$$

For (A.19a) and (A.19b) we recognise $\langle 0_l|(\mu-1-\nu)_l\rangle = \delta_{\mu,\nu+1}$, and $\langle 0_l|(\mu+1-\nu)_l\rangle = \delta_{\mu+1,\nu}$.

$$\langle \alpha_l e^{-\imath\omega_l t}|\hat{a}_l|\alpha_l e^{-\imath\omega_l t}\rangle = e^{-|\alpha|^2}e^{-\imath\omega_l t}\,(\alpha_l)\sum_{\nu=0}^{\infty}\frac{|\alpha_l|^{2\nu}}{\nu!} \;=\; \alpha_l e^{-\imath\omega_l t}, \tag{A.20a}$$

$$\langle \alpha_l e^{-\imath\omega_l t}|\hat{a}_l^{\dagger}|\alpha_l e^{-\imath\omega_l t}\rangle = e^{-|\alpha|^2}e^{\imath\omega_l t}\,(\alpha_l^*)\sum_{\mu=0}^{\infty}\frac{|\alpha_l|^{2\mu}}{\mu!} \;=\; \alpha_l^* e^{\imath\omega_l t}. \tag{A.20b}$$

We recognise that $\alpha_l = \alpha_l^*$ and $\langle N\rangle = \alpha^2$ to express (A.10),

$$\langle \alpha_l e^{-\imath\omega_l t}|\mathbf{E}(\mathbf{x})|\alpha_l e^{-\imath\omega_l t}\rangle \;=\; 2\sqrt{\frac{\hbar\omega_l}{2\epsilon_0}}\sqrt{\frac{\langle N\rangle}{V}}\,\boldsymbol{\epsilon}_l\cos(\omega_l t). \tag{A.21}$$

A.4 Chapter 3: Magnetic Field of a Linear Conductor

The two fundamental postulates of magnetostatics that specify the divergence and curl of $\mathbf{B}$ in free space [185] are,

$$\nabla\cdot\mathbf{B} = 0, \tag{A.22}$$

$$\nabla\times\mathbf{B} = \mu_0\mathbf{J} + \frac{\partial\mathbf{D}}{\partial t}, \tag{A.23}$$

where $\mathbf{J}$ is the current density. The first of these postulates denies the existence of isolated magnetic poles or mono-poles. The term $\partial\mathbf{D}/\partial t$ (which is called the displacement

current) was added to the second postulate (eq. (A.23)) by Maxwell in order to maintain the conservation of charge.

For a continuously differentiable vector field $\mathbf{P}$ we may explicitly write the divergence theorem and Stoke's theorem respectively as [186],

$$\iiint_V \nabla \cdot \mathbf{P}\, dV = \iint_{\partial V} \mathbf{P} \cdot d\mathbf{A}, \tag{A.24}$$

$$\iint_S \nabla \times \mathbf{P} \cdot d\mathbf{A} = \oint_C \mathbf{P} \cdot d\mathbf{l}, \tag{A.25}$$

where ∂V is surface bounding the volume V, and C is the contour bounding the surface S.

Returning to the postulate of eq. (A.23) we take the volume integral of the divergence of both sides, and assume $\partial \mathbf{D}/\partial t = 0$. Here our vector field $\mathbf{P} = \mathbf{J}$ and we arrive at,

$$\iiint_V \nabla \cdot (\nabla \times \mathbf{B})\, dV = \mu_0 \iiint_V \nabla \cdot \mathbf{J}\, dV, \tag{A.26}$$

To simplify the equation we use Gauss's theorem (eq. (A.24)). For the left hand side we set $\mathbf{P} = \nabla \times \mathbf{B}$ whereas

$$\iint_{\partial V} (\nabla \times \mathbf{B}) \cdot d\mathbf{A} = \mu_0 \iint_{\partial V} \mathbf{J} \cdot d\mathbf{A}, \tag{A.27}$$

Then using Stoke's theorem (eq. (A.25)) we may arrive at what is called Ampére's Circuital Law,[1]

$$\oint_C \mathbf{B} \cdot d\mathbf{l} = \mu_0 I, \tag{A.28}$$

since the current $I = \iint_{\partial V} \mathbf{J} \cdot d\mathbf{A}$.

As we stated earlier this relation is true for *any* closed path. The simplest path is of course a circle centered at right angles to the current carrying conductor. Therefore we can write the magnetic field at any point on the closed loop in cylindrical co-ordinates $(\hat{r}, \hat{\theta}, \hat{z})$ (shown in Fig. 3.6(a)) as, $\mathbf{B} \cdot d\mathbf{l} = B_w r d\theta \hat{\theta}$ and integrate over all angles, $\theta = 0 \to 2\pi$, we find a relation for the magnetic field at a distance r from the conductor. When the current in the wire I_w is aligned along the $+\hat{z}$ direction, the magnitude of the

[1] Ampére is widely acknowledged as being the father of electrodynamics and the unit of current, the Amp, is named after him. Most famous for establishing his "Force Law" between wires carrying direct current and the induction of current in one wire due to the current in another. Ampére's work has played a key role in establishing the fundamental postulates of magnetostatics in free space. However, a common misnomer is crediting Ampére with the original derivation of, what is known as, "Ampére's Circuital Law" [187]. This law was first discussed by Maxwell in his "Treatise on Electricity and Electromagnetism". To find the theorem, however, Maxwell based himself on Ampére's work, in particular on his concept of the magnetic shell.

magnetic field $B_w(r)$ at a distance r from the wire is,

$$\mathbf{B}(r) \;=\; B_w(r)\,\hat{\theta} \;=\; \frac{\mu_0 I_w}{2\pi r}\,\hat{\theta}. \tag{A.29}$$

A.5 Chapter 3: Commutator Evaluation

We make use of the Baker-Campbell-Hausdorff formula,

$$e^{\imath\lambda B} A e^{-\imath\lambda B} \;=\; A + \imath\lambda[B,A] + \frac{\imath^2\lambda^2}{2!}[B,[B,A]] + \frac{\imath^3\lambda^3}{3!}[B,[B,[B,A]]] + \dots. \tag{A.30}$$

Defining $\lambda = \omega_{\rm rf} t/\hbar$ we expand the two terms of interest in equation (3.71) as,

$$\begin{aligned} e^{\imath\lambda F_z} F_x e^{-\imath\lambda F_z} \;&=\; F_x + \imath\lambda[F_z,F_x] + \frac{\imath^2\lambda^2}{2!}[F_z,[F_z,F_x]] + \frac{\imath^3\lambda^3}{3!}[F_z,[F_z,[F_z,F_x]]] \\ &\quad + \dots + \frac{\imath^n\lambda^n}{n!}[F_z,[F_z,...[F_z,[F_z,F_x]]...]] + \dots, \qquad \text{(A.31a)} \\ e^{\imath\lambda F_z} F_y e^{-\imath\lambda F_z} \;&=\; F_y + \imath\lambda[F_z,F_y] + \frac{\imath^2\lambda^2}{2!}[F_z,[F_z,F_y]] + \frac{\imath^3\lambda^3}{3!}[F_z,[F_z,[F_z,F_y]]] \\ &\quad + \dots + \frac{\imath^n\lambda^n}{n!}[F_z,[F_z,...[F_z,[F_z,F_y]]...]] + \dots. \qquad \text{(A.31b)} \end{aligned}$$

From the identity $[F_i,F_j] \;=\; \imath\hbar\epsilon_{ijk}F_k$ of equation (3.73), we explicitly evaluate the first six terms in the above expansion. The terms of interest reduce to,

$$\begin{aligned} e^{\imath\lambda F_z} F_x e^{-\imath\lambda F_z} \;&=\; F_x + \imath\lambda\left(\imath\hbar F_y\right) + \frac{\imath^2\lambda^2}{2!}\left(\hbar^2 F_x\right) + \frac{\imath^3\lambda^3}{3!}\left(\imath\hbar^3 F_y\right) \\ &\quad + \frac{\imath^4\lambda^4}{4!}\left(\hbar^4 F_x\right) + \frac{\imath^5\lambda^5}{5!}\left(\imath\hbar^5 F_y\right) + \dots, \qquad \text{(A.32a)} \\ e^{\imath\lambda F_z} F_y e^{-\imath\lambda F_z} \;&=\; F_y + \imath\lambda\left(-\imath\hbar F_x\right) + \frac{\imath^2\lambda^2}{2!}\left(\hbar^2 F_y\right) + \frac{\imath^3\lambda^3}{3!}\left(-\imath\hbar^3 F_x\right) \\ &\quad + \frac{\imath^4\lambda^4}{4!}\left(\hbar^4 F_y\right) + \frac{\imath^5\lambda^5}{5!}\left(-\imath\hbar^5 F_x\right) + \dots. \qquad \text{(A.32b)} \end{aligned}$$

Collecting together the coefficients of the F_x and F_y terms, and substituting back in for λ, with $\lambda = \omega_{\rm rf} t/\hbar$, we have,

$$\begin{aligned} e^{\imath\frac{\omega_{\rm rf}t}{\hbar}F_z} F_x e^{-\imath\frac{\omega_{\rm rf}t}{\hbar}F_z} \;&=\; F_x\left(1 - \frac{(\omega_{\rm rf}t)^2}{2!} + \frac{(\omega_{\rm rf}t)^4}{4!} + \dots\right) \\ &\quad - F_y\left(\omega_{\rm rf}t - \frac{(\omega_{\rm rf}t)^3}{3!} + \frac{(\omega_{\rm rf}t)^5}{5!} - \dots\right), \qquad \text{(A.33a)} \\ e^{\imath\frac{\omega_{\rm rf}t}{\hbar}F_z} F_y e^{-\imath\frac{\omega_{\rm rf}t}{\hbar}F_z} \;&=\; F_y\left(1 - \frac{(\omega_{\rm rf}t)^2}{2!} + \frac{(\omega_{\rm rf}t)^4}{4!} + \dots\right) \\ &\quad + F_x\left(\omega_{\rm rf}t - \frac{(\omega_{\rm rf}t)^3}{3!} + \frac{(\omega_{\rm rf}t)^5}{5!} - \dots\right). \qquad \text{(A.33b)} \end{aligned}$$

Evaluating further commutators in the series, the above is found to satisfy,

$$e^{\imath\frac{\omega_{\rm rf}t}{\hbar}F_z}F_xe^{-\imath\frac{\omega_{\rm rf}t}{\hbar}F_z} = F_x\left(\sum_{n=0}^{\infty}\frac{(-1)^n(\omega_{\rm rf}t)^{2n}}{(2n)!}\right) - F_y\left(\sum_{m=1}^{\infty}\frac{(-1)^{m-1}(\omega_{\rm rf}t)^{2m-1}}{(2m-1)!}\right), \tag{A.34a}$$

$$e^{\imath\frac{\omega_{\rm rf}t}{\hbar}F_z}F_ye^{-\imath\frac{\omega_{\rm rf}t}{\hbar}F_z} = F_y\left(\sum_{n=0}^{\infty}\frac{(-1)^n(\omega_{\rm rf}t)^{2n}}{(2n)!}\right) + F_x\left(\sum_{m=1}^{\infty}\frac{(-1)^{m-1}(\omega_{\rm rf}t)^{2m-1}}{(2m-1)!}\right). \tag{A.34b}$$

These series expansions are quite simply the series expansions for the cosine and sine functions respectively. Finally these terms simplify to,

$$e^{\imath\frac{\omega_{\rm rf}t}{\hbar}F_z}F_xe^{-\imath\frac{\omega_{\rm rf}t}{\hbar}F_z} = F_x\cos\omega_{\rm rf}t - F_y\sin\omega_{\rm rf}t, \tag{A.35a}$$

$$e^{\imath\frac{\omega_{\rm rf}t}{\hbar}F_z}F_ye^{-\imath\frac{\omega_{\rm rf}t}{\hbar}F_z} = F_y\cos\omega_{\rm rf}t + F_x\sin\omega_{\rm rf}t. \tag{A.35b}$$

This is equation (3.74).

A.6 Chapter 4: N Spatial-Energetic Mode Relationship

In this appendix we detail a calculation that generalises the relationship between $N+1$ spatial and energetic modes, under the assumption that the condition (4.39) is upheld.

The Wavefunction And Hamiltonian In The Spatial Mode Basis

Given that we have a (potentially) satisfactory definition of the spatial mode ket (4.35) we may now explore the power of this definition. A quantum state is expanded in a linear superposition of the energetic modes as, [2]

$$|\Psi(t)\rangle = \sum_{\nu=0}^{N} c_\nu(t)|\psi_\nu\rangle. \tag{A.36}$$

The c-numbers evolve in time according to the system Hamiltonian as,
$c_\mu(t) = c_\mu e^{-(\imath/\hbar)\mathbf{H}t}$, with

$$\mathbf{H} = \hbar\sum_{\nu=0}^{\infty}\omega_\nu|\psi_\nu\rangle\langle\psi_\nu|. \tag{A.37}$$

Here we make use of the spatial mode projector (4.38) to relate the wavefunction in the spatial and energetic bases, and the Hamiltonian in the spatial and energetic bases.

[2] The summation limits can be written $\sum_{\nu=0}^{\infty}$, where we assume only $N+1$ of the complex coefficients c_ν have finite values. However, for the purposes of clarity and simplicity here we assume that only the lowest $N+1$ energy eigenfunctions are occupied.

The wavefunction in the spatial basis is related to its counterpart in the energetic basis via the identity projector (4.31) as,

$$|\Psi(t)\rangle_{\mathrm{R}} \;=\; \sum_{\eta=0}^{N} |\eta\rangle\langle\eta|\Psi(t)\rangle \;=\; \sum_{\eta=0}^{N} b_\eta(t)|\eta\rangle. \tag{A.38}$$

The complex numbers $b_\eta(t)$ are related to the coefficients in the energetic basis as,

$$b_\eta(t) \;=\; \sum_{\nu=0}^{N} c_\nu(t)\langle\eta|\psi_\nu\rangle. \tag{A.39}$$

Conversely we may 'rotate' back to the energetic basis by projecting with the identity on the wavefunction in the spatial basis,

$$|\Psi(t)\rangle \;=\; \sum_{\mu=0}^{\infty} |\psi_\mu\rangle\langle\psi_\mu|\Psi(t)\rangle_{\mathrm{R}} \;=\; \sum_{\mu=0}^{N} c_\mu(t)|\psi_\mu\rangle. \tag{A.40}$$

The complex numbers $c_\mu(t)$ are related to the coefficients in the spatial basis as,

$$c_\mu(t) \;=\; \sum_{\eta=0}^{N} b_\eta(t)\langle\psi_\mu|\eta\rangle. \tag{A.41}$$

As we can see the definition of the spatial mode ket (4.18) has allowed us to establish a projector in the spatial basis (4.31) which easily relates the wavefunction in both the spatial and energetic bases, (A.38) and (A.40).

The Hamiltonian in the Spatial and Energetic Bases

We can once again make use of the spatial mode identity (4.31) to rotate the Hamiltonian in the energetic basis to the spatial basis. We let $\mathbf{H}_{\mathrm{R}}$ denote the Hamiltonian in the spatial basis, and acknowledge that it is given by projecting the spatial identity (4.31) on both sides of the energetic mode Hamiltonian (A.37).

$$\mathbf{H}_{\mathrm{R}} \;=\; \sum_{\eta,\kappa=0}^{N} |\eta\rangle\langle\eta|\mathbf{H}|\kappa\rangle\langle\kappa| \;=\; \hbar\sum_{\mu=0}^{\infty}\sum_{\eta,\kappa=0}^{N} \omega_\mu|\eta\rangle\langle\eta|\psi_\mu\rangle\langle\psi_\mu|\kappa\rangle\langle\kappa|. \tag{A.42}$$

The first inner product reduces to,

$$\begin{aligned}\langle\eta|\psi_\mu\rangle \;&=\; \frac{1}{\sqrt{\rho_\eta(0)}}\sum_{m,n=0}^{N} c_n^*(0)\mathcal{D}^\eta_{nm}\langle\psi_m|\psi_\mu\rangle, \\ &=\; \frac{1}{\sqrt{\rho_\eta(0)}}\sum_{n=0}^{N} c_n^*(0)\mathcal{D}^\eta_{n\mu}.\end{aligned} \tag{A.43}$$

and the second inner product is,

$$\begin{aligned}\langle\psi_\mu|\kappa\rangle &= \frac{1}{\sqrt{\rho_\kappa(0)}}\sum_{p,q=0}^{N} c_p(0)\mathcal{D}^\kappa_{qp}\langle\psi_q|\psi_\mu\rangle, \\ &= \frac{1}{\sqrt{\rho_\kappa(0)}}\sum_{p=0}^{N} c_p(0)\mathcal{D}^\kappa_{\mu p}.\end{aligned} \tag{A.44}$$

Plugging in both of the above expressions into (A.42) the spatial Hamiltonian matrix is reduced to a simple form,

$$\mathbf{H}_\mathrm{R} = \hbar\sum_{\eta,\kappa=0}^{N}\Omega_{\eta\kappa}|\eta\rangle\langle\kappa|. \tag{A.45}$$

where,

$$\Omega_{\eta\kappa} = \frac{1}{\sqrt{\rho_\eta(0)\rho_\kappa(0)}}\sum_{\mu=0}^{\infty}\sum_{n,p=0}^{N}\omega_\mu\, c^*_n(0)c_p(0)\mathcal{D}^\eta_{n\mu}\mathcal{D}^\kappa_{\mu p}. \tag{A.46}$$

Making use of the identity (4.32) is not possible here, due to the presence of the ω_μ term above.

Here the definition of the spatial mode ket (4.35) and the projector in the spatial basis (4.31) allows us to easily relate the Hamiltonian in both the spatial and energetic bases, (A.37) and (A.45).

A.7 Chapter 4: Non Diagonal Hamiltonian Matrix

In this appendix we consider a Hamiltonian matrix which is not diagonal. As before the diagonal elements of the Hamiltonian matrix are the eigenenergies of the first two energetic modes $|\psi_0\rangle$ and $|\psi_1\rangle$, which is given by $\hbar\omega_0$ and $\hbar\omega_1$ respectively, where $\omega_0 < \omega_1$. These energetic modes are allowed to interact with a strength $\hbar\Gamma$, where the frequency Γ is real valued. As usual the quantum state is expanded as a linear superposition of these two basis states as,

$$|\Psi(t)\rangle = c_0(t)|\psi_0\rangle + c_1(t)|\psi_1\rangle. \tag{A.47}$$

In Euler form the initial state is $c_\nu(0) = c_\nu e^{\imath\varphi_\nu}$. Without loss of generality we assume that our initial state is real valued, with $\varphi_1 - \varphi_0 = 0$. The phase and amplitude evolution of the complex coefficients of the energetic modes then satisfies,

$$\begin{aligned}\mathbf{c}(t) &= \exp\left(-\frac{\imath}{\hbar}\mathbf{H}t\right)\mathbf{c}, \\ \begin{pmatrix}c_0(t)\\ c_1(t)\end{pmatrix} &= \exp\left(-\imath\begin{pmatrix}\omega_0 & \Gamma\\ \Gamma & \omega_1\end{pmatrix}t\right)\begin{pmatrix}c_0\\ c_1\end{pmatrix}.\end{aligned} \tag{A.48}$$

The eigenvalues of the Hamiltonian matrix **H** are,

$$\begin{aligned}\hbar\lambda_0 &= \frac{\hbar}{2}\left(\omega_{10}^{+} - \sqrt{(\omega_{10}^{-})^2 + 4\Gamma^2}\right),\\ \hbar\lambda_1 &= \frac{\hbar}{2}\left(\omega_{10}^{+} + \sqrt{(\omega_{10}^{-})^2 + 4\Gamma^2}\right),\end{aligned} \tag{A.49}$$

where we have defined,

$$\omega_{10}^{\pm} \equiv \omega_1 \pm \omega_0. \tag{A.50}$$

In the same manner as before, we focus on the mapping of this system into the left-right or $|0\rangle$-$|1\rangle$ basis. To simplify the calculation, we move to the eigenbasis of the Hamiltonian matrix **H**.

$$|\widetilde{\Psi}(t)\rangle = \tilde{c}_0(t)|\widetilde{\psi}_0\rangle + \tilde{c}_1(t)|\widetilde{\psi}_1\rangle. \tag{A.51}$$

The new eigenvectors are defined in terms of the old by,

$$\begin{aligned}|\widetilde{\psi}_0\rangle &= \frac{\lambda_0-\omega_1}{\sqrt{(\lambda_0-\omega_1)^2+\Gamma^2}}|\psi_0\rangle + \frac{\Gamma}{\sqrt{(\lambda_0-\omega_1)^2+\Gamma^2}}|\psi_1\rangle,\\ |\widetilde{\psi}_1\rangle &= \frac{\Gamma}{\sqrt{(\lambda_1-\omega_0)^2+\Gamma^2}}|\psi_0\rangle + \frac{\lambda_1-\omega_0}{\sqrt{(\lambda_1-\omega_0)^2+\Gamma^2}}|\psi_1\rangle,\end{aligned} \tag{A.52}$$

and the phase evolution of the new coefficients in this decoupled basis satisfies,

$$\begin{aligned}\tilde{c}_0(t) &= e^{-\imath\lambda_0 t}\left(\tfrac{c_0(\lambda_0-\omega_1)}{\sqrt{(\lambda_0-\omega_1)^2+\Gamma^2}} + \tfrac{c_1\Gamma}{\sqrt{(\lambda_0-\omega_1)^2+\Gamma^2}}\right),\\ \tilde{c}_1(t) &= e^{-\imath\lambda_1 t}\left(\tfrac{c_0\Gamma}{\sqrt{(\lambda_1-\omega_0)^2+\Gamma^2}} + \tfrac{c_1(\lambda_1-\omega_0)}{\sqrt{(\lambda_1-\omega_0)^2+\Gamma^2}}\right).\end{aligned} \tag{A.53}$$

Presently of interest are the temporal densities of the spatial regions. We discretise the Hilbert space into two spatial modes which are allowed to have an arbitrary size which remains constant over time. If the volume of the η-th spatial region is represented by $\mathcal{V}_\eta$ ($\eta = 0, 1$), and the sum of the volume elements equal the total space, we can define the operator that projects on exactly one of these regions as, [3]

$$\mathbf{P}_\eta = \int_{\mathcal{V}_\eta} d\mathbf{x}\ |\mathbf{x}\rangle\langle\mathbf{x}| = \sum_{\mu,\nu=0}^{1} \widetilde{\mathcal{D}}_{\mu\nu}^{\eta}|\widetilde{\psi}_\mu\rangle\langle\widetilde{\psi}_\nu|, \tag{A.54}$$

where $\widetilde{\mathcal{D}}_{\mu\nu}^{\eta}$ is a tensor whose elements are given by,

$$\widetilde{\mathcal{D}}_{\mu\nu}^{\eta} \equiv \int_{\mathcal{V}_\eta} d\mathbf{x}\ \langle\widetilde{\psi}_\mu|\mathbf{x}\rangle\langle\mathbf{x}|\widetilde{\psi}_\nu\rangle. \tag{A.55}$$

[3] Here we do not have a projector in the strictest sense as we are (in this case) not projecting on both sides with the identity as we did previously in chapter 4 i.e. with $\sum_{\nu=0}^{\infty}|\psi_\nu\rangle\langle\psi_\nu|$. However this projector (as we define in the following) is valid in the context within which we are using it.

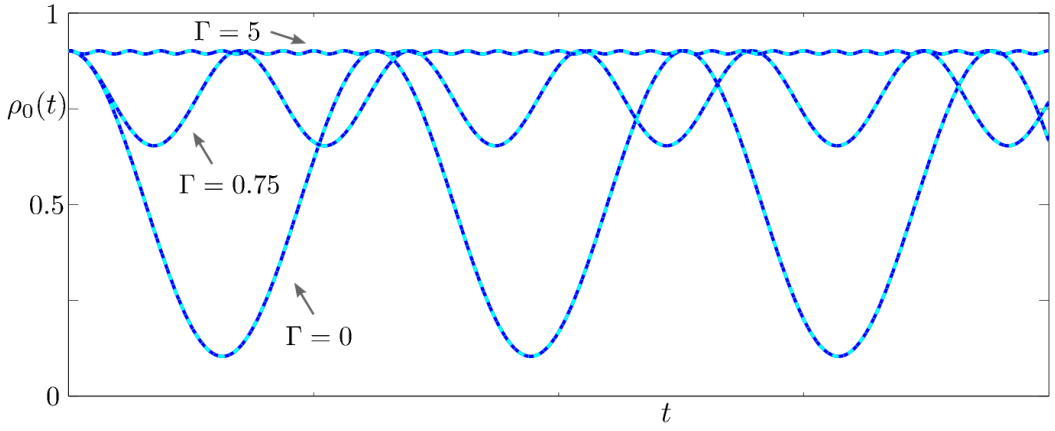


FIGURE A.1: The temporal density $\rho_0(t)$ (solid blue) and $|b_0(t)|^2$ (dashed cyan) of the $\eta = 0$ spatial mode with $\alpha = \pi/4$, $x_b = 0$, and $\Gamma = 0,\ 0.75,\ 5$ (inset) for the one dimensional harmonic oscillator.

By exploiting the completeness relations of the eigenfunctions $\{\psi_\mu\}$ and the fact that $\sum_\eta \mathbf{P}_\eta = \mathbb{1}$, it is easy to prove that $\widetilde{\mathcal{D}}^\eta_{\mu\nu} = \widetilde{\mathcal{D}}^\eta_{\nu\mu}$ and $\sum_\eta \widetilde{\mathcal{D}}^\eta_{\mu\nu} = \delta_{\mu\nu}$. The temporal density of the state (A.51) in the spatial regions $\eta = 0, 1$ is given by $\rho_\eta(t) = \langle\widetilde{\Psi}(t)|\mathbf{P}_\eta|\widetilde{\Psi}(t)\rangle$ which can be written as:

$$\rho_\eta(t) \;=\; \sum_{\mu,\nu=0}^{1} \tilde{c}^*_\mu(t)\tilde{c}_\nu(t)\ \widetilde{\mathcal{D}}^\eta_{\mu\nu}, \qquad \rho_\eta(t) \;=\; \mathcal{M}_\eta + \mathcal{N}_\eta\cos(\lambda^-_{10}t). \tag{A.56}$$

For brevity we have defined,

$$\lambda^\pm_{10} \equiv \lambda_1 \pm \lambda_0, \tag{A.57}$$

and,

$$\mathcal{M}_\eta \;\equiv\; \tilde{c}_0^{\,2}\widetilde{\mathcal{D}}^\eta_{00} + \tilde{c}_1^{\,2}\widetilde{\mathcal{D}}^\eta_{11}, \qquad \mathcal{N}_\eta \;\equiv\; 2\,\tilde{c}_0\tilde{c}_1\widetilde{\mathcal{D}}^\eta_{10}. \tag{A.58}$$

Here we note $\mathcal{N}_0 = -\mathcal{N}_1$. The elements of the spatial mode Hamiltonian are,

$$\begin{aligned}
\hbar\xi_0 &= \frac{\hbar\lambda^+_{10}}{2} - \frac{\hbar\lambda^-_{10}}{2}\cos(\theta),\\
\hbar\xi_1 &= \frac{\hbar\lambda^+_{10}}{2} + \frac{\hbar\lambda^-_{10}}{2}\cos(\theta),\\
\hbar\Omega &= \frac{\hbar\lambda^-_{10}}{2}\sin(\theta).
\end{aligned} \tag{A.59}$$

Progressing along the same lines outlined in chapter 4 we arrive at the same two mappings, A and B. The only difference between the following maps and those of section 4.2 is that the variables $\mathcal{M}_\eta$ and $\mathcal{N}_\eta$ are given by (A.58).

To briefly illustrate the contribution imparted by the Γ term to the evolution of the wavefunction, we have plotted in figure A.1 the density of the $|0\rangle$ spatial mode, for the one dimensional harmonic oscillator, with $\alpha = \pi/4$ for our initial state (4.17), with the

barrier located at the origin, $x_b = 0$. Three values of the coupling parameter are chosen $\Gamma = 0, 0.75, 5$, labelled in the figure. As we can see, increasing the value of Γ increases the frequency of the density oscillations whilst decreasing their amplitude. In the absence of any coupling, the density is seen to periodically oscillate about the mean value of 0.5. What is clear from the figure is that increasing the coupling term, Γ, localises the quantum state in its initial spatial mode.

The coupling term causes periodic transitions between the energetic modes of the quantum state, at a rate which is constant in time i.e. linear transitions. Similarly, the interaction (coupling) term $g_{1\mathrm{D}}$ in the Gross-Pitaevskii equation (3.89) causes periodic transitions between the energetic modes of the quantum state, albeit non-linear. Both equations exhibit the properties of quantum self trapping for large values of the coupling term. Of interest is a means of formally relating the coupling term Γ to the Gross-Pitaevskii coupling term $g_{1\mathrm{D}}$.

Appendix B

Numerical Techniques

In the following we outline the numerical methods employed for the numerical integration of the time dependent Schrödinger equation. We make use of two numerical techniques, the first is known as the split operator method (section B.1), and the second is called the finite difference method (section B.2). The split operator method allows may be employed in one, two and three dimensions, depending on the system considered. Whereas the finite difference method is a numerical diagonalisation technique, which allows for the recovery of the eigenfunctions of an arbitrary one dimensional potential. This numerical tool is quite powerful as it provides an insight as to the functional form of the eigenfunctions of a Hamiltonian, whose solutions may or may not be analytically known. The purpose of both approaches is to numerically propagate in time, a quantum state subject to a time dependent Hamiltonian of the form,

$$\mathbf{H}(t_n) \;=\; -\frac{\hbar^2}{2m}\frac{d^2}{d\mathbf{x}^2} + \mathbf{V}(\mathbf{x}, t_n). \tag{B.1}$$

where $\mathbf{x} = (x, y, z)$ for three dimensions, $\mathbf{x} = (x, y)$ for two, and $\mathbf{x} = (x)$ for one dimensional Hamiltonians.

B.1 The Split Operator Method

To begin, let us briefly review the integration of Schrödinger's equation of an arbitrary state $|\Psi(t_n)\rangle$, subject to the Hamiltonian $\mathbf{H}(t_n)$, to find the representation of the state at the time, t_{n+1}. The Hamiltonian is assumed to remain stationary for a period of time $t_{n+1} - t_n = \Delta t$, and this is the interval of interest here. In its general form the time

dependent Schrödinger equation reads,

$$\imath\hbar \frac{d}{dt}|\Psi(t)\rangle \;=\; \mathbf{H}(t)\,|\Psi(t)\rangle. \tag{B.2}$$

Rearranging we have,

$$\frac{d|\Psi(t)\rangle}{|\Psi(t)\rangle} \;=\; -\frac{\imath}{\hbar}\,dt\;\mathbf{H}(t). \tag{B.3}$$

This is typically integrated by assuming that the Hamiltonian is stationary for a period of time Δt. The differential equation is then integrated between to points in time, t_n and t_{n+1}. Formally we write,

$$\int_{|\Psi(t_n)\rangle}^{|\Psi(t_{n+1})\rangle} \frac{d|\Psi(t)\rangle}{|\Psi(t)\rangle} \;=\; -\frac{\imath}{\hbar}\int_{t_n}^{t_{n+1}} dt\;\mathbf{H}(t). \tag{B.4}$$

The solution to the above is given by,

$$|\Psi(t_{n+1})\rangle \;=\; \exp\left(-\frac{\imath}{\hbar}\,\mathbf{H}(t_n)\Delta t\right)\;|\Psi(t_n)\rangle. \tag{B.5}$$

The Hamiltonian of equation (B.1) consists of both kinetic and potential parts, $\mathbf{H}(t_n) = \mathbf{K} + \mathbf{V}(t_n)$. The kinetic and potential operators are made up of the position ($\mathbf{x}$) and momentum ($\mathbf{p}$) operators respectively. Explicitly these are,

$$\mathbf{K} \;=\; \frac{\mathbf{p}^2}{2m}, \tag{B.6a}$$

$$\mathbf{V}(t_n) \;=\; \mathbf{V}(\mathbf{x}, t_n), \tag{B.6b}$$

where, $\mathbf{p} = -\imath\hbar\, d/d\mathbf{x}$. For the purpose of abbreviation we define $\mathbf{V}(t_n) \equiv \mathbf{V}$.

For the numerical evaluation of (B.5) we make use of one form of the Baker-Campbell-Hausdorff formula, which is known as the Zassenhaus Formula. To do so, we expand the exponential term containing the operators, $\mathbf{K}$ and $\mathbf{V}$, by taking the necessary commutators. If we let $\lambda = -\imath \int_{t_n}^{t_{n+1}} dt/\hbar = -\imath\, \Delta t/\hbar$,

$$\exp\left(\lambda\mathbf{K} + \lambda\mathbf{V}\right) \quad = \quad \exp\left(\lambda\mathbf{K}\right)\exp\left(\lambda\mathbf{V}\right)\exp\left(-\frac{\lambda^2}{2}[\mathbf{K},\mathbf{V}]\right). \tag{B.7}$$

The third order and higher terms in the expansion are neglected since $[\mathbf{K}, \mathbf{V}]$ commutes with $\mathbf{K}$ and $\mathbf{V}$. If we evolve using a very small time step, the contribution from the last exponential can effectively be ignored, as it is of the order Δt^2. Hence we are justified in taking the following approximation,

$$\exp\left(\lambda\mathbf{K} + \lambda\mathbf{V}\right) \;\approx\; \exp\left(\lambda\mathbf{K}\right)\exp\left(\lambda\mathbf{V}\right), \tag{B.8}$$

However, Feit and Fleck [188] improved the above approximation by introducing a novel

propagation scheme which is strictly unitary. In this method the evolution operator is approximated by a symmetric splitting of the kinetic energy operator in the following way,

$$\exp(\lambda \mathbf{H}) \;=\; \exp\left(\frac{\lambda}{2}\mathbf{K}\right)\exp(\lambda \mathbf{V})\exp\left(\frac{\lambda}{2}\mathbf{K}\right) + O(\lambda^3). \tag{B.9}$$

The error in this splitting is of third order in Δt which can neglected when taking a small time step. Let us define the operation of applying a (fast) Fourier transform and inverse (fast) Fourier transform as, $\mathscr{F}[\ ]$ and $\mathscr{F}^{-1}[\ ]$, respectively. The wavefunction is then iteratively calculated as,

$$\langle \mathbf{x}|\Psi(t_{n+1})\rangle \;=\; \mathscr{F}^{-1}\left[\exp\left(\frac{\lambda}{2}\mathbf{K}\right)\mathscr{F}\left[\exp(\lambda \mathbf{V})\,\mathscr{F}^{-1}\left[\exp\left(\frac{\lambda}{2}\mathbf{K}\right)\mathscr{F}\Big[\langle \mathbf{x}|\Psi(t_n)\rangle\Big]\right]\right]\right]. \tag{B.10}$$

Provided the change to the Hamiltonian (B.1) are small and the chosen time step is small the above approach is stable.

B.2 The Finite Difference Method

For one dimensional systems we assume that the confinement in the y and z directions is much larger than the confinement in the x directions, i.e. $\omega_x \ll \omega_{y,z}$. Subsequently the model used for numerical purposes is one dimensional. For the numerical method outline here we scaled the spatial co-ordinates $\mathbf{x}$ with respect to the length $\sqrt{\hbar/m\omega}$. For illustrative purposes we use write (B.1) in scaled co-ordinates for some potential $V(x)$,

$$\mathbf{H} \;=\; -\frac{1}{2}\frac{d^2}{dx^2} + V(x). \tag{B.11}$$

Here we omit to include time dependence but it can be invoked by changing the functional form of the potential $V(x)$. We are looking to write a computer code that solves for the eigenfunctions $\psi(x)$ and eigenvalues E of the wave equation,

$$\left(-\frac{1}{2}\frac{d^2}{dx^2} + \frac{x^2}{2}\right)\psi(x) \;=\; E\psi(x). \tag{B.12}$$

The numerical solution to (B.12) is evaluated using the finite difference technique by replacing the second order derivative with an expression using finite differences. To proceed we discretise the one dimensional spatial region into nodes x_m where the distance between adjacent nodes is $x_{m+1} - x_m = \Delta x$, and $m = 0, 1, 2, \ldots, M$. The second derivative term is then written,

$$-\frac{1}{2}\frac{d^2}{dx^2}\psi(x_m) \;=\; \frac{-\psi(x_{m+1}) + 2\psi(x_m) - \psi(x_{m-1})}{2\Delta x^2}. \tag{B.13}$$

In matrix form, this is given by,

$$-\frac{1}{2}\frac{d^2}{dx^2}\psi(x) = \frac{1}{2\,\Delta x^2}\begin{pmatrix} 2 & -1 & 0 & \cdots & 0 \\ -1 & 2 & -1 & \cdots & \vdots \\ 0 & -1 & 2 & \ddots & 0 \\ \vdots & \vdots & \ddots & \ddots & -1 \\ 0 & \cdots & 0 & -1 & 2 \end{pmatrix}\begin{pmatrix} \psi(x_0) \\ \psi(x_1) \\ \psi(x_2) \\ \vdots \\ \psi(x_M) \end{pmatrix}. \tag{B.14}$$

The discretised potential is also written in matrix form,

$$V(x) = \begin{pmatrix} V(x_0) & 0 & 0 & \cdots & 0 \\ 0 & V(x_1) & 0 & \cdots & 0 \\ 0 & 0 & V(x_2) & \ddots & \vdots \\ \vdots & \vdots & \ddots & \ddots & 0 \\ 0 & 0 & \cdots & 0 & V(x_M) \end{pmatrix}. \tag{B.15}$$

Defining $\alpha_m \equiv (\Delta x)V(x_m) + 2$, the Hamiltonian is given by,

$$\mathbf{H} \;=\; \frac{1}{2\Delta x}\begin{pmatrix} \alpha_m & -1 & 0 & \cdots & 0 \\ -1 & \alpha_m & -1 & \cdots & \vdots \\ 0 & -1 & \alpha_m & \ddots & 0 \\ \vdots & \vdots & \ddots & \ddots & -1 \\ 0 & \cdots & 0 & -1 & \alpha_m \end{pmatrix}. \tag{B.16}$$

Numerical diagonalisation of the above Hamiltonian allows for the recovery of the correct eigenfunctions and eigenvalues that satisfy $\mathbf{H}\psi(x) - E\psi(x) = 0$.

Bibliography

[1] E. M. Purcell, H. C. Torrey, and R. V. Pound. **Resonance Absorption by Nuclear Magnetic Moments in a Solid**. *Phys. Rev.*, **69**:37–38, January 1946. URL `http://link.aps.org/doi/10.1103/PhysRev.69.37`.

[2] Daniel Kleppner. **Inhibited Spontaneous Emission**. *Physical Review Letters*, **47**:233–236, July 1981. URL `http://link.aps.org/doi/10.1103/PhysRevLett.47.233`.

[3] S. Giorgini, L. P. Pitaevskii, and S. Stringari. **Theory of Ultracold Atomic Fermi Gases**. *Reviews of Modern Physics*, **80**:1215–1274, 2008. URL `http://dx.doi.org/10.1103/RevModPhys.80.1215`.

[4] K. Helmerson, M. Xiao, and D. Pritchard. *IQEC'90 book of abstracts, QTHH4*, 1990.

[5] Th. Busch, J. R. Anglin, J. I. Cirac, and P. Zoller. **Inhibition of Spontaneous Emission in Fermi gases**. *Europhysics Letters*, **44**:001–006, October 1998. URL `http://iopscience.iop.org/0295-5075/44/1/001/`.

[6] J. Javanainen and J. Ruostekoski. **Off-Resonance Light Scattering From Low-Temperature Bose and Fermi Gases**. *Physical Review A*, **52**:3033–3046, October 1995. URL `http://pra.aps.org/abstract/PRA/v52/i4/p3033_1`.

[7] G. Modugno, F. Ferlaino, R. Heidemann, G. Roati, and M. Inguscio. **Production of a Fermi Gas of Atoms in an Optical Lattice**. *Physical Review A*, **68**: 011601(R), July 2003. URL `http://dx.doi.org/10.1103/PhysRevA.68.011601`.

[8] H. Moritz, T. Stöferle, K. Günter, M. Köhl, and T. Esslinger. **Confinement Induced Molecules in a 1D Fermi Gas**. *Physical Review Letters*, **94**:210401, June 2005. URL `http://dx.doi.org/10.1103/PhysRevLett.94.210401`.

[9] S. Aubin, S. Myrskog, M. H. T. Extavour, L. J. LeBlanc, D. McKay, A. Stummer, and J. H. Thywissen. **Rapid Sympathetic Cooling to Fermi Degeneracy on a Chip**. *Nature Physics*, **2**:384–387, May 2006. URL `http://dx.doi.org/10.1038/nphys309`.

[10] J.J. Sakurai. **Modern Quantum Mechanics**. *Addison Wesley Longman*, ISBN 020-153-929-2, 1994.

[11] E. Schrödinger. **On the Relation between the Quantum Mechanics of Heisenberg, Born, and Jordan, and that of Schrödinger**. *Annalem der Physick*, **79**, 1926.

[12] J. L. Basdevant, J. Dalibard, and M. Joffre. **Quantum Mechanics**. *Springer*, ISBN 354-027-706-4, 2005.

[13] C. Cohen-Tannoudji, J. Dupont-Roc, and G. Grynberg. **Atom Photon Interactions**. *Wiley*, ISBN 047-129-336-9, 1998.

[14] Mohsen Razavy. **Quantum Theory of Tunneling**. *World Scientific*, ISBN 981-238-018-3, 2003.

[15] Tetsuo Miyazaki. **Atom Tunneling Phenomena in Physics, Chemistry and Biology**. *Springer*, ISBN 354-001-526-4, 2004.

[16] A. Griffin, D. W. Snoke, and S. Stringari. **Bose-Einstein Condensation**. *Cambridge University Press*, ISBN 052-158-990-8, 1996.

[17] F. Dalfovo, S. Giorgini, L. P. Pitaevskii, and S. Stringari. **Theory of Bose-Einstein Condensation in Trapped Gases**. *Reviews of Modern Physics*, **71**: 463–512, April 1999. URL `http://dx.doi.org/10.1103/RevModPhys.71.463`.

[18] F. Serwane, G. Zürn, T. Lompe, T. B. Ottenstein, A. N. Wenz, and S. Jochim. **Deterministic Preparation of a Tunable Few-Fermion System**. *Science*, **332**:336–338, April 2011. URL `http://dx.doi.org/10.1126/science.1201351`.

[19] G. Zürn, F. Serwane, T. Lompe, A. N. Wenz, M. G. Ries, J. E. Bohn, and S. Jochim. **Fermionization of Two Distinguishable Fermions**. *Physical Review Letters*, **108**:075303, February 2012. URL `http://dx.doi.org/10.1103/PhysRevLett.108.075303`.

[20] D. A. Butts and D. S. Rokhsar. **Trapped Fermi Gases**. *Physical Review A*, **55**: 4346–4350, June 1997. URL `http://dx.doi.org/10.1103/PhysRevA.55.4346`.

[21] J. Schneider and H. Wallis. **Mesoscopic Fermi Gas in a Harmonic Trap**. *Physical Review A*, **57**:1253–1259, February 1998. URL `http://dx.doi.org/10.1103/PhysRevA.57.1253`.

[22] B. DeMarco and D. S. Jin. **Onset of Fermi Degeneracy in a Trapped Atomic Gas**. *Science*, **285**:1703–1706, September 1999. URL `http://dx.doi.org/10.1126/science.285.5434.1703`.

[23] Gabriele Ferrari. **Collisional Relaxation in a Fermionic Gas**. *Physical Review A*, **59**:4125–4128, June 1999. URL `http://dx.doi.org/10.1103/PhysRevA.59.R4125`.

[24] B. DeMarco, S. B. Papp, and D. S. Jin. **Pauli Blocking of Collisions in a Quantum Degenerate Atomic Fermi Gas**. *Physical Review Letters*, **86**:5409–5412, June 2001. URL `http://dx.doi.org/10.1103/PhysRevLett.86.5409`.

[25] J. Ruostekoski and J. Javanainen. **Optical Linewidth of a Low Density Fermi-Dirac Gas**. *Physical Review Letters*, **82**:4741–4744, June 1999. URL `http://dx.doi.org/10.1103/PhysRevLett.82.4741`.

[26] J. Javanainen, J. Ruostekoski, B. Vestergaard, and M. R. Francis. **One-Dimensional Modeling of Light Propagation in Dense and Degenerate Samples**. *Physical Review A*, **59**:649–666, January 1999. URL `http://dx.doi.org/10.1103/PhysRevA.59.649`.

[27] B. DeMarco and D. S. Jin. **Exploring a Quantum Degenerate Gas of Fermionic Atoms**. *Physical Review A*, **58**:4267–4270, December 1998. URL `http://dx.doi.org/10.1103/PhysRevA.58.R4267`.

[28] A. Görlitz, A. P. Chikkatur, and W. Ketterle. **Enhancement and Suppression of Spontaneous Emission and Light Scattering by Quantum Degeneracy**. *Physical Review A*, **63**:041601–4270, March 2001. URL `http://dx.doi.org/10.1103/PhysRevA.63.041601`.

[29] B. Shuve and J. H. Thywissen. **Enhanced Pauli Blocking of Light Scattering in a Trapped Fermi Gas**. *Journal of Physics B: Atomic, Molecular and Optical Physics*, **43**:015301, January 2010. URL `http://dx.doi.org/10.1088/0953-4075/43/1/015301`.

[30] C. Cohen-Tannoudji, B. Diu, and F. Laloe. **Quantum Mechanics**. *Wiley*, ISBN 047-116-433-X, 1977.

[31] M. Abramowitz and I. Stegun. **Handbook of Mathematical Functions**. *Dover New York*, ISBN 048-661-272-4, 1964.

[32] Wolfgang Ketterle. **When Atoms Behave as Waves: Bose-Einstein Condensation and the Atom Laser**. *Reviews of Modern Physics*, **74**:1131–1151, November 2002. URL `http://link.aps.org/doi/10.1103/RevModPhys.74.1131`.

[33] L. Pitaevskii and S. Stringari. **Bose-Einstein Condensation**. *Oxford University Press*, ISBN 052-158-990-8, 2003.

[34] M. H. Anderson, J. R. Ensher, M. R. Matthews, C. E. Wieman, and E. A. Cornell. **Observation of Bose-Einstein Condensation in a Dilute Atomic Vapor**. *Science*, **269**:198–201, July 1995. URL http://dx.doi.org/10.1126/science.269.5221.198.

[35] K. B. Davis, M.-O. Mewes, M. R. Andrews, N. J. van Druten, D. S. Durfee, D. M. Kurn, and W. Ketterle. **Bose-Einstein Condensation in a Gas of Sodium Atoms**. *Physical Review Letters*, **75**:3969–3973, November 1995. URL http://link.aps.org/doi/10.1103/PhysRevLett.75.3969.

[36] Edward W. Hagley, Lu Deng, William D. Philips, Keith Burnett, and Charles W. Clark. **The Atom Laser**. *Optics and Photonics News*, **12**, May 2001. URL http://www.osa-opn.org/Content/ViewFile.aspx?id=10785.

[37] Immanuel Bloch, Theodor W. Hnsch, , and Tilman Esslinger. **Atom Laser with a cw Output Coupler**. *Physical Review Letters*, **82**:3008–3011, December 1998. URL http://dx.doi.org/10.1103/PhysRevLett.82.3008.

[38] Christopher J. Foot. **Atomic Physics**. *Oxford University Press*, ISBN 019-850-696-1, 2005.

[39] J. H. Cole, A. D. Greentree, L. C. L. Hollenberg, and S. Das Sarma. **Spatial Adiabatic Passage in a Realistic Triple Well Structure**. *Physical Review B*, **77**:235418, June 2008. URL http://dx.doi.org/10.1103/PhysRevB.77.235418.

[40] Lenneke M. Jong and Andrew D. Greentree. **Interferometry using Spatial Adiabatic Passage in Quantum Dot Networks**. *Physical Review B*, **81**: 035311, January 2010. URL http://dx.doi.org/10.1103/PhysRevB.81.035311.

[41] C. D. Hill, A. D. Greentree, and L. C. L. Hollenberg. **Parallel Interaction-Free Measurement Using Spatial Adiabatic Passage**. *December*, **13**:125002, December 2011. URL http://dx.doi.org/10.1088/1367-2630/13/12/125002.

[42] Yu. Loiko, V. Ahufinger, R. Corbalán, G. Birkl, and J. Mompart. **Filtering of Matter-Wave Vibrational States via Spatial Adiabatic Passage**. *Physical Review A*, **83**:033629, March 2011. URL http://dx.doi.org/10.1103/PhysRevA.83.033629.

[43] J. Mompart A. Negretti, A. Benseny and T. Calarco. **Speeding Up the Spatial Adiabatic Passage of Matter Waves in Optical Microtraps by Optimal Control**. *Quantum Information Processing*, January 2012. URL http://dx.doi.org/10.1007/s11128-012-0357-z.

[44] A. Benseny, J. Bagudà, X. Oriols, and J. Mompart. **Need for Relativistic Corrections in the Analysis of Spatial Adiabatic Passage of Matter Waves**. *Physical Review A*, **85**:053619, May 2012. URL `http://dx.doi.org/10.1103/PhysRevA.85.053619`.

[45] Serge Haroche and Daniel Kleppner. **Cavity Quantum Electrodynamics**. *Physics Today*, **42**:24–30, January 1989. URL `http://dx.doi.org/10.1063/1.881201`.

[46] K. Bergmann, H. Theuer, and B. W. Shore. **Coherent Population Transfer Among Quantum States of Atoms and Molecules**. *Reviews of Modern Physics*, **70**:1003–1025, July 1998. URL `http://dx.doi.org/10.1103/RevModPhys.70.1003`.

[47] M. Fewell, B. W. Shore, and K. Bergmann. **Coherent Population Transfer among Three States: Full Algebraic Solutions and the Relevance of Non Adiabatic Processes to Transfer by Delayed Pulses**. *Australian Journal of Physics*, **50**:281–304, March 1997. URL `http://www.publish.csiro.au/paper/P96071.htm`.

[48] K.-P. Marzlin and B. C. Sanders. **Inconsistency in the Application of the Adiabatic Theorem**. *Physical Review Letters*, **93**:160408, October 1985. URL `http://dx.doi.org/10.1103/PhysRevLett.93.160408`.

[49] D. M. Tong, K. Singh, L. C. Kwek, and C. H. Oh. **Sufficiency Criterion for the Validity of the Adiabatic Approximation**. *Physical Review Letters*, **98**:150402, April 2007. URL `http://dx.doi.org/10.1103/PhysRevLett.98.150402`.

[50] M. H. S. Amin. **Consistency of the Adiabatic Theorem**. *Physical Review Letters*, **102**:220401, June 2009. URL `http://dx.doi.org/10.1103/PhysRevLett.102.220401`.

[51] D. M. Tong. **Quantitative Condition is Necessary in Guaranteeing the Validity of the Adiabatic Approximation**. *Physical Review Letters*, **104**:120401, March 2010. URL `http://dx.doi.org/10.1103/PhysRevLett.104.120401`.

[52] Albert Messiah. **Quantum Mechanics**. *Dover Publications*, ISBN 048-640-924-4, 1961.

[53] A. L. Migdall, J. V. Prodan, W. D. Phillips, T. H. Bergeman, and H. J. Metcalf. **First Observation of Magnetically Trapped Neutral Atoms**. *Physical Review Letters*, **54**:2596–2599, November 1985. URL `http://dx.doi.org/10.1103/PhysRevLett.54.2596`.

[54] D. Frese, B. Ueberholz, S. Kuhr, W. Alt, D. Schrader, V. Gomer, and D. Meschede. **Single Atoms in an Optical Dipole Trap: Towards a Deterministic Source of Cold Atoms**. *Physical Review Letters*, **85**:3777–3880, March 2000. URL http://dx.doi.org/10.1103/PhysRevLett.85.3777.

[55] M. Fleischhauer, A. Imamoglu, and J. P. Marangos. **Electromagnetically Induced Transparency: Optics in Coherent Media**. *Reviews of Modern Physics*, **77**:633–673, July 2005. URL http://dx.doi.org/10.1103/RevModPhys.77.633.

[56] K. Eckert, M. Lewenstein, R. Corbalán, G. Birkl, W. Ertmer, and J. Mompart. **Three-Level Atom Optics Via the Tunneling Interaction**. *Physical Review A*, **70**:023606, August 2004. URL http://dx.doi.org/10.1103/PhysRevA.70.023606.

[57] Andrew D. Greentree, Jared H. Cole, A. R. Hamilton, and Lloyd C. L. Hollenberg. **Coherent Electronic Transfer in Quantum Dot Systems Using Adiabatic Passage**. *Physical Review B*, **70**:235317, December 2004. URL http://link.aps.org/doi/10.1103/PhysRevB.70.235317.

[58] G. Birkl, F. B. J. Buchkremer, R. Dumke, and W. Ertmer. **Atom Optics With Microfabricated Optical Elements**. *Optics Communications*, **191**:67–81, April 2001. URL http://dx.doi.org/10.1016/S0030-4018(01)01107-5.

[59] Nikolay V. Vitanov, Thomas Halfmann, Bruce W. Shore, and Klaas Bergmann. **Laser-Induced Population Transfer By Adiabatic Techniques**. *Annual Review of Physical Chemistry*, **52**:763–809, October 2001. URL http://dx.doi.org/10.1146/annurev.physchem.52.1.763.

[60] D. F. Walls and G. J. Milburn. **Quantum Optics**. *Springer*, ISBN 354-058-831-0, 1995.

[61] Hagen Kleinert. **Gauge Fields in Condensed Matter**. *Springer*, ISBN 997-150-210-0, 1990.

[62] M. Rab, J. H. Cole, N. G. Parker, A. D. Greentree, L. C. L. Hollenberg, and A. M. Martin. **Spatial Coherent Transport of Interacting Dilute Bose Gases**. *Physical Review A*, **77**:061602(R), December 2008. URL http://dx.doi.org/10.1103/PhysRevA.77.061602.

[63] J. Siewerta, T. Brandesc, and G. Falci. **Adiabatic Passage with Superconducting Nanocircuits**. *Optics Communications*, **264**:435–440, August 2006. URL http://dx.doi.org/10.1016/j.optcom.2005.12.083.

[64] R. Rahman, R. P. Muller, J. E. Levy, M. S. Carroll, G. Klimeck, A. D. Greentree, and L. C. L. Hollenberg. **Coherent Electron Transport by Adiabatic Passage in an Imperfect Donor Chain**. *Physical Review B*, **82**:155315, October 2010. URL `http://dx.doi.org/10.1103/PhysRevB.82.155315`.

[65] B. Chen, W. Fan, and Y. Xu. **Adiabatic Quantum State Transfer in a Nonuniform Triple-Quantum-Dot System**. *Physical Review A*, **83**:014301, January 2011. URL `http://dx.doi.org/10.1103/PhysRevA.83.014301`.

[66] J. Rech and S. Kehrein. **Effect of Measurement Backaction on Adiabatic Coherent Electron Transport**. *Physical Review Letters*, **106**:136808, March 2011. URL `http://dx.doi.org/10.1103/PhysRevLett.106.136808`.

[67] F. Renzoni and T. Brandes. **Charge Transport Through Quantum Dots via Time-Varying Tunnel Coupling**. *Physical Review B*, **64**:245301, November 2001. URL `http://dx.doi.org/10.1103/PhysRevB.64.245301`.

[68] R. Rahman, S. H. Park, J. H. Cole, A. D. Greentree, R. P. Muller, G. Klimeck, and L. C. L. Hollenberg. **Atomistic Simulations of Adiabatic Coherent Electron Transport in Triple Donor Systems**. *Physical Review B*, **80**:035302, July 2009. URL `http://dx.doi.org/10.1103/PhysRevB.80.035302`.

[69] L. M. Jong, A. D. Greentree, V. I. Conrad, L. C. L. Hollenberg, and D. N. Jamieson. **Coherent Tunneling Adiabatic Passage With The Alternating Coupling Scheme**. *Nanotechnology*, **20**:405402, October 2009. URL `http://dx.doi.org/10.1088/0957-4484/20/40/405402`.

[70] K. Eckert, J. Mompart, R. Corbalán, M. Lewenstein, and G. Birkl. **Three Level Atom Optics in Dipole Traps and Waveguides**. *Optics Communications*, **264**:264–270, August 2006. URL `http://dx.doi.org/10.1016/j.optcom.2006.02.056`.

[71] B. T. Seaman, M. Kramer, D. Z. Anderson, and M. J. Holland. **Atomtronics: Ultracold-atom analogs of electronic devices**. *Physical Review A*, **75**, February 2007. URL `http://dx.doi.org/10.1103/PhysRevA.75.023615`.

[72] A. Benseny, S. Fernández-Vidal, J. Bagudà, R. Corbalán, A. Picón, L. Roso, G. Birkl, and J. Mompart. **Atomtronics With Holes: Coherent Transport of an Empty Site in a Triple-Well Potential**. *Physical Review A*, **82**:013604, July 2010. URL `http://dx.doi.org/10.1103/PhysRevA.82.013604`.

[73] M. Fuechsle, J. A. Miwa, S. Mahapatra, H. Ryu, S. Lee, O. Warschkow, L. C. L. Hollenberg, G. Klimeck, and M. Y. Simmons. **A Single-Atom Transistor**.

Nature Nanotechnology, **7**:242–246, February 2012. URL http://dx.doi.org/10.1038/nnano.2012.21.

[74] L. C. L. Hollenberg, A. D. Greentree, A. G. Fowler, and C. J. Wellard. **Two-dimensional Architectures for Donor-Based Quantum Computing**. *Physical Review B*, **74**:045311, July 2006. URL http://dx.doi.org/10.1103/PhysRevB.74.045311.

[75] Ping Zhang, Qi-Kun Xue, Xian-Geng Zhao, and X. C. Xie. **Generation of Spatially Separated Spin Entanglement in a Triple-Quantum-Dot System**. *Physical Review A*, **69**:042307, April 2004. URL http://dx.doi.org/10.1103/PhysRevA.69.042307.

[76] E. M. Graefe, H. J. Korsch, and D. Witthaut. **Mean-field Dynamics of a Bose-Einstein Condensate in a Time-Dependent Triple-well trap: Nonlinear Eigenstates, Landau-Zener Models, and Stimulated Raman Adiabatic Passage**. *Physical Review A*, **73**:013617, January 2006. URL http://dx.doi.org/10.1103/PhysRevA.73.013617.

[77] J. Fabian and U. Hohenester. **Entanglement Distillation by Adiabatic Passage in Coupled Quantum Dots**. *Phyical Review B*, **72**:201304(R), November 2005. URL http://dx.doi.org/10.1103/PhysRevB.72.201304.

[78] D. Petrosyana and P. Lambropoulos. **Coherent Population Transfer in a Chain of Tunnel Coupled Quantum Dots**. *Optics Communications*, **264**:419–425, August 2006. URL http://dx.doi.org/10.1016/j.optcom.2005.12.082.

[79] M. Rab, A. L. C. Hayward, J. H. Cole, A. D. Greentree, and A. M. Martin. **Interferometry using Adiabatic Passage in Dilute Gas Bose-Einstein Condensates**. *arXiv*, 2011. URL http://arxiv.org/abs/1207.6158.

[80] C. J. Bradly, M. Rab, A. D. Greentree, and A. M. Martin. **Coherent Tunneling via Adiabatic Passage in a Three-Well Bose-Hubbard System**. *Physical Review A*, **85**:053609, May 2012. URL http://dx.doi.org/10.1103/PhysRevA.85.053609.

[81] Stefano Longhi. **Adiabatic Passage of Light in Coupled Optical Waveguides**. *Physical Review E*, **73**:026607, February 2006. URL http://dx.doi.org/10.1103/PhysRevE.73.026607.

[82] S. Longhi, G. Della Valle, M. Ornigotti, and P. Laporta. **Coherent Tunneling by Adiabatic Passage in an Optical Waveguide System**. *Physics Review B*, **76**:201101, November 2007. URL http://dx.doi.org/10.1103/PhysRevB.76.201101.

[83] W. Hänsel, J. Reichel, P. Hommelhoff, and T. W. Hänsch. **Trapped-Atom Interferometer in a Magnetic Microtrap**. *Physical Review A*, **64**:063607, November 2001. URL http://dx.doi.org/10.1103/PhysRevA.64.063607.

[84] C.-S. Chuu, F. Schreck, T. P. Meyrath, J. L. Hanssen, G. N. Price, and M. G. Raizen. **Direct Observation of Sub-Poissonian Number Statistics in a Degenerate Bose Gas**. *Physical Review Letters*, **95**:260403, December 2005. URL http://dx.doi.org/10.1103/PhysRevLett.95.260403.

[85] A. Shevchenko, M. Heiliö, T. Lindvall, A. Jaakkola, I. Tittonen, and M. Kaivola. **Trapping Atoms on a Transparent Permanent-Magnet Atom Chip**. *Physical Review A*, **73**:051401(R), May 2006. URL http://dx.doi.org/10.1103/PhysRevA.73.051401.

[86] S. Bergamini, B. Darquié, M. Jones, L. Jacubowiez, A. Browaeys, and P. Grangier. **Holographic Generation of Microtrap Arrays for Single Atoms by use of a Programmable Phase Modulator**. *Journal of the Optical Society of America B*, **21**:1889–1894, November 2004. URL http://dx.doi.org/10.1364/JOSAB.21.001889.

[87] J. Reichel, W. Hänsel, and T. W. Hänsch. **Atomic Micromanipulation with Magnetic Surface Traps**. *Physical Review Letters*, **83**:3398–3401, October 1999. URL http://dx.doi.org/10.1103/PhysRevLett.83.3398.

[88] Dirk Müller, Dana Z. Anderson, Randal J. Grow, Peter D. D. Schwindt, and Eric A. Cornell. **Guiding Neutral Atoms Around Curves with Lithographically Patterned Current-Carrying Wires**. *Physical Review Letters*, **83**:5194–5197, December 1999. URL http://dx.doi.org/10.1103/PhysRevLett.83.5194.

[89] N. H. Dekker, C. S. Lee, V. Lorent, J. H. Thywissen, S. P. Smith, M. Drndić, R. M. Westervelt, and M. Prentiss. **Guiding Neutral Atoms on a Chip**. *Physical Review Letters*, **84**:1124–1127, February 2000. URL http://dx.doi.org/10.1103/PhysRevLett.84.1124.

[90] R. Folman, P. Krüger, D. Cassettari, B. Hessmo, T. Maier, and J. Schmiedmayer. **Controlling Cold Atoms using Nanofabricated Surfaces: Atom Chips**. *Physical Review Letters*, **84**:4749–4752, May 2000. URL http://dx.doi.org/10.1103/PhysRevLett.84.4749.

[91] W. Hänsel, P. Hommelhoff, T. W. Hänsch, and J. Reichel. **Bose Einstein Condensation on a Microelectronic Chip**. *Nature*, **416**:498–501, October 2001. URL http://dx.doi.org/10.1038/35097032.

[92] H. Ott, J. Fortagh, G. Schlotterbeck, A. Grossmann, and C. Zimmermann. **Bose Einstein Condensation in a Surface Microtrap**. *Physical Review Letters*, **87**:230401, November 2001. URL `http://dx.doi.org/10.1103/PhysRevLett.87.230401`.

[93] J. Beugnon, M. P. A. Jones, J. Dingjan, B. Darquié, G. Messin, A. Browaeys, and P. Grangier. **Quantum Interference Between Two Single Photons Emitted by Independently Trapped Atoms**. *Nature*, **440**:779–782, January 2006. URL `http://dx.doi.org/10.1038/nature04628`.

[94] J. Eschner, Ch. Raab, F. Schmidt-Kaler, and R. Blatt. **Light Interference from Single Atoms and Their Mirror Images**. *Nature*, **413**:495–498, July 2001. URL `http://dx.doi.org/10.1038/35097017`.

[95] Gavin K. Brennen, Carlton M. Caves, Poul S. Jessen, and Ivan H. Deutsch. **Quantum Logic Gates in Optical Lattices**. *Physical Review Letters*, **82**:1060–1063, February 1999. URL `http://dx.doi.org/10.1103/PhysRevLett.82.1060`.

[96] D. Jaksch, H.-J. Briegel, J. I. Cirac, C. W. Gardiner, and P. Zoller. **Entanglement of Atoms via Cold Controlled Collisions**. *Physical Review Letters*, **82**:1975–1978, March 1999. URL `http://dx.doi.org/10.1103/PhysRevLett.82.1975`.

[97] D. Jaksch, J. I. Cirac, P. Zoller, S. L. Rolston, R. Côté, and M. D. Lukin. **Fast Quantum Gates for Neutral Atoms**. *Physical Review Letters*, **85**:2208–2211, September 2000. URL `http://dx.doi.org/10.1103/PhysRevLett.85.2208`.

[98] M. Khudaverdyan, W. Alt, I. Dotsenko, L. Förster, S. Kuhr, D. Meschede, Y. Miroshnychenko, D. Schrader, and A. Rauschenbeutel. **Adiabatic Quantum State Manipulation of Single Trapped Atoms**. *Physical Review A*, **71**:031404(R), March 2005. URL `http://dx.doi.org/10.1103/PhysRevA.71.031404`.

[99] D. D. Yavuz, P. B. Kulatunga, E. Urban, T. A. Johnson, N. Proite, T. Henage, T. G. Walker, and M. Saffman. **Fast Ground State Manipulation of Neutral Atoms in Microscopic Optical Traps**. *Physical Review Letters*, **96**:063001, February 2006. URL `http://dx.doi.org/10.1103/PhysRevLett.96.063001`.

[100] Y. R. P. Sortais, H. Marion, C. Tuchendler, A. M. Lance, M. Lamare, P. Fournet, C. Armellin, R. Mercier, G. Messin, A. Browaeys, and P. Grangier. **Diffraction-Limited Optics For Single-Atom Manipulation**. *Physical Review A*, **75**:013406, January 2007. URL `http://dx.doi.org/10.1103/PhysRevA.75.013406`.

[101] K. M. Fortier, S. Y. Kim, M. J. Gibbons, P. Ahmadi, and M. S. Chapman. **Deterministic Loading of Individual Atoms to a High-Finesse Optical Cavity**.

Physical Review Letters, **98**:233601, June 2007. URL http://dx.doi.org/10.1103/PhysRevLett.98.233601.

[102] M. Zhang, P. Zhang, M. S. Chapman, and L. You. **Controlled Splitting of an Atomic Wave Packet**. *Physical Review Letters*, **97**:070403, August 2006. URL http://dx.doi.org/10.1103/PhysRevLett.97.070403.

[103] M. Karski, L. Förster, J. M. Choi, A. Steffen, W. Alt, D. Meschede, and A. Widera. **Quantum Walk in Position Space with Single Optically Trapped Atoms**. *Science*, **325**:174–177, July 2009. URL http://dx.doi.org/10.1126/science.1174436.

[104] T. L. Gustavson, A. P. Chikkatur, A. E. Leanhardt, A. Görlitz, S. Gupta, D. E. Pritchard, and W. Ketterle. **Transport of Bose-Einstein Condensates with Optical Tweezers**. *Physical Review Letters*, **88**:020401, December 2001. URL http://dx.doi.org/10.1103/PhysRevLett.88.020401.

[105] A. E. Leanhardt, A. P. Chikkatur, D. Kielpinski, Y. Shin, T. L. Gustavson, W. Ketterle, and D. E. Pritchard. **Propagation of Bose-Einstein Condensates in a Magnetic Waveguide**. *Physical Review Letters*, **89**:040401, July 2002. URL http://dx.doi.org/10.1103/PhysRevLett.89.040401.

[106] William D. Phillips. **Nobel Lecture: Laser Cooling and Trapping of Neutral Atoms**. *Reviews of Modern Physics*, **70**:721, 1998. URL http://dx.doi.org/10.1103/RevModPhys.70.721.

[107] Harold J. Metcalf and Peter van der Straten. **Laser Cooling and Trapping**. *Springer*, ISBN 110-700-217-6, 1999.

[108] A. Haase, D. Cassettari, B. Hessmo, and J. Schmiedmayer. **Trapping Neutral Atoms with a Wire**. *Physical Review A*, **64**:043405, September 2001. URL http://dx.doi.org/10.1103/PhysRevA.64.043405.

[109] Michael E. Peskin and Dan V. Schroeder. **An Introduction To Quantum Field Theory**. *Westview Press*, ISBN 020-150-397-2, 1995.

[110] B. Odom, D. Hanneke, B. D'Urso, and G. Gabrielse. **New Measurement of the Electron Magnetic Moment Using a One-Electron Quantum Cyclotron**. *Physical Review Letters*, **97**:030801, July 2006. URL http://dx.doi.org/10.1103/PhysRevLett.97.030801.

[111] Robert Eisberg and Robert Resnick. **Quantum Physics of Atoms, Molecules, Solids, Nuclei, and Particles**. *Wiley*, ISBN 047-187-373-X, 1985.

[112] R. Folman, P. Krüger, J. Schmiedmayer, J. Denschlag, and C. Henkel. **Microscopic Atom Optics: From Wires to an Atom Chip**. *Advances In Atomic, Molecular, and Optical Physics*, **48**:263–356, July 2002. URL `http://dx.doi.org/10.1016/S1049-250X(02)80011-8`.

[113] Shannon Whitlock. **Bose-Einstein Condensates On A Magnetic Film Atom Chip**. *PhD Thesis: University of Oxford - Supervisor: Andrei Sidorov*, 2007.

[114] B. H. Bransden and C. J. Joachain. **Quantum Mechanics**. *Prentice Hall*, ISBN 058-235-691-1, 2000.

[115] M. Jääskeläinen and S. Stenholm. **Localization in Splitting of Matter Waves**. *Physical Review A*, **68**:033607, September 2003. URL `http://dx.doi.org/10.1103/PhysRevA.68.033607`.

[116] B. O'Sullivan, P. Morrissey, T. Morgan, and Th. Busch. **Using Adiabatic Coupling Techniques in Atom-Chip Waveguide Structures**. *Physica Scripta*, **T140**:014029, September 2010. URL `http://dx.doi.org/10.1088/0031-8949/2010/T140/014029`.

[117] M. A. Cirone, A. Negretti, T. Calarco, P. Krüger, and J. Schmiedmayer. **A Simple Quantum Gate With Atom Chips**. *The European Physical Journal D*, **35**:165–171, June 2005. URL `http://dx.doi.org/10.1140/epjd/e2005-00175-8`.

[118] O. Zobay and B. M. Garraway. **Two-Dimensional Atom Trapping in Field-Induced Adiabatic Potentials**. *Physical Review Letters*, **86**:11951198, February 2001. URL `http://dx.doi.org/10.1103/PhysRevLett.86.1195`.

[119] O. Zobay and B. M. Garraway. **Atom Trapping and Two-Dimensional Bose-Einstein Condensates in Field-Induced Adiabatic Potentials**. *Physical Review A*, **69**:023605, February 2004. URL `http://dx.doi.org/10.1103/PhysRevA.69.023605`.

[120] O. Zobay and B. M. Garraway. **Two-Dimensional Atom Trapping in Field-Induced Adiabatic Potentials**. *Physical Review Letters*, **86**:1195–1198, February 2001. URL `http://dx.doi.org/10.1103/PhysRevLett.86.1195`.

[121] T. Schumm, S. Hofferberth, L. M. Andersson, S. Wildermuth, S. Groth, I. Bar-Joseph, J. Schmiedmayer, and P. Krüger. **A Double Well Interferometer on an Atom Chip**. *Quantum Information Processing*, **5**:537–558, December 2006. URL `http://dx.doi.org/10.1007/s11128-006-0033-2`.

[122] S. Hofferberth, B. Fischer, T. Schumm, J. Schmiedmayer, and I. Lesanovsky. **Ultracold Atoms in Radio-Frequency Dressed Potentials Beyond the**

Rotating-Wave Approximation. *Physical Review A*, **76**:013401, July 2007. URL http://dx.doi.org/10.1103/PhysRevA.76.013401.

[123] Ph. W. Courteille, B. Deh, A. Günther J. Fortágh, S. Kraft, C. Marzok, S. Slama, and C. Zimmermann. **Highly Versatile Atomic Micro Traps Generated by Multifrequency Magnetic Field Modulation**. *Journal of Physics B*, **39**:1055, February 2006. URL http://dx.doi.org/10.1088/0953-4075/39/5/005.

[124] T. Fernholz, R. Gerritsma, P. Krüger, and R. J. C. Spreeuw. **Dynamically Controlled Toroidal and Ring-Shaped Magnetic Traps**. *Physical Review A*, **75**:063406, June 2007. URL http://dx.doi.org/10.1103/PhysRevA.75.063406.

[125] I. Lesanovsky, T. Schumm, S. Hofferberth, L. M. Andersson, P. Krüger, and J. Schmiedmayer. **Adiabatic Radio-Frequency Potentials for the Coherent Manipulation of Matter Waves**. *Physical Review A*, **73**:033619, March 2006. URL http://dx.doi.org/10.1103/PhysRevA.73.033619.

[126] Jie Liu, Biao Wu, and Qian Niu. **Nonlinear Evolution of Quantum States in the Adiabatic Regime**. *Physical Review Letters*, **90**:170404, May 2003. URL http://dx.doi.org/10.1103/PhysRevLett.90.170404.

[127] Marcus Gildemeister. **Trapping Ultracold Atoms In Time-Averaged Adiabatic Potentials**. *PhD Thesis: University of Oxford - Supervisor: Christopher Foot*, 2010.

[128] W. Ketterle and N. J. van Druten. **Evaporative Cooling of Trapped Atoms**. *Advanced Molecular and Optical Physics*, **37**:181–236. URL http://dx.doi.org/10.1016/S1049-250X(08)60101-9.

[129] J. Mompart, K. Eckert, W. Ertmer, G. Birkl, and M. Lewenstein. **Quantum Computing with Spatially Delocalized Qubits**. *Physical Review Letters*, **90**:147901, April 2003. URL http://dx.doi.org/10.1103/PhysRevLett.90.147901.

[130] A. Smerzi, S. Fantoni, S. Giovanazzi, , and S. R. Shenoy. **Quantum Coherent Atomic Tunneling between Two Trapped Bose-Einstein Condensates**. *Physical Review Letters*, **79**:4950, December 1997. URL http://dx.doi.org/10.1103/PhysRevLett.79.4950.

[131] I. Marino, S. Raghavan, S. Fantoni, S. R. Shenoy, and A. Smerzi. **Bose-Condensate Tunneling Dynamics: Momentum-Shortened Pendulum With Damping**. *Physical Review A*, **60**:487–493, July 1999. URL http://dx.doi.org/10.1103/PhysRevA.60.487.

[132] M. Olshanii. **Atomic Scattering in the Presence of an External Confinement and a Gas of Impenetrable Bosons**. *Physical Review Letters*, **81**:938–941, August 1998. URL http://dx.doi.org/10.1103/PhysRevLett.81.938.

[133] Guan-Fang Wang, Di-Fa Ye, Li-Bin Fu, Xu-Zong Chen, and Jie Liu. **Landau-Zener Tunneling in a Nonlinear Three-Level System**. *Physical Review A*, **74**:033414, September 2006. URL http://dx.doi.org/10.1103/PhysRevA.74.033414.

[134] J. Bell. **Against Measurement**. *Physics World*, **3**:33–41, Aug 1990. URL http://physicsworldarchive.iop.org/summary/pwa-xml/3/8/phwv3i8a26.

[135] Yu. Kagan and A. J. Leggett. **Quantum Tunnelling in Condensed Media**. *North Holland*, ISBN 044-488-041-0, 1992.

[136] Steven Tomsovic. **Tunneling in Complex Systems**. *World Scientific*, ISBN 981-023-446-5, 1998.

[137] Joachim Ankerhold. **Quantum Tunneling in Complex Systems: The Semiclassical Approach**. *Springer*, ISBN 354-068-074-8, 2007.

[138] F. Hund. **Zur Quantentheorie des Atomkernes**. *Zeitschrift für Physik*, **40**: 742, 1927.

[139] G. Gamow. **Zur Quantentheorie des Atomkernes**. *Zeitschrift für Physik*, **51**: 204, 1928.

[140] Gurney and Condon. **Wave Mechanics and Radioactive Disintegration**. *Nature*, **122**:439, September 1928. URL http://dx.doi.org/10.1038/122439a0.

[141] B. V. Hall, S. Whitlock, R. Anderson, P. Hannaford, and A. I. Sidorov. **Condensate Splitting in an Asymmetric Double Well for Atom Chip Based Sensors**. *Physical Review Letters*, **98**:030402, January 2007. URL http://dx.doi.org/10.1103/PhysRevLett.98.030402.

[142] D. R. Dounas-Frazer, A. M. Hermundstad, and L. D. Carr. **Ultracold Bosons in a Tilted Multilevel Double-Well Potential**. *Physical Review Letters*, **99**: 200402, November 2007. URL http://dx.doi.org/10.1103/PhysRevLett.99.200402.

[143] C. Menotti, J. R. Anglin, J. I. Cirac, and P. Zoller. **Dynamic Splitting of a Bose-Einstein Condensate**. *Physical Review A*, **63**:023601, January 2001. URL http://dx.doi.org/10.1103/PhysRevA.63.023601.

[144] L. D. Carr, D. R. Dounas-Frazer, and M. A. Garcia-March. **Dynamical Realization of Macroscopic Superposition States of Cold Bosons in a Tilted Double Well**. *Europhysics Letters*, **90**:100005, April 2010. URL http://dx.doi.org/10.1209/0295-5075/90/10005.

[145] M. A. García-March, D. R. Dounas-Frazer, and L. D. Carr. **Macroscopic Superposition of Ultracold Atoms with Orbital Degrees of Freedom**. *Physical Review A*, **83**:043612, April 2011. URL http://dx.doi.org/10.1103/PhysRevA.83.043612.

[146] P. O. Löwdin. **Proton Tunneling in DNA and its Biological Implications**. *Reviews of Modern Physics*, **35**:724–732, 1963. URL http://dx.doi.org/10.1103/RevModPhys.35.724.

[147] H. W. Fink and C. Schönenberger. **Electrical Conduction Through DNA Molecules**. *Nature Letters*, **398**:407–410, April 1998. URL http://dx.doi.org/10.1038/18855.

[148] K. Kohen and J. P. Klinman. **Hydrogen Tunneling in Biology**. *Chemistry and Biology*, **6**:R191–R198, July 1999. URL http://dx.doi.org/10.1016/S1074-5521(99)80058-1.

[149] H. Yamada and K. Iguchi. **Some Effective Tight-Binding Models for Electrons in DNA Conduction: A Review**. *Physical Review Letters*, **2010**:380710, May 2010. URL http://dx.doi.org/10.1155/2010/380710.

[150] C. R. Moylan and J. I. Brauman. **Advances in Classical Trajectory Methods**. *JAI Press*, ISBN 999-479-042-0, 1994.

[151] John Clarke and Alex I. Braginski. **The SQUID Handbook: Fundamentals and Technology of SQUIDs and SQUID Systems**. *Wiley*, ISBN 352-740-229-2, 2004.

[152] C. Weitenberg, M. Endres, J. F. Sherson, M. Cheneau, P. Schauß, T. Fukuhara, I. Bloch, and S. Kuhr. **Single-Spin Addressing in an Atomic Mott Insulator**. *Nature*, **471**:319–324, March 2011. URL http://dx.doi.org/10.1038/nature09827.

[153] P. Harrison. **Quantum Wells Wires and Dots**. *Wiley*, ISBN 047-077-097-X, 2009.

[154] R. Grimm, M. Weidemüller, and Y. B. Ovchinnikov. **Optical Dipole Traps For Neutral Atoms**. *Advances In Atomic, Molecular, and Optical Physics*, **42**:95–170, April 2000. URL http://dx.doi.org/10.1016/S1049-250X(08)60186-X.

[155] P. Krüger, L. M. Andersson, S. Wildermuth, S. Hofferberth, E. Haller, S. Aigner, S. Groth, I. Bar-Joseph, and J. Schmiedmayer. **Potential Roughness Near Lithographically Fabricated Atom Chips**. *Physical Review A*, **76**:063621, December 2007. URL http://dx.doi.org/10.1103/PhysRevA.76.063621.

[156] J. E. Lye, L. Fallani, M. Modugno, D. S. Wiersma, C. Fort, and M. Inguscio. **Bose-Einstein Condensate in a Random Potential**. *Physical Review Letters*, **95**:070401, August 2005. URL http://dx.doi.org/10.1103/PhysRevLett.95.070401.

[157] G. Sinuco-León, B. Kaczmarek, P. Krüger, and T. M. Fromhold. **Atom Chips With Two-Dimensional Electron Gases: Theory Of Near-Surface Trapping And Ultracold-Atom Microscopy Of Quantum Electronic Systems**. *Physical Review A*, **83**:021401(R), February 2011. URL http://dx.doi.org/10.1103/PhysRevA.83.021401.

[158] B. D. Josephson. **Possible New Effects in Superconductive Tunnelling**. *Physics Letters*, **1**:251–253, 1962. URL http://dx.doi.org/10.1016/0031-9163(62)91369-0.

[159] J. M. Schmidt, A. N. Cleland, and J. Clarke. **Resonant Tunneling in Small Current-Biased Josephson Junctions**. *Physical Review B*, **43**:229–238, January 1991. URL http://dx.doi.org/10.1103/PhysRevB.43.229.

[160] A. J. Leggett. **Bose-Einstein Condensation in the Alkali Gases: Some Fundamental Concepts**. *Reviews of Modern Physics*, **73**:307–356, April 2001. URL http://dx.doi.org/10.1103/RevModPhys.73.307.

[161] L. J. LeBlanc, A. B. Bardon, J. McKeever, M. H. T. Extavour, D. Jervis, and J. H. Thywissen. **Dynamics of a Tunable Superfluid Junction**. *Physical Review Letters*, **106**:025302, January 2011. URL http://dx.doi.org/10.1103/PhysRevLett.106.025302.

[162] J. Javanainen. **Oscillatory Exchange of Atoms between Traps Containing Bose Condensates**. *Physical Review Letters*, **57**:3164–3166, December 1986. URL http://dx.doi.org/10.1103/PhysRevLett.57.3164.

[163] R. Gati, M. Albiez, J. Fölling, B. Hemmerling, and M. K. Oberthaler. **Realisation of a Single Josephson Junction for Bose-Einstein Condensates**. *Journal of Applied Physics B: Lasers And Optics*, **82**:207, December 2006. URL http://dx.doi.org/10.1007/s00340-005-2059-z.

[164] J. G. Milburn, J. Corney, E. M. Wright, and D. F. Walls. **Quantum Dynamics of an Atomic Bose-Einstein Condensate in a Double Well Potential**. *Physical Review A*, **55**:4318–4324, 1997. URL http://dx.doi.org/10.1103/PhysRevA.55.4318.

[165] S. Raghavan, A. Smerzi, S. Fantoni, and S. R. Shenoy. **Coherent Oscillations Between Two Weakly Coupled Bose-Einstein Condensates: Josephson Effects, Oscillations, and Macroscopic Quantum Self-Trapping**. *Physical Review A*, **59**:620, January 1999. URL http://dx.doi.org/10.1103/PhysRevA.59.620.

[166] M. Albiez, R. Gati, J. Fölling, S. Hunsmann, M. Cristiani, and M. K. Oberthaler. **Direct Observation of Tunneling and Nonlinear Self-Trapping in a Single Bosonic Josephson Junction**. *Physical Review Letters*, **83**:010402, June 2005. URL http://dx.doi.org/10.1103/PhysRevLett.95.010402.

[167] L. Fu and J. Liu. **Quantum Entanglement Manifestation of Transition to Nonlinear Self-Trapping for Bose-Einstein Condensates in a Symmetric Double Well**. *Physical Review A*, **74**:063614, December 2006. URL http://dx.doi.org/10.1103/PhysRevA.74.063614.

[168] G. Rastelli. **Semiclassical Formula For Quantum Tunneling in Asymmetric Double-Well Potentials**. *Physical Review A*, **86**:012106, July 2012. URL http://dx.doi.org/10.1103/PhysRevA.86.012106.

[169] E. Arimondo. **Coherent Population Trapping in Laser Spectroscopy**. *Progress In Optics*, **35**:257–354, 1996. URL http://dx.doi.org/10.1016/S0079-6638(08)70531-6.

[170] T. Opatrný and K. K. Das. **Conditions for Vanishing Central-Well Population in Triple-Well Adiabatic Transport**. *Physical Review A*, **79**:012113, January 2009. URL http://dx.doi.org/10.1103/PhysRevA.79.012113.

[171] T. Morgan, B. O'Sullivan, and Th. Busch. **Coherent Adiabatic Transport of Atoms in Radio-Frequency Traps**. *Physical Review A*, **83**:053620, May 2011. URL http://dx.doi.org/10.1103/PhysRevA.83.053620.

[172] K. Singer, U. Poschinger, M. Murphy, P. Ivanov, F. Ziesel, T. Calarco, and F. Schmidt-Kaler. **Colloquium: Trapped Ions as Quantum Bits: Essential Numerical Tools**. *Reviews of Modern Physics*, **82**:2609–2632, September 2010. URL http://dx.doi.org/10.1103/RevModPhys.82.2609.

[173] M. V. Berry. **Quantal Phase Factors Accompanying Adiabatic Changes**. *Proceedings of the Royal Society A*, **392**:45–57, March 1984. URL `http://rspa.royalsocietypublishing.org/content/392/1802/45`.

[174] K. Eckert, M. Lewenstein, R. Corbalán, G. Birkl, W. Ertmer, and J. Mompart. **Three-Level Atom Optics Via the Tunneling Interaction**. *arXiv/quant-ph/0308041*, August 2003. URL `http://arxiv.org/abs/quant-ph/0308041`.

[175] D. Chruściński and A. Jamiolkowski. **Geometric Phases in Classical and Quantum Mechanics**. *Birkhäuser*, ISBN 081-764-282-X, 2004.

[176] S. Pollock, J. P. Cotter, A. Laliotis, and E. A. Hinds. **Integrated Magneto-Optical Traps on a Chip Using Silicon Pyramid Structures**. *Optics InfoBase*, **17**:14109–14114, 2009. URL `http://dx.doi.org/10.1364/OE.17.014109`.

[177] B. Darquié, M.P.A. Jones, J. Dingjan, J. Beugnon, S. Bergamini, Y. Sortais, G. Messin, A. Browaeys, and P. Grangier. **Controlled Single-Photon Emission from a Single Trapped Two-Level Atom**. *Science*, **309**:454–456, July 2005. URL `http://dx.doi.org/10.1126/science.1113394`.

[178] B. Murphy and L. Vestergaard Hau. **Electro-Optical Nanotraps for Neutral Atoms**. *Physical Review Letters*, **102**:033003, January 2009. URL `http://dx.doi.org/10.1103/PhysRevLett.102.033003`.

[179] J. F. Sherson, C. Weitenberg, M. Endres, M. Cheneau, I. Bloch, and S. Kuhr. **Single-Atom-Resolved Fluorescence Imaging of an Atomic Mott Insulator**. *Nature*, **467**:68–72, August 2010. URL `http://dx.doi.org/10.1038/nature09378`.

[180] V. Boyer, R. M. Godun, G. Smirne, D. Cassettari, C. M. Chandrashekar, A. B. Deb, Z. J. Laczik, and C. J. Foot. **Dynamic Manipulation of Bose-Einstein Condensates with a Spatial Light Modulator**. *Physical Review A*, **73**:031402(R), March 2006. URL `http://dx.doi.org/10.1103/PhysRevA.73.031402`.

[181] J. R. Kuklinski, U. Gaubatz, F. T. Hioe, and K. Bergmann. **Adiabatic Population Transfer in a Three-Level System Driven by Delayed Laser Pulses**. *Physical Review A*, **40**:6741–6744, December 1989. URL `http://dx.doi.org/10.1103/PhysRevA.40.6741`.

[182] R. G. Unanyan, B. W. Shore, and K. Bergmann. **Laser-driven Population Transfer in Four-Level Atoms: Consequences of non-Abelian Geometrical Adiabatic Phase Factors**. *Physical Review A*, **59**:2910, August 1998. URL `http://dx.doi.org/10.1103/PhysRevA.59.2910`.

[183] J. D. Faires and R. Burden. **Numerical Methods**. *Brooks - Cole*, ISBN 053-440-761-7, 1998.

[184] S. Jin, S. Gong, R. Li, and Z. Xu. **Coherent Population Transfer and Superposition of Atomic States via Stimulated Raman Adiabatic Passage Using an Excited-Doublet Four-Level Atom**. *Physical Review A*, **69**:023408, February 2004. URL `http://dx.doi.org/10.1103/PhysRevA.69.023408`.

[185] David K. Cheng. **Field and Wave Electromagnetics**. *Addison-Wesley Publishing Company*, ISBN 020-112-819-5, 1992.

[186] James Stewart. **Calculus: Early Transcendentals**. *Brooks Cole*, ISBN 049-501-166-5, 2007.

[187] H. Erlichson. **Ampère was not the Author of Ampères Circuital Law**. *American Journal of Physics*, **67**:448–450, May 1999. URL `http://ajp.aapt.org/resource/1/ajpias/v67/i5/p448_s1`.

[188] M. D. Feit and J. A. Fleck. **Simple Spectral Method For Solving Propagation Problems in Cylindrical Geometry with Fast Fourier Transforms**. *Optics Letters*, **14**:662–664, March 1989. URL `http://dx.doi.org/10.1364/OL.14.000662`.